Stony Brook University

Multifunctional Iron-Based Metal Oxide Nanostructured Materials:

Synthesis, Characterization, and Properties

A Dissertation Presented

by

Tae-Jin Park

to

The Graduate School

in Partial Fulfillment of the

Requirements

for the Degree of

Doctor of Philosophy

in

Chemistry

Stony Brook University

August 2007

Stony Brook University

The Graduate School

Tae-Jin Park

We, the dissertation committee for the above candidate for the

Doctor of Philosophy degree, hereby recommend

acceptance of this dissertation.

Stanislaus S. Wong – Dissertation Advisor
Associate Professor, Department of Chemistry

Michael G. White – Chairperson of Defense
Professor and Chair, Department of Chemistry

David H. Hanson – Third Member
Professor, Department of Chemistry

Meigan Aronson – Outside Member
Professor, Department of Physics

This dissertation is accepted by the Graduate School

Lawrence Martin
Dean of the Graduate School

Abstract of the Dissertation

Multifunctional Iron-Based Metal Oxide Nanostructured Materials:

Synthesis, Characterization, and Properties

by

Tae-Jin Park

Doctor of Philosophy

in

Chemistry

Stony Brook University

2007

Iron-based metal oxides, such as iron oxides, iron-containing perovskites, and iron-containing perovskite composites or solid solutions, are promising materials for the design and synthesis of technologically important multifunctional materials. They are noteworthy for their unique and diverse properties including electronic, magnetic, and elastic ones. Stimulated by interest in the bulk properties of these materials as well as scientific potential and applications at the nanoscale, iron-based metal oxide nanostructured (FeMONS) materials are being considered as an interesting model system to investigate fundamental properties and for a host of potential applications as diverse as additives, catalysts, electronic devices, magnetic recording media, information storage, spintronics, and sensors.

Recent research on a multiferroic system, such as $BiFeO_3$, reveals that there are unique couplings among the independent physical properties including ferroelectricity, ferromagnetism, and ferroelasticity. Developing approaches to designing as well as investigating properties of new synthetic formulations of these transition metal oxide nanomaterials has been the recent focus of much of our efforts in this group. Multiferroic bismuth ferrite ($BiFeO_3$) nanoparticles have been synthesized employing a facile sol-gel method and their size-dependent magnetic properties have been studied and correlated with: (i) increased suppression of the known spiral spin structure (period length of ~62 nm) with decreasing nanoparticle size and (ii) uncompensated spins and strain

anisotropies at the surface. Moreover, $BiFeO_3$ nanotubes have been generated using a modified template methodology and extensively characterized. Furthermore, solid solutions of $BiFeO_3$ and typical perovskites, such as $BaTiO_3$ and $SrTiO_3$, have been prepared employing a molten salt method and the study has been extended to properties associated with their inherent compositions. Single-crystalline $Bi_2Fe_4O_9$ nanocubes have been fabricated utilizing a molten salt method and the role of various experimental parameters has been examined towards predictive control of shape and size. Single-crystalline iron oxide (α-Fe_2O_3) rhombohedra have been generated using environmentally friendly protocols and transformed into aggregates of magnetic nanocomposites of Fe and Fe_3O_4.

Dedicated to:

My family (wife, son and expectant daughter) and parents, with love

Table of Contents

List of Abbreviations

Γ: full width at half maximum
δ: isomer shift
θ: paramagnetic Curie temperature
μ_B: Bohr magneton
μm: micrometer (10^{-6} m)
θ_p: paramagnetic Curie temperature
ΔE_Q: quadrupole splitting
0-D: zero dimensional
1-D: one dimensional
2-D: two dimensional
AAO: porous anodic alumina
AFM: atomic force microscope
BFO: $BiFeO_3$
BSCCO: bismuth strontium calcium copper oxide
BTO: $BaTiO_3$
C: Curie constant
coth: hyperbolic cotangent
d: diameter
d: width
DOE: department of energy
DRAM: dynamic random access memory
E: electric field
ED: electron diffraction
EDS: energy-dispersive X-ray spectroscopy
EELS: electron energy loss near edge structure spectroscopy
EGB: entrance grid bias
ELNES: electron energy loss spectrum
EtOH: ethanol
eV: electron voltage
EY: electron yield
FC: field cooling
fcc: face-centered cubic
FeMONS: iron-based metal oxide nanostructured
FWHM: full width half maximum
H: an applied magnetic field
H_{appl}: applied magnetic field

H_C: coercivity
H_{ex}: exchange bias magnetization
H_{hf}: magnetic hyperfine field
HRTEM: high-resolution transmission electron microscope
HS: Hartree-Slater
IR: infrared
JCPDS: joint committee for powder emission studies
K: Kelvin
$L(x)$: Langevin function
l: length
M: magnetization
MEB: molecular beam epitaxy
MeOH: methanol
MOS: metal oxide semiconductor
MPMS: magnetic property measurement system
M_r: remnant magnetization
MS: multiple-scattering
M_S: saturation magnetization
NEXAFS: near edge X-ray absorption fine structure
nm: nanometer (10^{-9} m)
NP-9: Igepal® CO-630, nonylphenyl ether
NP: nanoparticle
NPs: nanoparticles
ns: nanoseconds (10^{-9} s)
NS: nanostructures
NSLS: national synchrotron light source
NT: nanotube
NTs: nanotubes
NVRAM: nonvolatile random access memory
^oC: degree Celsius
Oe: Oersted
O_h: Octahedral
ORR: oxygen reduction reaction
PEMFC: polymer electrolyte membrane fuel cell
PEY: partial electron yield
PLD: pulsed laser deposition
PZT: $Pb(Zr,Ti)O_3$
R: radius
RT: room temperature

S/V: surface-to-volume
SAED: selected area electron diffraction
SEM: scanning electron microscope
SI: international system of units
SPM: scanning probe microscope
SPM: superparamagnetic
SQUID: superconducting quantum interference device
STM: scanning tunneling microscope
T: temperature
t: wall thickness
T_B: blocking temperature
T_C: Curie temperature
T_d: tetrahedral
TEM: transmission electron microscope
T_{max}: spin-glass-like freezing temperature
T_N: Néel temperature
UHV: ultra-high vacuum
UV-Vis: ultraviolet-visible
w.r.t.: with respect to
XANES: X-ray absorption near edge spectroscopy
XAS: X-ray absorption spectroscopy
XPS: X-ray photoelectron spectroscopy
XRD: X-ray diffraction
ZFC: zero field cooling
ε: quadrupole splitting
σ: elastic force

List of Figures

List of Tables

Acknowledgements

First of all I would like to thank my advisor, Prof. Stanislaus S. Wong, for his support, insight, guidance, and encouragement at all times. His enthusiasm and drive have been an inspiration to me. I am immensely grateful to Prof. Michael G. White for his interest in my work, and encouragement and insight through these years. I am also very grateful to Prof. David M. Hanson for all of his comments and encouragement. Special thanks to Prof. Meigan Aronson for serving on my committee, as well as for all of her interest and help.

A special word of thanks to the members of the Wong group: Jingyi Chen, Hongjun Zhou, Fen Zhang, Alexander Santulli, Jonathan Patete, and Xiaohui Peng; and the Wong group alumni: Mandakini Kanungo, Sabarjit Banerjee, Tirandai Hemraj-Benny, Yuanbing Mao, Michael Kahn, Alexander Ho, and the late Yi Sun for their thoughtful discussions as well as sharing a great time with me in this group.

I gratefully acknowledge the support and assistance given to me by the students, faculty, scientists, and technical support staff of the Department of Chemistry (Stony Brook University) as well as Condensed Matter Physics and Materials Science Department (Brookhaven National Laboratory), both past and present. In particular, I would like to thank Dr. James Quinn for all of his help on electron microscopy. Without him research would have been very much delayed. I would also like to acknowledge Dr. Arnold R. Moodenbaugh for his thoughtful support on the use and analysis of magnetic property measurement system (MPMS) magnetometer. Dr. Daniel A. Fisher and Dr. Sharadha Sambasivan are gratefully acknowledged for their introducing me to the field of soft X-ray absorption spectroscopy and for useful discussions. I am extremely grateful to Dr. Won-Sub Yoon for his helpful discussions on NEXAFS data analysis, to Dr. Yongjae Lee for his thoughtful help and analysis on X7A XRD data, to Dr. Kyungha Kang for his many insightful discussions on SQUID as well as fundamentals of magnetic materials, and to Dr. Young-Suk Choi for his thoughtful help on SQUID measurements in need.

I would like to thank Dr. Georgia C. Papaefthymiou at Villanova University for her insightful discussions on Mössbauer and magnetic studies, whose knowledge I have drawn on so many times. I acknowledge Dr. K. Trohidou (NCSR Demokritos) and Dr. C. Binns (University of Leicester) for their valuable discusstions on Mössbauer data. I am also grateful to Dr. Jianyu Huang at Boston College for all of his assistance with the HRTEM work, and to Dr. Zhorro Nikolov at Drexel Univeristy for his help with the Raman measurements. ACS Division of Inorganic Chemistry (DIC) as well as Sigma Xi are acknowledged for support for travel.

I am greatly grateful to all of my Korean and Stony Brook friends, for their support and motivation. I thank my parents for being an example of hard work and for always

supporting and believing in me. Last but not least, I thank my wife and son for their presence and supports during all this years. Their love and support were essential.

Vita

Tae-Jin Park was born in Seoul, Korea. He earned BSc and MSc degrees in Chemistry from Yonsei University in 1997 and 1999, respectively. After completing mandatory military service in Republic of Korea (ROK) Army in 2001, he worked as a research scientist at the Korea Institute of Science and Technology (KIST). He has been a graduate student in Chemistry at Stony Brook University, New York since August 2002. He was one of the recipients of the Chemistry Award for Excellence in Doctoral Research at Stony Brook University in 2007. His Ph.D. research interests include the synthesis, characterization, and properties of nanoscale functional materials, such as iron-based metal oxide perovskites as well as the purification, functionalization and structural characterization of single-walled carbon nanotubes.

Publications

(13) Tae-Jin Park, Sharadha Sambasivan, Daniel A. Fischer, James A. Misewich, and Stanislaus S. Wong, "Electronic Structure and Chemistry of Iron-Based Metal Oxide Nanostructures: $BiFeO_3$, $Bi_2Fe_4O_9$, α-Fe_2O_3, Fe/Fe_3O_4," (2007) *in preparation*.

(12) Fen Zhang, Yuanbing Mao, Tae-Jin Park, and Stanislaus S. Wong, "Green Synthesis and Magneto-Optical Characterization of Single-Crystalline Perovskite Fluoride Nanorods," *Adv. Funct. Mater*. (2007) *submitted for publication*.

(11) Yuanbing Mao, Tae-Jin Park, Hongjun Zhou, Fen Zhang, and Stanislaus S. Wong, "Environmentally Friendly Methodologies of Nanostructure Synthesis," *Small* **3**, 1122 (2007).

(10) Tae-Jin Park, Georgia C. Papaefthymiou, Arthur J. Viescas, Arnold R. Moodenbaugh, and Stanislaus S. Wong, "Size-Dependent Magnetic Properties of Single-Crystalline Multiferroic $BiFeO_3$ Nanoparticles," *Nano Lett.* **7**, 766 (2007).

(9) Tae-Jin Park and Stanislaus S. Wong, "As-Prepared Single-Crystalline Hematite Rhombohedra and Subsequent Conversion into Monodisperse Aggregates of Magnetic Nanocomposites of Iron and Magnetite," *Chem. Mater*. **18**, 5289 (2006).

(8) Hongjun Zhou, Tae-Jin Park, and Stanislaus S. Wong, "Synthesis, Characterization, and Photocatalytic Properties of Pyrochlore $Bi_2Ti_2O_7$ Nanotubes," *J. Mater. Res.* **21**, 2941 (2006).

(7) Jung Su Park, Tae-Jin Park, Ki-Hyun Kim, Kyungeun Oh, Mi-Sook Seo, Hong-In Lee, Moo-Jin Jun, Wonwoo Nam, and Kwan Mook Kim, "Synthesis and Characterization of High-Spin Cobalt(II)-Based "Inorganic Tennis Ball"," *Bull. Korean Chem. Soc*. **27**, 193 (2006).

(6) Tae-Jin Park, Sarbajit Banerjee, Tirandai Hemraj-Benny, and Stanislaus S. Wong, "Purification strategies and purity visualization techniques for single-walled carbon nanotubes," *J. Mater. Chem*. (cover; Feature Article) **16**, 141 (2006).

(5) Yuanbing Mao, Tae-Jin Park, and Stanislaus S. Wong, "Synthesis of classes of ternary metal oxide nanostructures," *Chem. Commun.* (inside cover; Feature Article) **(46)**, 5721 (2005).

(4) Tae-Jin Park, Georgia C. Papaefthymiou, Arnold R. Moodenbaugh, Yuanbing Mao, and Stanislaus S. Wong, "Synthesis and characterization of submicron single-crystalline $Bi_2Fe_4O_9$ cubes," *J. Mater. Chem.* (inside cover; Hot Article) **15(21)**, 2099 (2005).

(3) Tae-Jin Park, Yuanbing Mao, and Stanislaus S. Wong, "Synthesis and characterization of multiferroic $BiFeO_3$ nanotubes," *Chem. Commun.* **(23)**, 2078 (2004).

(2) Seong Huh, Youngmee Kim, Seongsoon Park, Tae-Jin Park, and Moo-Jin Jun, "*trans*-Carbonyl[η^2-dihydrobis(pyrazol-1-yl-N^2)borato]hydridobis(triphenylarsine)ruthenium(II) monohydrate," *Acta Cryst*. *C* **55**, 850 (1999).

(1) Tae-Jin Park, Seong Huh, Youngmee Kim, and Moo-Jin Jun, "Dichloro[ferrocene-1,1'-diylbis(diphenylphosphine-*P*)]cobalt(II)," *Acta Cryst*. *C* **55**, 848 (1999).

Chapter I. Introduction

1.1. Nanoscience and nanotechnology

One of the most interesting and promising areas in modern science and technology is the study of nanomaterials due to their numerous potential applications in various fields. Scientific journals including *Nature Materials, Nano Letters, Small, Nanotechnology, Journal of Nanoscience and Nanotechnology, International Journal of Nanosciences,* and *International Journal of Nanotechnology* have all devoted special issues to various aspects of this field of "Nanoscience." The focus of this particular dissertation is based on chemical nanoscience, specifically the synthesis, characterization, and properties of nanomaterials.

"Nano" is derived from the Greek word for *dwarf* and is a prefix in the SI system of units denoting a factor of 10^{-9}. Thus, nano- is used in prefixing time or length units, for example, nanoseconds (ns) and nanometers (nm). In particular, one nanometer is equal to one-billionth of a meter, and ten nanometers are equal to one-thousandth the diameter of human hair. Moreover, nano- can be used as a prefix for something other than a unit of measure, as in nanoscience, which relates to nanotechnology or to a scale of nanometers. To provide clear perspective of the nanometer scale, the chart of "The scale of things", which is available on the website of Office of Basic Energy Sciences,[1] illustrates the sizes of things natural as well as man-made, as shown in Figure 1.1. Atoms are below a nanometer scale, whereas many molecules, including some of proteins, range from a nanometer and upwards.

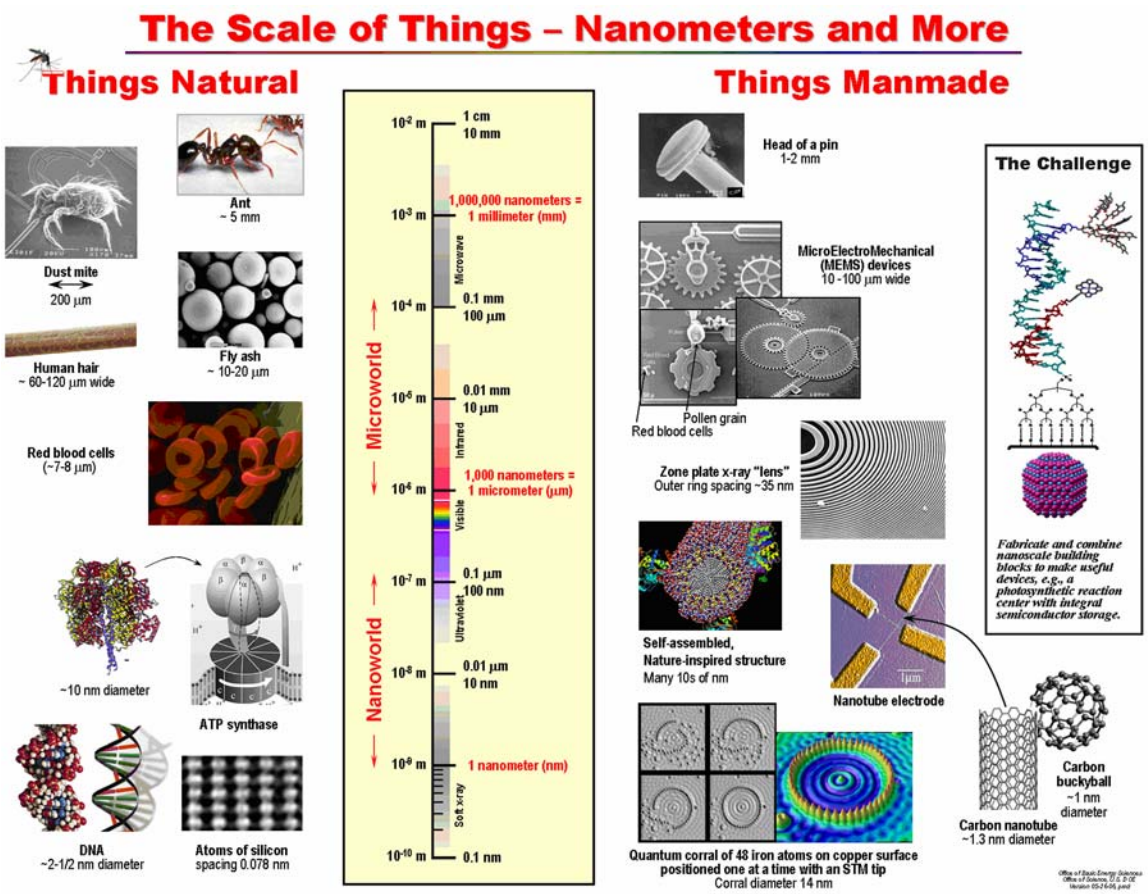

Figure 1.1. Natural as well as man-made things at a nanometer length scale and a micrometer length scale for comparison. Reproduced from the DOE website: http://www.science.doe.gov/bes/scale_of_things.html.

Since the discovery of the carbon nanotubes by Sumio Ijima in 1991,[2] the term "nano" has become widely used as a ubiquitous prefix in science and technology. Exploring the science of nanostructures has become, in just a few years, a new theme common to many disciplines, and "nano" is now recognized far more widely than is applicable due to the following reasons. Nanoscale building blocks, often called nanostructures, having at least one dimension of about 1 to 100 nm, have been found to exhibit a broad range of enhanced mechanical, optical, magnetic, and electronic properties relative to that of bulk materials or of microstructures of the same chemical composition.

In fact, the most successful example of nanoscience and nanotechnology can be found in Nature. Nature, as usual, has provided a considerable amount of proof that nanotechnology works, from the liposomes in cells that manufacture proteins atom by atom, to the chloroplasts of plants that turn sunlight, carbon dioxide, and water into copies of themselves.[3] Many colors and associated optical properties in the natural world also depend on nanostructures.[4,5] Since biological machines exist and work, scientists need to figure out how to build and apply synthetic nanostructures to this multidisciplinary and interdisciplinary nanoscience field. Furthermore, nanoscience was predicted very early on. For example, in his December 1959 Caltech talk, "There's plenty of room at the bottom", R.P. Feynmann envisaged the possibility of direct manipulation of individual atoms as a more powerful form of synthetic chemistry than those used at the time.[6]

For decades, microstructures, which are thousands of times larger than nanostructures, have formed the basis of our current technologies mostly in the materials science area, *e.g.*, in ceramics and alloy fabrication as well as in electronics. Although microstructures are small on the scale of direct human experience, their physics are still predominantly the same as that of macroscopic systems. It is only in recent years that sophisticated tools including the scanning tunneling microscope (STM) in 1982 and atomic force microscope (AFM) in 1986 have been developed so as to measure, characterize, and manipulate matters at nanoscale.[7] These instruments use nanoscale probes to image a surface with atomic resolution, and are also capable of picking up, sliding, or dragging atoms or molecules around on surfaces to build rudimentary nanostructures.[8]

Nanostructures are fundamentally different from microstructures. The characteristics of nanostructures, especially their electronic and magnetic properties, exhibit often significantly different properties from the same material in the bulk. Nanostructures are, in a sense, a unique state of matter – one with particular promise for new and potentially very useful products in electronics, catalysis, condensed matter physics, materials sciences, and molecular biology.[9-14] Thus, the ability to precisely control spatial arrangements of impurities and defects with respect to each other, and the

ability to integrate perfect inorganic and organic nanostructures holds forth the promise of a completely new generation of advanced composites.

Recent efforts to determine further the precise definition of nanoscience suggest that it could be the study of a single atom or a single molecule, that is, of one entity at time, and not only for groups of such entities where statistics or interactions between them come into play.[15] Whereas to provide reasonable universal agreement on the emerging and promising field of "nano", a Royal Society of London report *Nanoscience, and Nanotechnology: Opportunities and Uncertainties*, defined 'nanoscience' as follows[16]:

Nanoscience is the study of phenomena and manipulation of materials at atomic, molecular and macromolecular scales, where properties differ significantly from those at a larger scale.

In this dissertation, nanoscience refers to the definition suggested by Royal Society of London, and nanotechnology is associated with the design, characterization, production, and application of the matter by controlling its shape and size at either their nanoscale or atomic and molecular level in order to obtain materials and systems with significantly improved properties.

1.2. Categorization of nanomaterials

As we discussed in section 1.1, nanomaterials, either as nanoscale building blocks or nanostructures, are defined as possessing at least one dimension between 1 and 100 nm, a size that is small by engineering standards, common according to biological standards, and large with respect to chemists. In this dissertation, we categorize nanomaterials by their dimensional characteristics, such as zero-dimensional (0-D), one-dimensional (1-D), and two-dimensional (2-D) nanostructures.

0-D nanostructures include materials of which all of three dimensions occur at in the nanoscale (*i.e.*, 1 – 100 nm), such as isotropic nanoparticles (quantum dots, precipitates, colloids, cubes, fullerenes), as well as anisotropic nanoparticles (*e.g.*, rhombohedra).[17] A rich variety of chemical methods has been developed for generating quantum dots with well-controlled dimensions and from a broad range of materials.[18] With quantum dots as a model system, considerable amounts of interesting chemistry and physics can be learned by investigating the evolution of their fundamental properties with size.[19] For most of its applications, it is believed that the dimension of an individual quantum dot may represent the ultimate limit to the miniaturization of currently existing functional devices.

1-D nanostructures represent materials of which two of three dimensions are at the nanoscale (and extended in one dimension), including tubes (*e.g.*, carbon nanotubes), wires, rods, belts, and ribbons. It is generally accepted that 1-D nanomaterials provide a model system to investigate the dependence of electrical and thermal transport or mechanical properties on dimensionality and size reduction (or quantum confinement). Recent synthetic strategies for the fabrication of 1-D nanostructures include (i) anisotropic growth dictated by the crystallographic structure of a solid material; (ii) anisotropic growth confined and directed by various templates; and (iii) anisotropic growth kinetically controlled by supersaturation or through the use of an appropriate capping reagent.[20] However, even successful synthetic methods are currently characterized as "trained serendipity".[21] These 1-D nanostructures are supposed to be significant for potential applications in fields such as optics, electronics, magnetism, advanced catalysis, energy storage or conversion, and the fabrication of nanoscale devices including scanning probe microscopy tips.[21-24]

2-D nanostructures (or quantum wells)[25] are materials of which one of the three dimensions exists in the nanoscale (and extended in the other two dimension), including layered structures such as thin films or surface coatings. Thin films have been extensively studied by the semiconductor community because they can be conveniently prepared, employing techniques such as molecular beam epitaxy (MBE).[26] For example, most electronics devices predominantly rely on thin films for their operation in the silicon integrated-circuit industry.[27]

1.3. Novel properties of nanomaterials

Nanomaterials are fundamentally interesting not only because they are small but also because they possess fascinating size-dependent optical, electronic, thermal, mechanical, chemical, and catalytic properties, which are potentially distinct from their bulk counterparts as well as from the atomic or molecular precursors from whence they were derived.[28] This unique chemical and physical behavior of nanomaterials can in general be ascribed to an increased relative surface area and the dominance of quantum effects. These two factors are interrelated because the surface-to-volume (S/V) ratio dramatically increases as particle size decreases.

As a particle decreases in size, a greater proportion of atoms is found at the surface as compared with that inside the core of a particle. For a spherical particle, the S/V ratio is inversely proportional to its radius, R ($S/V = (4\pi R^2)/(4/3 \cdot \pi R^3) = 3/R$). For example, a particle built up by hexagonal or cubic close-packed atoms measuring 30 nm in diameter possesses 5% of its atoms on its surface. A 10 nm-sized nanoparticle possess 20% of its atoms on its surface, whereas a 3 nm-sized nanoparticle has 50% of its atoms on its surface. Thus, nanoparticles maintain a much greater surface area per unit volume as compared with bulk. Surface atoms are chemically more active (in other words, less stable) as compared with core atoms due to their relative lack of coordination with other atoms and also due to the presence of unsaturated sites or dangling bonds. In fact, it is generally accepted that the property of a matter depends strongly on the surface atoms of a materials. Thus, a greater surface area per unit volume ratio is anticipated to result in greater, enhanced reactivity for the unit system.

In conjunction with surface-area effects, quantum effects can begin to affect the properties of matter as its size is reduced to the nanoscale. These can significantly affect the optical, electric, and magnetic properties of materials, in particular as the structure or particle size approaches the smaller end of the nanoscale. Simultaneously, the imperfection of the particle surface induces additional electronic states in the band gap, which act as electron or hole trap centers.[28] With a high density of surface defects, for example, a decrease in the observed transition energy and a red-shifted emission band can be observed due to defect band formation.[29] In addition, surface states near the gap can mix with intrinsic states to a substantial extent. Materials that exploit these effects include quantum dots and quantum well lasers for optoelectronics.[30]

For crystalline solids, as the size of their structural components decreases, there is a much greater interface area within the solids, which can greatly affect both their mechanical and electrical properties. For example, most metals are composed of relatively small crystalline grains; the boundaries between the grains can arrest the propagation of defects when the solid is stressed, thus providing for the metal's hardness.[31] Moreover, nanoscale crystalline solids may contain unusual forms of

structural disorder (*e.g.*, bond length contractions, random disorder, and a type of disorder characterized by correlated atomic displacements) that can substantially modify a material's properties.[32] Moreover, a nanoparticle structure possessing internal strain, which results from lattice contraction and disorder, can noticeably modify the electronic properties of nanoscale analogues of crystalline solids, such as with ZnS.[32]

1.3.1. Magnetic properties of magnetic nanomaterials

Nanoparticles, which are generated from ferro- or ferrimagnetic materials and which are below a certain size, in general 10 – 20 nm, can exhibit a unique form of magnetization called superparamagnetism. Superparamagnetism is a phenomenon by which magnetic materials may exhibit a behavior similar to paramagnetism even at temperatures below the Curie or the Néel temperature. This is a small length-scale phenomenon, where the energy required to change the direction of the magnetic moment of a particle is comparable to that of the ambient thermal energy. The term superparamagnetism is chosen due to the similarity of the magnetization characteristics of these materials to paramagnetic materials, of which the magnetic dipole moments of the atoms are randomly aligned (Figure 1.2A). A representative ordering of the magnetic dipoles (*i.e.*, paramagnetic, ferromagnetic, antiferromagnetic, and ferrimagnetic ordering) in magnetic materials is shown in Figure 1.2.

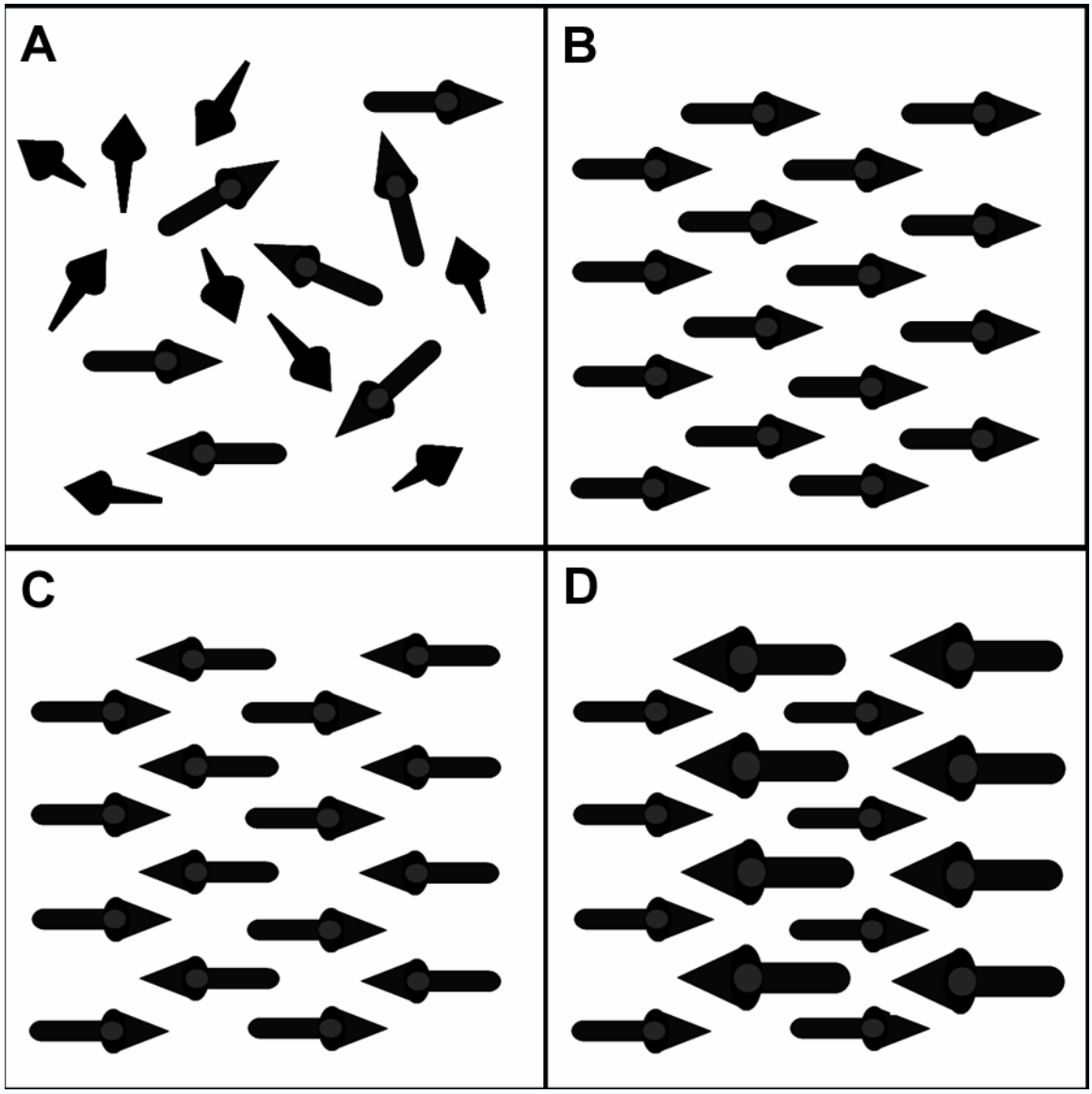

Figure 1.2. Paramagnetic (A), ferromagnetic (B), antiferromagnetic (C), and ferrimagnetic (D) ordering of the magnetic dipoles in magnetic materials.

1.3.1.1. Ordering of magnetic dipoles in magnetic materials

In macroscopic materials, a ferromagnetic material is one that undergoes a phase transition from a high-temperature phase that does not have a magnetic moment to a low-temperature phase that has a spontaneous magnetization even in the absence of an applied magnetic field (H). This transition temperature is, in general, called the Curie temperature (T_C). The macroscopic magnetization of a ferromagnetic material is originated by the magnetic dipole moments of the atoms tending to line up in the same direction, as shown in Figure 1.2B, whereas they are aligned randomly in a paramagnetic phase due to an ambient thermal energy that can overcome coupling forces over T_C (Figure 1.2A). Their spontaneous magnetization means that ferromagnetic materials tend to concentrate magnetic flux density which leads to their widespread use in technologically important applications, such as permanent magnets, transformer cores, electromagnets, and information storage devices, where large magnetic fields are required.

An antiferromagnetic material can be described as comprising of two spin sublattices with ferromagnetic interactions within one sublattice and antiferromagnetic interactions between sublattices. In an antiferromagnet, the spins of electrons align in a regular pattern with neighboring spins pointing in opposite directions, as shown in Figure 1.2C. Generally, antiferromagnetic materials exhibit antiferromagnetism at a low temperature, and become disordered above a certain temperature; this transition temperature is called the Néel temperature (T_N). Using an identical principle with a ferromagnetic material, an antiferromagnetic material is typically paramagnetic above its Néel temperature.

A ferrimagnetic (or weak ferromagnetic) material is one in which the magnetic dipole moments of the atoms on the different sublattices are opposed, as in antiferromagnetism. However, the opposing moments are unequal and a spontaneous magnetization remains (Figure 1.2D). In general, this phenomenon happens when the sublattices consist of different materials or ions, such as Fe^{2+} and Fe^{3+}, as in ferrites. Ferrimagnetic materials are similar to ferromagnets in that they possess a spontaneous magnetization below their T_C, and show paramagnetic behavior below their T_C.

1.3.1.2. Magnetization curves of magnetic nanomaterials

Magnetic characteristics of magnetic materials (or nanomaterials) can be effectively and extensively characterized by magnetization curves based on the relationship between the magnetization (M) and applied field (H), or between magnetization (M) and temperature (T). Typical magnetization curves are shown in Figure 1.3.[33]

In a magnetization curve, plotted as a function of an applied field (M/H curves, Figure 1.3A), ferromagnetic (or ferrimagnetic) materials exhibit a similar behavior such as hysteresis in magnetization and flux density, due to the subsequent alignment and reorientation of the domains upon the application of the magnetic field. Ferromagnetic (or ferrimagnetic) materials start in an unmagnetized state (M = 0, H = 0), and as the applied magnetic field increases in the positive direction, the magnetic induction increases from zero to a value for the saturation magnetization (M_S). The saturation magnetization (M_S), which is a measure of the maximum amount of field that can be generated by the cumulative strength of the dipole moments associated with atoms that make up the ferromagnetic (or ferrimagnetic) material, is also referred to as the spontaneous magnetization, although this term tends to refer to magnetization within a single magnetic domain.

When the magnetic field is applied in the opposite direction after the saturation (M_S) is achieved in these materials, the magnetic induction within ferromagnetic (or ferrimagnetic) materials decreases to the remnant magnetization value (M_r). To attain the initial unmagnetized state (M = 0) of ferromagnetic (or ferrimagnetic) materials, we need to apply a further magnetic field in the opposite direction, which is called coercivity (or coercive field, H_C). When the coercivity of a ferromagnetic material is large, the material is called a hard or permanent magnet. When H_C is small, the material is referred to as a soft magnet.

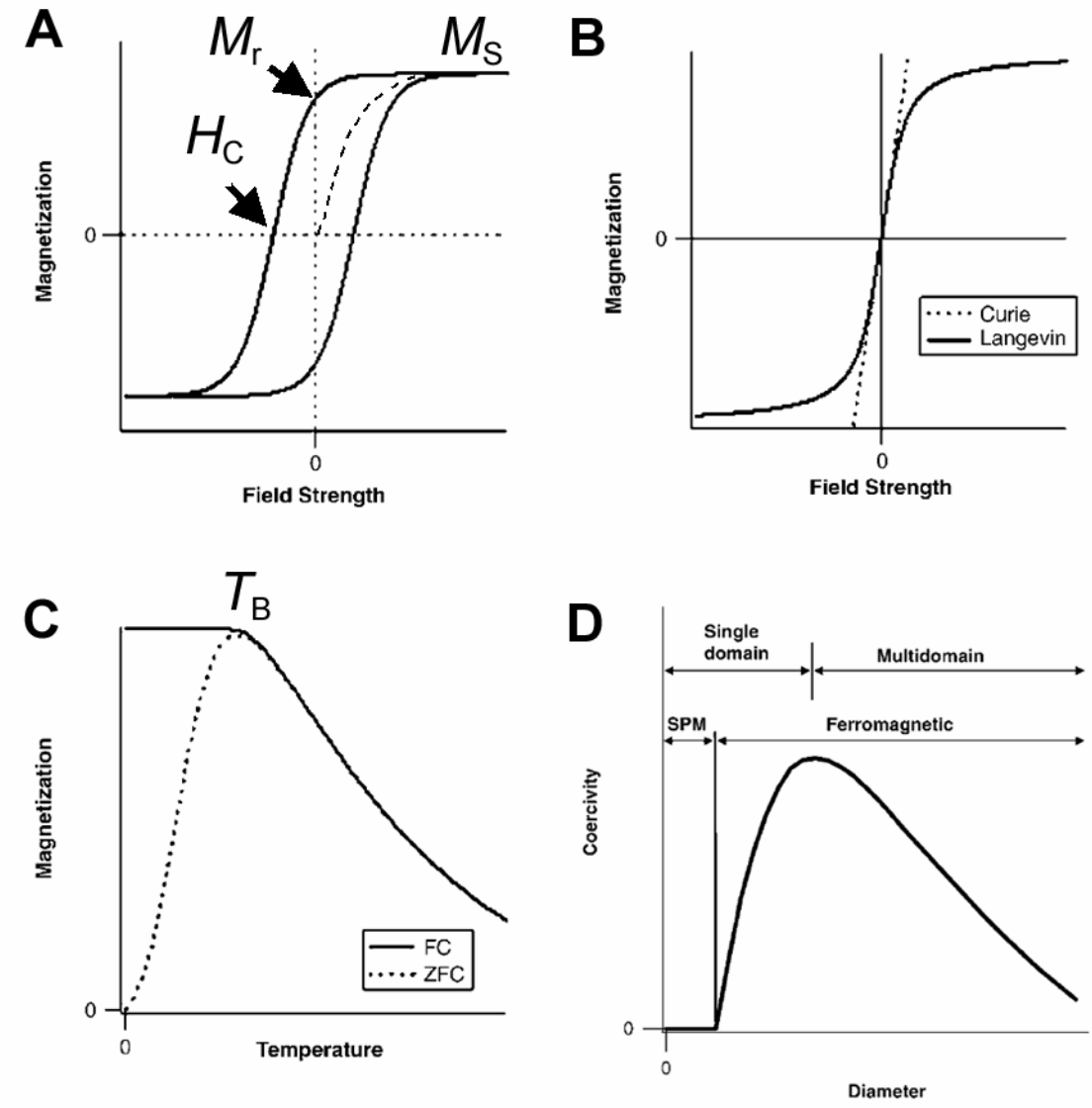

Figure 1.3. Idealized magnetization curves of magnetic materials and superparamagnetism. (A) *M* versus *H* curves for ferromagnetic (or ferrimagnetic) materials. The saturated magnetization (M_S), remnant magnetization (M_r), and coercivity (H_C) are labled. (B) *M* versus *H* curves for a superparamagnetic material. Curie's law is accurate at low fields, whereas the Langevin equation fits the magnetization behavior at all fields. Note the lack of hysteresis, *i.e.*, $H_C = 0$. (C) *M* versus *T* curves including zero-field cooled (ZFC) and field cooled (FC) curves for a superparamagnetic material. The blocking temperature is labeled. (D) Coercivity of magnetic nanoparticles. SPM stands for "superparamagnetic". Reproduced and modified from Huber, D. L. *Small* **2005**, *1*, 482.[33]

Superparamagnetism refers to a balance between magnetic energy and thermal energy as a function of the size of magnetic materials, and thus, the phenomenon occurs over a limited range. Below a certain temperature, there is insufficient thermal energy to allow for easy spin realignment, and coercivity (H_C) appears. This temperature is called the blocking temperature (T_B) and below this T_B, the materials' behavior is ferromagnetic (or ferrimagnetic). Figure 1.3 includes typical M versus H and M versus H curves above their T_B as well as coercivity relationships for superparamagnetic materials.

In magnetic materials, the size of magnetic domains, which depends on the minimization of the overall energy of the system, is determined by a competition between the energy increase due to the external magnetic flux and the energy cost of additional domain walls for flipping the direction of spins. Thus, the size of magnetic domains varies, based on the magnetic materials studied, but the characteristic size of the domains is, in general, in the range of tens of nanometers. If a particle is smaller than this characteristic domain size, the system contains a single magnetic domain (*i.e.*, no domain wall exists).[34-36] The thermal energy above T_B is, therefore, sufficiently high enough to change the direction of the magnetic moment of the magnetic nanoparticles. Consequently, superparamagnetic nanomaterials share a number of macroscopic magnetic properties with paramagnetic materials.

Figure 1.3B shows idealized M/H curves for superparamagnetic materials. There is no coercivity exhibited in M/H hysteresis loops. In addition, magnetic characteristics of superparamagnetic materials include Curie's law behavior at low fields, Langevin behavior at all fields, and an inverse temperature dependence of magnetization (Figure 1.3B).[33] Curie's law states that magnetization scales directly with field and inversely with temperature ($M = C\cdot(H/T)$, where C is the Curie constant) whereas Langevin behavior yields an expression for magnetic polarizations in paramagnetic materials (Langevin function: $L(x) = C\cdot(\coth(x) - x^{-1})$, where C is the Curie constant).

A representative M/T curve for a superparamagnetic material is shown in Figure 1.3C. To create a zero-field-cooled (ZFC) curve, the material is cooled to near 0 K in the absence of a magnetic field. Then a weak field (typically 100 – 200 Oe) is applied, and the material can be slowly warmed up to the desired temperature. As thermal energy becomes available, individual spins in the material begin to align so as to coincide with the applied field. The spin alignment within a material reaches a maximum at T_B, then decreases as $1/T$ (as predicted by the Curie equation) as the thermal energy overcomes the energy gained by alignment of the spins. The field-cooled (FC) curve is produced by recooling the material in the presence of the same weak field. There is no hysteresis exhibited above T_B, where the sample is superparamagnetic. At T_B, the spins become blocked and unable to reorient themselves, and they remain in their maximally aligned state (FC, solid line).

Figure 1.3D shows coercivity relationships with respect to the size of

superparamagnetic (SPM) nanomaterials. The qualitative behavior of the coercivity of nanomaterials is illustrated in this curve. When the size of magnetic nanomaterials exceeds a superparamagnetic limit at a given temperature, the magnetic behaviors of these materials do not immediately revert to that of bulk materials. With increasing size, magnetic nanomaterials become blocked as thermal energy becomes insufficient to permit the free rotation of their spins. The coercivity of magnetic materials increases with increasing diameter (yet preserving a single magnetic domain) until their maximum coercivity is obtained. At this maximum, their single domain of magnetic nanomaterials can break into multiple magnetic domains and the coercivity begins to decrease. This discussion only considers coercivity resulting from the magnetocrystalline anisotropy within spherical nanoparticles. Magnetic nanomaterials with anisotropic morphologies, such as acicular particles (particularly needles), can possess greatly enhanced coercivity due to shape anisotropy leading to applications, for instance, in magnetic recording.

1.4. Fe-based metal oxide nanostructured (FeMONS) materials: $BiFeO_3$, $BiFeO_3$–$BaTiO_3$, $Bi_2Fe_4O_9$, α-Fe_2O_3, and Fe/Fe_3O_4.

Iron-based metal oxide systems, including iron oxides, iron-containing perovskite materials as well as their composite analogues, represent promising materials due to their technologically significant electronic as well as magnetic properties, relevant for multifunctional systems. Iron-containing materials especially have been considered as essential components in exhibiting many interesting and practically important magnetic properties including ferromagnetism, antiferromagnetism, and ferrimagnetism (and/or weak ferromagnetism). Moreover, metal oxide systems, in particular, represent one of the most diverse classes of functional materials for broad applications with important structure-related properties, including superconductivity, ferroelectricity, magnetism, conductivity, catalytic activity, and gas-sensing capability, to name a few. Thus, one of the main challenges is how to precisely incorporate these technologically useful multifunctionalities into one system. Thus, we have mainly focused on the chemistry of iron-containing ternary metal oxides, such as perovskite systems, which are models for multifunctional and smart materials.

Even though the synthesis of a bulk iron-based metal oxide system is already of technological importance, the generation of this class of "iron-based metal oxide nanostructured (FeMONS) materials" is essential from a nanoscience and nanotechnology perspective. Moreover, FeMONS materials are noteworthy for their unique and diverse characteristics, including their highly favorable optical, electronic, and magnetic properties, which are critical for a host of potential applications as diverse as additives, catalysts, electronic devices, magnetic recording media, information storage, spintronics, and sensors.[37-42]

Since the chemistry associated with the exploration of new synthetic strategies as well as the creation of novel FeMONS materials can play a profound role in this study, we have conducted our major efforts in developing synthetic strategies of these FeMONS materials. In addition, our synthetic efforts with most of the FeMONS materials in this study complement broad areas associated with the fabrication of technologically important ternary metal oxide nanostructures. In fact, comparatively little work has been performed on the fabrication of ternary metal oxide nanomaterials, which has hindered detailed experimental investigations into their size-dependent properties, as compared with that of binary oxide and semiconductor nanostructures as well as of carbon nanotubes.

In this dissertation, we have prepared some particularly important multifunctional FeMONS materials systems: *e.g.*, $BiFeO_3$, $BiFeO_3$–$BaTiO_3$, $Bi_2Fe_4O_9$, α-Fe_2O_3, and Fe/Fe_3O_4. A description of each of these classes of materials follows. In addition, a systematic, detailed structural characterization and their corresponding property

measurements including magnetic ones, as well as a correlation of the electronic structure and structural chemistry of these intriguing FeMONS materials will be discussed.

1.4.1. $BiFeO_3$ nanostructures

1.4.1.1. Multiferroics

Bismuth iron oxides or bismuth ferrites ($BiFeO_3$) are one of the most interesting iron-containing perovskites due to their unique multifunctional properties which are of high technological and fundamental importance. $BiFeO_3$ is also a multiferroic. Multiferroics[43] are noteworthy for their unique and strong couplings of electric, magnetic, and structural order parameters giving rise to simultaneous ferroelectricity, ferromagnetism, and ferroelasticity.[44] As a result, multiferroic materials possess a spontaneous polarization, magnetization, and piezoelectricity that can be switched on by an applied field, a magnetic field, and an elastic force or stress, respectively. Moreover, the coupling among two or more of all of the ferroic orders coexisting in the same phase can be induced by an applied field of a different origin which suggests the development of "smart materials" for a whole range of potential applications.[45,46] In particular, ferroelectromagnets (or multiferroic magnetoelectrics) maintain a magnetization and dielectric polarization, which can be modulated and activated by an electric field and magnetic field, respectively.[47] This property is termed as a magnetoelectric effect.[48] It is not surprising, therefore, that multiferroic materials have been considered for a host of potential applications as diverse as additives, magnetic recording media, information storage, spintronics, and sensors.[49-51] The relationship between multiferroic and magnetoelectric materials as well as the classification of a multiferroic is summarized in Figure 1.4 and Table 1.1, respectively.[49]

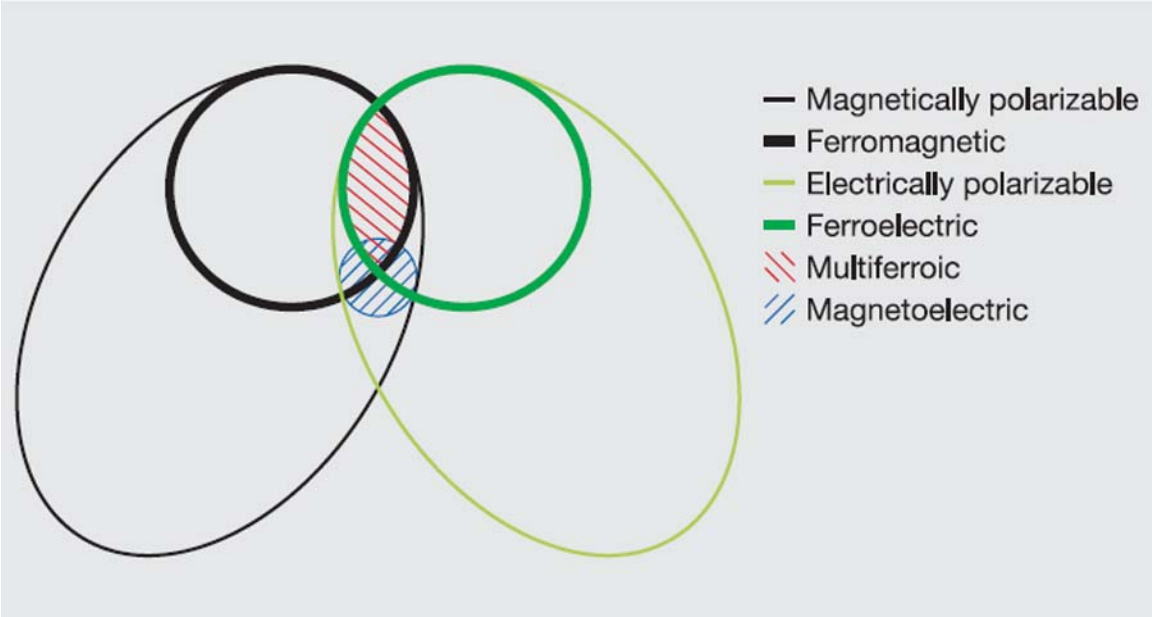

Figure 1.4. The relationship between multiferroic and magnetoelectric materials. Ferromagnets (ferroelectrics) form a subset of magnetically (electrically) polarizable materials such as paramagnets and antiferromagnets (paraelectrics and antiferroelectrics). The intersection (red hatching) represents materials that are multiferroic. Magnetoelecrtic coupling (blue hatching) is an independent phenomenon that can, but need not, arise in any of the materials that are both magnetically and electrically polarizable. In practice, it is likely to arise in all such materials, either directly or via strain. Reproduced from Eerenstein, *et al*., *Nature* **2006**, *442*, 759.

Table 1.1. Summary of terms associated with multiferroics. Reproduced and modified from Eerenstein, *et al*., *Nature* **2006**, *442*, 759.

Origin	Ferroics
Electric (E)	*Ferroelectric* materials possess a spontaneous polarization that is stable and that can be switched on hysteretically by an applied electric field.
	Antiferroelectric materials possess ordered dipole moments that cancel each other completely within each crystallographic unit cell.
Magnetic (H)	*Ferromagnetic* materials possess a spontaneous magnetization that is stable and can be switched on hysteretically by an applied magnetic field.
	Antiferromagnetic materials possess ordered magnetic moments that cancel each other completely within each magnetic unit cell.
	Ferrimagnetic materials differ from antiferromagnets because the magnetic moment cancellation is incomplete in such a way that there is a net magnetization that can be switched by an applied magnetic field.
Elastic (σ)	*Ferroelastic* materials display a spontaneous deformation that is stable and can be switched on hysteretically by an applied stress.
Origin	Order parameter coupling
($H + E$)	*Magnetoelectric* coupling describes the influence of an applied magnetic (electric) field on the polarization (magnetization) of a material.
($\sigma + E$)	*Piezoelectricity* describes either a change in strain as a linear function of the applied electric field, or a change in polarization as a linear function of applied stress.
($\sigma + H$)	*Piezomagnetism* describes either a change in strain as a linear function of applied magnetic field, or a change in magnetization as a linear function of applied stress.
($\sigma + E$)	*Electrostriction* describes a change in strain as a quadratic function of the applied electric field.
($\sigma + H$)	*Magnetostriction* describes a change in strain as a quadratic function of the applied magnetic field.

Although ferroelectromagnets have been studied from 1958, very few multiferroics, in Nature or in the laboratory, have been reported so far.[52] It is still not clear why there are so few magnetic ferroelectrics. However, recent research has provided some clues that multiferroism involves a number of subtle competing factors, with *d* electron occupancy on the transition metal being a critical variable.[45] It is through the study of those clues that we have determined that most ferromagnetic oxides maintain a center of symmetry and do not allow for the existence of an electric polarization. However, most of the ferroelectric oxides do require a structural distortion from a prototypical high-symmetry phase that removes the center of symmetry and hence allows for a spontaneous electric polarization, so as to satisfy the requirement for multiferroism, such as symmetry, electrical properties, and a formal charge corresponding to the *d* electron configuration on the B cation.[45] Further understanding of the scarcity of ferromagnetic ferroelectrics materials is associated with the counter balance between the conventional mechanism for cation off-centering in ferroelectrics (which requires formally empty *d* orbitals), and the formation of magnetic moments (which usually results from partially filled *d* orbitals in these materials).[53] In other words, ferroelectrics and ferromagnetics are, in a sense, mutually exclusive. Till now, ~80 single-phase multiferroics have been grown either as a discrete composition or as a solid solution, and representative examples of existing intrinsic multiferroics are shown as follows: $RMnO_3$ (with R=Sc, Y, In, Ho-Lu), $BiMnO_3$, and the focus material in Chapter 2, $BiFeO_3$.[47,54]

1.4.1.2. $BiFeO_3$ nanoparticles and nanotubes

Incorporation of ferroelectric, ferrimagnetic, and ferroelastic multiferroic $BiFeO_3$ materials into practical devices, thus far, has been hindered by leakage problems that lead to low electrical resistivity which has prevented practical transport measurements of $BiFeO_3$ materials as either piezoelectric or magnetoelectric functional components in the bulk. The relatively high conductivity of $BiFeO_3$ is presumably a result of defects and non-stoichiometry related issues, which is believed to be due to the reduction of Fe^{3+} species to Fe^{2+}, creating oxygen vacancies for charge compensation. Hence, there has been a pressing need to generate high-quality samples. Recent approaches have mainly focused on two broad strategies: (i) incorporating $BiFeO_3$ into solid solutions with other ABO_3 perovskites including $PbTiO_3$, $BaTiO_3$, and $SrTiO_3$ and (ii) developing novel structural formulations, such as 0-D, 1-D and 2-D nanostructures, of $BiFeO_3$ materials.[37,55-57]

In fact, the Ramesh group in 2003 reported enhanced physical properties such as polarization, magnetization, and piezoelectricity of such strained epitaxial thin films of $BiFeO_3$, whose properties makes this material a practical room temperature application of a smart material.[37] Due to its high impact in the materials sciences community, this report is generally regarded as the beginning of intense scientific attention on nanostructures of $BiFeO_3$ materials. For example, the graph plotting scientific publications per year with 'multiferroic' and '$BiFeO_3$' as a keyword, respectively, shows a sharp increase, after the initial report in year 2003 as shown in Figure 1.5. From a nanoscience perspective, the majority of prior analyses on such systems has been performed on oriented, epitaxial thin films (2-D nanostructures) of $BiFeO_3$ grown on a range of substrates including Si, $SrTiO_3$, $SrRuO_3$, $LaAlO_3$, Pt/Ti/SiO_2/Si, and Pt/TiO_2/SiO_2/Si.[58-62]

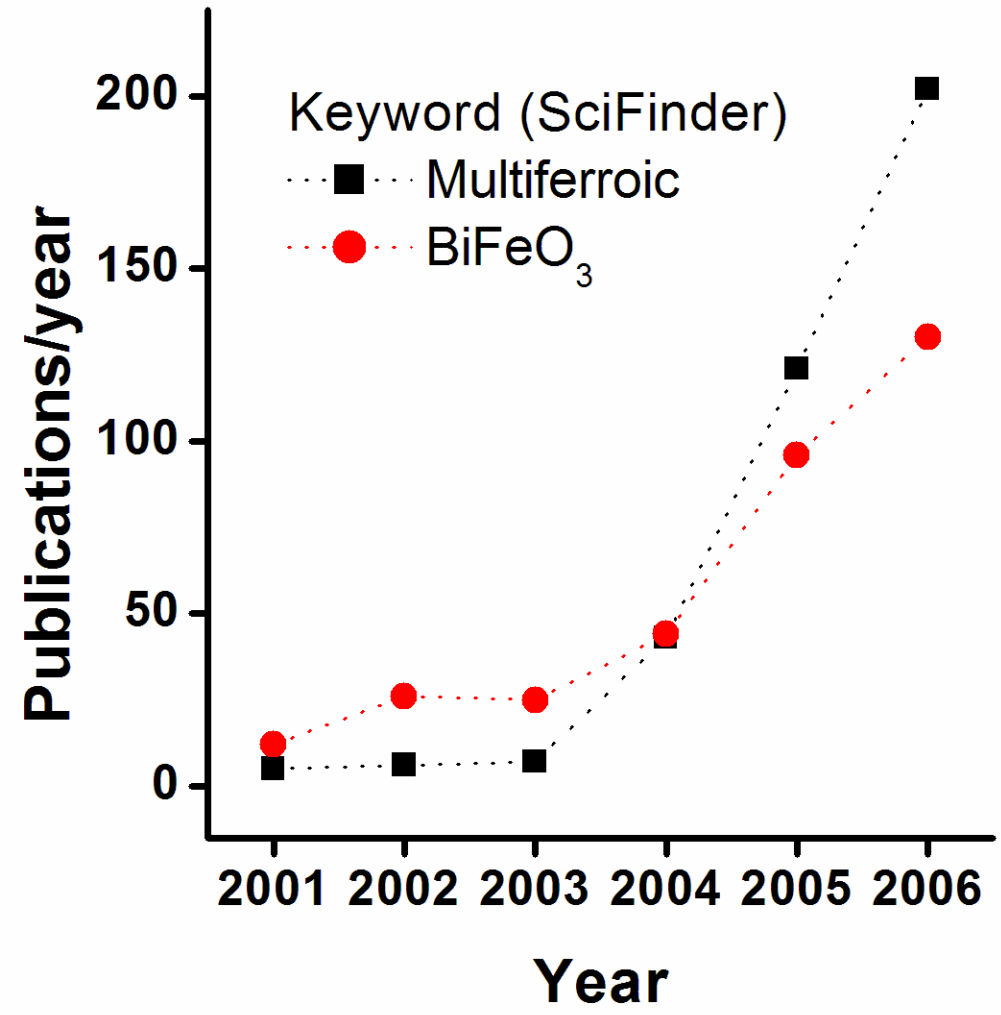

Figure 1.5. Publications per year using 'multiferroic' as well as '$BiFeO_3$' as a keyword.

In spite of such intense study, however, a fundamental understanding of structure-property correlations in $BiFeO_3$ is still lacking. Specifically, the nature of the magnetic response as well as the fundamental dependence of ferroelectric behavior on the size and precise chemical composition (e.g. presence of doping) are issues of deep interest.[63-69] Attention has recently focused on the unique and unusual spin spiral structures of this multiferroic material.[70]

However, to date, little if any effort has been expended in research associated with the synthesis of substrate-free nanostructures of $BiFeO_3$. Moreover, there have not been any viable reports on single-crystalline nanostructure analogues associated with 0-D and/or 1-D structural motifs. Thus, the generation of nanoparticles (0-D) as well as nanotubes (1-D) of $BiFeO_3$ provides a complete, complementary nanoscience perspective to intensely studied thin film (2-D) structures.

In Chapter 2, we explore synthetic approaches for single-crystalline $BiFeO_3$ nanoparticles employing a facile sol-gel methodology based on the glycol-gel reaction.[38] Their sizes have been thermodynamically controlled in order to obtain reproducible size variations ranging from less than 15 nm to greater than 100 nm. As-prepared single-crystalline nanoparticles of $BiFeO_3$, especially those with a diameter range on the order of or smaller than the 62 nm wavelength of their intrinsic spiral-modulated spin structure, show strong property correlations with: (i) increased suppression of the known spiral spin structure with decreasing nanoparticle size and (ii) uncompensated spin and strain anisotropies at the surface. Zero-field-cooled and field-cooled magnetization curves exhibit spin-glass freezing behavior due to a complex interplay between finite size effects, interparticle interactions, and a random distribution of anisotropy axes in our nanoparticle assemblies. Properties of as-prepared $BiFeO_3$ nanoparticles (0-D nanostructures) especially represent an attainable goal that can be ascribed essentially to size effects alone, without the potentially distracting issues either of epitaxial strain (characteristic of thin films) or of oxygen vacancy defects.

In addition, we have employed a modified template-based technique for the fabrication of 1-D nanostructures of $BiFeO_3$ materials ($BiFeO_3$ nanotubes).[55] A schematic of the overall experimental procedure is shown in Figure 1.6. Magnetic property measurements of as-prepared $BiFeO_3$ nanotubes demonstrate an appreciable level of magnetization, unlike for bulk pure $BiFeO_3$ which shows no spontaneous magnetic moment even up to very high fields and low temperatures. As-prepared $BiFeO_3$ 1-D nanotubes were subsequently characterized by a number of techniques, including XRD, SEM, TEM, HRTEM as well as EDX and SAED. This work has attracted scientific interest especially in $BiFeO_3$ nanostructures, as a first report on the fabrication of 1-D $BiFeO_3$ nanostructures. Additional work on these systems has focussed on magnetic property measurements of $BiFeO_3$ nanowires as well as on polarization measurements of $BiFeO_3$ nanowire arrays.[71-73]

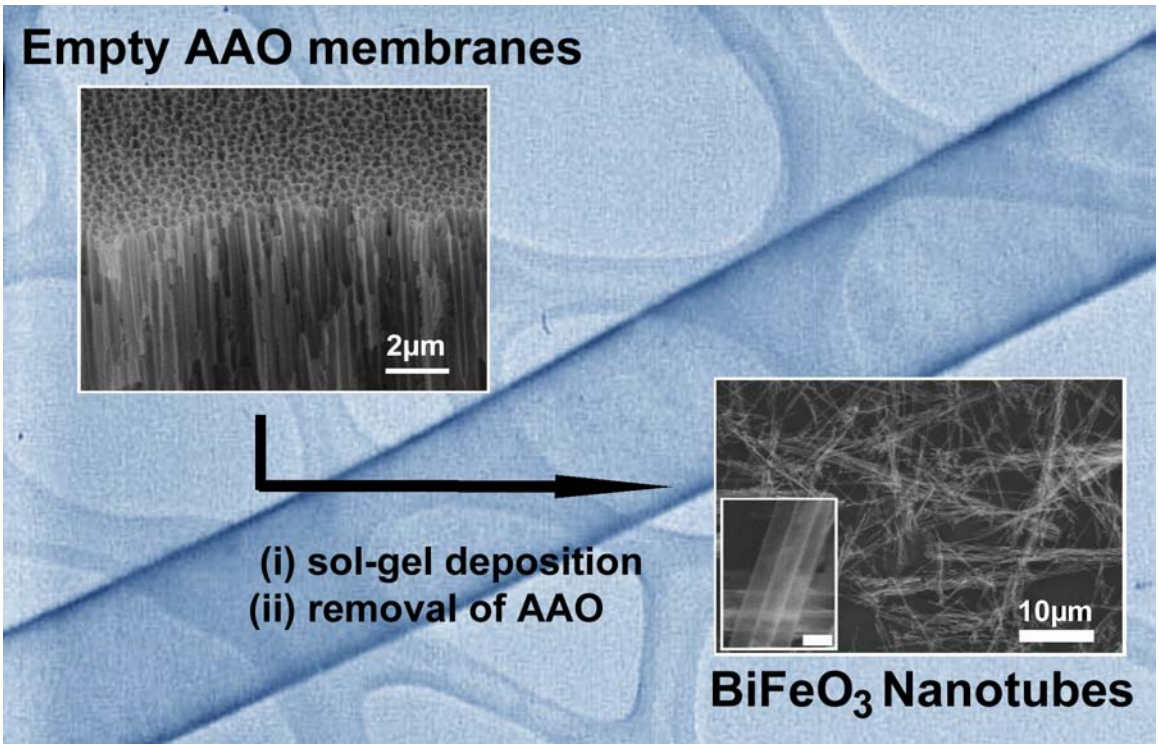

Figure 1.6. A schematic of the fabrication of $BiFeO_3$ nanotubes using a template methodology, which is superimposed upon a TEM image of the resultant product tube (Chapter 2).

1.4.2. $BiFeO_3$–$BaTiO_3$ solid solutions

As discussed previously in section 1.4.1.2, the incorporation of multiferroic $BiFeO_3$ materials into practical devices in their bulk form has been hindered by their intrinsic leakage problems that lead to low electrical resistivity. Practical transport measurements of $BiFeO_3$ materials as either piezoelectric or magnetoelectric functional components have proven to be difficult to show. For instance, reliable ferroelectric loops are hard to obtain, due to a relatively high conductivity, presumably due to defects and non-stoichiometry related issues. Thus, there has been a pressing need for $BiFeO_3$ materials to prevent any reduction of Fe^{3+} species to Fe^{2+}, creating oxygen vacancies for charge compensation. Recent approaches associated with solid state chemistry include (i) the incorporation of $BiFeO_3$ into solid solutions with other cubic ABO_3 perovskites including $PbTiO_3$ (or $Pb(Zr,Ti)O_3$ (PZT)), $BaTiO_3$, and $ReFeO_3$,[74-77] and (ii) the application of dopants such as Ba, La, Nb, Ti, Ni, and Sr ions in $BiFeO_3$ materials.[78-83]

In spite of an intense study focused on $BiFeO_3$-based solid solution materials, a fundamental understanding of structure-property correlations in $BiFeO_3$ is still lacking. Moreover, the effect of the crystallinity as well as the fundamental dependence of ferroic ordering behavior on the size and precise chemical composition represents issues of deep interest. The magnetic response of $BiFeO_3$ materials with respect to their size (*e.g.*, nanostructures) as well as that of $BiFeO_3$–$BaTiO_3$ solid solutions with respect to their composition is a main focus of this dissertation. For example, the size-dependent magnetic properties of single-crystalline $BiFeO_3$ nanoparticles and polycrystalline $BiFeO_3$ nanotubes have been explored in Chapter 2. In Chapter 3, research associated with the synthesis of nanostructures of $BiFeO_3$ with other perovskites as well as the magnetic properties of as-prepared single-crystalline $BiFeO_3$–$BaTiO_3$ solid solution structures are presented.

Briefly, we have employed a large scale, facile, and environmentally friendly solid state reaction as a means of generating single-crystalline $BiFeO_3$–$BaTiO_3$ (BFO–BTO) solid solutions in a NaCl medium in the presence of a nonionic surfactant. $BaTiO_3$ has been selected for its dielectric properties which are lacking and are complementary to those of $BiFeO_3$, and for their previous practicability in molten salt reactions.[84] Perovskite $(BFO)_x$–$(BTO)_{1-x}$ solid solutions with x values of 0.9, 0.8, 0.7, 0.6 and 0.5 have shown an appreciable magnetic response, which is absent in bulk $BiFeO_3$ (*i.e.*, x = 1), corresponding to their structural phase transition, an assertion which has been confirmed from superconducting quantum interference device (SQUID) and X-ray powder diffraction (XRD) measurements.

1.4.3. $Bi_2Fe_4O_9$ nanostructures

Another FeMONS material with a ternary oxide structure associated with Bi is $Bi_2Fe_4O_9$, which is the focus material of Chapter 4. $Bi_2Fe_4O_9$ has been considered either as an impurity or as a second phase material in the synthesis of $BiFeO_3$ materials. However, because of their high sensitivity to ethanol and acetone vapors, bismuth ferrites have been recently considered as new materials for semiconductor gas sensors.[85] Moreover, the general class of bismuth ferrites, including $BiFeO_3$, $Bi_2Fe_4O_9$, and $Bi_4Fe_2O_9$, consists of semiconductors, possessing interesting properties which are significant for applications in various fields as diverse as optics, electronics, magnetism, information processing and storage. In particular, the catalytic potential of $Bi_2Fe_4O_9$ for ammonia oxidation to NO is of current interest, as these iron-based materials may likely replace current, irrecoverable, and costly catalysts based on platinum, rhodium, and palladium.[86,87]

Despite the evident importance of $Bi_2Fe_4O_9$ as a functional material, very few reports have appeared, associated with nanoscale structural motifs of this bismuth ferrite. In fact, sheet-like nanoparticulate powders have been formed[87] but neither one-dimensional analogues (such as nanotubes and nanorods) nor nanocube analogues have been prepared. The fabrication of well-defined, monodisperse sizes and shapes (*e.g.*, cubes) of $Bi_2Fe_4O_9$ is of fundamental importance in investigating the size correlation of the basic physical properties of these materials, with implications for their device applications.

In Chapter 4, we report the fabrication of discrete single-crystalline, nanosized $Bi_2Fe_4O_9$ cubic structures as well as their elongation into orthorhombic and rod-like structures, employing a molten salt technique in the presence of a nonionic surfactant.[88] A schematic illustration as well as microscopic images of cubic, orthorhombic, and rod-like structures of $Bi_2Fe_4O_9$ is shown in Figure 1.7. The roles of surfactant, salt, precursor identity, as well as alterations in the molar ratio of precursors were systematically examined and correlated with the predictive formation of different shapes of $Bi_2Fe_4O_9$ products.

Moreover, Mössbauer and SQUID measurements have been performed on $Bi_2Fe_4O_9$ nanocubes and the results of magnetization versus temperature curves exhibited a slightly lower T_N of the cubes (~250 K) as compared with that of bulk (~264 K).[88] Since an initial report, additional work on these systems has focused on $Bi_2Fe_4O_9$ nanowire fabrication[89] and on the hydrothermal synthesis of $Bi_2Fe_4O_9$ nanocubes[42,90]. Furthermore, a very slight modification of an experimental parameter associated with our reported molten salt methodology (*i.e.*, use of NaCl-Na_2SO_4 instead of NaCl) for $Bi_2Fe_4O_9$ nanostructures has proven to be rather effective for the generation of single-crystalline $BiFeO_3$ nanostructures.[91]

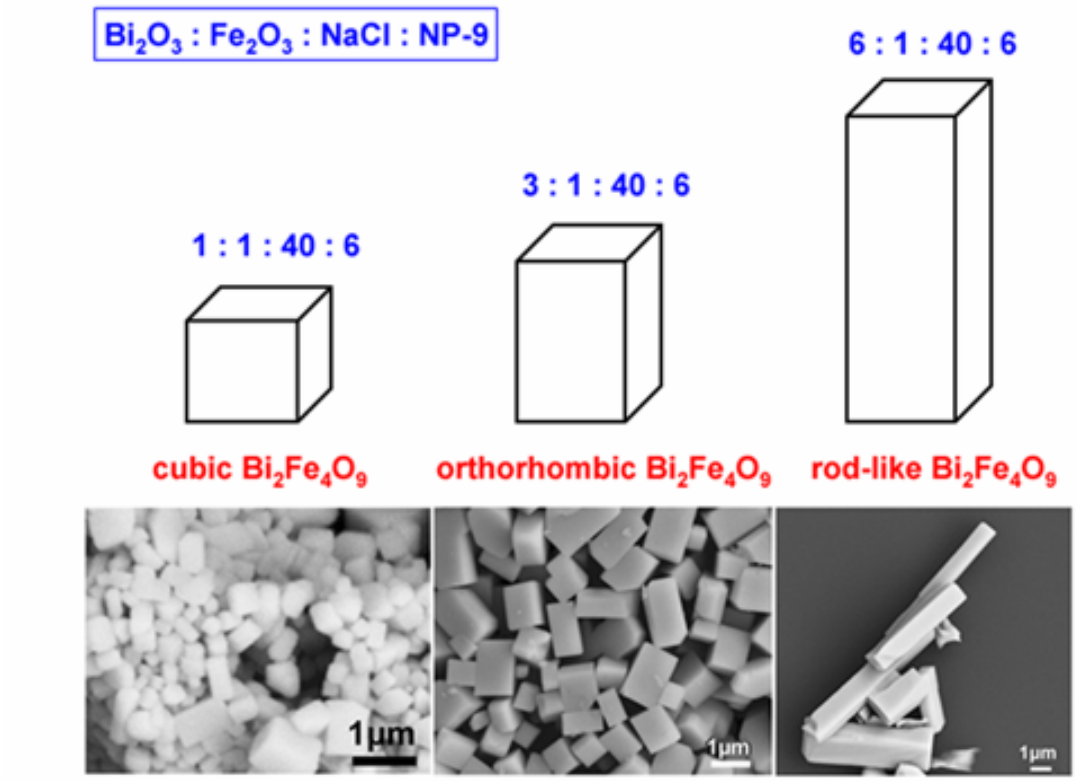

Figure 1.7. A schematic illustration as well as microscopic images of cubic, orthorhombic, and rod-like structures of $Bi_2Fe_4O_9$ (Chapter 4).

1.4.4. α-Fe_2O_3 and Fe/Fe_3O_4 nanostructures

1.4.4.1. Morphology of nanoparticles

It has been found that the morphology and/or shape of a nanoparticle, which determines the exposed crystallographic surface (and its corresponding surface energy) enclosing the particle, can have a dramatic effect on its properties. As an example, a 10-fold higher activity of the $Pt_3Ni(111)$-surface in the oxygen reduction reaction (ORR) in the polymer electrolyte membrane fuel cell (PEMFC), has recently been observed as compared with that of $Pt_3Ni(110)$-surface.[92] In self-assembly science, the resultant morphologies of PbSe nanowires are strongly dependent on the initial morphology of PbSe nanocrystals through oriented attachments along identical crystal faces on the surface as building blocks.[93] Moreover, the relative intensities of X-ray diffraction peaks, the positions of bands in optical spectra, and the magnitudes of sublimation energies of a wide variety of materials, including Au and Ag_2S, are intrinsically coupled with particle morphology (such as icosahedra, cubes, and tetrahedra).[94-96]

With hematite in particular, changes in microhardness, electrical conductivity (*i.e.*, mobility enhancement), as well as in superparamagnetic blocking behavior are strongly associated with its physical and structural characteristics.[97-99] As another relevant example of the significance of shape, for magnetic nanoparticles, in particular, such as the Fe/Fe_3O_4 composite synthesized herein, shape anisotropy and crystalline anisotropy are expected to have a profound influence on their intrinsic magnetic properties (such as coercivity).[39] In fact, the magnetic anisotropy (*i.e.*, higher coercivity) present in rod-shaped magnetic particles, which by contrast is not observed in symmetrically-shaped spheres or cubes, has been exploited in the use of these acicular particles in commercial magnetic recording media.

1.4.4.2. α-Fe_2O_3 and Fe/Fe_3O_4 rhombohedra

We demonstrate our ability to prepare discrete hematite products as well as discrete aggregates of Fe/Fe_3O_4 nanocomposites with controlled size, shape, and monodispersity in Chapter 6. Specifically, the synthesis of rhombohedral hematite is a significant advance in nanoparticle chemistry not only because this particular morphology is a rarely observed structural motif of this material but also because this work represents the large-scale generation of a high-surface-area formulation of an industrially important iron oxide material. Our multi-step synthesis steps through the initial production of a hematite precursor, a single-crystalline rhombohedral crystal with the corundum structure, which had been previously difficult to synthesize, are shown in Figure 1.8.

We also note that our molten-salt, solid-state reactions are of particular significance in the green chemistry area, due to their relative environmental friendliness, simplicity, relative non-toxicity, facility of use, and versatility, as practical, generalizable, large-scale approaches to generating single-crystalline metal oxide nanomaterials.[84,100-103] In these reactions, by-products include only water and sodium chloride. Since the nature of the net products strongly depends on the structural and chemical nature of the initial iron precursors, one of the main challenges of applying molten salt methods to the production of hematite has been the development of reproducible control over the size, shape, and crystallinity of the resulting structures.[104] Though this need for reliable control explains our strong motivation for generating hematite rhombohedra, there are other fundamental reasons for doing so.

Rhombohedra represent a high-surface-area, anisotropic formulation of an industrially important iron oxide material which is an active component of gas sensors, photocatalysts, and other types of catalytic materials. In addition, α-Fe_2O_3 hematite rhombohedra present themselves as a practical, low-cost chemical precursor material to the subsequent synthesis of magnetite. Developments of a facile and economically viable synthetic strategy for the synthesis of hydrophilic, biocompatible magnetic particles (including magnetite) would benefit their technical use in biomedical fields, such as biomolecular separations, targeted drug delivery, tags for sensing and imaging, antitumor therapy, as well as magnetic resonance imaging.

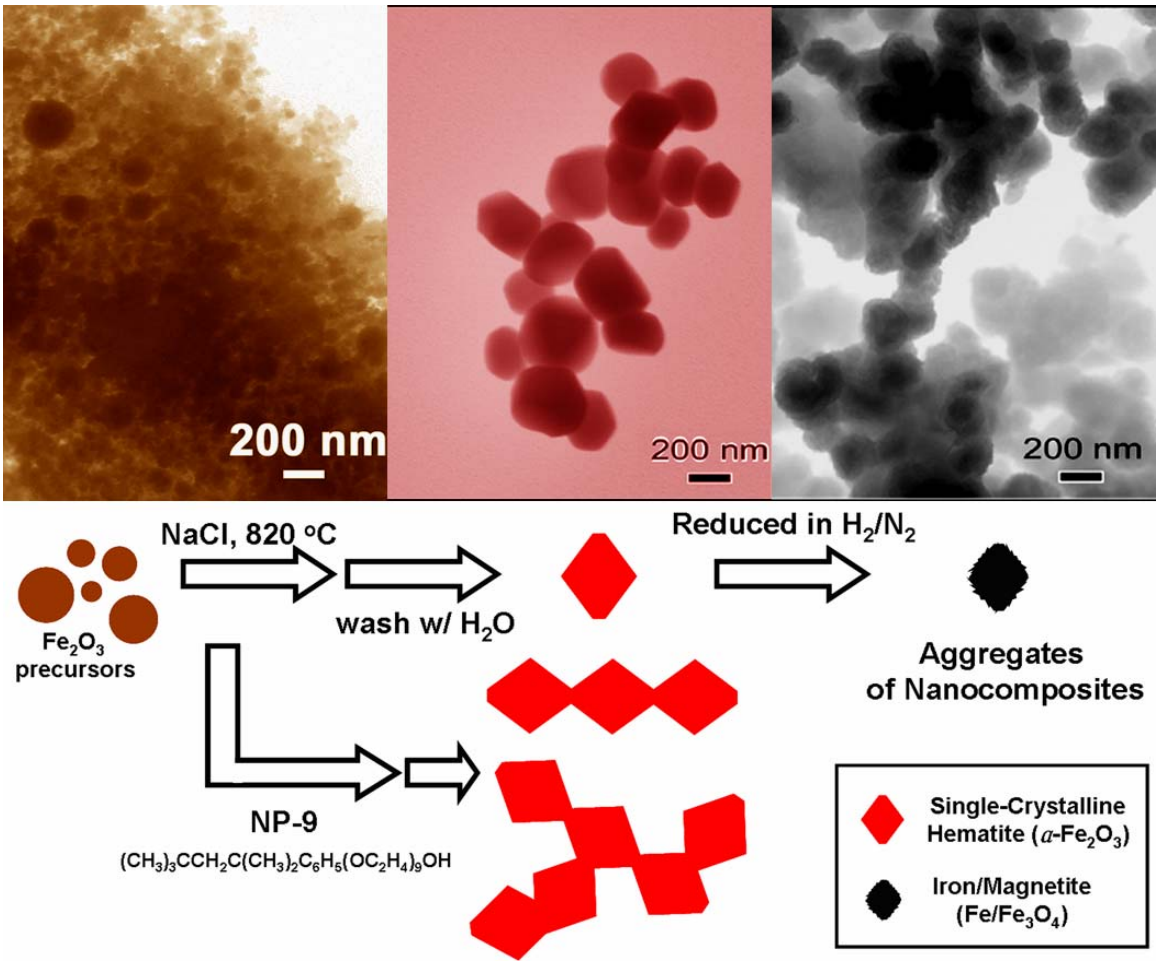

Figure 1.8. Electron microscopic images as well as a schematic illustration of the generation of single-crystalline hematite rhombohedra (as well as other hematite structural motifs) and corresponding Fe/Fe_3O_4 nanocomposites (Chapter 5).

In the experiments reported in Chapter 5, we were able to generate distinctive structural polymorphs of hematite iron oxide from relatively polydisperse, commercially available starting precursor materials. We were subsequently able to transform these single-crystalline α-Fe_2O_3 rhombohedral structures into their magnetic nanocrystalline composite counterparts, Fe/Fe_3O_4. These samples were characterized by a number of techniques, including scanning electron microscopy (SEM), transmission electron microscopy (TEM), high-resolution TEM (HRTEM), energy-dispersive X-ray spectroscopy (EDS), selected area electron diffraction (SAED), X-ray diffraction (XRD), and superconducting quantum interference device (SQUID) measurements.

Magnetic properties measured for both of the rhombohedral structures show the Morin transition[105] and Verwey transition[106] at a temperature of ~252 K and ~135 K, respectively, which are potentially associated with applications ranging from gas sensing, catalysis, solar energy conversion, pigmentation, advanced magnetic materials, a heterogeneous Fenton system, to medical diagnostic instrumentation.

1.4.5. Electronic structure and chemistry of FeMONS materials

Chapter 6 reports a systematic and detailed structural characterization and correlation of the electronic structure and structural chemistry of these intriguing nanomaterials: α-Fe_2O_3, γ-Fe_2O_3, Fe/Fe_3O_4, $BiFeO_3$, and $Bi_2Fe_4O_9$. Despite the evident importance of all of these iron-based metal oxides as functional materials as we discussed thus far, very few fundamental soft X-ray absorption spectroscopy (XAS) studies, such as near edge X-ray absorption fine structure (NEXAFS and also known as X-ray absorption near edge spectroscopy (XANES)) analyses, associated with nanoscale motifs, exist. In fact, it has been difficult to adequately correlate the structural character of these materials with their chemistry and electronic structure.

NEXAFS involves the excitation of electrons from a core level to partially filled and empty states. The decay of core hole states results in the emission of Auger electrons from valence molecular orbitals, resulting in an electron yield spectrum. Hence, the peak positions and spectral lineshape in a NEXAFS spectrum can be directly correlated with the nature of these unoccupied electronic states. The decay of core holes may also occur via the emission of fluorescent photons, which originate from the top 200 nm of the target sample as opposed to Auger electrons, which arises from the top 10 nm of the surfaces of these materials. Thus, this technique is both surface and bulk sensitive and is capable of simultaneously probing the electronic structures as well as surface imperfections and surface strain anisotropies of these small nanoparticles. Transition matrix elements and the corresponding intensities of the π^* and σ^* transitions also possess an angular dependence with respect to the plane of single-crystalline, epitaxially grown $BiFeO_3$ thin films.

In Chapter 6, we have demonstrated our ability to employ NEXAFS spectroscopy as a particularly useful and effective technique for the systematic investigation of the electronic structure and surface properties of FeMONS materials. In particular, we have correlated the specific atomic arrangement and electronic structure within each FeMONS system with the position and intensity of different characteristic features of the relevant associated spectra.

1.5. Materials characterization methods

X-ray powder diffraction (XRD). Crystallographic information on FeMONS materials was obtained on a Scintag diffractometer, operating in the Bragg configuration using Cu Kα radiation (λ = 1.54 Å). XRD samples were generated by thorough grinding in ethanol using a mortar and pestle, followed by loading onto glass slides and subsequent drying in air. Diffraction patterns were collected between 10 and 80^{o} (2-theta) at a scanning rate of 2^{o} per minute with a step size of 0.02^{o}. The range of 2-theta used was specific to certain samples. Parameters used for slit widths and accelerating voltage were identical for all samples.

Scanning electron microscopy (SEM). The particle size and morphology of the resulting FeMONS materials were initially characterized using a field emission SEM (Leo 1550) at accelerating voltages of 15 kV. This instrument was equipped with energy-dispersive X-ray spectroscopy (EDS) capabilities. Specifically, FeMONS materials were deposited onto Si wafers, which were then attached onto the surface of SEM brass stubs using a Cu tape. Samples were then conductively coated with gold by sputtering them for 10 seconds twice to minimize charging effects under standard SEM imaging conditions.

Transmission electron microscopy (TEM). Specimens for TEM and high-resolution TEM (HRTEM) were obtained by drying FeMONS materials droplets from an ethanolic dispersion onto a 300 mesh Cu grid coated with a lacey carbon film. TEM images were taken at an accelerating voltage of 120 kV on a Philip CM12 instrument. High resolution images were obtained on a JEOL 2010F HRTEM at an accelerating voltage of 200 kV. This instrument was equipped with an Oxford INCA EDS system with the potential of performing selected area electron diffraction (SAED) to further characterize individual FeMONS materials.

Mössbauer spectroscopy. Mössbauer spectra were collected using a conventional, constant acceleration transmission Mössbauer spectrometer. The source was a 30-mCi-^{57}Co radioactive source in Rh matrix, maintained at room temperature. The spectrometer was calibrated using a 7-μm iron foil enriched in ^{57}Fe. Isomer shifts were reported relative to metallic iron at room temperature. Low temperatures were achieved with a Superveritemp cryostat (Janis Research Co.). Experimental data were least square fitted to theoretical spectra using the WMoss software package (Web Research Co.) and assuming Lorentzian absorption lines.

Superconducting quantum interference device (SQUID) measurements. Magnetization measurements were obtained using a magnetic property measurement

system (MPMS) magnetometer. Powder samples of the FeMONS materials were pressed lightly, then loaded into a gel cap, and covered with silica wool. This was held within a uniform drinking straw, which was attached to the sample rod of the MPMS apparatus. Signals generated by measurements of an empty sample holder demonstrated that the holder assembly contributed <1% to the overall magnetic signal.

Raman spectroscopy. Specimens were prepared by depositing a droplet of FeMONS materials from an ethanolic dispersion onto a Si wafer. The spectra were acquired with a Raman micro spectrometer (Renishaw 1000, Drexel University Central Characterization Facility) using an Ar ion laser (514.5 nm) in back-scattering geometry. A 50x objective and low laser power density were chosen for irradiation of the sample and signal collection. The laser power was kept low enough to avoid heating of the samples by optical filtering and/or defocusing the laser beam at the samples surface. Spectra were collected in the range 1000 to 100 cm^{-1} with a resolution of 1 cm^{-1}.

X-ray photoelectron spectroscopy (XPS). Pressed sample wafers were attached to stainless-steel holders using conductive double-sided tape and placed in the vacuum chamber of a Model DS800 XPS surface analysis system (Kratos Analytical Plc., Manchester, UK). The chamber was evacuated to a base pressure of ~5×10^{-9} torr (1 torr ~1.33 Pa). A hemispherical energy analyzer was used for electron detection. XPS spectra were first collected using a Mg Kα X-ray source at 80 eV pass energy and in 0.75 eV steps for each sample survey spectrum. As-obtained spectra were plotted and used to generate estimates of the atomic and weight concentrations of the elements indicated by the peaks present in the spectral data. High-resolution spectra were collected for the major elements detected to study their chemical bonding structures and were obtained at a pass energy 40 eV and in 0.1 eV in order to correct for differential charging effects noted during data collection. High-resolution data were then peak fitted, plotted and tabulated to highlight the chemical species present for each major element detected.

1.6. References

(1) http://www.science.doe.gov/bes/scale_of_things.html.
(2) Iijima, S. *Nature* **1991**, *354*, 56.
(3) Huczko, A. *Appl. Phys. A* **2000**, *70*, 365.
(4) Srinivasarao, M. *Chem. Rev.* **1999**, *99*, 1935-1961.
(5) Pfaff, G.; Reynders, P. *Chem. Rev.* **1999**, *99*, 1963-1981.
(6) Feynman, R. P., There's Plenty of Room at the Bottom (the talk on December 1959) *http://www.zyvex.com/nanotech/feynman.html*.
(7) Binning, G.; Rohrer, H.; Gerber, C.; Weibel, E. *Phys. Rev. Lett.* **1982**, *49*, 57.
(8) Eigler, D. M.; Schweizer, E. K. *Nature* **1990**, *344*, 524.
(9) Sohn, L. L. *Nature* **1998**, *394*, 131.
(10) Awschalom, D. D.; DiVincenzo, D. P.; Smyth, J. F. *Science* **1992**, *258*, 414.
(11) Scheer, E.; Agrait, N.; Cuevas, J. C.; Yeyati, A. L.; Ludoph, B.; Martin-Rodero, A.; Bollinger, G. R.; van Ruitenbeek, J. M.; Urbina, C. *Nature* **1998**, *394*, 154.
(12) Xia, Y.; Rogers, J. A.; Paul, K. E.; Whitesides, G. M. *Chem. Rev.* **1999**, *99*, 1823-1848.
(13) Piraux, L.; George, J. M.; Despres, J. F.; Leroy, C.; Ferain, E.; Legras, R.; Ounadjela, K.; Fert, A. *Appl. Phys. Lett.* **1994**, *65*, 2484.
(14) Whitney, T. M.; Jiang, J. S.; Searson, P. C.; Chien, C. L. *Science* **1993**, *261*, 1316.
(15) Joachim, C. *Nat. Mater.* **2005**, *4*, 107.
(16) *Nanoscience, and Nanotechnology: Opportunities and Uncertainties* Document 19/04 (The Royal Society, London, 2004).
(17) Alivisatos, A. P. *Pure Appl. Chem.* **2000**, *72*, 3.
(18) Fendler, J. H. *Chem. Rev.* **1987**, *87*, 877.
(19) Nirmal, M.; Brus, L. *Acc. Chem. Res.* **1999**, *32*, 407.
(20) Xia, Y.; Yang, P.; Sun, Y.; Wu, Y.; Mayers, B.; Gates, B.; Yin, Y.; Kim, F.; Yan, H. *Adv. Mater.* **2003**, *15*, 353.
(21) Patzke, G. R.; Krumeich, F.; Nesper, R. *Angew. Chem. Int. Ed.* **2002**, *41*, 2446-2461.
(22) Xia, Y.; Yang, P.; Sun, Y.; Wu, Y.; Mayers, B.; Gates, B.; Yin, Y.; Kim, F.; Yan, H. *Adv. Mater.* **2003**, *15*, 353-389.
(23) Rao, C. N. R.; Nath, M. *Dalton Trans.* **2003**, 1-24.
(24) Wong, S. S.; Joselevich, E.; Woolley, A. T.; Cheung, C. L.; Lieber, C. M. *Nature* **1998**, *394*, 52.
(25) *Physics of Quantum Well Devices* (Ed: B. R. Nag), Kluwer, Dordrecht, The Netherlands, in 2000.
(26) *Molecular Beam Epitaxy: Fundamentals and Current Status* (Eds: M. A. Herman, H. Sitter), Springer, Berlin, in 1996.
(27) Kaiser, N. *Appl. Optics* **2002**, *41*, 3053.

(28) Burda, C.; Chen, X.; Narayanan, R.; El-Sayed, M. A. *Chem. Rev.* **2005**, *105*, 1025.
(29) Alivisatos, A. P. *Science* **1996**, *271*, 933.
(30) Alivisatos, A. P. *Nat. Biotech.* **2004**, *22*, 47.
(31) Kaner, R. B.; Gilman, J. J.; Tolbert, S. H. *Science* **2005**, *308*, 1268.
(32) Gilbert, B.; Huang, F.; Zhang, H.; Waychunas, G. A.; Banfield, J. F. *Science* **2004**, *305*, 651.
(33) Huber, D. L. *Small* **2005**, *1*, 482.
(34) Frenkel, J.; Dorfman, J. *Nature* **1930**, *126*, 274.
(35) Bloch, F. *Z. Phys.* **1932**, *74*, 295.
(36) Elmore, W. C. *Phys. Rev.* **1938**, *54*, 1092.
(37) Wang, J.; Neaton, J. B.; Zheng, H.; Nagarajan, V.; Ogale, S. B.; Liu, B.; Viehland, D.; Vaithyanathan, V.; Schlom, D. G.; Waghmare, U. V.; Spaldin, N. A.; Rabe, K. M.; Wuttig, M.; Ramesh, R. *Science* **2003**, *299*, 1719.
(38) Park, T.-J.; Papaefthymiou, G. C.; Viescas, A. J.; Moodenbaugh, A. R.; Wong, S. S. *Nano Lett.* **2007**, *7*, 766.
(39) Hyeon, T. *Chem. Commun.* **2003**, 927.
(40) Zeng, H.; Li, J.; Liu, J. P.; Wang, Z. L.; Sun, S. *Nature* **2002**, *420*, 395.
(41) Chen, J.; Xu, L.; Li, W.; Gou, X. *Adv. Mater.* **2005**, *17*, 582.
(42) Han, J.-T.; Huang, Y.-H.; Wu, X.-J.; Wu, C.-L.; Wei, W.; Peng, B.; Huang, W.; Goodenough, J. B. *Adv. Mater.* **2006**, *18*, 2145.
(43) Schmid, H. *Ferroelectrics* **1994**, *162*, 317.
(44) Smolenskii, G. A.; Chupis, I. E. *Sov. Phys. Usp.* **1982**, *25*, 475.
(45) Hill, N. A. *J. Phys. Chem. B* **2000**, *104*, 6694.
(46) Schmid, H. *Ferroelectrics* **1999**, *221*, 9.
(47) Fiebig, M. *J. Phys. D: Appl. Phys.* **2005**, *38*, R123.
(48) O'Dell, T. H. *The Electrodynamics of Magneto-Electric Media*; North-Holland: Amsterdam, 1970.
(49) Eerenstein, W.; Mathur, N. D.; Scott, J. F. *Nature* **2006**, *442*, 759.
(50) Cheong, S.-W.; Mostovoy, M. *Nat. Mater.* **2007**, *6*, 13.
(51) Ramesh, R.; Spaldin, N. A. *Nat. Mater.* **2007**, *6*, 21.
(52) Smolenskii, G. A.; Agranovskaya, A. I. *Sov. Phys. Tech. Phys.* **1958**, *3*, 1981.
(53) Spaldin, N. A.; Fiebig, M. *Science* **2005**, *309*, 391.
(54) Fiebig, M.; Lottermoser, T.; Fröhlich, D.; Goltsev, A. V.; Pisarev, R. V. *Nature* **2002**, *419*, 818.
(55) Park, T.-J.; Mao, Y.; Wong, S. S. *Chem. Commun.* **2004**, 2708.
(56) Ghosh, S.; Dasgupta, S.; Sen, A.; Maiti, H. S. *J. Am. Ceram. Soc.* **2005**, *88*, 1349.
(57) Ueda, K.; Tabata, H.; Kawai, T. *Appl. Phys. Lett.* **1999**, *75*, 555-557.
(58) Kim, J. S.; Cheon, C. I.; Lee, C. H.; Jang, P. W. *J. Appl. Phys.* **2004**, *96*, 468.
(59) Qi, X.; Dho, J.; Blamire, M.; Jia, Q.; Lee, J. S.; Foltyn, S.; MacManus-Driscoll, J. L.

J. Magn. Magn. Mater. **2004**, *283*, 415.
(60) Singh, S. K.; Kim, Y. K.; Funakubo, H.; Ishiwara, H. *Appl. Phys. Lett.* **2006**, *88*, 162904.
(61) Lee, Y.-H.; Wu, J.-M.; Chen, Y.-C.; Lu, Y.-H.; Lin, H.-N. *Electrochem. Solid State Lett.* **2005**, *8*, F43.
(62) Wang, Y.; Jiang, Q.-h.; He, H.-c.; Nan, C.-W. *Appl. Phys. Lett.* **2006**, *88*, 142503.
(63) Eerenstein, W.; Morrison, F. D.; Dho, J.; Blamire, M. G.; Scott, J. F.; Mathur, N. D. *Science* **2005**, *307*, 1203a.
(64) Bai, F.; Wang, J.; Wuttig, M.; Li, J.; Wang, N.; Pyatakov, A. P.; Zvezdin, A. K.; Cross, L. E.; Viehland, D. *Appl. Phys. Lett.* **2005**, *86*, 032511.
(65) Wang, J.; Scholl, A.; Zheng, H.; Ogale, S. B.; Viehland, D.; Schlom, D. G.; Spaldin, N. A.; Rabe, K. M.; Wuttig, M.; Mohaddes, L.; Neaton, J.; Waghmare, U.; Zhao, T.; Ramesh, R. *Science* **2005**, *307*, 1203b.
(66) Xu, G.; Hiraka, H.; Shirane, G.; Li, J.; Wang, J.; Viehland, D. *Appl. Phys. Lett.* **2005**, *86*, 182905.
(67) Ederer, C.; Spaldin, N. A. *Phys. Rev. B* **2005**, *71*, 060401.
(68) Ederer, C.; Spaldin, N. A. *Phys. Rev. B* **2005**, *71*, 224103.
(69) Neaton, J. B.; Ederer, C.; Waghmare, U. V.; Spaldin, N. A.; Rabe, K. M. *Phys. Rev. B* **2005**, *71*, 014113.
(70) Tokura, Y. *Science* **2006**, *312*, 1481.
(71) Gao, F.; Wang, K. F.; Y., C. X.; Chen, F.; Liu, J.-M. *Appl. Phys. Lett.* **2006**, *89*, 102506.
(72) Zhang, X. Y.; Dai, J. Y.; Lai, C. W. *Prog. Solid State Chem.* **2005**, *33*, 147.
(73) Zhang, X. Y.; Lai, C. W.; Zhao, X.; Wang, D. Y.; Dai, J. Y. *Appl. Phys. Lett.* **2005**, *87*, 143102.
(74) Kounga Njiwa, A. B.; Aulbach, E.; Rodel, J.; Turner, S. L.; Comyn, T. P.; Bell, A. J. *J. Am. Ceram. Soc.* **2006**, *89*, 1761.
(75) Zhu, W. M.; Ye, Z.-G. *Ceram. Int.* **2004**, *30*, 1435.
(76) Woodward, D. I.; Reaney, I. M.; Eitel, R. E.; Randall, C. A. *J. Appl. Phys.* **2003**, *94*, 3313.
(77) Kanai, T.; Ohkoshi, S.-i.; Nakajima, Akira; Watanabe, T.; Hashimoto, K. *Adv. Mater.* **2001**, *13*, 487.
(78) Wang, D. H.; Goh, W. C.; Ning, M.; Ong, C. K. *Appl. Phys. Lett.* **2006**, *88*, 212907.
(79) Jiang, Q.-H.; Nan, C.-W.; Shen, Z.-J. *J. Am. Ceram. Soc.* **2006**, *89*, 2123.
(80) Jun, Y.-K.; Moon, W.-T.; Chang, C.-M.; Kim, H.-S.; Ryu, H. S.; Kim, J. W.; Kim, K. H.; Hong, S.-H. *Solid State Commun.* **2005**, *135*, 133.
(81) Lee, D.; Kim, M. G.; Ryu, S.; Jang, H. M.; Lee, S. G. *Appl. Phys. Lett.* **2005**, *86*, 222903.
(82) Qi, X.; Dho, J.; Tomov, R.; Blamire, M. G.; MacManus-Driscoll, J. L. *Appl. Phys.*

Lett. **2005**, *86*, 062903.
(83) Li, J.; Duan, Y.; He, H.; Song, D. *J. Alloys Comp.* **2001**, *315*, 259.
(84) Mao, Y.; Banerjee, S.; Wong, S. S. *J. Am. Chem. Soc.* **2003**, *125*, 15718.
(85) Poghossian, A. S.; Abovian, H. V.; Avakian, P. B.; Mkrtchian, S. H.; Haroutunian, V. M. *Sens. Actuators B* **1991**, *4*, 545.
(86) Zakharchenko, N. I. *Kinet. Catal.* **2002**, *43*, 95.
(87) Xiong, Y.; Wu, M.; Peng, Z.; Jiang, N.; Chen, Q. *Chem. Lett.* **2004**, *33*, 502.
(88) Park, T.-J.; Papaefthymiou, G. C.; Moodenbaugh, A. R.; Mao, Y.; Wong, S. S. *J. Mater. Chem.* **2005**, *15*, 2099.
(89) Yang, Z.; Huang, Y.; Dong, B.; Li, H.-L.; Shi, S.-Q. *J. Solid State Chem.* **2006**, *179*, 3324.
(90) Han, J.-T.; Huang, Y.-H.; Jia, R.-J.; Shan, G.-C.; Guo, R.-Q.; Huang, W. *J. Cryst. Growth* **2006**, *294*, 469.
(91) Chen, J.; Xing, X.; Watson, A.; Wang, W.; Yu, R.; Deng, J.; Yan, L.; Sun, C.; Chen, X. *Chem. Mater.* **2007**, *19*, 3598.
(92) Stamenkovic, V. R.; Fowler, B.; Mun, B. S.; Wang, G.; Ross, P. N.; Lucas, C. A.; Marković, N. M. *Science* **2007**, *315*, 493.
(93) Cho, K.-S.; Talapin, D. V.; Gaschler, W.; Murray, C. B. *J. Am. Chem. Soc.* **2005**, *127*, 7140.
(94) Kim, F.; Connor, S.; Song, H.; Kuykendall, T.; Yang, P. *Angew. Chem. Int. Ed.* **2004**, *43*, 3673.
(95) Lim, W. P.; Zhang, Z.; Low, H. Y.; Chin, W. S. *Angew. Chem. Int. Ed.* **2004**, *43*, 5685.
(96) Tanigaki, T.; Suzuki, H.; Kimura, Y.; Kaito, C.; Saito, Y. *Surf. Rev. Lett.* **2003**, *10*, 455.
(97) Zysler, R. D.; Vasquez-Mansilla, M.; Arciprete, C.; Dimitrijewits, M.; Rodriguez-Sierra, D.; Saragovi, C. *J. Magn. Magn. Mater.* **2001**, *224*, 39.
(98) Stevenson, M. E.; Kaji, M.; Bradt, R. C. *J. Eur. Ceram. Soc.* **2002**, *22*, 1137.
(99) Miller, E. L.; Paluselli, D.; Marsen, B.; Rocheleau, R. E. *Thin Solid Films* **2004**, *466*, 307.
(100) Park, T.-J.; Mao, Y.; Wong, S. S. *Chem. Commun.* **2004**, 2078.
(101) Park, T.-J.; Papaefthymiou, G. C.; Moodenbaugh, A. R.; Mao, Y.; Wong, S. S. *J. Mater. Chem.* **2005**, *15*, 2099.
(102) Mao, Y.; Wong, S. S. *J. Am. Chem. Soc.* **2004**, *126*, 15245.
(103) Mao, Y.; Park, T.-J.; Wong, S. S. *Chem. Commun.* **2005**, 5721.
(104) Zboril, R.; Mashlan, M.; Petridis, D. *Chem. Mater.* **2002**, *14*, 969.
(105) Morin, F. J. *Phys. Rev.* **1950**, *78*, 819.
(106) Verwey, E. J. W. *Nature* **1939**, *144*, 327.

Chapter II: $BiFeO_3$ Nanostructures

Bismuth iron oxides or bismuth ferrites including $BiFeO_3$ are one of the most interesting iron-containing perovskite materials due to their unique multifunctional properties which are of great technological and fundamental importance. $BiFeO_3$ is also a multiferroic. In addition, bismuth ferrite ($BiFeO_3$) has been a focal point of research because in its bulk form, it is an antiferromagnetic, ferroelectric, and ferroelastic multiferroic material with electrical, magnetic, and structural ordering temperatures well above room temperature. In particular, $BiFeO_3$ possesses ferroelectricity with a high Curie temperature (T_C) of ~1103 K, and antiferromagnetic properties below a Néel temperature (T_N) of ~643 K.

One particularly interesting characteristic of this $BiFeO_3$ material is that the combined action of exchange and spin-orbit interactions in $BiFeO_3$ produces spin canting away from perfect antiferromagnetic ordering. The direction of the resulting small moment, however, rotates, superimposing a spiral spin arrangement with a wavelength of 62 nm, thereby producing a helimagnetic order and a vanishing magnetization in the bulk.[1,2] Thus, size confinement (less than 62 nm) of this $BiFeO_3$ material induces a perturbation of its physical properties by destroying its spiral spin structure. The significance of the size confinement for the spiral spin structure of $BiFeO_3$ is discussed in this chapter.

Thus far, incorporation of bismuth ferrite into practical devices has been hindered by leakage problems that lead to low resistivity, presumably due to defect and non-stoichiometry related issues. Hence, there has been a pressing need to generate high-quality samples. Recent approaches have focused on developing novel structural formulations, such as 0-D, 1-D and 2-D nanostructures, of $BiFeO_3$ materials.[3-5] The majority of prior analyses on such systems has been performed on oriented, epitaxial thin films of $BiFeO_3$ grown on a range of substrates including Si, $SrTiO_3$, $SrRuO_3$, $LaAlO_3$, $Pt/Ti/SiO_2/Si$, and $Pt/TiO_2/SiO_2/Si$.[6-10]

In spite of intense study, a fundamental understanding of structure-property correlations in $BiFeO_3$ is still lacking. Specifically, the nature of the magnetic response as well as the fundamental dependence of ferroelectric behavior on the size and precise chemical composition (*e.g.*, presence of doping) are issues of deep interest.[1,11-16] However, to date, little if any effort has been expended in research associated with the synthesis of substrate-free nanostructures of $BiFeO_3$. Moreover, there have not been any viable reports on their single-crystalline nanostructure analogues associated with 0-D and/or 1-D structural motifs.

For the $BiFeO_3$ nanoparticles, we have employed a facile sol-gel methodology based on the glycol-gel reaction in the synthesis of single-crystalline $BiFeO_3$

nanoparticles. Their sizes have been thermodynamically controlled in order to obtain reproducible size variations ranging from less than 15 nm to greater than 100 nm. As-prepared nanoparticles of $BiFeO_3$, especially those with a diameter range on the order of, or, smaller than the 62 nm wavelength of their intrinsic spiral-modulated spin structure, show strong property correlations with their sizes, an assertion which has been confirmed from SQUID and Mössbauer measurements.

For the synthesis of $BiFeO_3$ nanotubes (NTs), we have employed a template-based technique[17,18] because of its practicality in the sol-gel process, its relative simplicity, and its prior versatility in the preparation of high aspect ratio nanostructures of ternary metal oxides.[19,20] As-prepared $BiFeO_3$ 1-D NTs were subsequently characterized by a number of techniques, including diffraction, spectroscopy, microscopy, as well as magnetic property measurements.

2.1. $BiFeO_3$ Nanoparticles

2.1.1. Materials and Preparation

Bismuth(III) nitrate pentahydrate (Aldrich, 98+%), bismuth(III) oxide (Aldrich, 99.99%), iron(III) nitrate nonahydrate (Aldrich, 98+%), and iron(III) oxide (Aldrich, nanopowder) were used as supplied. In a typical synthesis of $BiFeO_3$ nanoparticles, 5 mmol of $Bi(NO_3)_3 \cdot 5H_2O$ and $Fe(NO_3)_3 \cdot 9H_2O$ were added successively to 12 ml of ethylene glycol. The mixture was stirred at 80^oC, after which a transparent sol was recovered upon evaporation of the excess ethylene glycol. Thereafter, the resultant gel samples were preheated to 400^oC in three separate runs at a ramp-rate of 5^oC/min in order to remove excess hydrocarbons and NO_x impurities. To obtain reasonable size variation, samples were further annealed at 400, 450, 500, 550, 600, 650, 700 and 800 ^oC for 30 min, respectively. As-obtained samples were subsequently ground in a mortar, washed with distilled water upon sonication, and later collected by centrifugation.

As a comparison, the bulk sample was prepared following the solid-state procedure reported by Achenbach *et al*.[21] Briefly, Bi_2O_3 and Fe_2O_3 with a molar ratio of 2 : 1 were ground thoroughly, and the mixture was annealed at 750 ^oC for 3 h, followed by air quenching. Residual Bi_2O_3 was removed by a multiple-step nitric acid (17%) leaching process. The resultant sample was washed several times with distilled water and lastly with ethanol. As-obtained samples were ground into a fine powder.

2.1.2. Results and Discussion

2.1.2.1. XRD measurements: purity, crystallinity, and size dependence of as-prepared $BiFeO_3$ nanoparticles

The purity and crystallinity of as-prepared $BiFeO_3$ nanoparticles as well as of the bulk were examined by powder XRD measurements (Figure 2.1). XRD peaks from $BiFeO_3$ samples annealed at 400, 450, 500, 550, 600, 650, 700 and 800 ^oC are shown in Figure 2.1(b), (c), (d), (e), (f), (g), (h) and (i), respectively. By means of comparison, XRD peaks from a bulk sample are shown in Figure 2.1(j). It is evident that the observed patterns of the collected powders displayed all of the expected peaks emanating from the $BiFeO_3$ structure, with very few, if any, impurity peaks. In effect, diffraction peaks in Figure 2.1 can be indexed to the rhombohedral structure of $BiFeO_3$ (space group: $R3c$) with lattice constants of $a = b = c = 5.63$ Å and $\alpha = \beta = \gamma = 59.4^\circ$, which are in good agreement with literature results (*i.e.,* JCPDS #20-0169, (a)). We note that peaks corresponding to $BiFeO_3$ samples annealed at 700 and 800 ^oC (shown in Figure 2.1(g) and (h), respectively) show a trace of secondary signals (indicated as asterisks) emanating mainly from $Bi_2Fe_4O_9$ structures. We have also observed that the intensities of these impurity peaks tend to increase with annealing temperatures over 700 ^oC.

Peaks from samples annealed at 400 ^oC (Figure 2.1(b)) show complete overlap in several regions. For instance, the expected differentiation between distinctive rhombohedral peaks located at 31.8º and 32.1º is missing. This observation can be attributed to peak broadening, likely arising from the smaller sizes of these as-prepared $BiFeO_3$ nanoparticles. It is evident that the size-dependent peak broadening effect becomes less important for $BiFeO_3$ samples annealed at successively higher temperatures (450 to 650 ^oC, (c) to (g), respectively), indicating that larger particles are formed at higher annealing temperatures.

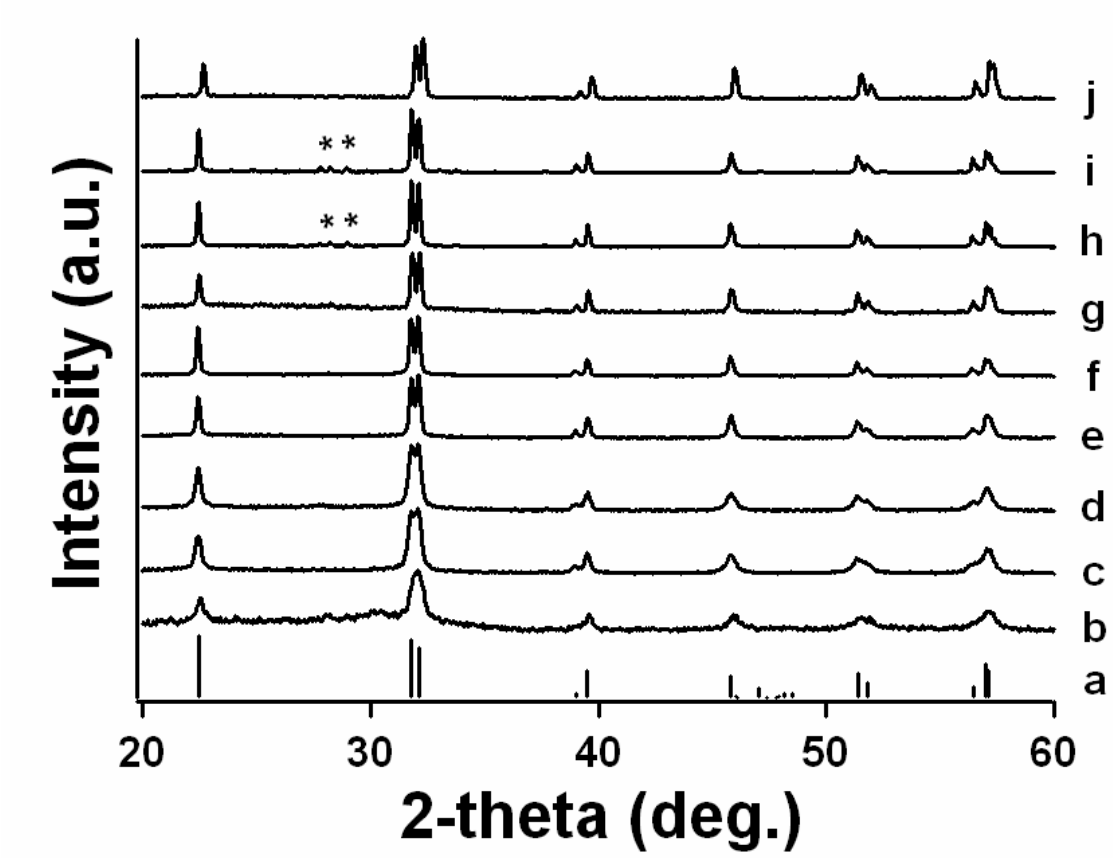

Figure 2.1. XRD patterns of $BiFeO_3$ materials from the JCPDS #20-0169 database standard (a), and of as-prepared $BiFeO_3$ nanoparticles annealed at 400 (b), 450 (c), 500 (d), 550 (e), 600 (f), 650 (g), 700 (h), and 800 (i) ^{o}C, respectively. As a comparison, XRD patterns from the bulk prepared herein are shown in (j). In (h) and (i), the presence of second phase peaks, which mostly originate from $Bi_2Fe_4O_9$ structures, has been indicated by asterisks. Reproduced from Park, T.-J. *et al*., *Nano Lett*. **2007**, *7*, 766.

2.1.2.2. SEM measurements: size, shape, and chemical composition of as-prepared $BiFeO_3$ nanoparticles

Figure 2.2 shows SEM images revealing the morphologies of as-prepared $BiFeO_3$ nanoparticles. It is evident that the size of these as-prepared $BiFeO_3$ nanoparticles is directly related to the annealing temperature used to synthesize these materials. That is, particle size decreases with lower annealing temperatures, an interpretation in good agreement with XRD results. Our data show that $BiFeO_3$ products annealed at temperatures lower than or equal to 600 ^oC mainly consist of solid, crystalline nanoparticles with mean sizes below 100 nm (Figure 2.2A – E). In particular, the size of $BiFeO_3$ nanoparticles annealed at 400 ^oC is comparable with that of particulate gold (measuring 10-20 nm), deposited on a Si substrate (Figure 2.2A). This observation is compatible with calculations derived from XRD measurements. Sizes of our as-prepared $BiFeO_3$ nanostructures annealed at 450, 500, 550, and 600 ^oC, were measured to be 41 ± 15 (B), 51 ± 7 (C), 75 ± 17 (D), and 95 ± 28 (E) nm, respectively. While these data reflect the qualitative trend obtainable from XRD, size measurements, obtainable from SEM, of our as-prepared $BiFeO_3$ nanoparticles deviate somewhat from XRD calculations using the Debye-Schërrer equation suggesting that our as-synthesized nanomaterials likely possess a more complex morphology such as the presence of multi-grained, coalesced structures.

The morphologies of the $BiFeO_3$ products annealed at temperature at 650 and 700 ^oC are shown in Figure 2.2F and 2.2G, respectively. Although these images clearly show the presence of crystalline particles with smooth faces and clear edges, it is also evident that these particles are not only significantly larger with sizes measuring in the range of 245 ± 81 and 342 ± 100 nm, respectively, but also that their size distribution is far more polydisperse and associated SEM images show the presence of increased debris. Therefore, coupled with XRD results, it is reasonable to assert that annealing temperatures less than 700 ^oC should be used in order to obtain reasonably-sized $BiFeO_3$ nanostructures in the current sol-gel system. As a comparison in terms of morphology and size, the SEM image of a bulk $BiFeO_3$ sample is shown in Figure 2.2H.

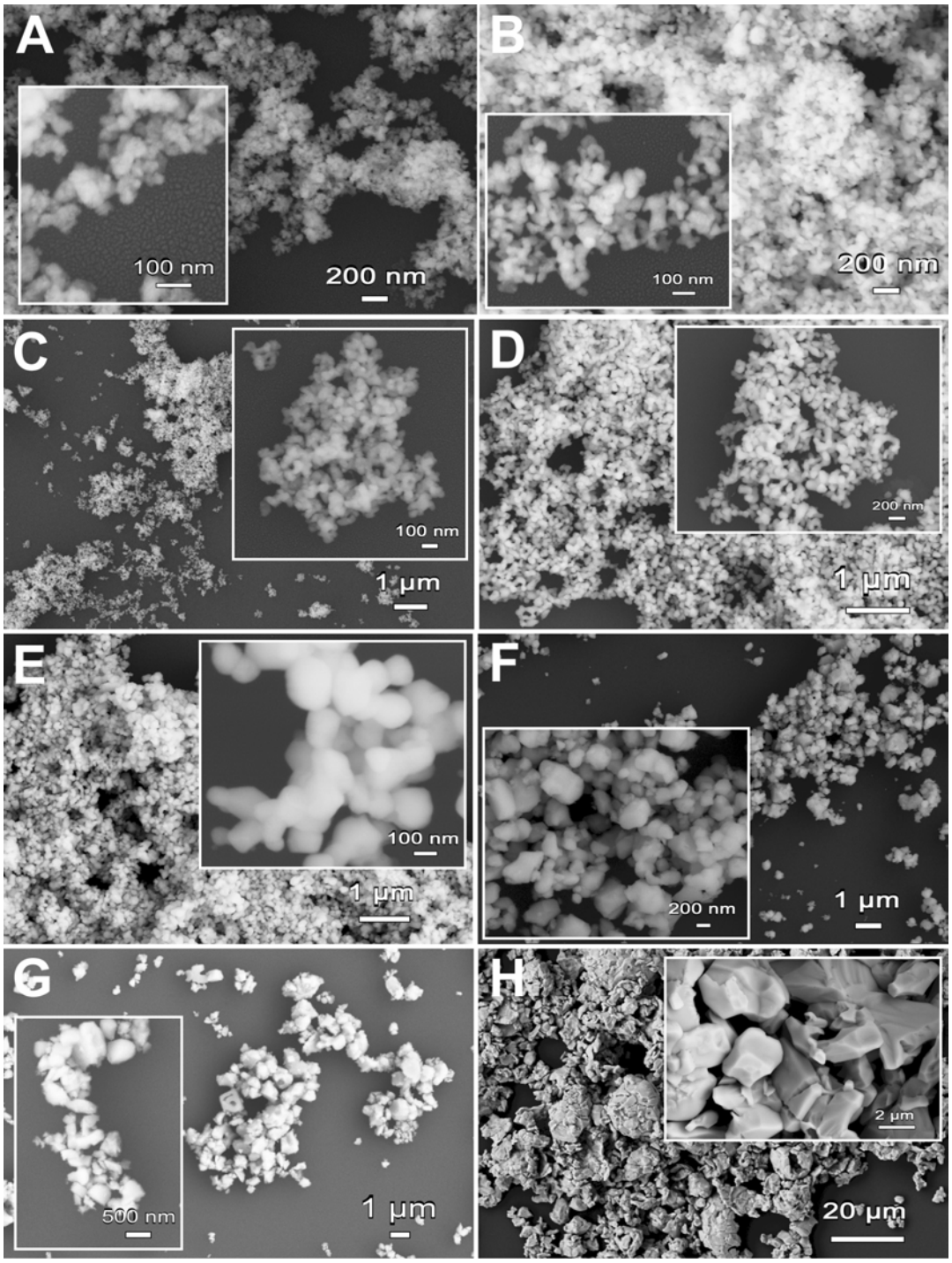

Figure 2.2. SEM images of as-prepared $BiFeO_3$ nanoparticles annealed at 400 (A), 450 (B), 500 (C), 550 (D), 600 (E), 650 (F), and 700 (G) ^{o}C, as well as a bulk sample (H). Insets show corresponding higher magnification images of as-prepared $BiFeO_3$ nanoparticles, respectively. Reproduced from Park, T.-J. *et al*., *Nano Lett*. **2007**, *7*, 766.

2.1.2.3. TEM, HRTEM measurements: size, shape, chemical composition, crystallinity, and lattice spacings of as-prepared $BiFeO_3$ nanoparticles

A typical TEM image of as-prepared $BiFeO_3$ nanoparticles (95 nm), generated at 600ºC from the current sol-gel method as described above, is shown in Figure 2.3A. SAED data taken from individual particles (Figure 2.3B) show the presence of sharp diffraction spots, which are indicative of the formation of well-formulated, single-crystalline $BiFeO_3$. In order to confirm the chemical composition of these as-prepared structures, EDS spectra (Figure 2.3C), taken at a number of selected positions of the sample, show the expected presence of Bi, Fe, and O. In Figure 2.3D, a HRTEM image obtained from a portion of an individual $BiFeO_3$ nanoparticle is displayed in order to further confirm the single-crystalline nature of our as-prepared $BiFeO_3$ samples. This image shows a typical crystalline domain with interplanar spacings of about 3.74 and 2.63 Å, compatible with literature values for bulk $BiFeO_3$ of 3.95 and 2.81 Å, respectively. The lattice spacings described above correspond to the {101} and {012} planes of a rhombohedral phase $BiFeO_3$ crystal (JCPDS #20-0169).

Figure 2.4 also shows a typical TEM (A), SAED (B), EDS (C), and HRTEM (D) results for the as-prepared $BiFeO_3$ nanoparticles (75 nm) generated at 550 ^oC from the experimental protocol described herein. We could apply qualitatively similar interpretations of this data for $BiFeO_3$ nanoparticles possessing a diameter of ~ 95 nm. We note that this interpretation can also be expanded to the rest of as-prepared $BiFeO_3$ nanoparticles having diameters of 51, 41, and 14 nm. Thus, this microscopic investigation confirms the single-crystallinity as well as the chemical composition of the as-prepared $BiFeO_3$ nanoparticles. Additional SAED and HRTEM results for as-prepared $BiFeO_3$ nanoparticles with a typical diameter of 14 and 41 nm are shown in Figure 2.5.

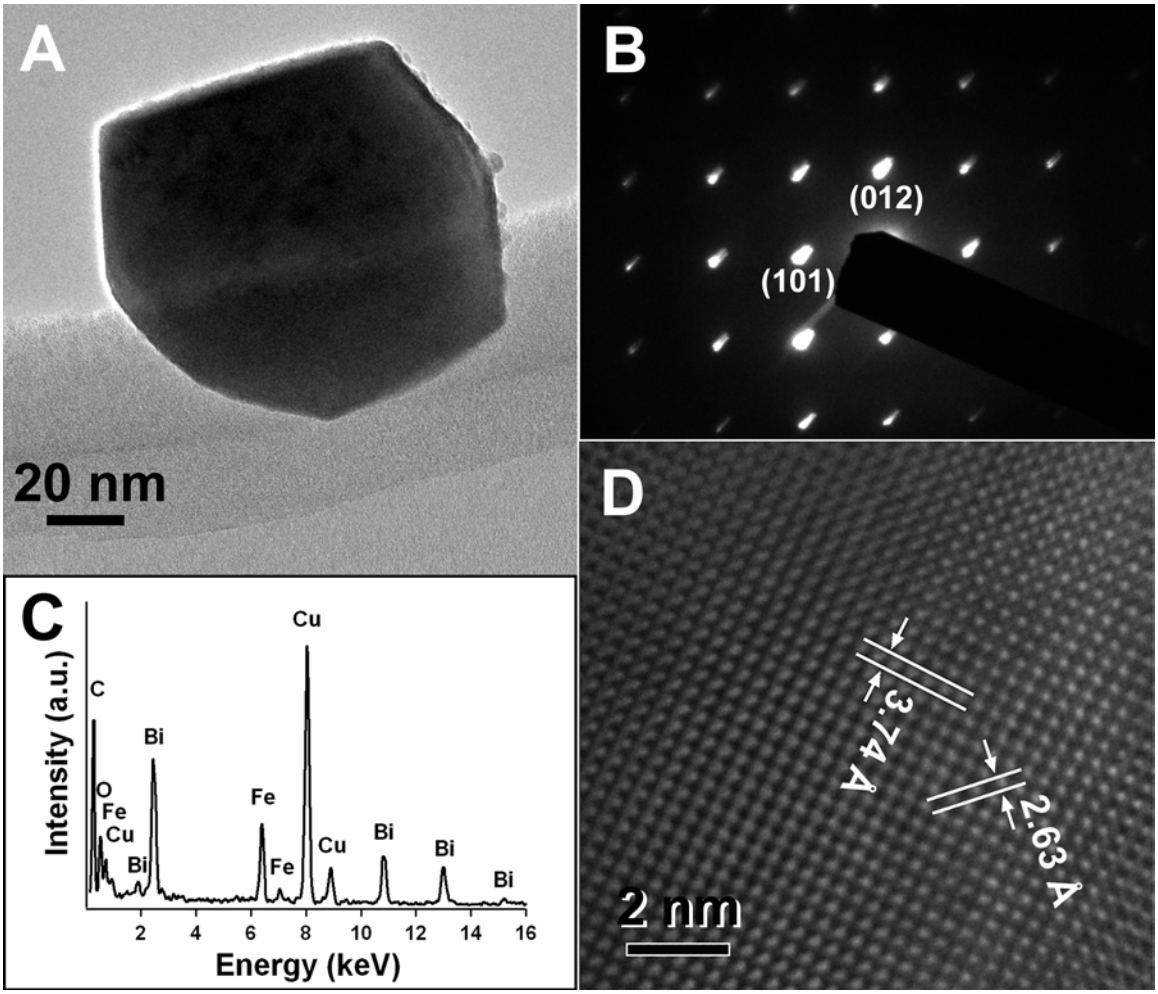

Figure 2.3. TEM image (A) as well as SAED pattern (B) of an individual $BiFeO_3$ nanoparticle (95 nm) generated from an annealing temperature at 600 ºC, and its corresponding EDS (C). The Cu and C peaks originate from the TEM grid. (D) HRTEM image of an enlarged portion of a representative $BiFeO_3$ nanoparticle. Reproduced from Park, T.-J. *et al*., *Nano Lett*. **2007**, *7*, 766.

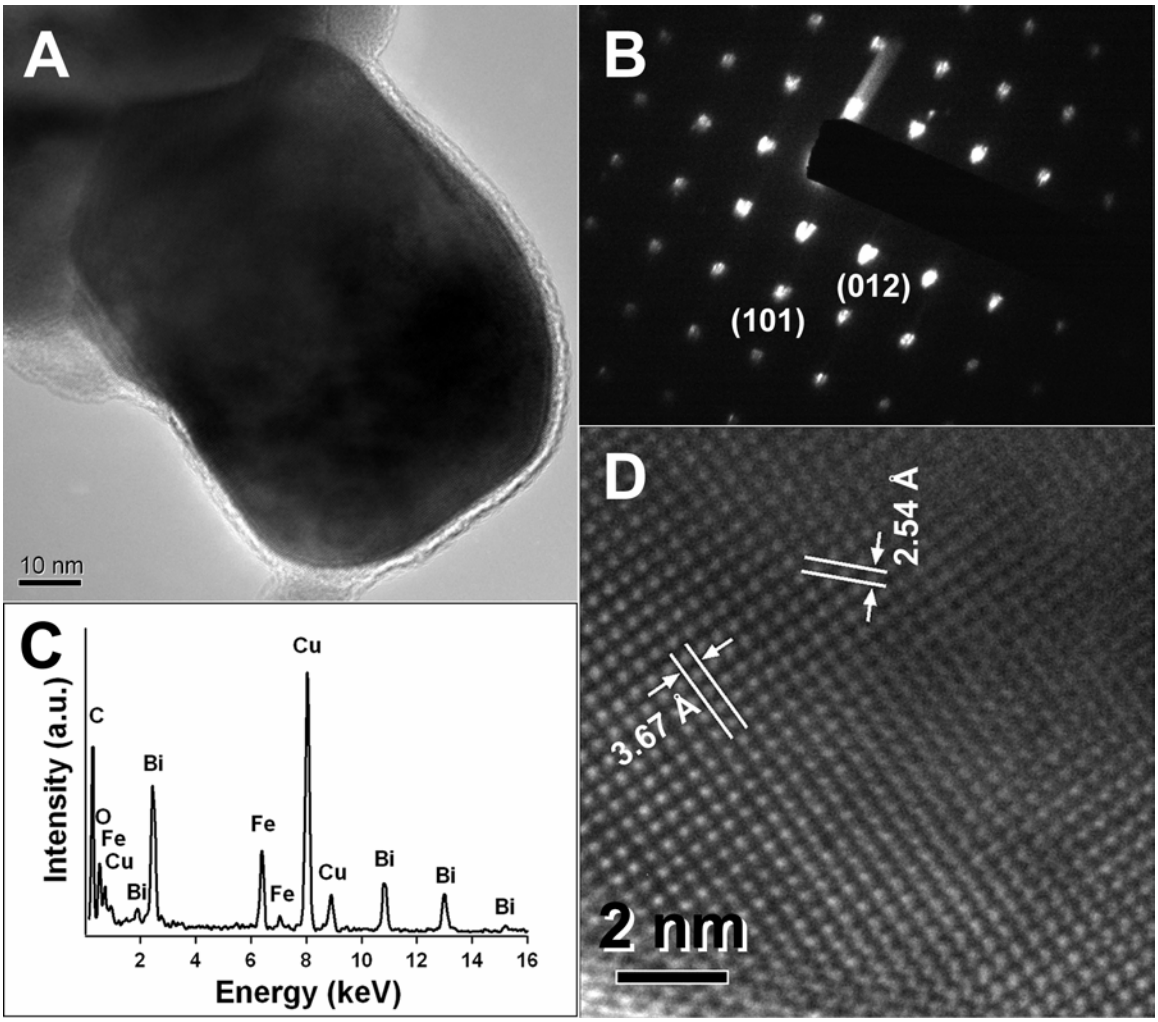

Figure 2.4. TEM image (A) as well as SAED pattern (B) of an individual $BiFeO_3$ nanoparticle (75 nm) generated from an annealing temperature at 550 ^{o}C and its corresponding EDS (C). The Cu and C peaks originate from the TEM grid. (D) HRTEM image of an enlarged portion of a representative $BiFeO_3$ nanoparticle showing a lattice spacing of 3.67 and 2.54 Å, respectively. Reproduced from Park, T.-J. *et al*., *Nano Lett*. **2007**, *7*, 766.

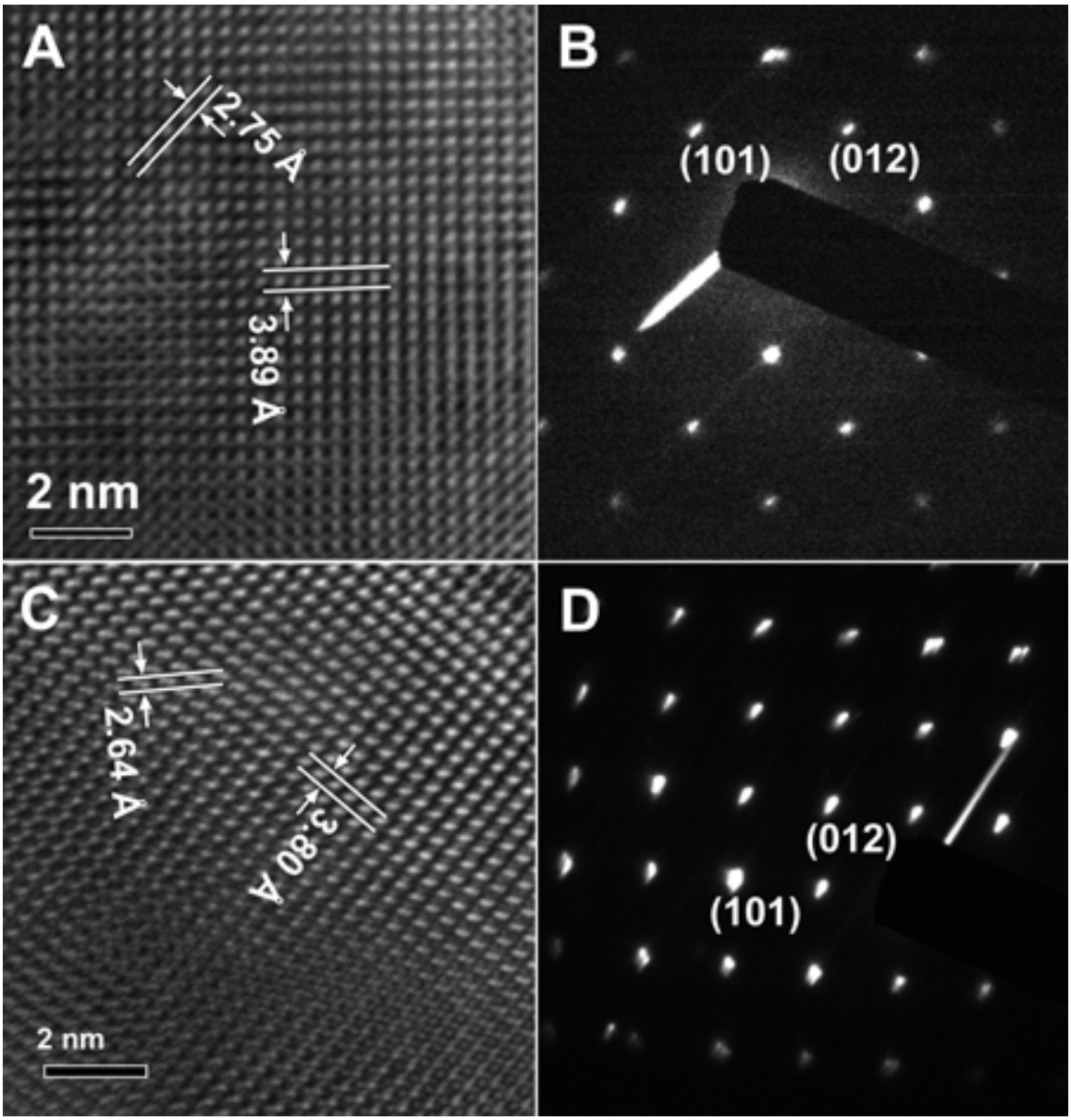

Figure 2.5. HRTEM image of a representative section of a $BiFeO_3$ nanoparticle (14 and 41 nm), generated from annealing at 400 (A) and 500 (C) ^oC, as well as its corresponding SAED patterns, (B) and (D), respectively. Reproduced from Park, T.-J. *et al*., *Nano Lett*. **2007**, *7*, 766.

2.1.2.4. SQUID measurements: size-dependent magnetic properties of as-prepared $BiFeO_3$ nanoparticles

In order to investigate the magnetic properties of assemblies of our bismuth ferrite nanoparticles, magnetic measurements were performed on these samples as well as a bulk $BiFeO_3$ using a magnetic property measurement system (MPMS) magnetometer (Figure 2.6). The magnetic response observed as a function of the applied magnetic field increases systematically with decreasing size of the as-prepared $BiFeO_3$ nanoparticles. Moreover, we note that the magnetic properties of bismuth ferrite nanoparticles with a mean size of 245 nm, prepared at an annealing temperature of 650ºC, show a remarkable similarity to that of the bulk. In both cases, the spontaneous magnetization measured was not appreciable.

Our SQUID results (Figure 2.6) suggest that a magnetic response in $BiFeO_3$ can be initiated when the size of the system is less than about 95 nm (Figure 2.6B). That is, whereas relatively larger $BiFeO_3$ nanoparticles, annealed at 600ºC, with an average diameter of 95 nm, display a low level of spontaneous magnetization, the magnetic response of $BiFeO_3$ nanoparticles rapidly increases in the range of 270 to 460% for samples below 62 nm, the period length of the spiral-modulated spin structure of $BiFeO_3$, as compared with that of the bulk. A summary of the behavior of recorded $BiFeO_3$ magnetization values as a function of size is plotted in the inset to Figure 2.6A. In addition, to illustrate the large hysteresis intrinsic to $BiFeO_3$ nanoparticles with dimensions smaller than 62 nm, the magnetization behavior for the smallest nanoparticles (~14 nm) has been recorded at 10 K as well as 300 K (Figure 2.6C). Magnetic parameters associated with nanoparticulate $BiFeO_3$ are summarized in Table 2.1. From our data (Figure 2.6B), it is evident that the favorable magnetic properties of $BiFeO_3$ nanoparticles with typical dimensions below 62 nm strongly correlate with the size of the nanostructures themselves, due to their grain size confinement, an effect which has been found to modify the long-range spiral-modulated spin structure of $BiFeO_3$.[22]

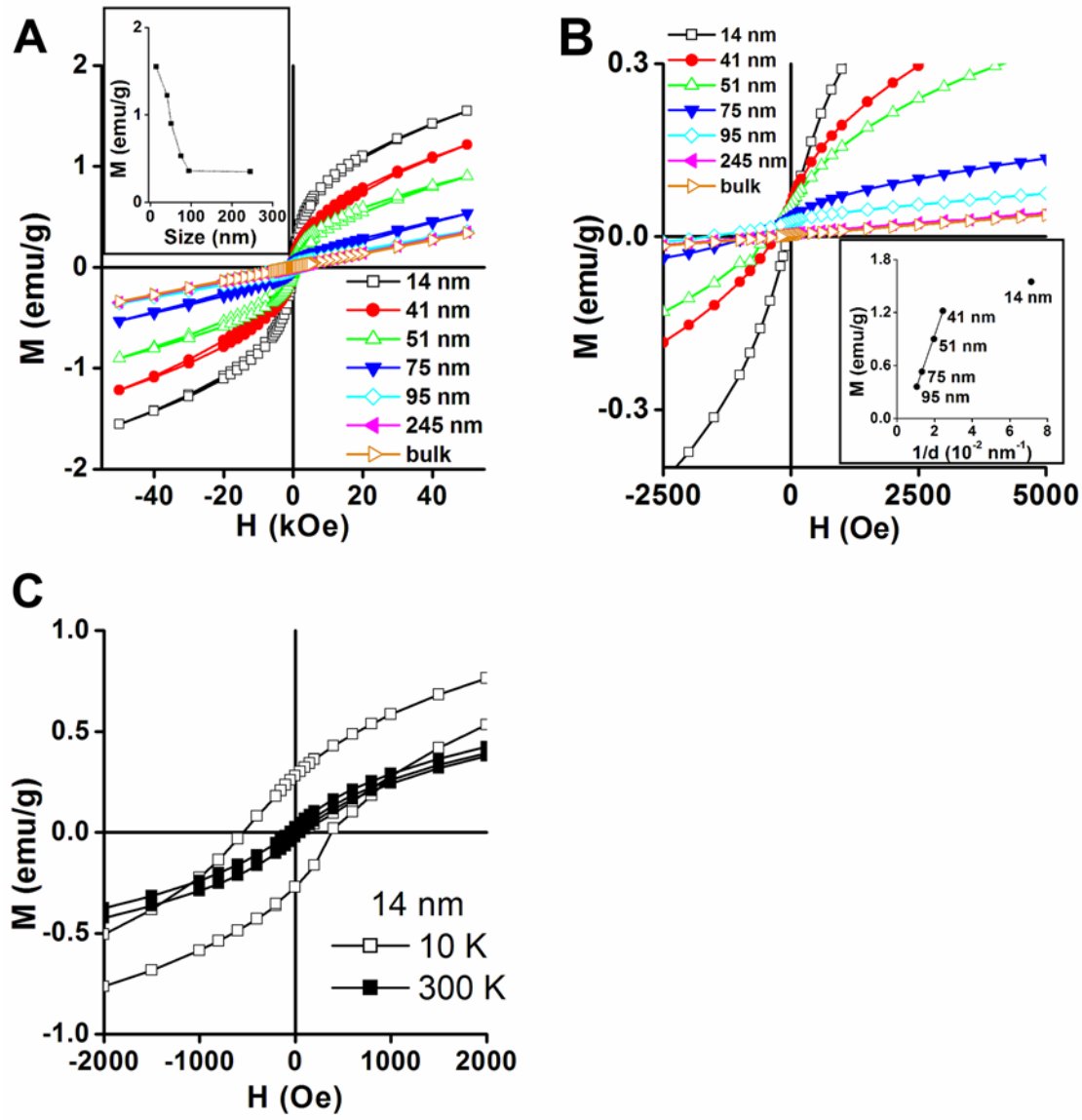

Figure 2.6. (A) Hysteresis loops at 300 K for $BiFeO_3$ nanoparticles with indicated sizes. The inset shows the magnetization behavior of as-prepared $BiFeO_3$ nanoparticles at 50 kOe as a function of size (diameter, *d*). (B) Expanded plots of magnetization of as-synthesized $BiFeO_3$ nanoparticles with the return branches of the hysteresis loops omitted for clarity. The inset shows the corresponding magnetization values at 50 kOe as a function of 1/*d*. (C) Corresponding magnetization data for the smallest nanoparticle prepared in this study (14 nm) at 10 K and 300 K, respectively, are also presented. Reproduced from Park, T.-J. *et al*., *Nano Lett*. **2007**, *7*, 766.

Table 2.1. Derived Room-Temperature Magnetic Parameters for $BiFeO_3$ nanoparticles as well as bulk.*

Size (d, nm)	$1/d$ (nm^{-1})	M_S at 50 kOe		H_C (Oe)	H_{ex} (Oe)	M_r/M_S
		(emu/g)	(μ_B/Fe)			
14	0.071	1.55	0.093	58	2.5	0.02
41	0.025	1.22	0.073	305	5	0.05
51	0.020	0.90	0.054	425	25	0.06
75	0.013	0.53	0.032	775	25	0.06
95	0.011	0.36	0.022	1550	50	0.07
245	0.004	0.35	0.021	-	-	-
bulk	-	0.34	0.020	-	-	-

* Size (d) represents the diameter of as-prepared $BiFeO_3$ nanoparticles. M_S is the magnetization observed at H = 50 kOe. The magnetic moments are defined in units of emu/g as well as in Bohr magnetons per Fe atom (μ_B/Fe). H_C and H_{ex} represents derived coercivity and exchange bias parameters, respectively, while M_r stands for remnant magnetization. Reproduced from Park, T.-J. *et al*., *Nano Lett*. **2007**, *7*, 766.

An antiferromagnet can be described as comprising two spin sublattices with ferromagnetic interactions within one sublattice and antiferromagnetic interactions between sublattices. Néel[23-25] attributed the magnetic moment of small antiferromagnetic particles to incomplete magnetic compensation between these two sublattices. This incomplete spin compensation possible in antiferromagnetically ordered materials becomes measurable only in small antiferromagnetic systems, where the long-range antiferromagnetic order is frequently interrupted at the particle surfaces. In small structures, the surface-to-volume ratio becomes very large with decreasing particle size, enhancing the tangible contribution to the particle's overall magnetization by uncompensated spins at the surface. For single-domain antiferromagnetic particles, the magnetization is expected to scale as ~1/d (where d is the diameter of the particle), that is, as the surface to volume ratio[26].

A plot of the magnetization, measured at the maximum applied field of H_{appl} = 50 kOe, as a function of 1/d, is presented in the inset to Figure 2.6B. For particles ranging in diameter from 95 to 41 nm, a linear dependence is observed, indicating that the simple Néel model is applicable.[27] Initially, the ferromagnetic moments on the surface were thought to be oriented along the antiferromagnetic axis of the particle core. It is now believed that the actual microscopic moment arrangement is such that the ferromagnetic surface spins are actually orthogonal to the antiferromagnetic axis of the core.[28] The smallest of the particles measured, *i.e.*, the 14 nm diameter particle, deviates considerably from the expected behavior, indicating that at this particle size range, the particle can no longer be modeled by the superposition of an antiferromagnetic core and a ferromagnetic surface. Rather, as the lattice size diminishes to extremely small particle dimensions, surface strain[29] introduces a coordination distortion and a lattice disorder that permeate throughout the entire particle, as opposed to being confined only at the surface, with the net result that different frustrated spin structures are produced. In addition, as the particle's magnetization increases, interparticle interactions within the nanoparticle assemblies become stronger, producing a spin-disordered system, as discussed later.

The maximum magnetization, M_S, obtained corresponds to M_S ~ 1.55 emu/g for the 14 nm particles. Furthermore, a linear extrapolation of our experimental magnetization data from 14 to 75 nm $BiFeO_3$ samples suggests that the highest magnetization achievable for substrate-free bismuth ferrite nanoparticles can attain values of up to about 1.82 emu/g (0.11 μ_B/Fe). To put this value in context, magnetization values of 0.06 ~ 1 μ_B/Fe for epitaxially grown $BiFeO_3$ thin films have been previously reported though are not considered to be fully determinate.[11,12] By contrast, the magnetization values reported for our as-prepared $BiFeO_3$ nanoparticles represent an attainable magnetization that can be ascribed essentially due to size effects alone, without the potentially distracting issues either of epitaxial strain (characteristic of thin films) or of oxygen vacancy defects. We note that this magnetization attainable from exploiting the sheer size effect of these

nanoparticles is relatively small for general applicability in memory devices, although the outlook for specific applications at room temperature, involving spintronics and spin valves, remains highly promising with these nanoscale materials.[30]

The modeling of the magnetization of our particles according to Néel is further supported by the observation of shifted hysteresis loops (Figure 2.6C), which can be interpreted by the presence of exchange coupling between the ferromagnetic surfaces and the antiferromagnetic cores. Derived coercivities, H_C, and exchange fields, H_{ex}, are given in Table 2.1. These recorded values, however, most definitely also reflect exchange and dipolar interparticle interactions in addition to interfacial cross grain-boundary interactions due to the high packing volume fraction in our system of particles.[31] As expected, evidence for strong interparticle interactions is provided for by the shape of our hysteresis loops, which exhibit very small remnant magnetization, M_r, for all particles studied and a lack of saturation. Monte Carlo calculations[31] of hysteresis loops of interacting single domain magnetic particle arrays as a function of particle concentration indicate that the hysteresis loops become progressively tilted towards the *x*-axis with drastically decreasing M_r/M_S ratios with increasing particle concentration, manifested in this case by an increase in interparticle interactions.

The presence of interparticle interactions can also be gleaned from temperature-dependent magnetization studies presented in Figure 2.7, as evidenced by the relative insensitivity of particle size with respect to the temperature of maximum magnetization observed. Specifically, magnetization measurements as a function of temperature at an applied field strength of 200 Oe, after zero-field cooling (ZFC) and also, with field cooling (FC) were studied. We note that the apparent sharp cusps observed in the magnetization curves at 50 K are reproducible for bismuth ferrite samples with particle dimensions over 95 nm (*e.g.*, 245 nm and bulk), as shown in Figure 2.7B. For $BiFeO_3$ nanoparticles possessing diameters of $\leq$ 95 nm, associated data curves exhibit a broad magnetization maximum around T_{max} = 85 K, more precisely ranging only from 75 to 95 K. If the observed T_{max} had represented a blocking temperature[32] associated with superparamagnetic relaxation processes of isolated magnetic nanoparticles, one would have expected a much greater dependence of T_{max} on particle size[33]. However, this is not the case. Another feature of the magnetization curves consistent with the presence of interparticle interactions is the more or less linear decrease of the magnetization above T_{max}, whereas for isolated superparamagnetic particles,[34] a $1/T$ dependence would have been expected.[35] Thus, T_{max} represents a spin-glass-like freezing temperature due to the high packing volume fraction as well as to a complex interplay between finite size effects[22,24], interparticle interactions, and a random distribution of anisotropy axes in our nanoparticle assembly.[36]

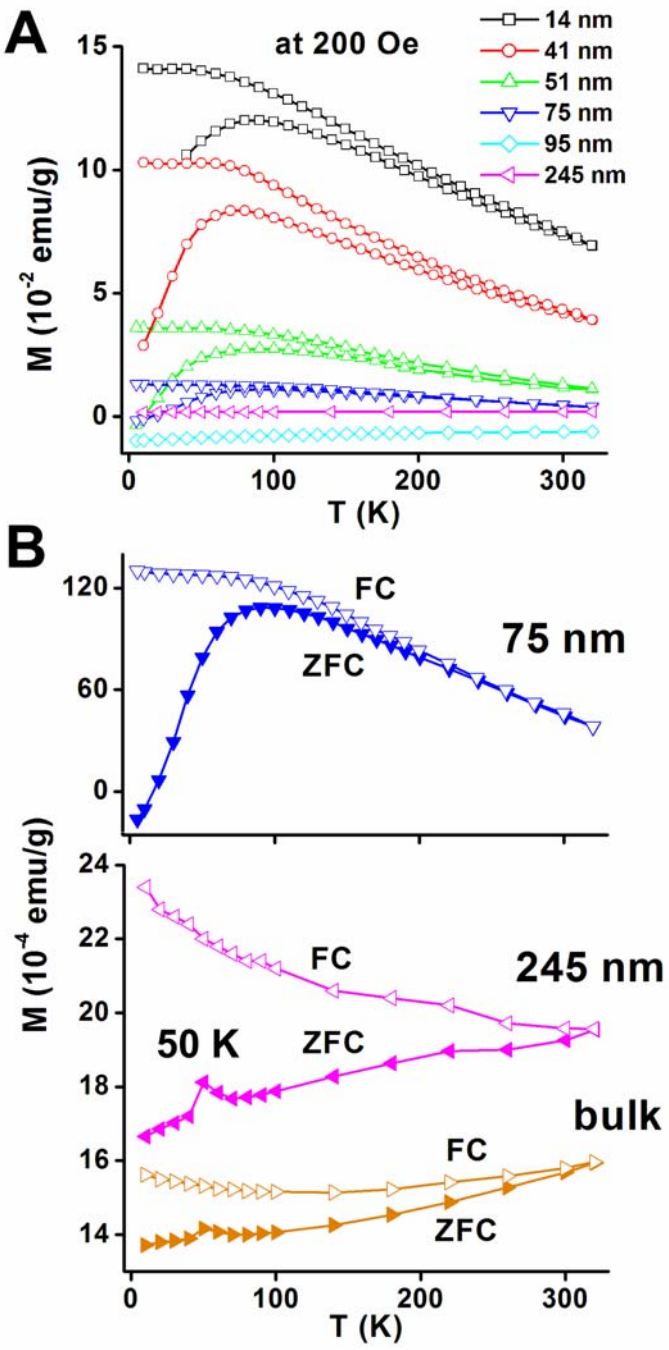

Figure 2.7. (A) Temperature dependence of the magnetization for $BiFeO_3$ nanoparticles of varying sizes, showing zero field cooling (ZFC, solid symbol) and field cooling (FC, open symbol) curves, with an applied magnetic field set at 200 Oe. (B) Expanded plots of ZFC and FC curves for $BiFeO_3$ nanoparticles with diameters of 75 and 245 nm, as well as for the bulk, respectively. A sharp cusp at 50 K is observed for the 245 nm $BiFeO_3$ sample as well as for the bulk and may result from domain wall pinning effects as a result of local structural distortions. Reproduced from Park, T.-J. *et al*., *Nano Lett*. **2007**, *7*, 766.

2.1.2.5. Mössbauer spectroscopy measurements: size-dependent electronic and magnetic properties, and structural defects of as-prepared $BiFeO_3$ nanoparticles

The electronic and magnetic properties of bismuth ferrite nanoparticles were also systematically investigated by Mössbauer spectroscopy. Mössbauer spectra of $BiFeO_3$ nanoparticles, with typical diameters of 14, 51 and 95 nm, respectively, are shown in Figures 2.8 and 2.9, together with corresponding spectra of bulk $BiFeO_3$. As seen in Figure 2.8a and 2.8b, at room temperature, a superposition of quadrupolar (doublet) and magnetic (sixplet) absorption spectra is observed. The spectra become progressively more magnetic with increasing annealing temperature. The collapsed quadrupolar spectra are associated with the subset of smallest particles within the size distribution synthesized within a given sample. Agglomeration leading to the formation of larger particles takes place upon high-temperature annealing, approaching behavior similar to that of bulk material when the average particle size in the distribution measures ~95 nm and above. This tendency to a greater preponderance of larger particles with increasing annealing temperature was also observed in our SEM data.

The magnetic spectral signature corresponds to high spin ferric ions in the $BiFeO_3$ crystal lattice. The characteristic asymmetric, magnetic spectra of the bulk have been previously reported and have been reproduced by our bulk material (Figure 2.8d).[37] The observed asymmetry has been attributed to the presence of Fe^{3+} in two different crystallographic environments that differ primarily in the size of the electric field gradient.[37] Least square fits of our experimental data to theoretical spectra give values for the isomer shift (δ), quadrupole splitting (ΔE_Q), and magnetic hyperfine field (H_{hf}) which are consistent with the presence of primarily ferric ions (Table 2.2).

Above its Néel temperature (T_N ~ 643 K), $BiFeO_3$ has been reported to exhibit a single doublet with a quadrupole splitting of about ΔE_Q = 0.44 mm/s indicating a slightly distorted octahedral symmetry at the Fe^{3+} site.[37] This is consistent with the crystal lattice of $BiFeO_3$ which is known to be a rhombohedrally distorted perovskite structure and in which the Bi^{3+} and Fe^{3+} cations are displaced from their centrosymmetric positions along the (111) axis. Below T_N, the magnetic interaction dominates with the quadrupolar interaction, contributing a small perturbation to the observed overall magnetic structure.

Above the spin-glass-like freezing temperature, thermal activation and fluctuations can induce fast reversals of the particle's magnetic moment leading to the observation of zero average internal magnetic field.[32,38] The smallest particles in the distribution, with a blocking temperature for the characteristic measuring time of Mössbauer spectroscopy $T_{B(Möss)} < 300$ K, will experience such sufficiently fast spin reversals at room temperature that a collapse of their magnetic spectra to quadrupolar spectra is expected. These particular systems are composed primarily of two inequivalent subsites that differ in the degree of site coordination distortion, as reflected by the values of the quadrupole

splitting (δ_1 = 0.32 mm/s, δ_2 = 0.31 mm/s, ΔE_{Q1} = 0.71 mm/s, ΔE_{Q2} = 1.09 mm/s for the sample with average particle size of 14 nm, Table 2.2). We note that the observed quadrupole splittings are larger than that of the paramagnetic state, above the Néel temperature. It is reasonable to postulate that surface imperfections and surface strain anisotropies[29] in the smaller particles induce distortion and site in-equivalence in the crystallographic structure, resulting in an increase in the value of ΔE_Q, due to magnetostrictive effects.[39] This observation is in accordance with the known multiferroic behavior of this system and the strong coupling between dielectric and magnetic properties.[40] For larger particles, two inequivalent magnetic sub-sites are observed with slightly different values of magnetic hyperfine fields (H_{hf1} = 484 kOe and H_{hf2} = 489 kOe for the 95 nm sample; Table 2.2). These values are consistent with previously reported values for bulk $BiFeO_3$ at 80 K by ^{57}Fe-Mössbauer and ^{57}Fe-NMR spectroscopies.[37,41]

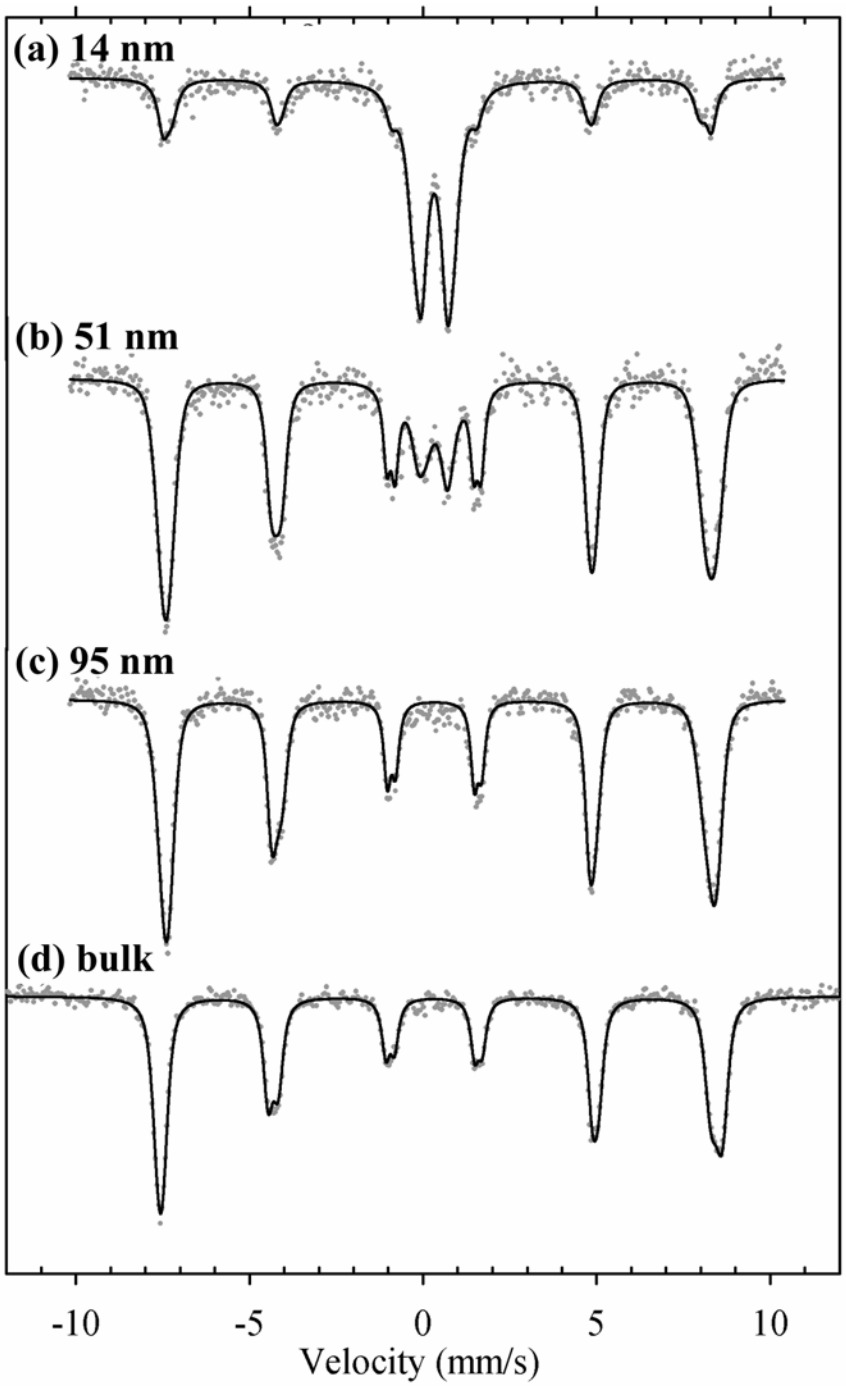

Figure 2.8. Room-temperature Mössbauer spectra of bulk and as-prepared $BiFeO_3$ nanoparticles: (a) 14 nm, (b) 51 nm, (c) 95 nm, and (d) bulk $BiFeO_3$. The solid line is a least-squares fit of the experimental data to theoretical spectra, assuming a superposition of inequivalent iron sites with Lorentzian absorption lines. Derived Mössbauer parameters are tabulated in Table 3.2. Reproduced from Park, T.-J. *et al*., *Nano Lett*. **2007**, *7*, 766.

Table 2.2. Mössbauer parameters of single crystalline $BiFeO_3$ nanoparticles and of $BiFeO_3$ bulk at T = 300 K unless other wise indicated.

Sample	δ [a] (mm/s)	ΔE_Q or ε [b] (mm/s)	H_{hf} [c] (kOe)	Γ [d] (mm/s)	Area (%)	Particle Size (nm)
Preheated at 300 °C	0.33	0.79	-	0.23	73	Not measured (< 14 nm)
	0.31	1.29	-	0.23	25	
	1.33	2.47	-	0.23	2	
Measured at T = 4.2 K	0.49	-0.02	458	1.17	66	
	0.49	0.13	544	0.53	34	
Annealed at 400 °C	0.32	0.71	-	0.40	34	14
	0.31	1.09	-	0.51	32	
	0.35	0.04	471	0.44	16	
	0.37	0.09	488	0.35	18	
Annealed at 500 °C	0.41	0.64	-	0.63	6	51 ± 7
	0.28	0.82	-	0.63	12	
	0.37	0.08	483	0.45	43	
	0.38	0.32	488	0.41	39	
Annealed at 600 °C	0.39	0.0565	484	0.42	46	95 ± 28
	0.38	0.321	489	0.35	54	
Bulk	0.39	-0.103	493	0.36	47	
	0.38	0.340	499	0.34	53	

[a] Isomer shifts (δ) are relative to α-Fe at room temperature.
[b] Quadrupole splitting (ΔE_Q or ε).
[c] Average hyperfine magnetic field (H_{hf}) at the iron nucleus.
[d] Full width at half maximum (Γ).
Reproduced from Park, T.-J. *et al*., *Nano Lett*. **2007**, *7*, 766.

As discussed earlier, the oxygen deficiency in the $BiFeO_3$ structure is known to produce leakage problems, compromising this promising material from device applications. Mössbauer spectroscopy is uniquely suited for the detection of oxygen deficiency due to the fact that it results in the reduction of $Fe^{3+} \rightarrow Fe^{2+}$ at the location of the oxygen vacancy. We have carefully examined our spectroscopic data for the presence of Fe^{2+}. No such signal was detected for any of our annealed samples with particles possessing a diameter, $d \geq 14$ nm. We also recorded the Mössbauer spectra of a sample that was not annealed, but rather had been only preheated at 300 ^{o}C (Figure 2.9). Because of the small size, $\leq$ 14 nm, of the particle, the room-temperature spectra evince a superparamagnetic signature, while at 4.2 K, the full magnetic spectrum is recovered (Figure 2.9). This is the only spectrum exhibiting a very weak Fe^{2+} signature, associated with a ~2% effect, contributing no more than 0.01 μ_B/Fe to the observed magnetic signal (Figure 2.9). Hence, the large increase in magnetization observed with decreasing particle size cannot be explained away by the presence of Fe^{2+}, that is, the presence of oxygen defects. Instead, the increase in magnetization is due to the fact that, as the particle size diminishes and the surface-to-volume ratio increases, the contribution of surface spins to the total magnetic moment of the particle increases.[42] In small particle magnetism, it is well established that surface anisotropies dominate magnetic behavior. Thus, we believe that the increase of magnetization in nanoscale bismuth ferrite nanoparticles is due primarily to the contribution of uncompensated spins at the surface, strain anisotropies and non-collinear magnetic ordering, leading to frustrated spin systems in addition to an increased suppression of the material's intrinsic spiral spin structure below a certain particle size, as previously discussed.[43]

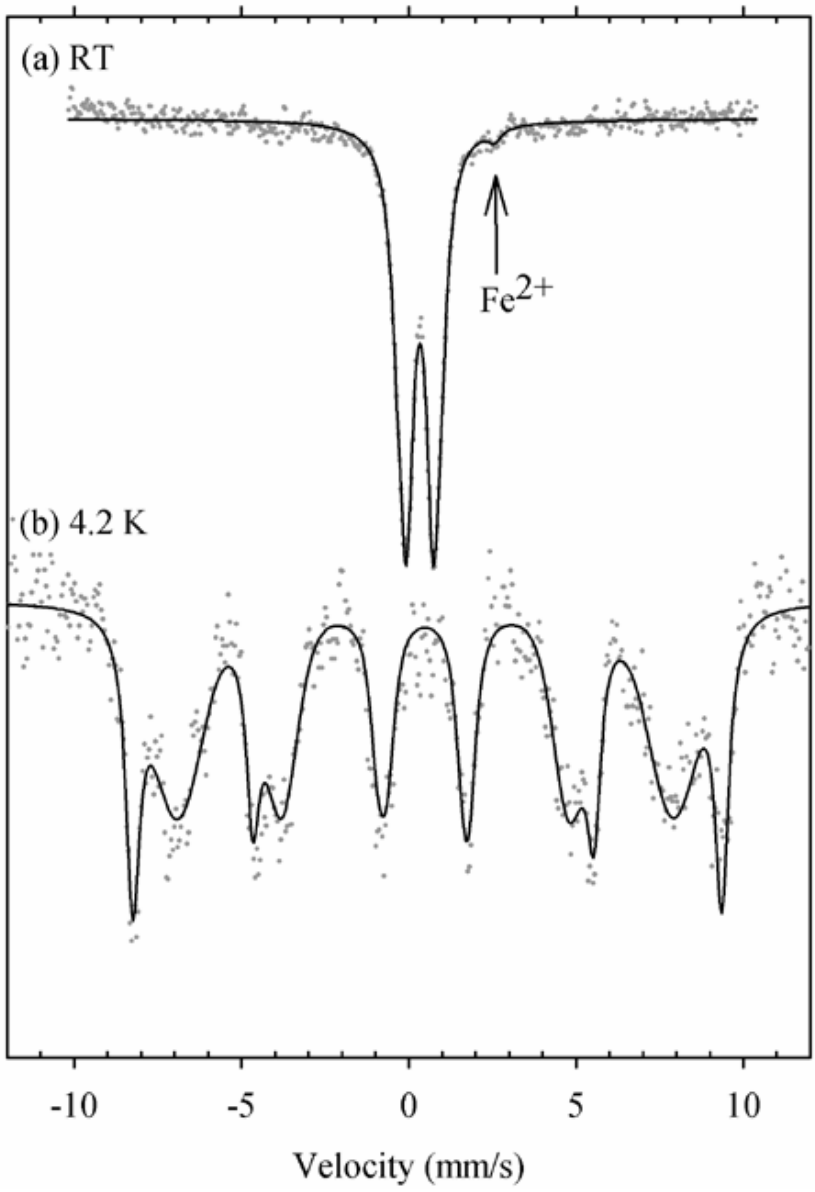

Figure 2.9. Mössbauer spectra of an as-prepared, 300ºC preheated sample measured at (a) 300 K and (b) 4.2 K. Solid lines are least square fits of the experimental points to theoretical spectra, assuming a superposition of inequivalent iron sites with Lorentzian absorption lines. Derived Mössbauer parameters are given in Table 2.2. Reproduced from Park, T.-J. *et al*., *Nano Lett*. **2007**, *7*, 766.

2.1.2.6. Raman spectroscopy measurements: coupling of electronic and magnetic properties of as-prepared $BiFeO_3$ nanoparticles

To look for evidence of any coupling between the magnetic and electric properties in our nanoscale system as well as to corroborate our SQUID and Mössbauer data, we also completed a Raman study of randomly-oriented, as-prepared $BiFeO_3$ nanoparticles, shown in Figure 2.10. The peak at 136 cm^{-1} (denoted by an arrow) can be assigned to the first normal A_1 mode for the rhombohedral $BiFeO_3$ system.[44] Calculations suggested that the most dominant force constant for all three normal A_1 modes in $BiFeO_3$ system can be ascribed to Bi-O1, suggesting the relatively more important contribution of Bi-O bonds to the observation of optical phonon modes as compared with that of Fe-O bonds. The decrease in peak intensity of this normal A_1 mode with decreasing particle size is indicative of the suppression of the contribution of the Bi-O1 vibrational mode, which can most likely be attributed to enhanced coupling of magnetic, ferroelectric and/or structural order parameters due to size confinement considerations and accompanying lattice distortions in as-prepared $BiFeO_3$ nanoparticles.

The decrease in the intensity of the 136 cm^{-1} peak, observed for $BiFeO_3$ nanoparticles with size ranges up to 95 nm (Figure 2.10a – e), coincides with the appearance of an appreciable spontaneous magnetization and hysteretic behavior in the corresponding SQUID measurements (Figure 2.6). By contrast, the lack of an appreciable hysteresis in SQUID data was correlated with an increased intensity of the 136 cm^{-1} Raman peak for $BiFeO_3$ samples larger than 95 nm (Figure 2.10f and g).

We also compare the Raman spectrum, shown in Figure 2.10h with that of polycrystalline Bi-based superconductor/insulator (BSCCO/$BiFeO_3$) composites; a number of peaks were reliably assigned to that of $BiFeO_3$ itself, in good agreement with that of previously reported data.[45] In addition, our Raman study is comparable with a temperature-dependent Raman scattering study on single-crystals of $BiFeO_3$ revealing the presence of a ferroelectric-to-paraelectric phase transition as well as colossal phonon anomalies around the Néel temperature (T_N). These observations are indicative of a very strong spin-phonon coupling and are attributable to interactions between magnetic and ferroelectric order parameters.[46]

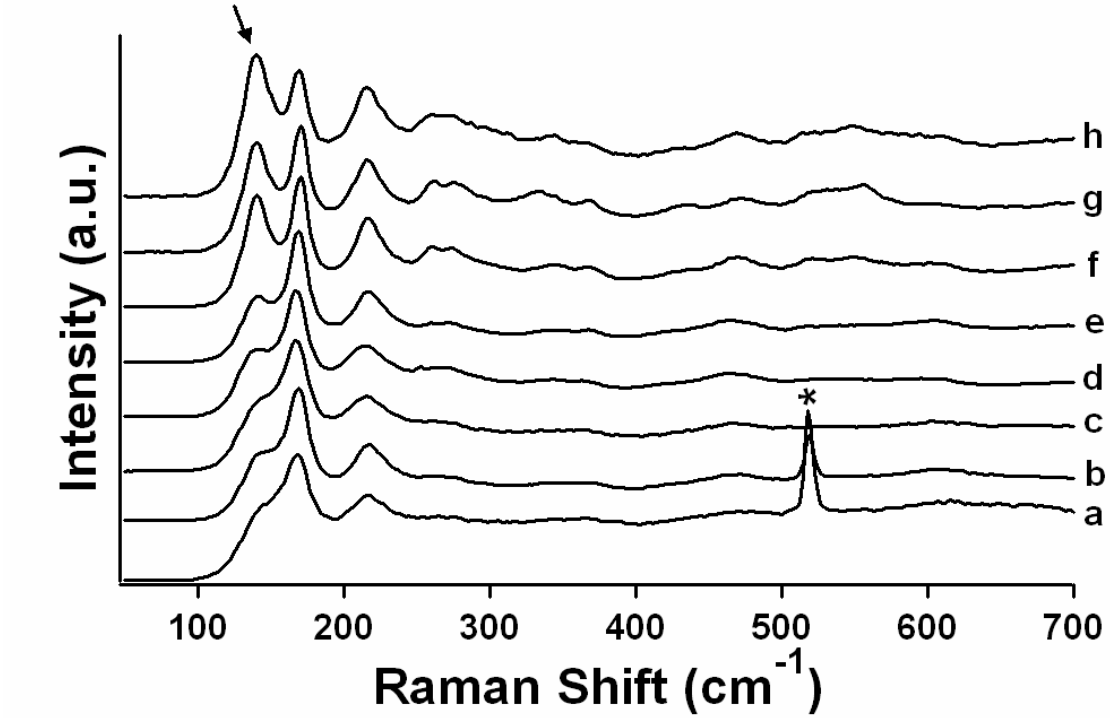

Figure 2.10. Raman spectra of as-prepared $BiFeO_3$ nanoparticles with typical dimensions of (a) 14 nm, (b) 41 nm, (c) 51 nm, (d) 75 nm, (e) 95 nm, (f) 245 nm, and (g) 342 nm, respectively, as well as of the bulk (h). The Si substrate peaks are indicated by an asterisk ((a) and (b)). The arrow refers to the peak at 136 cm^{-1}, corresponding to the first normal A_1 mode of bulk $BiFeO_3$. Reproduced from Park, T.-J. *et al*., *Nano Lett*. **2007**, *7*, 766.

2.2. $BiFeO_3$ Nanotubes

2.2.1. Materials and Preparation

$Bi(NO_3)_3 \cdot 5H_2O$ (Aldrich, 98+%) and $Fe(NO_3)_3 \cdot 9H_2O$ (Aldrich, 98+%) were used, as supplied. In a typical synthesis, $Bi(NO_3)_3 \cdot 5H_2O$ and $Fe(NO_3)_3 \cdot 9H_2O$ with a molar ratio of 1:1 were added successively to ethylene glycol.[47,48] The resulting mixture was stirred at 80 ºC for 1 h, after which a transparent sol was recovered upon evaporation of the excess ethylene glycol. Droplets of the sol were deposited using a syringe onto a porous anodic alumina (AAO) template (Whatman Anodisc®) surface with application of pressure.[49] AAO membranes with different pore sizes, such as 200 nm and 100 nm, have been used. The resultant samples, *i.e.*, AAO templates containing the $BiFeO_3$ precursors, were subsequently oven-dried at 100 ^oC for an hour, and then preheated to 400 ^oC for three separate runs at a ramp-rate of 5 ^oC/min in order to get rid of excess hydrocarbons and NO_x impurities. The sample was further annealed at 600 ^oC for 30 min. $BiFeO_3$ nanotubes (NTs) were isolated after removal of AAO template, following its immersion in 6M NaOH solution at room temperature for 24 h. Thereafter, to retrieve reasonable quantities of nanotubes, the base solution was diluted in several steps with distilled water and lastly ethanol. Tubes were collected by centrifugation.

2.2.2. Results and Discussion

2.2.2.1. XRD measurements: purity and crystallinity of as-prepared $BiFeO_3$ nanotubes

The purity and crystallinity of both the $BiFeO_3$ bulk and NT samples were examined using powder XRD (Figure 2.11, part A). Very few if any impurity peaks were present in the bulk samples, prepared by an identical experimental protocol. Peaks can be indexed to the rhombohedral structure of $BiFeO_3$ which is in good agreement with literature results (*i.e.*, JCPDS#20-0169). The XRD pattern of $BiFeO_3$ NTs is also shown for comparison and is in agreement with bulk and reference data. We note that since the template synthesis method produces relatively small amounts of confined nanostructures for XRD, data for the $BiFeO_3$ NTs were obtained indirectly (Figure 2.11, part B) by subtracting the signal due to the alumina template from that of the template/$BiFeO_3$ sample itself.

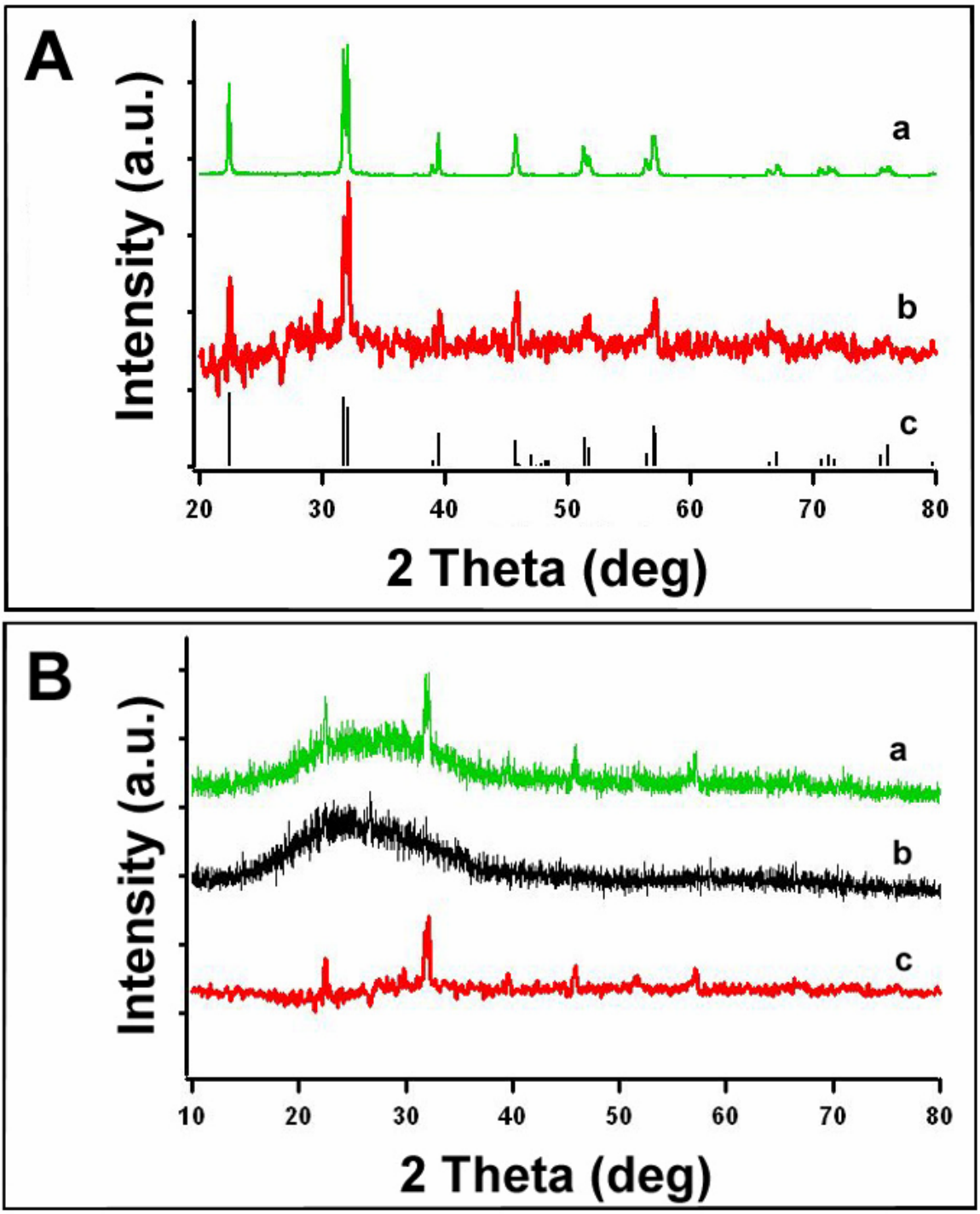

Figure 2.11. (A) Powder X-ray diffraction (XRD) of bulk $BiFeO_3$ (a), $BiFeO_3$ NTs (b), and comparison with literature results (JCPDS#20-0169) (c). (B) $BiFeO_3$ NTs' X-ray diffraction patterns (c) were deduced by subtracting the diffraction signal of the alumina template/$BiFeO_3$ (a) from that of the alumina template itself (b). Reproduced from Park, T.-J. *et al*., *Chem. Commun.* **2004**, 2708.

2.2.2.2. SEM measurements: size, shape, and chemical composition of as-prepared $BiFeO_3$ nanotubes

Figure 2.12 shows scanning electron microscopy (SEM) images revealing the morphologies of $BiFeO_3$ NTs. Figure 2.12A and 2.12B illustrate as-prepared $BiFeO_3$ NTs, grown in AAO membranes having 200 nm and 100 nm sized pores, respectively. The micrographs show dispersed individual $BiFeO_3$ NTs as well as some degree of NT bundling. It is evident that $BiFeO_3$ NTs generated from AAO membranes having pore sizes of 200 nm (Figure 2.12A) mainly consist of straight and smooth structures with relatively few extraneous particulate debris. These tubes have outer diameters in the range of 240 to 300 nm, with lengths ranging from several microns to as much as 50 μm, corresponding to the entire length of the template membranes used. In the case of $BiFeO_3$ NTs generated from 100 nm diameter pores (Figure 2.12B), the lengths of the NTs are not only understandably shorter but also more irregular and polydisperse. Their lengths attain several microns at best with diameters in the range of 140 to 180 nm. Tubular morphologies show a higher degree of roughness, as compared with those of $BiFeO_3$ NTs possessing larger diameters. The larger diameters of NTs can be presumably ascribed to larger internal diameters than the reported surface diameters of AAO membranes used.[48,49]

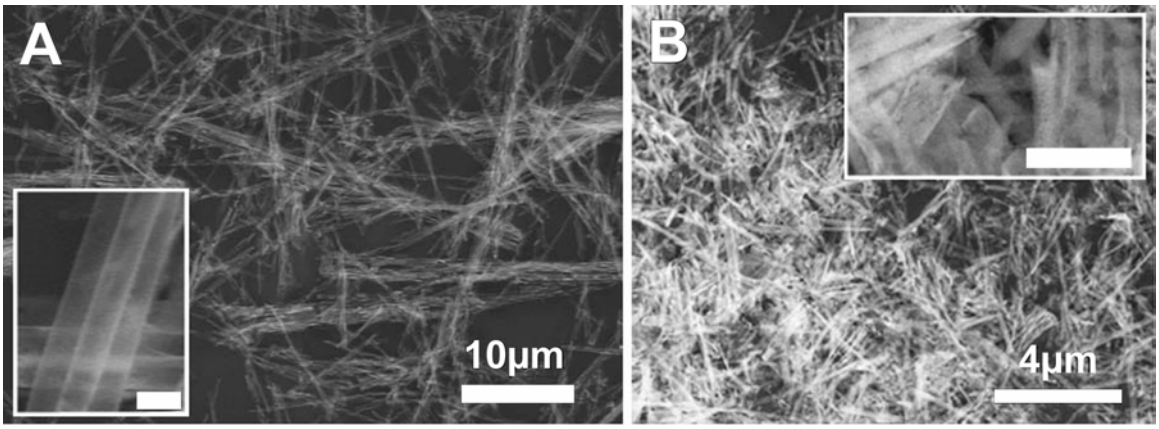

Figure 2.12. SEM images of $BiFeO_3$ nanotubes (NTs) prepared in alumina membranes with 200 nm (A) and 100 nm (B) diameter pores, respectively. Insets of (A) and (B) show higher magnification images of as-prepared $BiFeO_3$ NTs, respectively. Scale bars in the insets of (A) and (B) indicate 500 nm. Reproduced from Park, T.-J. *et al*., *Chem. Commun.* **2004**, 2708.

2.2.2.3. TEM, HRTEM measurements: size, shape, chemical composition, crystallinity and lattice spacings of as-prepared $BiFeO_3$ nanotubes

Figure 2.13A and 2B illustrate TEM images of an individual NT, generated from the alumina membrane with 100 nm and 200 nm diameter pores, respectively. Diameters are consistent with measurements from SEM data. EDS data (Figure 2.13C) show the expected elemental signals of NTs arising from Bi, Fe, and O. We do observe varying intensities of Al peaks, ascribed to residues from the template. Even though both of the tubes have similar levels of Al layers on their surface, discrepancies between the morphologies of each tube can be clearly seen. Figure 2.13B shows straight and relatively smooth structures, while Figure 2.13A indicates that straight but relatively rough and irregular structures are observed. The wall thickness for a $BiFeO_3$ NT obtained from the template with 200 nm diameter pores was ~10 nm (Figure 2.13B). Not surprisingly, analogous measurements for $BiFeO_3$ NTs generated from 100 nm diameter pores could not be properly obtained due to the roughness of the tube surface (Figure 2.13A). Precedence for observation of this type of morphology has been found with Co_3O_4 fibers synthesized using a sol-gel process.[50]

SAED data taken from each individual $BiFeO_3$ NT show identical ring patterns. The broad continuous ring patterns in the insets of Figure 2.13A and B validate our view that the generated $BiFeO_3$ NTs consist of polycrystalline as well as amorphous states. HRTEM images further confirm the crystalline nature and composition of our as-prepared NTs. Figure 2.13D shows a typical crystalline domain with an interplanar spacing of about 2.82 Å, which corresponds to the (110) ring in the SAED spectrum.

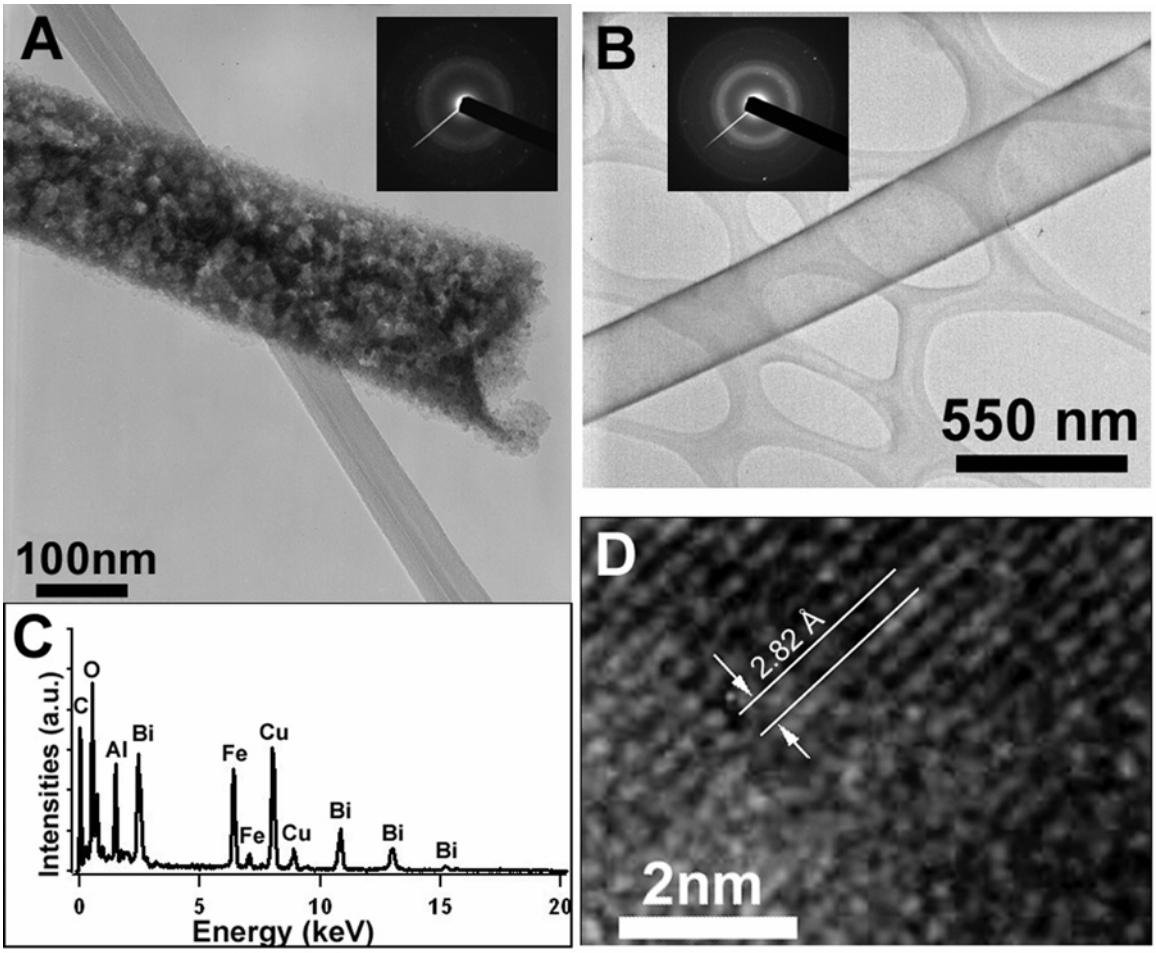

Figure 2.13. TEM images of individual $BiFeO_3$ nanotubes (NTs) prepared in alumina membranes with 100 nm (A) and 200 nm (B) diameter pores, respectively. Insets of (A) and (B) are the corresponding SAED patterns of the individual NTs, respectively. (C) EDS data indicate that this individual NT is composed of Bi, Fe, and O and contains an Al impurity. The Cu and C peaks originate from the TEM grid. (D) HRTEM image of $BiFeO_3$ NTs generated from a template having 200 nm diameter pores. Reproduced from Park, T.-J. *et al*., *Chem. Commun.* **2004**, 2708.

2.2.2.4. Role of alumina template and pressure-filter technique in template synthesis of $BiFeO_3$ nanotubes

In order to further demonstrate the efficacy of template synthesis procedure employed in this study for the generation of 1-D nanostructures, $BiFeO_3$ bulk samples were prepared by identical experimental protocols (but without a template) to that of $BiFeO_3$ NTs. Figure 2.14 shows an image of the surface of $BiFeO_3$ bulk samples. In comparison with previous SEM images of bulk samples, the surface morphologies of our bulk $BiFeO_3$ are similar to those of thin films grown on $Pt/TiO_2/SiO_2/Si$ substrate using a pulsed-laser deposition (PLD) technique.[51] However, the grain sizes of particles in our samples are much smaller (range of 100-500 nm), as compared with samples (range of 1-3 μm) prepared by a typical solid state reaction method.[52,53]

In this work, to overcome the lack of wettability of the template by the sol, we employed a pressure-filter technique to force reagents into the pores.[48,49] Hence, the nature of the wetting of the precursor sol on the inner surface of the template membrane likely had a substantial effect on the morphology of the final products. For example, the duration of sol deposition as well as the viscosity of the sol itself are all important factors in considering interactions of sol constituents with the template membranes.[54] That is, the difference in morphology of the tubes synthesized in 100 vs. 200 nm pore-sized templates could have arisen not only from differential chemical interactions of the various sol constituents deposited with the pore walls themselves but also from contrasting geometric configurations of the sol constituent molecules within each individual template membrane, induced by spatial constraints. Moreover, as the nucleation of the $BiFeO_3$ particles likely starts from sites randomly located on the wall of the template, the net effect would be formation of polycrystalline $BiFeO_3$ NTs, consistent with the SAED and HRTEM results observed.

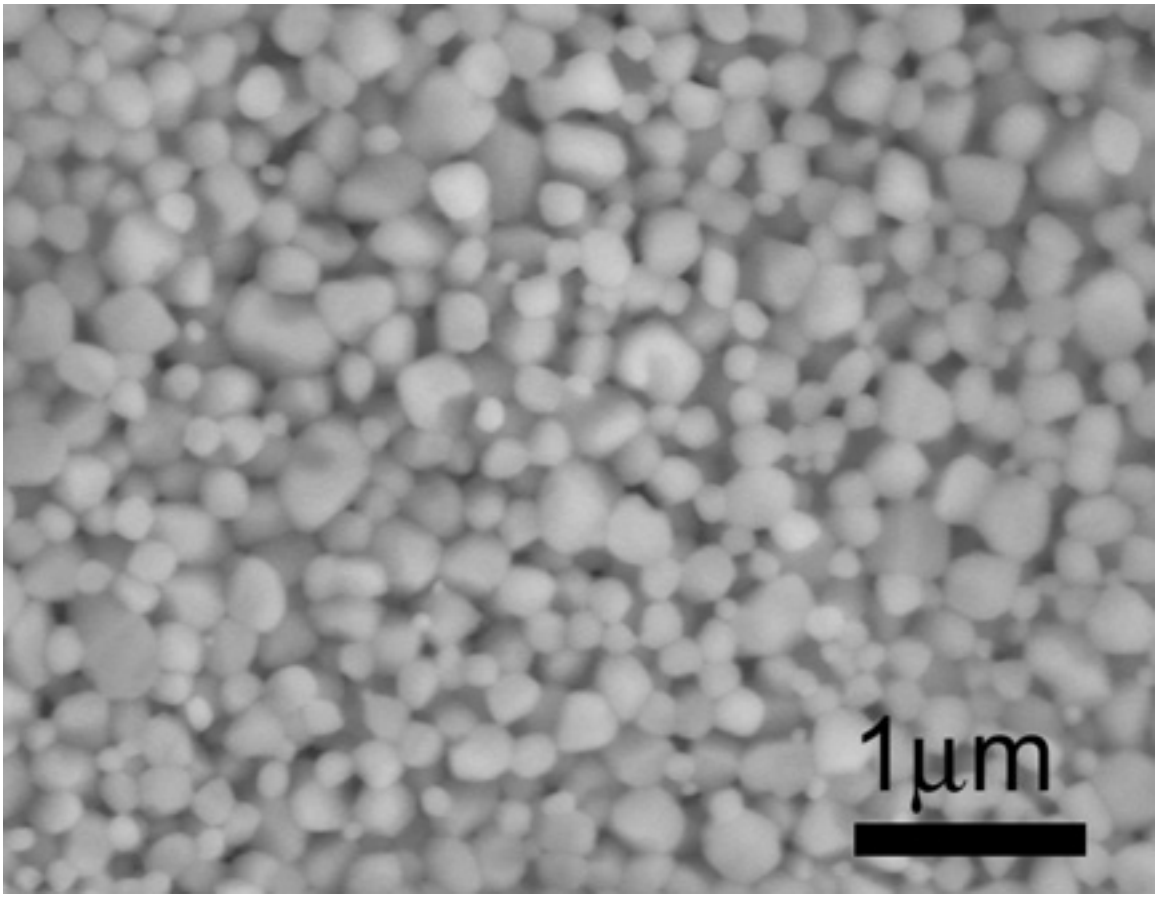

Figure 2.14. Scanning electron microscopy (SEM) images of bulk $BiFeO_3$ prepared using identical experimental procedures. Reproduced from Park, T.-J. *et al*., *Chem. Commun.* **2004**, 2708.

2.2.2.5. SQUID measurements: magnetic properties of as-prepared $BiFeO_3$ nanotubes

These preliminary magnetic property measurements data were taken using the superconducting quantum interference device (SQUID, Figure 2.15). As further experimental details, we note that the alumina template was not removed in these experiments. Hence, since the sample (the template/$BiFeO_3$) contains small quantities of nanotubes, sample data shown are presented after an appropriate, mass-corrected background subtraction of the signal due to the alumina template itself and hence, reflect genuine magnetic behavior of the nanotubes themselves.

The net result is that there does indeed appear to be a small though appreciable level of magnetization, unlike for bulk pure $BiFeO_3$ which does not show any spontaneous moment even up to very high fields and low temperatures.[55] The precise nature of this nanoscale effect, however, has not as yet been fully discerned as more comprehensive data on our nanotubes are still being taken. Moreover, a detailed comparative evaluation[5] with the bulk is limited because of the lack of any published data on single crystals.

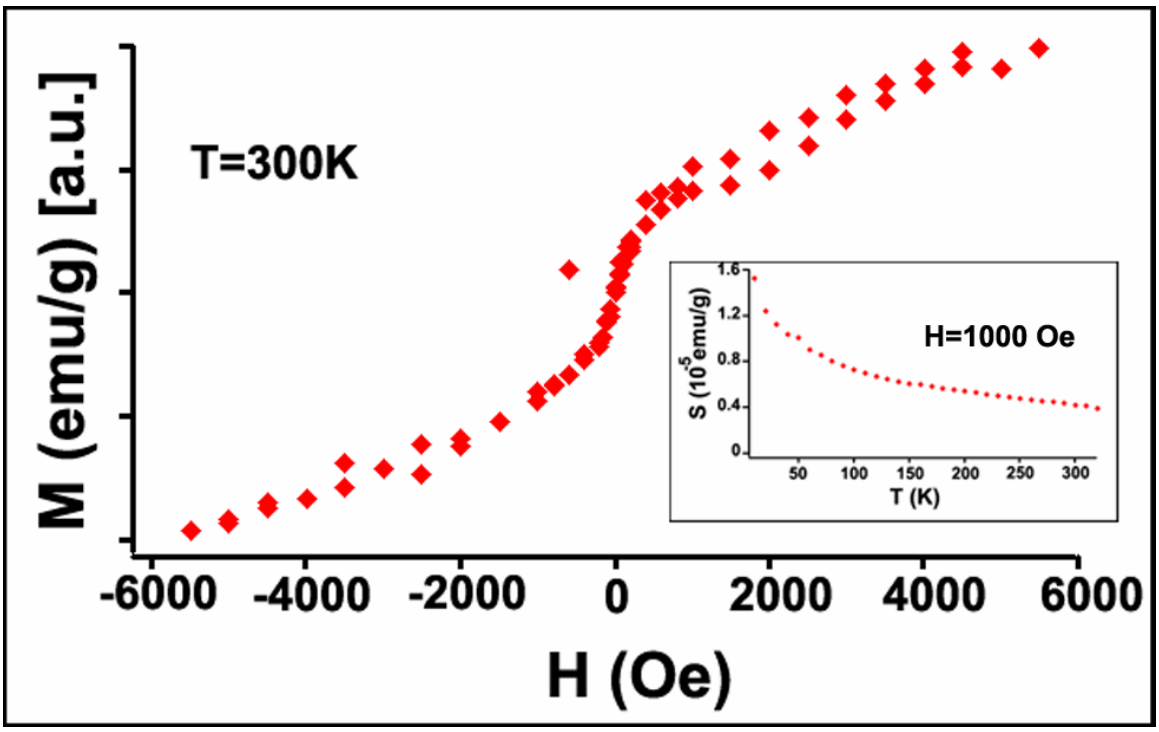

Figure 2.15. Hysteresis loop at 300 K of as-prepared $BiFeO_3$ NTs, grown in AAO membranes having 100 nm sized pores. Inset shows the magnetic susceptibility of $BiFeO_3$ nanotubes as a function of temperature with the magnetic field set at 1000 Oe. Reproduced from Park, T.-J. *et al*., *Chem. Commun.* **2004**, 2708.

2.3. Conclusions

In summary, Chapter II includes the first reported study of the synthesis and characterization of 0-D as well as 1-D nanostructures of $BiFeO_3$ materials. The generation of nanoparticles (0-D) as well as nanotubes (1-D) of $BiFeO_3$ materials provides a complete, complementary nanoscience perspective to intensely studied thin film (2-D) structures. $BiFeO_3$ nanoparticles represent a pure-phase, substrate-free, and relatively strain-free (as compared with epitaxially grown films)[10] single-crystalline specimen. In addition, $BiFeO_3$ nanotubes (1-D nanostructures) are considered as a new formulation of $BiFeO_3$ materials which suggest the relevancy for the design of future nanoscale building blocks for soft magnetic materials with applications in transformers and inductors.

Our nanoparticles exhibit size-dependent magnetic behavior wherein the particles are analogous to incomplete magnetic supercells that retain a net magnetic moment. The critical observations relevant to potential applications are (a) increased magnetization values at the nanoscale due to size-confinement effects at room temperature and (b) the presence of insignificant amounts of Fe^{2+} indicating the absence or great suppression of defects associated with oxygen deficiency. Oxygen vacancies that contribute to leakage problems in ceramic preparations of $BiFeO_3$ are primarily responsible for hindering potential device applications. Suppression of oxygen vacancies is known to increase the resistivity and multiferroic behavior of these systems. Thus, samples derived from our nanoscale systems should possess high resistivity and enhanced multiferroic properties with promising potential. The observation of hysteresis at room temperature is especially auspicious and could be further enhanced by rationally tailored shape anisotropy.

Room-temperature magnetic property measurements on as-prepared $BiFeO_3$ nanotubes exhibit an appreciable net magnetization as an analogue to $BiFeO_3$ nanoparticles. However, their lack of coercivity reveals a superparamagnetic behavior of $BiFeO_3$ nanotubes possessing ~160 nm diameters. In addition, a qualitative analysis based on *M*/*H* curves of as-prepared nanotubes of $BiFeO_3$, grown in 100 versus 200 nm pore-sized templates has further revealed that the pore size and surface morphology of $BiFeO_3$ nanotubes may play a crucial role in determining the size-dependent magnetic properties of 1-D nanostructures of $BiFeO_3$ materials (Figure 2.16). We note that as-prepared $BiFeO_3$ nanotubes having ~270 nm diameters exhibit a coercivity value (~175 Oe, Figure 2.16B), which is comparable to that of as-prepared nanoparticles having a diameter ranging from 14 to 41 nm (Table 3.1).

Unlike for as-prepared nanoparticles, constituting the majority of our magnetization studies, both as-prepared $BiFeO_3$ nanotubes having diameters of ~270 and ~160 nm contain the alumina templates that interfere with SQUID measurements, respectively. Thus, the sample (the template/$BiFeO_3$ NTs) data shown (Figure 2.16) are

not as sufficient to provide for further quantitative analysis as compared with data for our as-prepared nanoparticles. A complementary approach, aimed at the acquisition of magnetic data without consideration of the template, as well as a study of size and shape dependent properties such as magnetization, electric polarization, and elastic strain of $BiFeO_3$ nanotubes merits further attention.

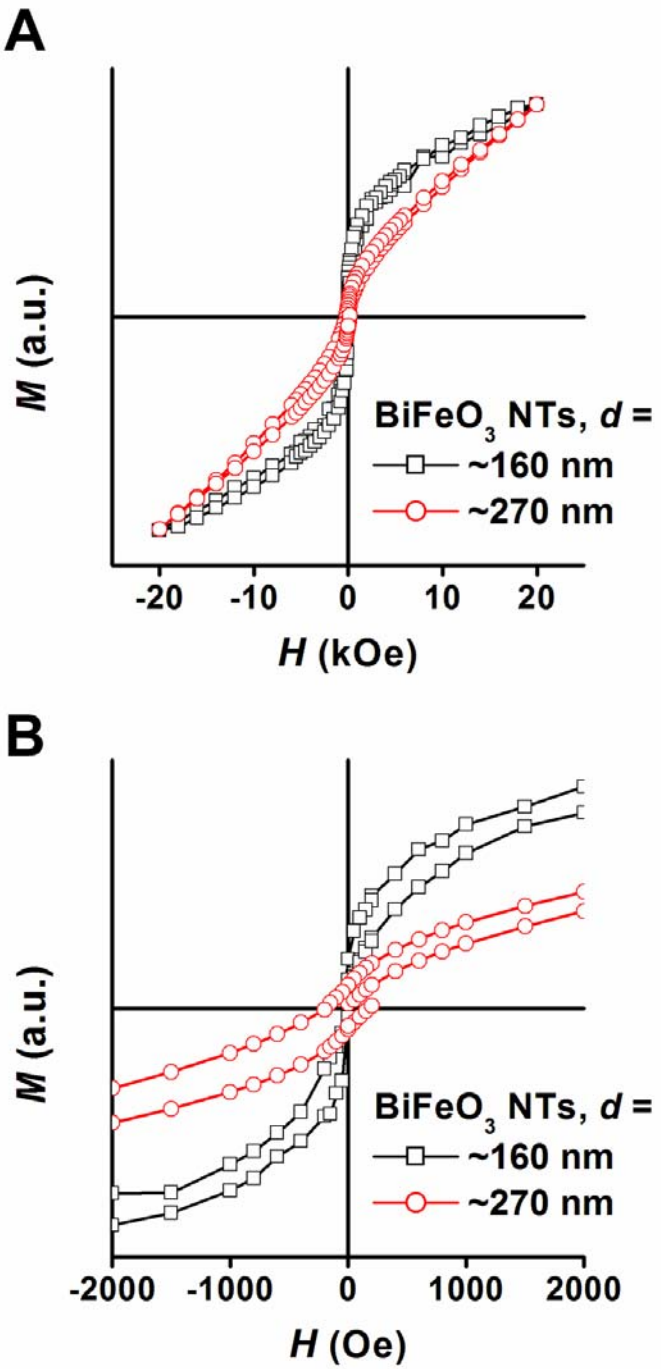

Figure 2.16. (A) Comparisons between hysteresis loops at 300 K of as-prepared $BiFeO_3$ NTs, grown in AAO membranes having 200 and 100 nm sized pores, respectively. (B) Expanded plots of hysteresis loops of as-prepared $BiFeO_3$ NTs.

2.4. References

(1) Ederer, C.; Spaldin, N. A. *Phys. Rev. B* **2005**, *71*, 060401.
(2) Sosnowska, I.; Peterlin-Neumaier, T.; Steichele, E. *J. Phys. C Solid State Phys.* **1982**, *15*, 4835.
(3) Park, T.-J.; Papaefthymiou, G. C.; Viescas, A. J.; Moodenbaugh, A. R.; Wong, S. S. *Nano Lett.* **2007**, *7*, 766.
(4) Park, T.-J.; Mao, Y.; Wong, S. S. *Chem. Commun.* **2004**, 2708.
(5) Wang, J.; Neaton, J. B.; Zheng, H.; Nagarajan, V.; Ogale, S. B.; Liu, B.; Viehland, D.; Vaithyanathan, V.; Schlom, D. G.; Waghmare, U. V.; Spaldin, N. A.; Rabe, K. M.; Wuttig, M.; Ramesh, R. *Science* **2003**, *299*, 1719.
(6) Kim, J. S.; Cheon, C. I.; Lee, C. H.; Jang, P. W. *J. Appl. Phys.* **2004**, *96*, 468.
(7) Qi, X.; Dho, J.; Blamire, M.; Jia, Q.; Lee, J. S.; Foltyn, S.; MacManus-Driscoll, J. L. *J. Magn. Magn. Mater.* **2004**, *283*, 415.
(8) Singh, S. K.; Kim, Y. K.; Funakubo, H.; Ishiwara, H. *Appl. Phys. Lett.* **2006**, *88*, 162904.
(9) Lee, Y.-H.; Wu, J.-M.; Chen, Y.-C.; Lu, Y.-H.; Lin, H.-N. *Electrochem. Solid State Lett.* **2005**, *8*, F43.
(10) Wang, Y.; Jiang, Q.-h.; He, H.-c.; Nan, C.-W. *Appl. Phys. Lett.* **2006**, *88*, 142503.
(11) Eerenstein, W.; Morrison, F. D.; Dho, J.; Blamire, M. G.; Scott, J. F.; Mathur, N. D. *Science* **2005**, *307*, 1203a.
(12) Bai, F.; Wang, J.; Wuttig, M.; Li, J.; Wang, N.; Pyatakov, A. P.; Zvezdin, A. K.; Cross, L. E.; Viehland, D. *Appl. Phys. Lett.* **2005**, *86*, 032511.
(13) Wang, J.; Scholl, A.; Zheng, H.; Ogale, S. B.; Viehland, D.; Schlom, D. G.; Spaldin, N. A.; Rabe, K. M.; Wuttig, M.; Mohaddes, L.; Neaton, J.; Waghmare, U.; Zhao, T.; Ramesh, R. *Science* **2005**, *307*, 1203b.
(14) Xu, G.; Hiraka, H.; Shirane, G.; Li, J.; Wang, J.; Viehland, D. *Appl. Phys. Lett.* **2005**, *86*, 182905.
(15) Ederer, C.; Spaldin, N. A. *Phys. Rev. B* **2005**, *71*, 224103.
(16) Neaton, J. B.; Ederer, C.; Waghmare, U. V.; Spaldin, N. A.; Rabe, K. M. *Phys. Rev. B* **2005**, *71*, 014113.
(17) Martin, C. R. *Science* **1994**, *266*, 1961.
(18) Martin, C. R. *Acc. Chem. Res.* **1995**, *28*, 61-68.
(19) Hernandez, B. A.; Chang, K.-S.; Fisher, E. R.; Dorhout, P. K. *Chem. Mater.* **2002**, *14*, 480.
(20) Limmer, S. J.; Seraji, S.; Forbess, M. J.; Wu, Y.; Chou, T. P.; Nguyen, C.; Cao, G. *Adv. Mater.* **2001**, *13*, 1269.
(21) Achenbach, G. D.; James, W. J.; Gerson, R. *J. Am. Ceram. Soc.* **1967**, *50*, 437.
(22) Sosnowska, I.; Schäfer, W.; Kockelmann, W.; Andersen, K. H.; Troyanchuk, I. O.

Appl. Phys. A **2002**, *74*, S1040.
(23) Néel, L. *Compt. Rend.* **1961**, *253*, 203.
(24) Néel, L. *Compt. Rend.* **1961**, *252*, 4075.
(25) Néel, L. *Compt. Rend.* **1961**, *253*, 9.
(26) Richardson, J. T.; Yiagas, D. I.; Turk, B.; Forster, K.; Twigg, M. V. *J. Appl. Phys.* **1991**, *70*, 6977.
(27) Néel, L., in *Low Temperature Physics*, edited by C. DeWitt, B. Dreyfus and P. G. DeGennes (Gordon and Beach, London, 1962), p. 411.
(28) O'Handley, R. C., *Modern Magnetic Materials Principles and Applications*; John Wiley & Sons, Inc. (New York, Chichester, Weinheim, Brisbane, Singapore, Toronto) 1999, p. 439.
(29) Papaefthymiou, G. C. *J. Magn. Magn. Mater.* **2004**, *272*, E1227.
(30) Dho, J.; Qi, X.; Kim, H.; MacManus-Driscoll, J. L.; Blamire, M. *Adv. Mater.* **2006**, *18*, 1445.
(31) Lamba, S.; Annapoorni, S. *Eur. Phys. J. B* **2004**, *39*, 19.
(32) Néel, L. *Ann. Geophys.* **1949**, *5*, 99.
(33) Mamiya, H.; Nakatani, I.; Furubayashi, T. *Phys. Rev. Lett.* **1998**, *80*, 177.
(34) Krechrakos, D.; Trohidou, K. N. *Phys. Rev. B* **1998**, *58*, 12169.
(35) Binns, C.; Maher, M. J.; Pankhurst, Q. A.; Kechrakos, D.; Trohidou, K. N. *Phys. Rev. B* **2002**, *66*, 184413.
(36) Labarta, A.; Battle, X.; Iglesias, Ò., In *Surface Effects in Magnetic Nanoparticles*: Fiorani, D., Ed.; Springer: Berlin, 2005.
(37) Blaauw, C.; Van der Woude, F. *J. Phys. C: Solid State Phys.* **1973**, *6*, 1422.
(38) Brown, W. F., Jr., *J. Appl. Phys.* **1968**, *39*, 993.
(39) del Moral, A., *Magnetostriction: Principles and Applications*; Institute of Physics Publications: Bristol, 2004.
(40) Salje, E. K. H., *Phase Transitions in Ferroelastic and Co elastic Crystals*; Cambridge University Press: Cambridge, 1990.
(41) Zalessky, A. V.; A., F. A.; Khimich, T. A.; Bush, A. A.; Pokatilov, V. S.; Zvezdin, A. K. *Europhys. Lett.* **2000**, *50*, 547.
(42) Park, T.-J.; Papaefthymiou, G. C.; Moodenbaugh, A. R.; Mao, Y.; Wong, S. S. *J. Mater. Chem.* **2005**, *15*, 2099.
(43) Coey, J. M. D. *Phys. Rev. Lett.* **1971**, *27*, 1140.
(44) Singh, M. K.; Ryu, S.; Jang, H. M. *Phys. Rev. B* **2005**, *72*, 132101.
(45) Nadifi, H.; Ouali, A.; Grigorescu, C.; Faqir, H.; Monnereau, O.; Tortet, L.; Vacquier, G.; Boulesteix, C. *Supercond. Sci. Technol.* **2000**, *13*, 1174.
(46) Haumont, R.; Kreisel, J.; Bouvier, P.; Hippert, F. *Preprint, Condensed Matter* **2005**, 1.
(47) Wada, T.; Kajima, A.; Inoue, M.; Fujii, T.; Arai, K. I. *Mater. Sci. Eng.* **1996**,

A217/218, 414-418.

(48) Toshimitsu, K.; Shin-ichi, O.; Dazuhito, H. *J. Phys. Chem. Solids* **2003**, *64*, 391-397.

(49) Steinhart, M.; Wendorff, J. H.; Greiner, A.; Wehrspohn, R. B.; Nielsch, K.; Schilling, J.; Choi, J.; Gosele, U. *Science* **2002**, *296*, 1997.

(50) Lakshmi, B. B.; Dorhout, P. K.; Martin, C. R. *Chem. Mater.* **1997**, *9*, 857-862.

(51) Palkar, V. R.; John, J.; Pinto, R. *Appl. Phys. Lett.* **2002**, *80*, 1628.

(52) Mahesh Kumar, M.; Palkar, V. R.; Srinivas, K.; Suryanarayana, S. V. *Appl. Phys. Lett.* **2000**, *76*, 2764.

(53) Mahesh Kumar, M.; Srinivas, A.; Suryanarayana, S. V. *J. Appl. Phys.* **2000**, *87*, 855.

(54) Steinhart, M.; Wehrspohn, R. B.; G?ele, U.; Wendorff, J. H. *Angew. Chem. Int. Ed.* **2004**, *43*, 1334.

(55) Mahesh Kumar, M.; Srinath, S.; Kumar, G. S.; Suryanarayana, S. V. *J. Magn. Magn. Mater.* **1998**, *188*, 203.

Chapter III. $BiFeO_3$–$BaTiO_3$ Solid Solutions

3.1. Introduction

As we have discussed in Chapter II, incorporation of multiferroic $BiFeO_3$ materials into practical devices in their bulk form has been hindered by their intrinsic leakage problems that lead to low electrical resistivity. Practical transport measurements of $BiFeO_3$ materials as either piezoelectric or magnetoelectric functional components have proven to be difficult to show. For instance, reliable ferroelectric loops are hard to obtain due to a relatively high conductivity presumably due to defects and non-stoichiometry related issues. Thus, there has been a pressing need for the synthesis of pure $BiFeO_3$ materials so as to prevent any reduction of Fe^{3+} species to Fe^{2+}, creating oxygen vacancies for charge compensation. Recent approaches associated with the solid state chemistry area to tackle this challenge include (i) incorporation of $BiFeO_3$ into solid solutions with other cubic ABO_3 perovskites including $PbTiO_3$ (or $Pb(Zr,Ti)O_3$ (PZT)), $BaTiO_3$, and $ReFeO_3$,[1-4] and (ii) the application of dopants such as Ba, La, Nb, Ti, Ni, and Sr ions in $BiFeO_3$ materials.[5-10]

$BiFeO_3$ materials form binary solid solutions with a number of other perovskites of ABO_3 type. It can be observed that their structural transformations are strongly dependent upon increasing the content of the secondary phase of perovskites. For example, in $BiFeO_3$–$BaTiO_3$ solid solutions, rhombohedral symmetry is maintained to a 67 mole % of $BiFeO_3$, after which a cubic symmetry is formed to a level of 7 mole % of $BiFeO_3$, after which tetragonal symmetry sets in.[11-13] Moreover, in $BiFeO_3$–$PbTiO_3$ solid solutions, the structure transforms from rhombohedral to cubic at 78 mole % of $BiFeO_3$, supon incorporation of $PbTiO_3$.[14] Similarly, rhombohedral symmetry dominates in the $BiFeO_3$-rich phases for the other solid solution systems.[15,16] Since the structural transformations of $BiFeO_3$-based binary solid solutions are correlated with their magnetic as well as electronic properties, a rational design and control of their composition would attract fundamental as well as practical scientific interest, e.g., resolution for leakage issues of bulk $BiFeO_3$.

In spite of an intense study focused on $BiFeO_3$-based solid solution materials, a fundamental understanding of structure-property correlations in $BiFeO_3$ is still lacking. Moreover, the effect of the crystallinity as well as the fundamental dependence of ferroic ordering behavior on size and precise chemical composition remains issues of deep interest. However, to date, little if any effort has been expended in research associated with the synthesis of nanostructures of $BiFeO_3$ with other perovskites. Moreover, there have not been any viable reports on the preparation of the single-crystalline $BiFeO_3$-ABO_3 solid solution structures. The magnetic response of $BiFeO_3$ materials with respect

to their size (*e.g.*, nanostructures) as well as that of $BiFeO_3$–$BaTiO_3$ solid solutions with respect to their composition represents a main focus of this dissertation. For example, the size-dependent magnetic properties of single-crystalline $BiFeO_3$ nanoparticles and polycrystalline $BiFeO_3$ nanotubes have been explored in Chapter II. In Chapter III, research associated with the synthesis of nanostructures of $BiFeO_3$ with other perovskites as well as the magnetic properties of as-prepared single-crystalline $BiFeO_3$–$BaTiO_3$ solid solutions structures are presented.

Briefly, we have employed a large scale, facile, and environmentally friendly solid state reaction as a means of generating single-crystalline $BiFeO_3$–$BaTiO_3$ (BFO–BTO) solid solutions in a NaCl medium in the presence of a nonionic surfactant. $BaTiO_3$ has been selected for its dielectric properties which are lacking in and which are moreover complementary to those of $BiFeO_3$, and for their previous practicability in molten salt reactions.[17] Perovskite $(BFO)_x$–$(BTO)_{1-x}$ solid solutions with x values of 0.9, 0.8, 0.7, 0.6 and 0.5 have shown an appreciable magnetic response, which is absent in bulk $BiFeO_3$ (*i.e.*, $x = 1$), corresponding to their structural phase transition, an assertion which has been confirmed from superconducting quantum interference device (SQUID) and X-ray powder diffraction (XRD) measurements.

3.2. Experimental Section

3.2.1. Materials and Preparation

Bismuth(III) acetate (Aldrich, 99.99+%), bismuth (III) oxide (Aldrich, 99.99%), iron(III) oxide (Aldrich, nanopowder), barium oxalate (95%, Alfa Aesar), titanium dioxide (Aldrich, anatase 99.7+%), barium titanate (Aldrich, 99+%), NP-9 surfactant (Aldrich, polyoxyethylene(9)nonylphenyl ether), and sodium chloride (Mallinckrodt) were used as supplied. The choice of the surfactant was governed by its prior versatility in the preparation of various metal oxide systems, its relative nontoxicity, and comparative facility of use.[18-20] A series of $(BiFeO_3)_x$-$(BaTiO_3)_{1-x}$ solid solution cubes has been prepared using a variation of the molar ratios of the Bi, Fe, Ba, and Ti precursors in the procedure. Stoichiometric amounts of ($BiAc_3$, $½Fe_2O_3$), (BaC_2O_4, TiO_2), NaCl and NP-9 were mixed (in molar ratios of 1 : 1 : 20 : 3, 0.9 : 0.1 : 20 : 3, 0.8 : 0.2 : 20 : 3, 0.7 : 0.3 : 20 : 3, 0.6 : 0.4 : 20 : 3, respectively, for the generation of varying concentration of BFO-BTO solid solutions), thoroughly ground in an agate mortar, and subsequently sonicated.

In a typical synthesis of single-crystalline BFO-BTO solid-solution cubes, 1, 0.5, 1, and 1 mmol of $BiAc_3$, Fe_2O_3, BaC_2O_4, and TiO_2, respectively, along with 20 mmol of NaCl were thoroughly mixed in an agate mortar. The resulting mixture was meticulously mixed for at least 30 min after which 2 mL of NP-9 was subsequently added. Identical procedures were employed for samples containing different molar ratios of initial precursors. The resulting mixture was then placed in a ceramic crucible, inserted into a quartz tube, heated at a ramp rate of 5 ^oC per min up to an annealing temperature at 820 ^oC for 3.5 h, and cooled thereafter to room temperature. As-prepared material was subsequently washed several times with distilled water, collected by centrifugation, and dried at 120^oC in a drying oven.

By comparison, a commercial $BaTiO_3$ sample was used. The bulk $BiFeO_3$ sample was prepared following the solid-state procedure reported by Achenbach *et al*.[21] Briefly, Bi_2O_3 and Fe_2O_3 with a molar ratio of 2 : 1 were ground thoroughly, and the mixture was annealed at 750 ^oC for 3 h, followed by air quenching. Residual Bi_2O_3 was removed by a multiple-step nitric acid (17%) leaching process. The resultant sample was washed several times with distilled water and lastly with ethanol. Samples obtained were ground into a fine powder.

3.3. Results and Discussion

3.3.1. XRD measurements: purity, crystallinity, and phase transformation of as-prepared $(BiFeO_3)_x$–$(BaTiO_3)_{1-x}$ solid solutions

The purity and crystallinity of as-prepared $(BiFeO_3)_x$–$(BaTiO_3)_{1-x}$ solid solution cubes were examined by powder XRD measurements (Figure 3.1). XRD peaks from $(BiFeO_3)_x$–$(BaTiO_3)_{1-x}$ solid solution samples with x values of 1, 0.9, 0.8, 0.7, 0.6, 0.5 and 0 are shown in Figure 3.1(a), (b), (c), (d), (e), (f), and (g), respectively. We note that the sample (a) and (g), by means of comparison with the solid solution samples, are the as-prepared $BiFeO_3$ (x = 1) and commercial $BaTiO_3$ (x = 0), respectively. It is evident that the observed patterns of the collected powders displayed all of the expected peaks emanating from the $BiFeO_3$ and $BaTiO_3$ structure, with very few impurity peaks. In effect, diffraction peaks in Figure 3.1(a) can be indexed to the rhombohedral structure of $BiFeO_3$ (space group: $R3c$) with lattice constants of $a = b = c = 5.63$ Å and $\alpha = \beta = \gamma = 59.4^\circ$, which are in good agreement with literature results (*i.e.*, JCPDS #20-0169). Likewise, diffraction peaks in Figure 3.1(g) can be indexed to the cubic lattice (space group: $Pm3m$) of $BaTiO_3$, and the calculated lattice constant is a = 4.003 Å, a value in good agreement with literature results (a = 4.031 Å, JCPDS#31-0714).

It can be observed that XRD patterns exhibit that all of as-prepared $(BiFeO_3)_x$–$(BaTiO_3)_{1-x}$ solid solutions consist of peaks between 2-theta at 31 and 33°, and that their peaks continuously shifted to a lower angle with decreasing x. Moreover, structural transformations of our $(BiFeO_3)_x$–$(BaTiO_3)_{1-x}$ solid solution nanocubes, *e.g.*, rhombohedral (x = 1.0, 0.9, 0.8, and 0.7) → cubic (x = 0.6 and 0.5) → tetrahedral (x = 0, $BaTiO_3$) have been observed with increasing concentration of the second constituent (*i.e.*, $BaTiO_3$). This structural transition behavior is compatible with literature results for the bulk.[11-13]

To further expand structural transition analysis of our as-prepared $(BiFeO_3)_x$–$(BaTiO_3)_{1-x}$ solid solutions, monochromatic synchrotron X-ray powder diffraction setup at beamline X7A at the National Synchrotron Light Source (NSLS) was used and the observed changes in peak positions are shown in Figure 3.2. It can be clearly observed that the patterns for Fe-containing constituent ($BiFeO_3$, Figure 3.2a) as well as Ti-containing constituent ($BaTiO_3$, Figure 3.2e) exhibit signals consistent with rhombohedral and tetragonal structures, respectively. Between these 'extremes', a systematic phase transition is observed and the patterns for $(BiFeO_3)_{0.5}$–$(BaTiO_3)_{0.5}$ solid solutions (Figure 3.2d) can be ascribed to perfect cubic structures. Further analyses based on these data, *e.g.*, peak fittings, structure refinements, and lattice parameters, are currently under investigation.

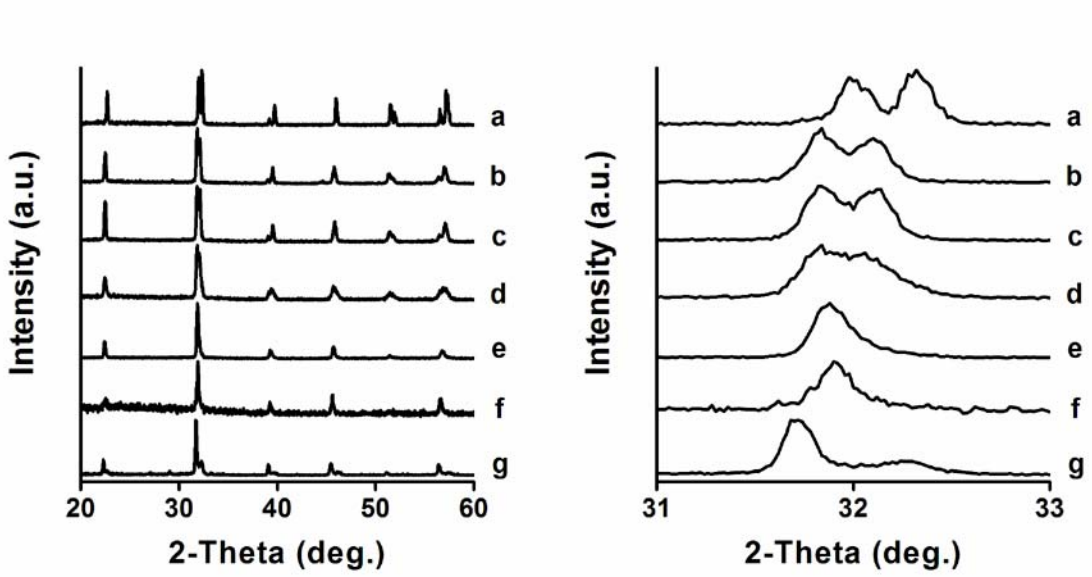

Figure 3.1. (A) XRD patterns of (a) $BiFeO_3$ bulk materials (*i.e.*, $x = 1$), of $(BiFeO_3)_x$–$(BaTiO_3)_{1-x}$ solid solutions with x values of (b) 0.9, (c) 0.8, (d) 0.7, (e) 0.6, and (f) 0.5, and of (g) $BaTiO_3$ materials (*i.e.*, $x = 0$). (B) Expanded plots of XRD patterns of $(BiFeO_3)_x$–$(BaTiO_3)_{1-x}$ solid solutions between 31 and 33° to show phase transitions with respect to the compositions of the solid solutions.

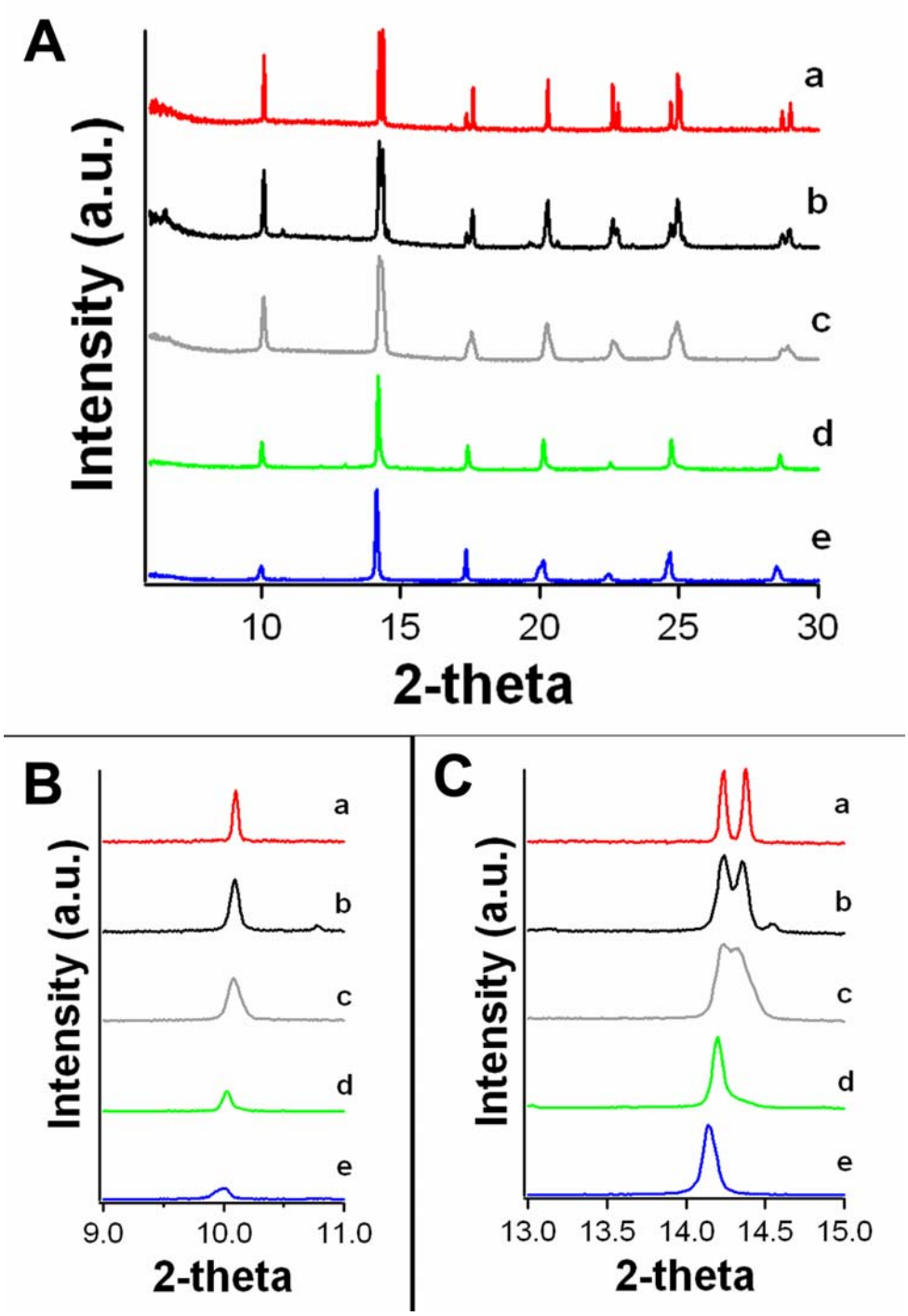

Figure 3.2. (A) XRD patterns of (a) $BiFeO_3$ bulk materials (*i.e.*, $x = 1$), of $(BiFeO_3)_x$–$(BaTiO_3)_{1-x}$ solid solutions with x values of (b) 0.9, (c) 0.7, (d) 0.5, and of (e) $BaTiO_3$ materials (*i.e.*, $x = 0$). Expanded plots of XRD patterns are shown between 31 and 33° (B) as well as between 13 and 15° (C) to illustrate phase transitions with respect to the compositions of the BFO–BTO solid solutions.

3.3.2. SEM measurements: size, shape, and chemical composition of as-prepared $(BiFeO_3)_x$–$(BaTiO_3)_{1-x}$ solid solution nanocubes

Figure 3.3 shows SEM images revealing the morphologies of as-prepared $(BiFeO_3)_x$–$(BaTiO_3)_{1-x}$ solid solution nanocubes. It can be observed that $(BiFeO_3)_x$–$(BaTiO_3)_{1-x}$ solid solution products, prepared using a molten salt method, mainly consist of discrete cubic structures with smooth surfaces (Figure 3.3A, B, and C). Sizes of our as-prepared $(BiFeO_3)_x$–$(BaTiO_3)_{1-x}$ solid solutions with x values of 0.5 (A), 0.7 (B), and 0.9 (C), were measured to be 200 ± 63, 157 ± 48, and 149 ± 79 nm, respectively. We note that SEM images of $(BiFeO_3)_x$–$(BaTiO_3)_{1-x}$ solid solutions with x values of 0.6 and 0.8 also exhibit similar shapes as compared with those of (A), (B), and (C). It can also be observed that the faces of as-prepared $(BiFeO_3)_x$–$(BaTiO_3)_{1-x}$ solid solutions are essentially flat though some of the corners of these structures are slightly truncated.

The morphologies of bulk $BiFeO_3$ products prepared by a solid state reaction are shown in Figure 3.3D. Although these images clearly show the presence of crystalline particles with smooth faces, it is also evident that these particles are not only significantly larger with sizes measuring in the range of tens of microns, but also that their size distribution is far more polydisperse and associated morphologies show randomly structured shapes. This observation, thus, confirms the effectiveness of our molten salt method to generated discrete faceted nanostructures of $(BiFeO_3)_x$–$(BaTiO_3)_{1-x}$ solid solution systems, with control over their compositions.

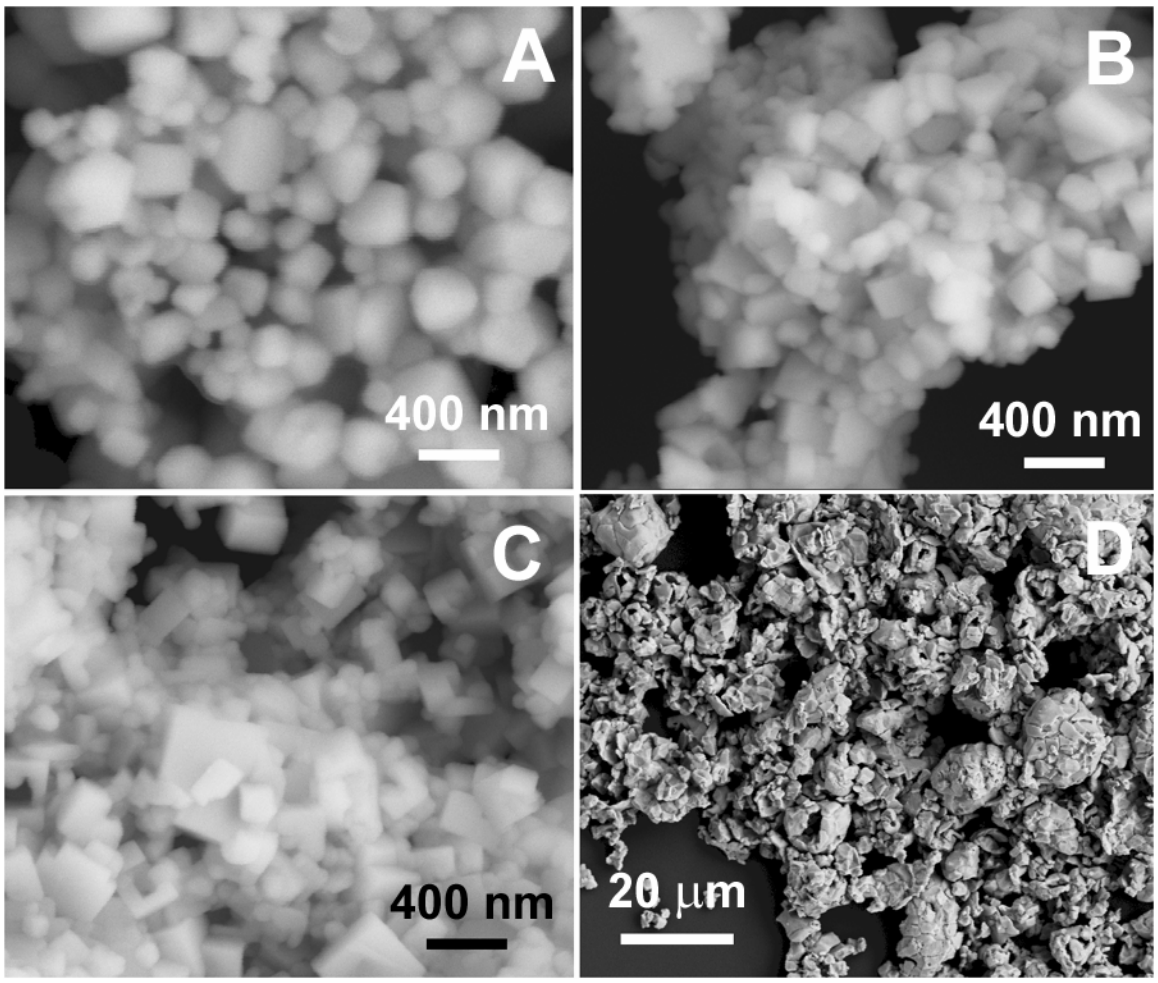

Figure 3.3. SEM images of as-prepared $(BiFeO_3)_x$–$(BaTiO_3)_{1-x}$ solid solutions, with x values of 0.5 (A), 0.7 (B), 0.9 (C), and of $BiFeO_3$ materials, *i.e.*, $x = 1$ (D).

3.3.3. SQUID measurements: magnetic properties of as-prepared $(BiFeO_3)_x$–$(BaTiO_3)_{1-x}$ solid solution cubes

To investigate the magnetic properties of as-prepared $(BiFeO_3)_x$–$(BaTiO_3)_{1-x}$ solid solutions at room temperature, magnetic measurements were performed on these as well as on bulk BFO using a superconducting quantum interference device (SQUID) magnetometer (Figure 3.4). The magnetic response observed as a function of the applied field for our as-prepared $(BiFeO_3)_x$–$(BaTiO_3)_{1-x}$ solid solutions and for bulk $BiFeO_3$ show noticeably different behaviors in terms of hysteresis shape. Bulk $BiFeO_3$ (*i.e.*, $x = 1$) evinces no hysteric behavior in its hysteresis loop as expected, and the accompanying magnetization value is relatively low (~0.34 emu/g) as compared with that of solid solution samples. By contrast, the magnetic response observed for our as-prepared $(BiFeO_3)_x$–$(BaTiO_3)_{1-x}$ solid solutions shows obviously appreciable hysteric behaviors in their graphs and the strength of the response observed at an applied magnetic field of 50 kOe is in the following order (M_S in emu/g): $(BiFeO_3)_{0.8}$–$(BaTiO_3)_{0.2}$, M_S ~1.88 > $(BiFeO_3)_{0.7}$–$(BaTiO_3)_{0.3}$, M_S ~1.61 > $(BiFeO_3)_{0.6}$–$(BaTiO_3)_{0.4}$, M_S ~1.49 > $(BiFeO_3)_{0.9}$–$(BaTiO_3)_{0.1}$, M_S ~1.04 ≅ $(BiFeO_3)_{0.5}$–$(BaTiO_3)_{0.5}$, M_S ~1.05. The $(BiFeO_3)_{0.8}$–$(BaTiO_3)_{0.2}$ solid solution exhibits the largest magnetic response (M_S ~1.88) as a function of the applied magnetic field among $(BiFeO_3)_x$–$(BaTiO_3)_{1-x}$ solid solutions.

The maximum magnetization, M_S, obtained at 300 K for as-prepared $(BiFeO_3)_{0.8}$–$(BaTiO_3)_{0.2}$ solid solution corresponds to M_S ~1.88 emu/g, which is comparable with that of substrate-free $BiFeO_3$ nanoparticles (~1.55 emu/g, Chapter II). In effect, the maximum magnetization of $BiFeO_3$ nanoparticles attained from a linear extrapolation reaches values of up to ~1.82 emu/g.[22] Thus, approaches focused on the design of $(BiFeO_3)_x$–$(BaTiO_3)_{1-x}$ solid solutions exhibit a slightly higher attainable magnetization. However, we note that this magnetization generated by incorporation of $BiFeO_3$ into $BaTiO_3$ to generate solid solutions is relatively small for general applicability in memory devices, although the outlook for specific applications at room temperature, involving spintronics and spin valves, remains highly promising with these nanoscale materials.[22]

To put our magnetization value measured in context, we compare the remnant magnetization of our as-prepared $(BiFeO_3)_{0.8}$–$(BaTiO_3)_{0.2}$ solid solution nanostructures with that of bulk $(BiFeO_3)_{0.8}$–$(BaTiO_3)_{0.2}$ solid solution which has been previously reported.[23] The remnant magnetization (M_r: ~0.75 emu/g) measured for our nanostructures is almost a magnitude higher than that (~0.08 emu/g) for the literature value reported.[23] Thus, we believe that the size effect associated with our nanostructured solid solutions plays an important role in enhancing the magnetic response of $(BiFeO_3)_x$–$(BaTiO_3)_{1-x}$ solid solutions. In addition, the shape control of solid solutions (cubes for our as-prepared samples in this case) needs to be included in our observations. For example,

the M_r value observed for nanosized $(BiFeO_3)_{0.7}$–$(BaTiO_3)_{0.3}$ solid solution ceramics (200 – 300 nm) exhibited an even lesser M_r value as compared with that (0.08 emu/g) for the bulk.[24] Thus, we note that M_r values which have been previously reported are not considered to be fully representative of similar materials studied.

In addition, our as-prepared $(BiFeO_3)_{0.8}$–$(BaTiO_3)_{0.2}$ solid solution nanocubes exhibit relatively lower coercivity (H_C: 660 Oe) as compared with bulk coercivity (H_C: 1000 Oe).[23] This result further indicates the significance of the size and shape effect at the nanoscale with respect to the coercivity of $(BiFeO_3)_x$–$(BaTiO_3)_{1-x}$ solid solution structures. However, as described above, magnetic parameters of $(BiFeO_3)_x$–$(BaTiO_3)_{1-x}$ solid solution structures need further scientific attention due to the sample dependent nature of previously reported data. The coercivities for our as-prepared solid solutions deviate from those in the literature and moreover, the coercivities reported for $(BiFeO_3)_x$–$(BaTiO_3)_{1-x}$ solid solution structures deviate, as well, *e.g.*, for x = 0.9: ~50,[25] 1261[11] Oe, for x = 0.8: ~1000,[23] 2260[11] Oe, for x = 0.75: ~150,[25] 1000[26] Oe, for x = 0.7: ~0,[24] 200,[27] ~250[28] Oe, and for x = 0.5: ~0[23] Oe. Derived magnetic parameters (*e.g.*, M_S, M_r, and H_C) for our as-prepared $(BiFeO_3)_x$–$(BaTiO_3)_{1-x}$ solid solution nanocubes are summarized in Table 3.1.

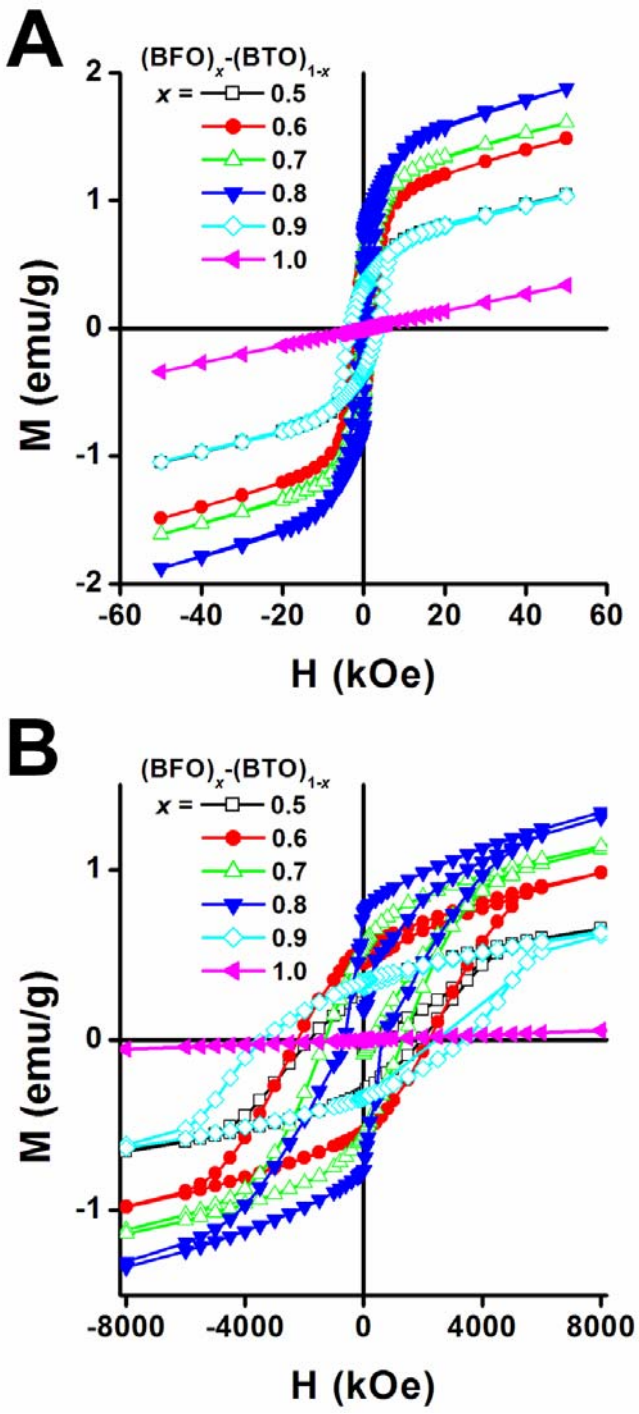

Figure 3.4. (A) Hysteresis loops at 300 K for as-prepared $(BiFeO_3)_x$–$(BaTiO_3)_{1-x}$ solid solutions with indicated *x* values. (B) Expanded plots of magnetization at 300 K of as-synthesized $(BiFeO_3)_x$–$(BaTiO_3)_{1-x}$ solid solutions with indicated *x* values.

The magnetic response observed at 10 K as a function of the applied field for our as-prepared $(BiFeO_3)_x$–$(BaTiO_3)_{1-x}$ solid solutions and for bulk $BiFeO_3$ are shown in Figure 3.5A and 3.5B. Qualitatively speaking, hysteresis loops at 10 K show similarity with that at room temperature, indicating little structural changes of these solid solutions at low temperature. The spontaneous magnetization observed for our as-prepared $(BiFeO_3)_x$–$(BaTiO_3)_{1-x}$ solid solutions at 10 K also exhibit appreciable hysteric behaviors, but with enhanced magnetization as compared with that at 300 K, in their graphs. By comparison, hysteresis loops of a $(BiFeO_3)_{0.5}$–$(BaTiO_3)_{0.5}$ solid solution at 10 K as well as at 300 K are shown in Figure 3.5C. Low temperature magnetic characteristics show an obviously enhanced strength of magnetic parameters including M_S, M_r, and H_C, with the exception of bulk $BiFeO_3$. The spontaneous magnetization value observed at 10 K for as-prepared $(BiFeO_3)_x$–$(BaTiO_3)_{1-x}$ solid solutions is in the same order as that at 300 K and a comparison between M_S measured at 10 K and 300 K is represented in Figure 3.5D. In addition, derived magnetic parameters (*e.g.*, M_S, M_r, and H_C) are summarized in Table 3.1.

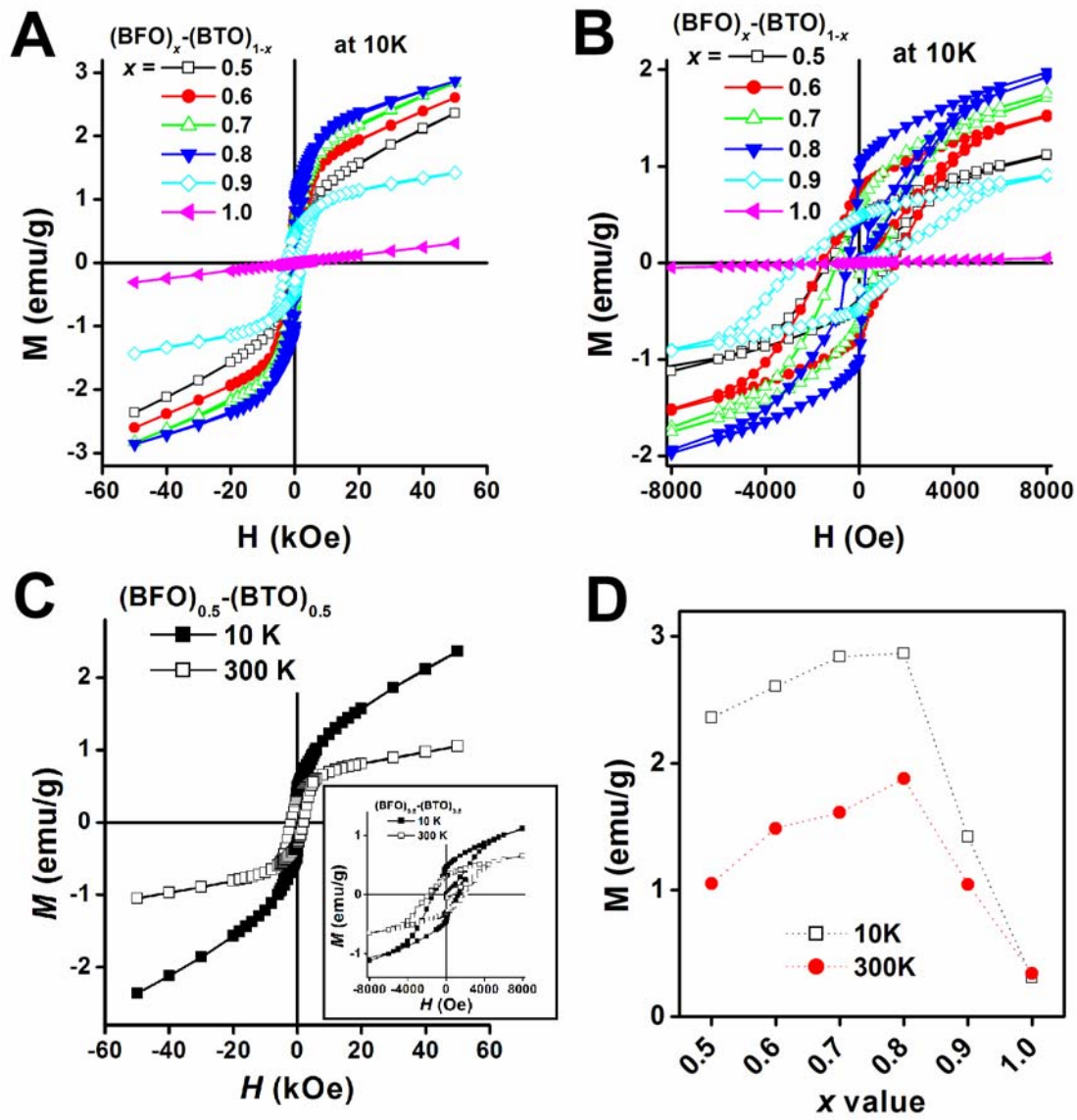

Figure 3.5. (A) Hysteresis loops at 10 K for as-prepared $(BiFeO_3)_x$–$(BaTiO_3)_{1-x}$ solid solutions with indicated *x* values. (B) Expanded plots of magnetization at 10 K of as-synthesized $(BiFeO_3)_x$–$(BaTiO_3)_{1-x}$ solid solutions with indicated *x* values. (C) Corresponding magnetization data for as-prepared $(BiFeO_3)_{0.5}$–$(BaTiO_3)_{0.5}$ solid solution samples at 10 K and 300 K, respectively, are also presented. The inset shows expanded plots of magnetization at 10 K and 300 K, respectively. (D) Spontaneous magnetization values, at 10 K and 300 K, of as-prepared $(BiFeO_3)_x$–$(BaTiO_3)_{1-x}$ solid solutions at 50 kOe as a function of *x* values, respectively.

Table 3.1. Derived magnetic parameters for $(BiFeO_3)_x$–$(BaTiO_3)_{1-x}$ solid solution cubes as well as for $BiFeO_3$ bulk [a].

x	M_S at 50 kOe (emu/g)		M_r (emu/g)		H_C (Oe)	
	300 K	10 K	300 K	10 K	300 K	10 K
0.5	1.05	2.36	0.32	0.46	1840	1300
0.6	1.49	2.61	0.54	0.77	2240	1560
0.7	1.61	2.84	0.56	0.60	1320	910
0.8	1.88	2.87	0.75	0.99	660	480
0.9	1.04	1.42	0.34	0.48	3400	2500
1.0 [a]	0.34	0.31	-	-	-	-

[a] $BiFeO_3$ bulk show no spontaneous magnetization.
M_S is the magnetization observed at H = 50 kOe. M_r stands for remnant magnetization. The magnetic moments are defined in units of emu/g. H_C represents derived coercivity.

3.4. Conclusions

We have demonstrated our ability to generate $BiFeO_3$-based binary solid solutions with perovskite structures, *i.e.*, $(BiFeO_3)_x$–$(BaTiO_3)_{1-x}$, with x values ranging from 0.9, 0.8, 0.7, 0.6, to 0.5 employing a molten salt methodology. Structural transformations of our $(BiFeO_3)_x$–$(BaTiO_3)_{1-x}$ solid solution nanocubes, *e.g.*, rhombohedral (x = 1.0, 0.9, 0.8, and 0.7) → cubic (x = 0.6 and 0.5) → tetrahedral (x = 0, $BaTiO_3$) have been observed with increasing concentration of the second constituent (*i.e.*, $BaTiO_3$). Magnetic property measurements have revealed that the strength of the magnetic response observed is in the following order: $x = 0.8 > 0.7 > 0.6 > 0.5 \cong 0.9$. With a consideration of their relative similarity in size and shape, structure-property correlations of as-prepared $BiFeO_3$–$BaTiO_3$ solid solutions in terms of magnetic properties have been discussed. The $BiFeO_3$–$BaTiO_3$ solid solution system will provide us with further fundamental information regarding interactions between the magnetic and electric properties in ferroelectric ferromagnets. Moreover, we can investigate and correlate various physical properties and functionalities of ferroelectric ferromagnets in a wide compositional range with accompanying structural changes.

3.5. References

(1) Kounga Njiwa, A. B.; Aulbach, E.; Rodel, J.; Turner, S. L.; Comyn, T. P.; Bell, A. J. *J. Am. Ceram. Soc.* **2006**, *89*, 1761.
(2) Zhu, W. M.; Ye, Z.-G. *Ceram. Int.* **2004**, *30*, 1435.
(3) Woodward, D. I.; Reaney, I. M.; Eitel, R. E.; Randall, C. A. *J. Appl. Phys.* **2003**, *94*, 3313.
(4) Kanai, T.; Ohkoshi, S.-i.; Nakajima, Akira; Watanabe, T.; Hashimoto, K. *Adv. Mater.* **2001**, *13*, 487.
(5) Wang, D. H.; Goh, W. C.; Ning, M.; Ong, C. K. *Appl. Phys. Lett.* **2006**, *88*, 212907.
(6) Jiang, Q.-H.; Nan, C.-W.; Shen, Z.-J. *J. Am. Ceram. Soc.* **2006**, *89*, 2123.
(7) Jun, Y.-K.; Moon, W.-T.; Chang, C.-M.; Kim, H.-S.; Ryu, H. S.; Kim, J. W.; Kim, K. H.; Hong, S.-H. *Solid State Commun.* **2005**, *135*, 133.
(8) Lee, D.; Kim, M. G.; Ryu, S.; Jang, H. M.; Lee, S. G. *Appl. Phys. Lett.* **2005**, *86*, 222903.
(9) Qi, X.; Dho, J.; Tomov, R.; Blamire, M. G.; MacManus-Driscoll, J. L. *Appl. Phys. Lett.* **2005**, *86*, 062903.
(10) Li, J.; Duan, Y.; He, H.; Song, D. *J. Alloys Comp.* **2001**, *315*, 259.
(11) Mahesh Kumar, M.; Srinath, S.; Kumar, G. S.; Suryanarayana, S. V. *J. Magn. Magn. Mater.* **1998**, *188*, 203.
(12) Mahesh Kumar, M.; Srinivas, A.; Suryanarayana, S. V. *J. Appl. Phys.* **2000**, *87*, 855.
(13) Ismailzade, I. H.; Ismailov, I. M.; Alekberov, A. I.; Salaev, F. M. *Phys. Stat. Sol. (a)* **1980**, *68*, K81.
(14) Fedulov, S. A.; Ladyzhinskii, P. B.; Pyatigorskaya, I. L.; Venevtsev, Y. N. *Sov. Phys. Solid State* **1964**, *6*, 375.
(15) Smith, R. T.; Achenbach, G. D.; Gerson, R.; James, W. J. *J. Appl. Phys.* **1968**, *39*, 70.
(16) Michel, C.; Moreau, J.-M.; Achenbach, G. D.; Gerson, R.; James, W. J. *Solid State Commun.* **1969**, *7*, 70.
(17) Mao, Y.; Banerjee, S.; Wong, S. S. *J. Am. Chem. Soc.* **2003**, *125*, 15718.
(18) Park, T.-J.; Papaefthymiou, G. C.; Moodenbaugh, A. R.; Mao, Y.; Wong, S. S. *J. Mater. Chem.* **2005**, *15*, 2099.
(19) Park, T.-J.; Wong, S. S. *Chem. Mater.* **2006**, *18*, 5289.
(20) Mao, Y.; Wong, S. S. *Adv. Mater.* **2005**, *17*, 2194.
(21) Achenbach, G. D.; James, W. J.; Gerson, R. *J. Am. Ceram. Soc.* **1967**, *50*, 437.
(22) Park, T.-J.; Papaefthymiou, G. C.; Viescas, A. J.; Moodenbaugh, A. R.; Wong, S. S. *Nano Lett.* **2007**, *7*, 766.
(23) Kim, J. S.; Cheon, C. I.; Lee, C. H.; Jang, P. W. *J. Appl. Phys.* **2004**, *96*, 468.
(24) Buscaglia, M. T.; Mitoseriu, L.; Buscaglia, V.; Pallecchi, I.; Viviani, M.; Nanni, P.; Siri, A. S. *J. Eur. Ceram. Soc.* **2006**, *26*, 3027.

(25) Mahesh Kumar, M.; Srinivas, A.; Kumar, G. S.; Suryanarayana, S. V. *J. Phys.: Condens. Matter* **1999**, *11*, 8131.
(26) Horibe, Y.; Nakayama, M.; Hosokoshi, Y.; Asaka, T.; Matsui, Y.; Asada, T.; Koyama, Y.; Mori, S. *Jpn. J. Appl. Phys.* **2005**, *44*, 7148.
(27) Ueda, K.; Tabata, H.; Kawai, T. *Appl. Phys. Lett.* **1999**, *75*, 555.
(28) Fujii, T.; Jinzenji, S.; Asahara, Y. *J. Appl. Phys.* **1988**, *64*, 5434.

Chapter IV. $Bi_2Fe_4O_9$ Nanostructures

4.1. Introduction

The other FeMONS material with a ternary oxide system associated with Bi is $Bi_2Fe_4O_9$, which is the focus material of this chapter. $Bi_2Fe_4O_9$ has been considered as an impurity or as a second phase material in the synthesis of $BiFeO_3$ materials. However, because of their high sensitivity to ethanol and acetone vapors, bismuth ferrites have been recently considered as new materials for semiconductor gas sensors.[1] Moreover, the general class of bismuth ferrites, including $BiFeO_3$, $Bi_2Fe_4O_9$, and $Bi_4Fe_2O_9$, consists of semiconductors possessing interesting properties which are significant for applications in various fields as diverse as optics, electronics, magnetism, information processing and storage. In particular, the catalytic potential of $Bi_2Fe_4O_9$ for ammonia oxidation to NO is of current interest as these iron-based materials may likely replace current, irrecoverable, and costly catalysts based on platinum, rhodium, and palladium.[2,3]

The crystal structure and magnetic characterization of $Bi_2Fe_4O_9$ have been previously reported through a host of bulk X-ray powder diffraction, neutron diffraction, electron microscopy and Mössbauer measurements. It is an orthorhombic system (space group: *Pbam*) with lattice constants of a = 7.965 Å, b = 8.440 Å, and c = 5.994 Å. The formula units in the $Bi_2Fe_4O_9$ are evenly distributed between FeO_6 octahedra and FeO_4 tetrahedra with a lower packing density than those of closed packed structures.[4] The Bi^{3+} ions are surrounded by eight oxygen atoms with shorter mutually orthogonal BiO_3 and longer BiO_5. In building-up 3-D structures, the isolated BiO_3 groups (nonmagnetic planes) are connected along the c axis sharing oxygen atoms with FeO_4 groups, intercalating the FeO_6 and FeO_4 groups. Moreover, $Bi_2Fe_4O_9$ is paramagnetic at room temperature and undergoes a transition to an antiferromagnetic state at $T_N = 264 \pm 3$ K. The kinetics of the solid-state reaction forming $Bi_2Fe_4O_9$ as well as magnetic properties (*i.e.*, magnetic susceptibility) associated with its structural analogues, such as $Bi_2Fe_{4-x}Ga_xO_9$ and $Bi_2Fe_{4-x}Al_xO_9$, have also been probed.[5-7]

Despite the evident importance of $Bi_2Fe_4O_9$ as a functional material, very few reports have appeared, associated with nanoscale structural motifs of this bismuth ferrite. In fact, sheet-like nanoparticulate powders have been formed[3] but neither one-dimensional analogues (such as nanotubes and nanorods) nor nanocube analogues have been prepared. The fabrication of well-defined, monodisperse particles with controllable sizes and shapes (*e.g.*, cubes), of $Bi_2Fe_4O_9$ is of fundamental importance in investigating the size correlation of the basic physical properties of these materials, with implications for their device applications.

Monodispersed inorganic mesoscopic structures with well-defined sizes, shapes, chemical composition, and crystallinity, such as nanospheres, nanorods, nanowires and nanocubes, have attracted extensive synthetic attention as a result of their novel morphology-dependent properties, which are likely to be different from that of the bulk.[8-11] These materials have applications including biosensing, catalysis, optics, and data storage.[12-14] For future applications of nanomaterials, such as device elements, it is evident that determining particle shapes, particularly the crystallographic faces exposed on the particle's outer surfaces, are crucial.[15] Controlling the shape of the nanoparticles can be achieved either (i) using a template that physically confines the size and shape of growing nanoparticles or (ii) in solution, by employing appropriate capping agents, such as ionic or nonionic organic surfactants, to control nanoparticle growth direction.[16]

Among various classes of nanostructures, nanocubes have recently generated interest as potential building blocks in nanodevices, nanosensors, and functional nanomaterials. Much though remains to be investigated with regards to the controllable synthesis and property evaluation of these morphological novelties.[17-19] For example, a variety of nanocubes, such as metallic Ag/Au, zerovalent Fe, photoluminescent $In(OH)_3/In_2O_3$, narrow band-gap semiconducting Ag_2S, *p*-type semiconducting Cu_2O, luminescent CaF_2, and magnetic p-type semiconducting Co_3O_4, have been successfully synthesized primarily through solution-mediated reactions.[20-24] These have tended to be based on hydrothermal treatments with varying salt and/or surfactant concentrations. However, comparatively little work has been performed on the fabrication of nanocubes of technologically important transition metal oxide and related materials, including perovskites, such as $La_{1-x}Ba_xMnO_3$, $NaTaO_3/KTaO_3$, and $KMnF_3$.[25-27] Developing approaches to prepare and scale up new synthetic formulations of these transition metal oxides has been the recent focus of our efforts in this group.

In this Chapter 4, for the synthesis of submicron-sized $Bi_2Fe_4O_9$ cubes, we employed a molten salt technique. As-prepared, single-crystalline $Bi_2Fe_4O_9$ cubes were subsequently characterized by a number of techniques, including XRD, SEM, TEM, HRTEM, EDS, SAED, as well as SQUID and Mössbauer measurements.

4.2. Experimental section

4.2.1. Materials and preparation

Bismuth(III) oxide (Aldrich, 99.99%), iron(III) oxide (Aldrich, nanopowder), bismuth(III) acetate (Aldrich) and Igepal® CO-630 (NP-9, polyoxyethylene(9)nonylphenyl ether, Aldrich) were used as supplied. The choice of this NP-9 surfactant was governed by its relative non-toxicity and facility of use. Stoichiometric amounts of Bi_2O_3, Fe_2O_3, NP-9, and NaCl were mixed (in molar ratios of 1 : 1 : 40 : 6, 3 : 1 : 40 : 6, and 6 : 1 : 40 : 6, respectively, for generation of varying structural motifs), thoroughly ground in an agate mortar, and sonicated.

In a typical synthesis of $Bi_2Fe_4O_9$ cubes, 0.5 mmol each of Bi_2O_3 and Fe_2O_3 along with 20 mmol of NaCl were mixed thoroughly, to which 2 ml of NP-9 was subsequently added. The resulting mixture was ground for at least 30 min prior to sonication for an additional 5 min. Identical procedures were employed for samples containing different molar ratios of initial precursors. The processed mixture was ultimately placed in a ceramic crucible, inserted into a quartz tube, heated at a ramp rate of 5°C per minute up to an annealing temperature at 820 °C for 3.5 h, and cooled thereafter to room temperature. Samples were subsequently washed several times with distilled water, nitric acid, and distilled water. The as-prepared material was collected by centrifugation and dried at 120 °C in a drying oven.

4.3. Results and discussion

4.3.1. XRD measurements: purity and crystallinity of as-prepared $Bi_2Fe_4O_9$ nanocubes

The purity and crystallinity of as-prepared $Bi_2Fe_4O_9$ cube samples were examined by powder XRD measurements (Figure 4.1). It is evident that the observed pattern of the collected powder displayed all of the expected peaks emanating from the $Bi_2Fe_4O_9$ structure, with very few if any impurity peaks. In effect, diffraction peaks in Figure 4.1B can be indexed to the orthorhombic structure of $Bi_2Fe_4O_9$ (space group: *Pbam*) with lattice constants of a = 7.965 Å, b = 8.440 Å, and c = 5.994 Å, which are in good agreement with literature results (*i.e.*, JCPDS #25-0090, Figure 4.1A). In addition, the relative intensity of the reflection of the (220) signal to that of the other peaks has been found to be stronger than that of the corresponding bulk materials, an observation which can be ascribed to the preferential formation of the (220) orientation during the synthesis process.

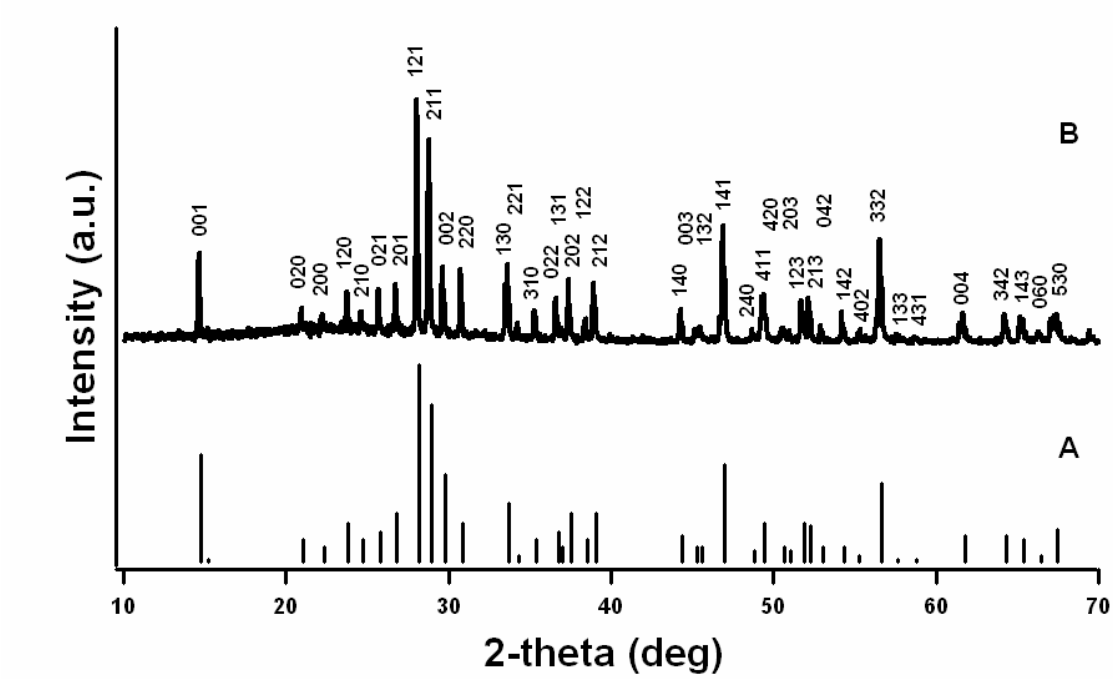

Figure 4.1. XRD patterns of $Bi_2Fe_4O_9$ materials from the JCPDS #25-0090 database standard (A), and from as-prepared cubes (B). Reproduced from Park, T.-J. *et al*., *J. Mater. Chem.* **2005**, *15*, 2099.

4.3.2. SEM, TEM measurements: size, shape, chemical composition, single-crystallinity, and lattice spacings of as-prepared $Bi_2Fe_4O_9$ nanocubes

Figure 4.2 shows SEM images revealing the morphologies of as-prepared $Bi_2Fe_4O_9$. It can be observed that the $Bi_2Fe_4O_9$ product mainly consists of cubic structures. The mean edge length of the $Bi_2Fe_4O_9$ structures obtained was 386 (± 147) nm, though particles were formed with a range of ~166 – 833 nm. It is observed that the faces of the $Bi_2Fe_4O_9$ structures are essentially flat though some of the corners and edges of these structures are slightly truncated. Figure 4.2B shows a representative individual $Bi_2Fe_4O_9$ structure with truncated edges which could be schematically described by the illustration shown in the inset.

A typical TEM image of $Bi_2Fe_4O_9$ submicron cubes, generated from the current molten salt method described above, is shown in Figure 4.3A. SAED data taken from individual cubes (Figure 4.3B) show the presence of sharp diffraction spots indicating the formation of well-developed, single-crystalline $Bi_2Fe_4O_9$. We note that the electron diffraction patterns obtained from different areas of the cube also show similarly sharp diffraction spots. In order to confirm the chemical composition of the as-prepared structures, EDS spectra (Figure 4.3C) were taken at a number of selected positions of the sample. The elemental signatures obtained are identical within experimental accuracy, and essentially Bi, Fe, and O were observed. The Cu and C signals arise from the TEM grid. In Figure 4.3D, a HRTEM image obtained from part of an individual $Bi_2Fe_4O_9$ cube is displayed in order to further confirm the single-crystalline nature of our as-prepared structures. This image shows a typical crystalline domain with an interplanar spacing of about 2.64 Å, compatible with the literature value of 2.654 Å, which corresponds to the {130} plane of an orthorhombic phase $Bi_2Fe_4O_9$ crystal (JCPDS #25-0090).

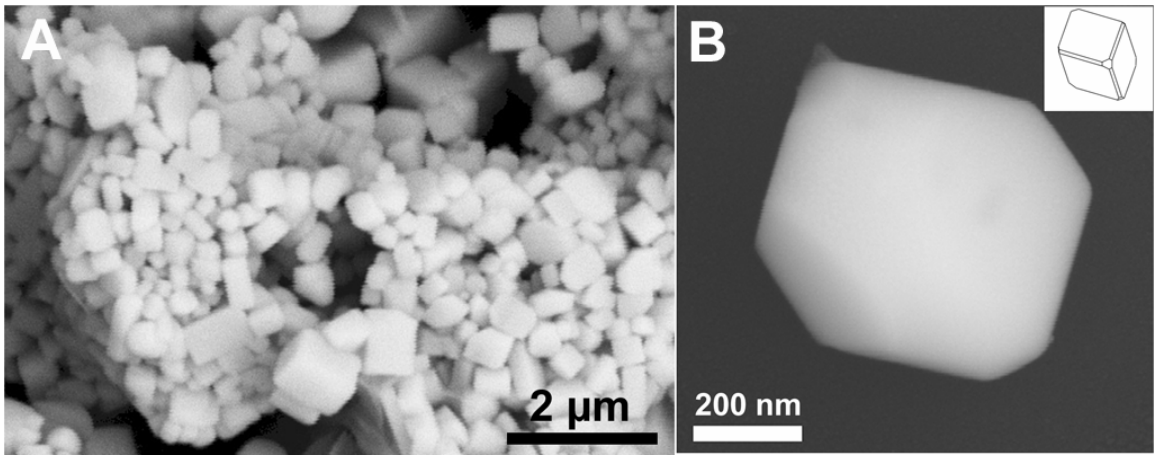

Figure 4.2. SEM images of $Bi_2Fe_4O_9$ cubes prepared using a molten salt method (A). A typical individual cube is shown in (B). The inset illustrates a schematic of the facets of an individual cube. Reproduced from Park, T.-J. *et al*., *J. Mater. Chem.* **2005**, *15*, 2099.

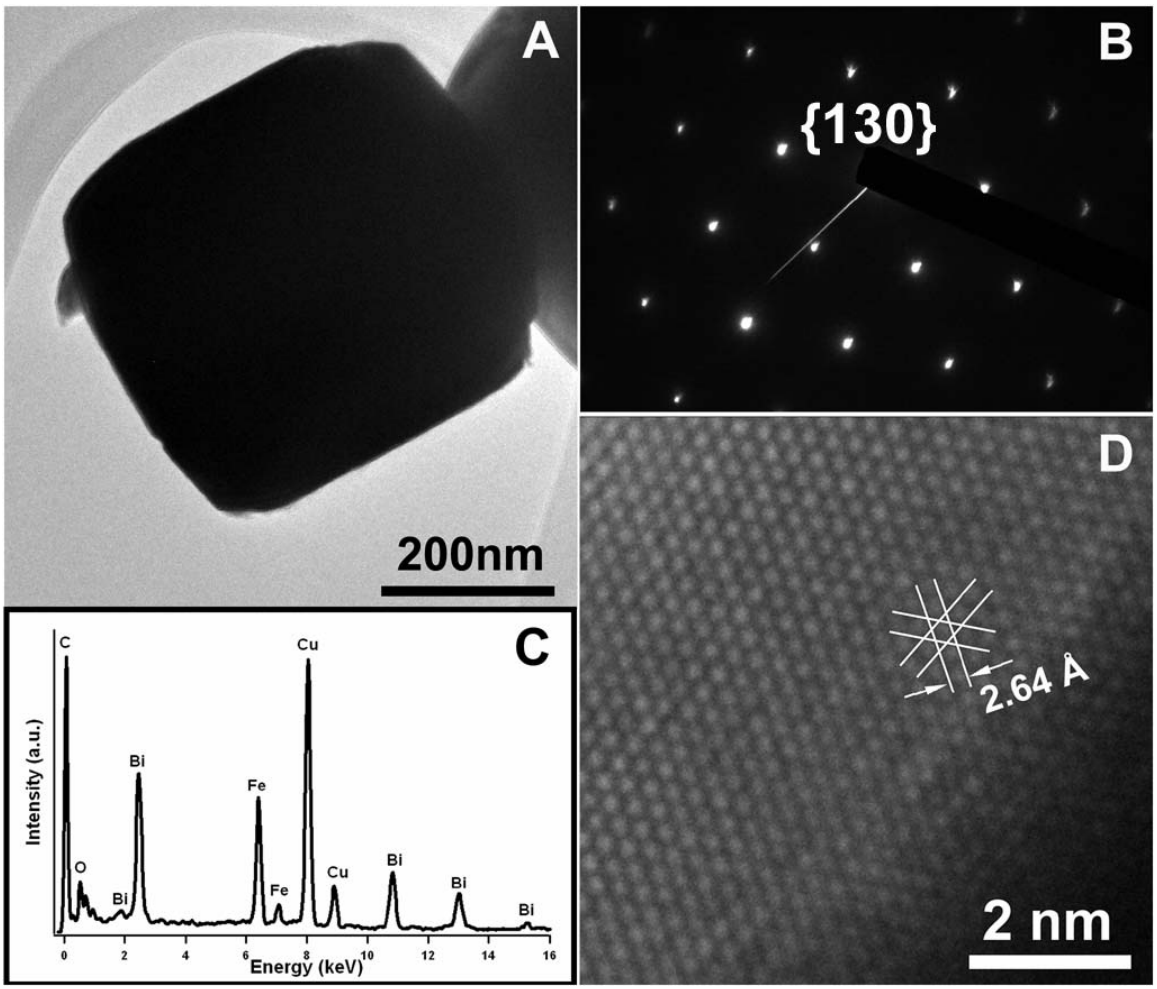

Figure 4.3. (A) TEM image of an individual $Bi_2Fe_4O_9$ cube. (B) HRTEM image of a representative portion of an individual $Bi_2Fe_4O_9$ cube. (C) EDS of an as-prepared $Bi_2Fe_4O_9$ cube. The Cu and C peaks originate from the TEM grid. (D) SAED pattern of a $Bi_2Fe_4O_9$ cube. Reproduced from Park, T.-J. *et al*., *J. Mater. Chem.* **2005**, *15*, 2099.

4.3.3. SQUID measurements: magnetic properties of as-prepared $Bi_2Fe_4O_9$ nanocubes

Figure 4.4A shows the magnetic susceptibility of cubes as a function of temperature at an applied magnetic field strength of 1000 Oe after zero field cooling (ZFC) and also, with field cooling (FC). The *M*/T curves show hysteresis below ~250 K, from the point at which the ZFC and FC plots are no longer parallel. We note that the signals of ZFC and FC are slightly offset from each other, possibly due to a minor, remnant magnetic component with a higher T_C, such as Fe_2O_3. However, the curves do present specific antiferromagnetic behavior, as detected by other groups for this system.[7,27] Our observations are moreover consistent with characteristics of antiferromagnetic materials, with negative values of the paramagnetic Curie temperature (θ) reported.[7,27] The Curie-Weiss law, $\chi = C/(T - \theta)$ above T_N, provides for a value of the paramagnetic temperature for our $Bi_2Fe_4O_9$ structures, herein experimentally determined to be –1433.7 K. Figure 4.4B shows a detailed plot of the inverse magnetic susceptibility ($1/\chi$) vs. temperature (K). Even though the data were not measured through a large linear region, the straight-line fit above T_N gives values comparable to previously reported data.[6,28]

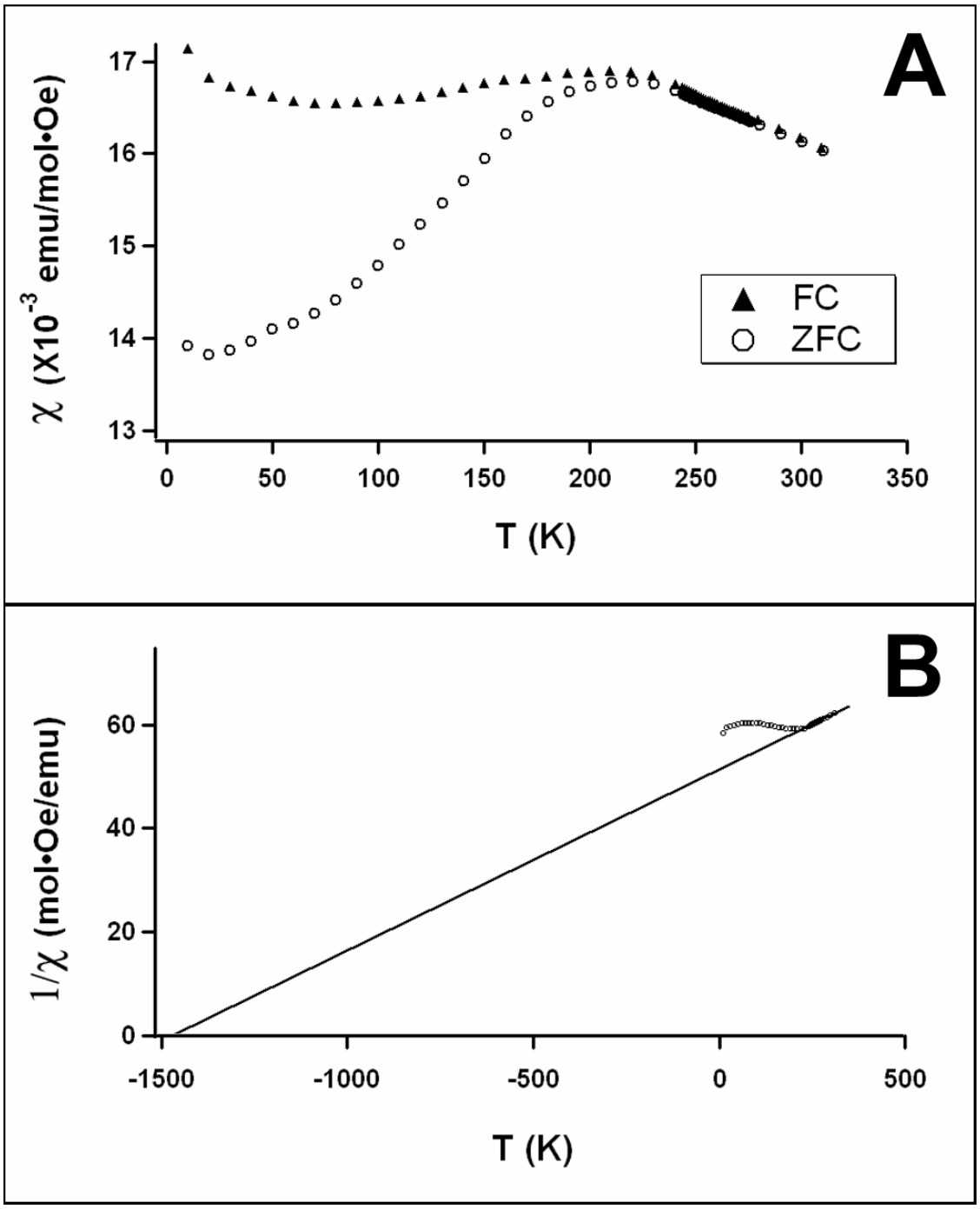

Figure 4.4. (A) The temperature dependence of the magnetic susceptibility for $Bi_2Fe_4O_9$ structures, showing zero field cooling (ZFC, open circles) and field cooling (FC, closed triangles) curves with an applied magnetic field set at 1000 Oe. (B) The inverse magnetic susceptibility (represented as open circles) and fit of the Curie-Weiss law above T_N (represented as a solid line) to the experimental data for $Bi_2Fe_4O_9$ structures. Reproduced from Park, T.-J. *et al*., *J. Mater. Chem.* **2005**, *15*, 2099.

4.3.4. Mössbauer spectroscopy measurements: electronic, magnetic, and structural properties of as-prepared $Bi_2Fe_4O_9$ nanoparticles

Mössbauer spectra of the as-prepared $Bi_2Fe_4O_9$ samples were obtained at room temperature and 4.2 K, shown in Figure 4.5. Room temperature spectra, Figure 4.5A, were fitted to the superposition of two paramagnetic subsites, corresponding to Fe^{3+} in tetrahedral and octahedral coordination. The Mössbauer parameters obtained for the tetrahedral site (bar diagram A) were: isomer shift, $\delta = 0.24$ mm/s, quadrupole splitting, $\Delta E_Q = 0.94$ mm/s, and line width, $\Gamma = 0.30$ mm/s, contributing 51% of the absorption area. For the octahedral site (bar diagram B), we obtained: $\delta = 0.36$ mm/s, $\Delta E_Q = 0.38$ mm/s, and $\Gamma = 0.29$ mm/s, contributing 49% of the absorption area. These Mössbauer parameters (Table 4.1) are consistent with previously reported data on bulk $Bi_2Fe_4O_9$.[7,29]

At 4.2 K, the spectra are magnetically split. This is in accord with the ZFC/FC magnetic susceptibility studies of these submicron-sized particles, presented in Figure 4.4A, which indicate that the samples undergo a magnetic phase transition below 250 K. In the bulk, $Bi_2Fe_4O_9$ has been reported to enter into an antiferromagnetically ordered state at T_N =263 K,[30] although somewhat lower transition temperature values, ranging between 245 K and 263 K, have also been reported.[6,28-31]

The 4.2 K Mössbauer data were analyzed assuming the superposition of two, well-resolved, magnetic subsites corresponding to Fe^{3+} occupying the tetrahedral and octahedral coordination sites, depicted in bar diagrams A and B, respectively, in Figure 4.5B. Mössbauer parameters obtained from least square fits, which included magnetic field distributions about an average value, were: isomer shift $\delta = 0.35$ mm/s, average magnetic hyperfine field H_{hf} = 468 kOe, comprising 54% of the absorption area, for the tetrahedral site; and $\delta = 0.35$ mm/s and H_{hf} = 508 kOe, contributing 46% of the absorption area, for the octahedral site. An increase in the values of the isomer shifts at 4.2 K, as compared to those at room temperature, is consistent with a second order Doppler shift.[32] Within the statistical precision of the experimental data, the relative intensity of the two subsites at 4.2 K is consistent with an approximately equal iron ion distribution between octahedral and tetrahedral coordination, as is also indicated by the room temperature data. The above results are in agreement with previously reported data on bulk $Bi_2Fe_4O_9$ (Table 4.1).

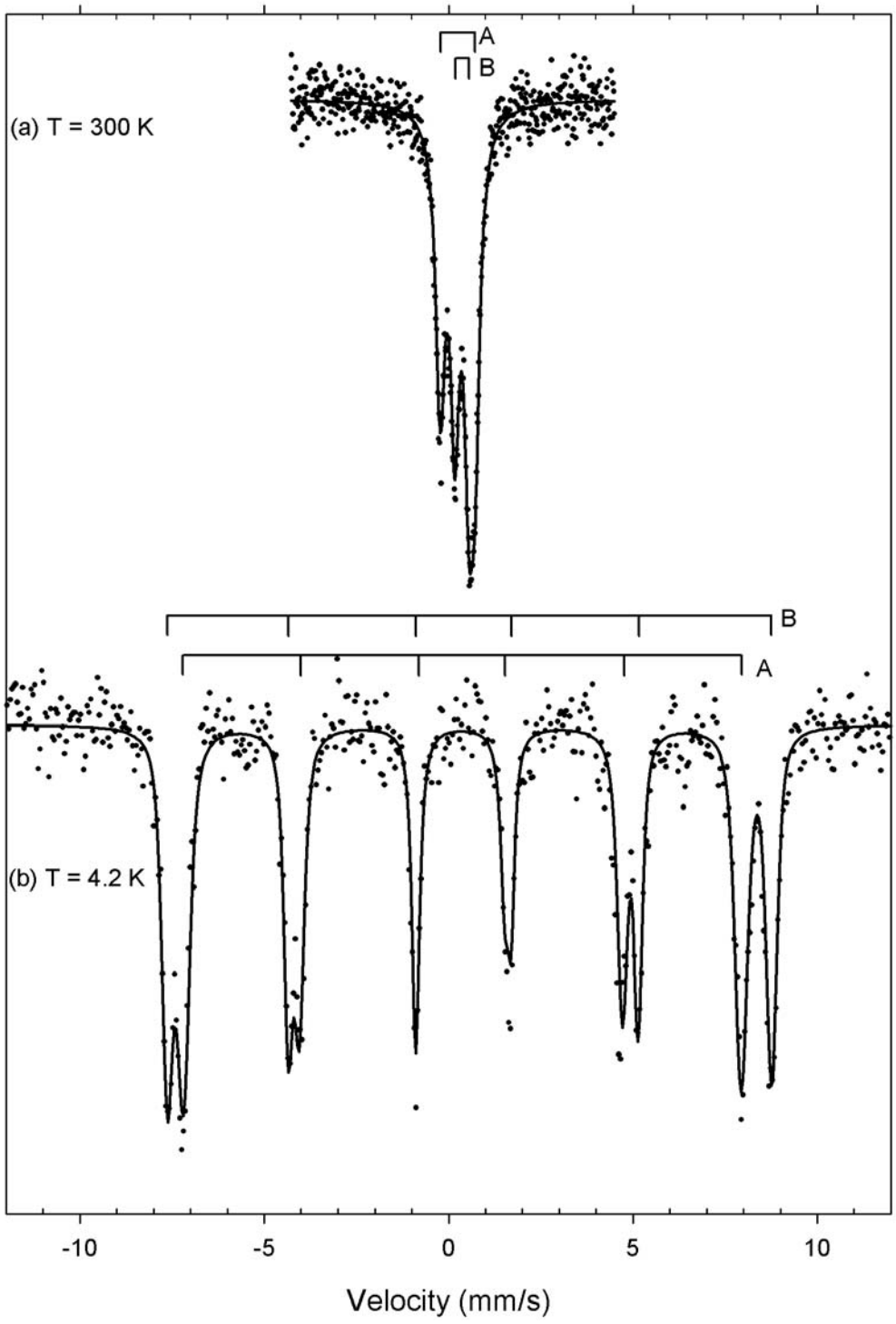

Figure 4.5. Mössbauer spectra of submicron sized $Bi_2Fe_4O_9$ cubes at (a) 300 K and (b) 4.2 K. Solid lines are least square fits to experimental points, assuming a superposition of two different iron subsites, i.e. a tetrahedral (bar diagram A) one and an octahedral (bar diagram B) one. Reproduced from Park, T.-J. *et al*., *J. Mater. Chem.* **2005**, *15*, 2099.

Table 4.1. Selected Mössbauer parameters for nanoscale $Bi_2Fe_4O_9$ and bulk. Reproduced from Park, T.-J. *et al*., *J. Mater. Chem.* **2005**, *15*, 2099.

Size	T (K)	Site	δ [a] (mm s^{-1})	ΔE_Q or ε (mm s^{-1})	H_{hf} [b] (kOe)	H_{dist} [c] (kOe)	Γ [d] (mm s^{-1})	Fractional area	Ref.
~385 (nm)	300	T_d	0.24	0.94	-	-	0.30	0.51	This study
		O_h	0.36	0.38	-	-	0.29	0.49	
	4.2	T_d	0.35	0.05	468	14.7	0.26	0.54	This study
		O_h	0.48	0.17	507	14.8	0.20	0.46	
bulk	300	T_d	0.24	0.95	-	-	-	0.50	29
		O_h	0.36	0.37	-	-	-	0.50	
	4.2	T_d	0.34	0.16	467	-	-	0.50	7
		O_h	0.48	0.15	505	-	-	0.50	

[a] Isomer shifts (δ) are relative to α-Fe at room temperature.
[b] Average hyperfine magnetic field (H_{hf}) at the iron nucleus.
[c] Full width at half maximum (FWHM) of the hyperfine field distribution (H_{dist}), assumed to be Gaussian.
[c] Full width at half maximum (Γ).

4.3.5. Effect of varying experimental parameters on sample size and shape

4.3.5.1. Role of molar ratio of precursors

In order to examine the role of the molar ratio of the precursor metal ions, we prepared $Bi_2Fe_4O_9$ structures using an identical molten salt method with varying molar ratios of Bi_2O_3 to Fe_2O_3. In conventional bulk ceramic approaches, use of an excess Bi_2O_3 as the reactive precursor has been employed to generate corresponding amounts of similarly-shaped $Bi_2Fe_4O_9$ materials. However, in this system, the use of different molar ratios of Bi^{3+} to Fe^{3+} was found to generate dissimilar morphologies of $Bi_2Fe_4O_9$ products with almost identical crystallinity. SEM images and XRD measurements for samples prepared using different molar ratios are presented in Figure 4.6.

For example, the morphologies of $Bi_2Fe_4O_9$ materials, prepared using a current molten salt method with 3:1 and 6:1 molar ratios of Bi^{3+} to Fe^{3+}, respectively, are shown in Figure 4.6A and 4.6B. It can be observed that as-prepared $Bi_2Fe_4O_9$ structures, using a 3:1 molar ratio of Bi_2O_3 to Fe_2O_3, mainly consist of orthorhombic structures composed of smooth surfaces, showing some slightly truncated corners or edges (Figure 4.6A). The mean lengths of the shorter and longer edges of the rectangular structures were measured to be 662 ± 181 and 1043 ± 350 nm, respectively. Figure 4.6B shows typical morphologies of the $Bi_2Fe_4O_9$ structures generated from the precursors, derived from a 6:1 (Bi^{3+}: Fe^{3+}) molar ratio. It is evident that the products are mostly smooth, straight, and rod-like structures. The lengths of the rods attain ~10 microns with a width of only a few microns. We also note that there is some degree of fracture and fragmentation in the product.

If we compare among product morphologies generated from precursors of 1 : 1 (Figure 4.2A), 3 : 1 (Figure 4.6A), and 6 : 1 (Figure 4.6B) molar ratios of Bi^{3+}/Fe^{3+}, respectively, it is evident that the relative molar ratios of the metal ions, in the presence of surfactant, play a key role not only in the preparation of but also in the control over the final shapes of the resultant single-crystalline $Bi_2Fe_4O_9$ products. That is, whereas use of a 1:1 molar ratio of $Bi^{3+}$to Fe^{3+} generated smaller sized particles with cubic-like features, the highest molar ratio employed, *i.e*., 6:1 molar ratio of Bi^{3+} to Fe^{3+}, yielded larger-sized structures with rod-like, rectangular shapes. Not surprisingly, the product generated using a 3:1 molar ratio of $Bi^{3+}$to Fe^{3+} precursors produced intermediate-sized, orthorhombically-shaped materials.

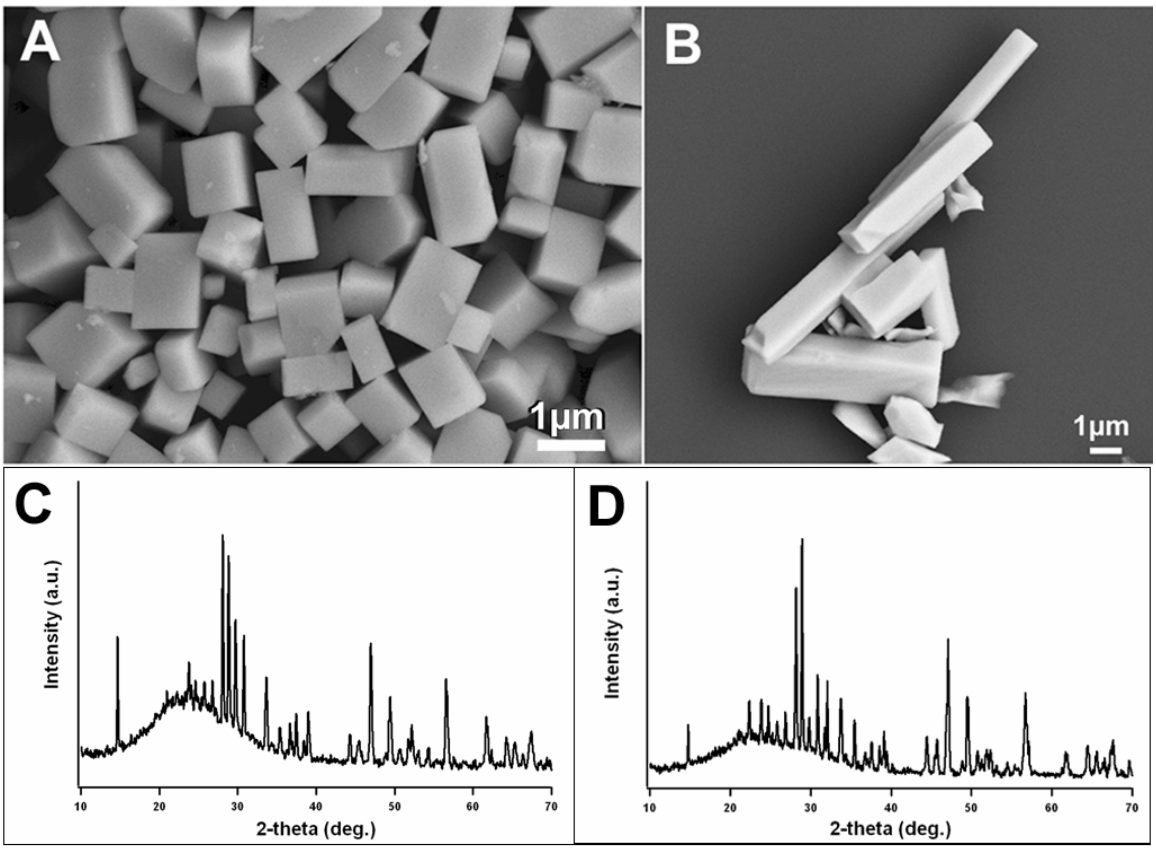

Figure 4.6. SEM images of the $Bi_2Fe_4O_9$ materials prepared using a molten salt method with a 3:1 (A) and 6:1 (B) molar ratio of Bi_2O_3 to Fe_2O_3 precursors, respectively. Corresponding powder XRD patterns of as-prepared (A) and (B) $Bi_2Fe_4O_9$ materials are shown in (C) and (D), respectively. Reproduced from Park, T.-J. *et al*., *J. Mater. Chem.* **2005**, *15*, 2099.

4.3.5.2. Role of surfactant, salt, and precursor identity

To analyze the role of (i) surfactant in the reaction, $Bi_2Fe_4O_9$ products were prepared by employing the identical, as-reported molten salt method in the absence of any surfactant. Morphologies of the resultant products generated from mixtures of 1:1 and 3:1 molar ratios of Bi^{3+} to Fe^{3+} precursors, respectively, are shown in Figures 4.7A and 4.7B. Although the images clearly show the presence of crystalline particles (Figures 4.7C and 4.7D) with smooth faces and clear, well-defined edges, it is evident that these particles are not only significantly larger, stretching from several to tens of microns but also the size distribution observed is far more polydisperse. In addition, the effect of precursor ratio on product morphologies is not as evident, since Figures 4.7A and 4.7B are practically indistinguishable from each other. Hence, to underlie the importance of the presence of surfactant in this reaction, it is apparent that the $Bi_2Fe_4O_9$ system loses its selectivity in terms of product shape in the absence of surfactant, regardless of the molar ratio of metal ions used.

We have also studied the importance of (ii) salt as well as (iii) the identity of selected precursors in this system. In separate experiments, we prepared samples employing an identical method either in the absence of any salt or in the presence of different types of precursors, *e.g.*, $Bi(CH_3CO_2)_3$ as opposed to Bi_2O_3. Figure 4.8 shows XRD patterns obtained from each of the samples generated, all in the presence of surfactant, from a stoichiometric 1 : 1 molar ratio of $Bi(CH_3CO_2)_3$ to Fe_2O_3 precursors (Figure 4.8C), and a 1 : 1 molar ratio of Bi_2O_3 to Fe_2O_3 in the absence of any salt, *i.e.*, NaCl (Figure 4.8D), respectively. In addition, JCPDS database results for $Bi_2Fe_4O_9$ (#25-0090) and $BiFeO_3$ (#20-0169) are shown, respectively, in Figure 4.8A and 4.8B. It is evident that the sample obtained from a stoichiometric 1:1 molar ratio of $Bi(CH_3CO_2)_3$ to 0.5 Fe_2O_3 precursors (Figure 4.8C) was essentially a mixture of pure $BiFeO_3$ (70%) and $Bi_2Fe_4O_9$ (30%) materials based on the analysis of the highest intensity peaks for each material. In addition, the sample prepared conventionally without the presence of salt (Figure 4.8D) yielded an XRD pattern, similar to that seen in Figure 4.8C, that contained significantly more impurity phases as well as dissimilar intensities of existing peaks. An example of the polydisperse nature of the resulting product morphology of that sample is shown in Figure 4.9.

The observations described above confirm that there is a only very narrow combination of experimental parameters such as (a) a 1:1 molar ratio of precursors, (b) the addition of salt, (c) the presence of surfactant, and (d) the usage of specific elemental precursors, that collectively will yield single-crystalline $Bi_2Fe_4O_9$ products with predictive control of shape and size. The presence of salt is expected to decrease the overall reaction temperature. As well, the liquid-like phase of the molten flux is expected to increase the mobility of its constituent components.[33]

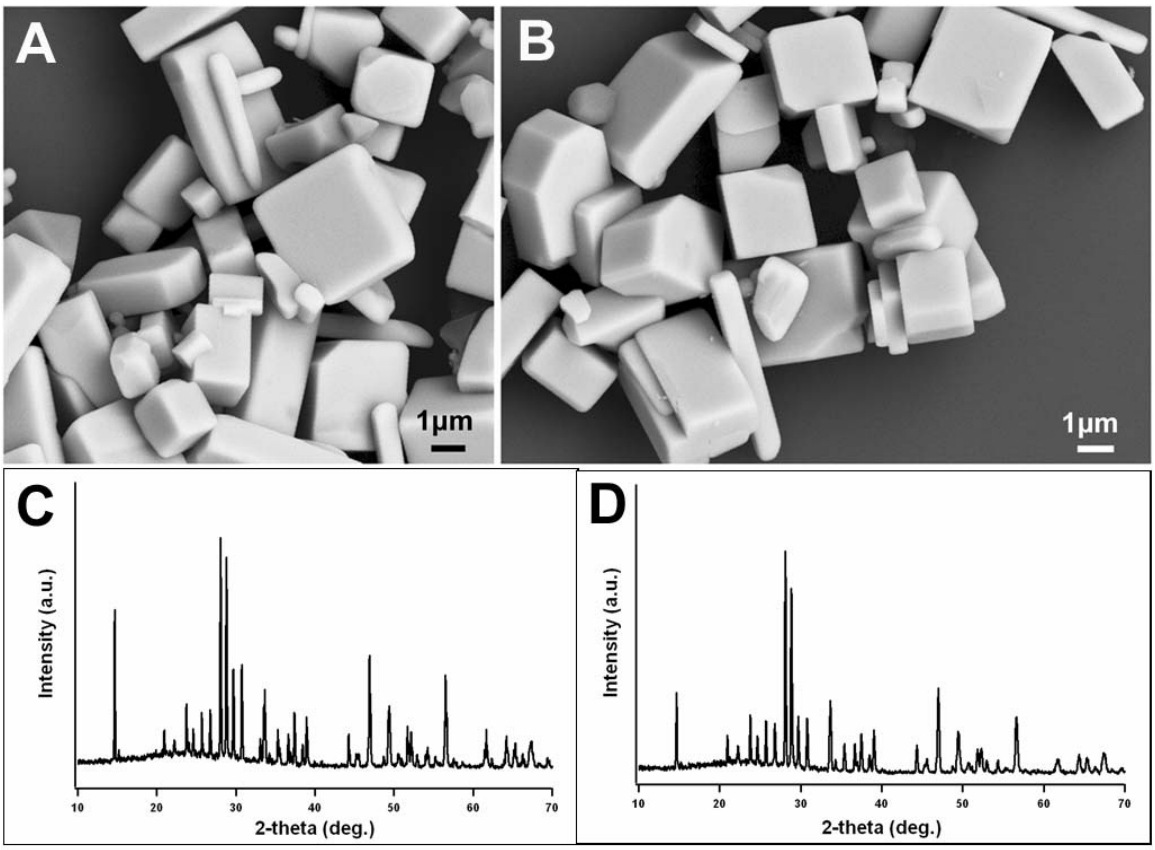

Figure 4.7. SEM images of as-prepared $Bi_2Fe_4O_9$ materials prepared using an identical method, but in the absence of surfactants. Products synthesized using 1:1 (A) and 3:1 (B) molar ratios of Bi^{3+} to Fe^{3+} precursors, respectively. Corresponding XRD measurements are shown in (C) and (D) for as-prepared (A) and (B) $Bi_2Fe_4O_9$ materials, respectively. Reproduced from Park, T.-J. *et al*., *J. Mater. Chem.* **2005**, *15*, 2099.

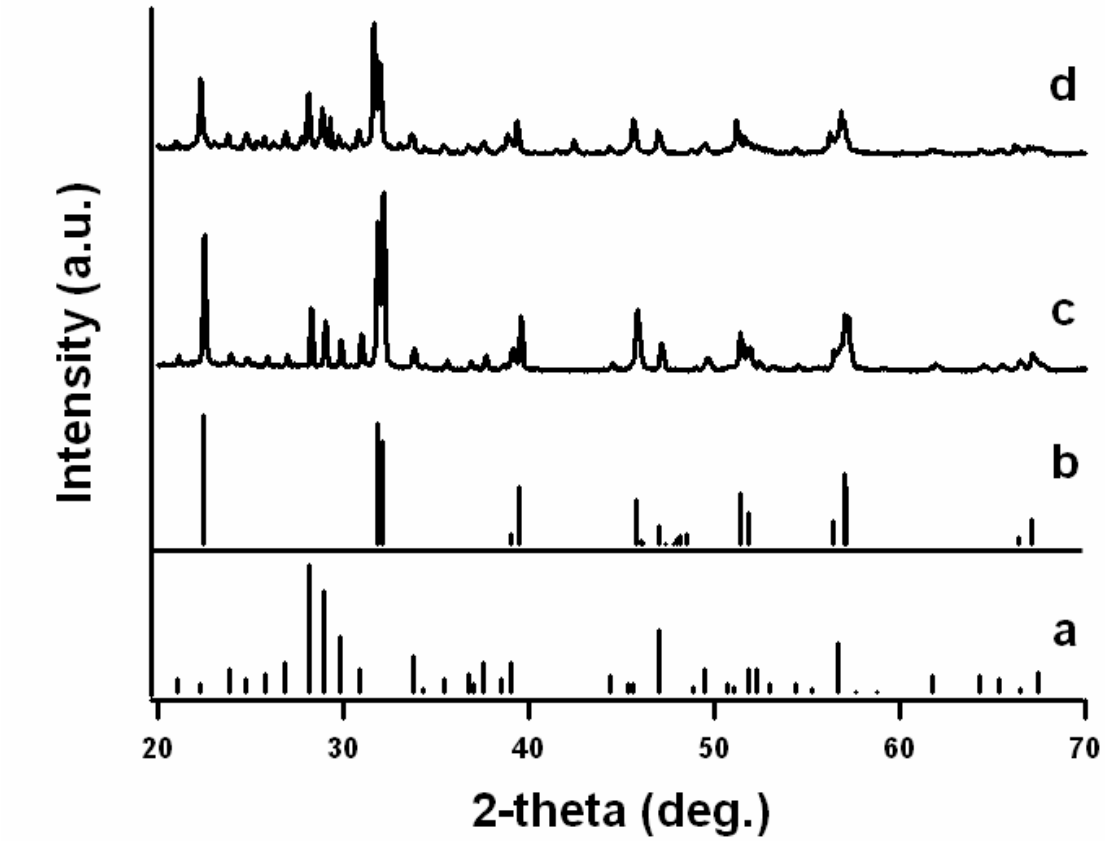

Figure 4.8. Powder XRD patterns of $Bi_2Fe_4O_9$ and $BiFeO_3$ materials from the JCPDS #25-0090 (a) and #20-0169 (b) database standards, respectively. XRD of samples generated, in the presence of surfactant, from a stoichiometric 1:1 molar ratio of $Bi(CH_3CO_2)_3$ to 0.5 Fe_2O_3 precursors, and a 1:1 molar ratio of Bi_2O_3 to Fe_2O_3 in the absence of any salt, *i.e.*, NaCl, are shown in (c) and (d), respectively. Reproduced from Park, T.-J. *et al*., *J. Mater. Chem.* **2005**, *15*, 2099.

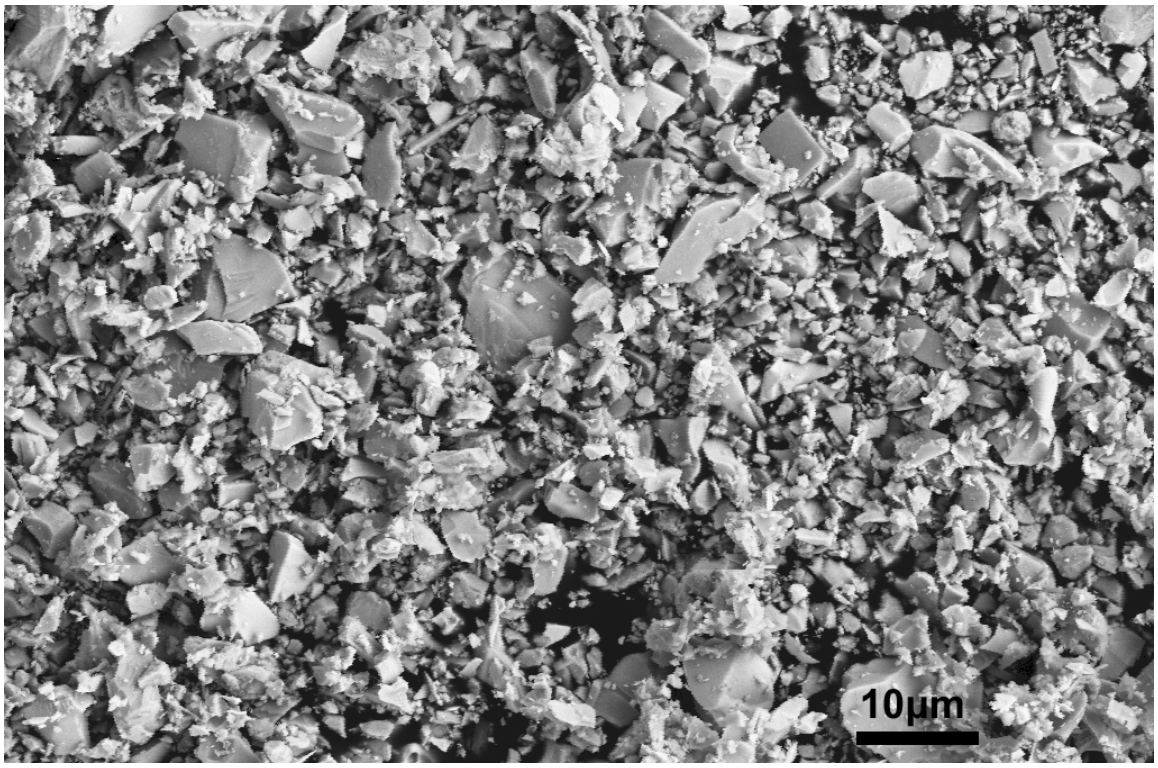

Figure 4.9. SEM image of $Bi_2Fe_4O_9$ materials prepared using the method described herein but in the absence of NaCl. Reproduced from Park, T.-J. *et al*., *J. Mater. Chem.* **2005**, *15*, 2099.

4.4. Conclusion

The current work demonstrates the synthesis of discrete single-crystalline submicron $Bi_2Fe_4O_9$ structures, including cubic, orthorhombic, and rod-like structures using a simple, one-step, solid-state chemical reaction in the presence of NaCl and a nonionic surfactant. The resulting cubic structures have been extensively characterized using a variety of microscopy, diffraction, and spectroscopy results. Because of the simplicity and versatility of the approach used, it is anticipated that this methodology can be generalized to the large-scale preparation of other important metal oxides with controllable size and shape. Future research will focus on the investigation of property measurements, such as catalytic activity and gas sensitivity, as well as mechanistic studies of the formation of $Bi_2Fe_4O_9$ for the purposes of synthetic optimization.

4.5. References

(1) Poghossian, A. S.; Abovian, H. V.; Avakian, P. B.; Mkrtchian, S. H.; Haroutunian, V. M. *Sens. Actuators B* **1991**, *4*, 545.
(2) Zakharchenko, N. I. *Kinet. Catal.* **2002**, *43*, 95.
(3) Xiong, Y.; Wu, M.; Peng, Z.; Jiang, N.; Chen, Q. *Chem. Lett.* **2004**, *33*, 502.
(4) Niizeki, N.; Wachi, M. *Zeit. Kristallogra. B* **1968**, *127*, 173.
(5) Mukherjee, J. L.; Wang, F. F. Y. *J. Am. Ceram. Soc.* **1971**, *54*, 31.
(6) Giaquinta, D. M.; Papaefthymiou, G. C.; Davis, W. M.; Zur Loye, H.-C. *J. Solid State Chem.* **1992**, *99*, 120.
(7) Giaquinta, D. M.; Papaefthymiou, G. C.; Zur Loye, H.-C. *J. Solid State Chem.* **1995**, *114*, 199.
(8) Alivisatos, A. P. *Science* **1996**, *271*, 933.
(9) Cui, Y.; Lieber, C. M. *Science* **2001**, *291*, 851.
(10) Sun, Y.; Xia, Y. *Science* **2002**, *298*, 2176.
(11) Ahmadi, T. S.; Wang, Z. L.; Green, T. C.; Henglein, A.; El-Sayed, M. A. *Science* **1996**, *272*, 1924.
(12) Bruchez, M.; Moronne, M.; Gin, P.; Weiss, S.; Alivisatos, A. P. *Science* **1998**, *281*, 2013.
(13) Sun, S.; Murray, C. B.; Weller, D.; Folks, L.; Moser, A. *Science* **2000**, *287*, 1989.
(14) Wang, J.; Gudiksen, M. S.; Duan, X.; Cui, Y.; Lieber, C., M. *Science* **2001**, *293*, 1455.
(15) Lim, W. P.; Zhang, Z.; Low, H. Y.; Chin, W. S. *Angew. Chem. Int. Ed.* **2004**, *43*, 5685.
(16) Gou, L.; Murphy, C. J. *J. Mater. Chem.* **2004**, *14*, 735.
(17) Kim, F.; Connor, S.; Song, H.; Kuykendall, T.; Yang, P. *Angew. Chem. Int. Ed.* **2004**, *43*, 3673.
(18) Dumestre, F.; Chaudret, B.; Amiens, C.; Renaud, P.; Fejes, P. L. *Science* **2004**, *303*, 821.
(19) Gou, L.; Murphy, C. J. *Nano Lett.* **2003**, *3*, 231.
(20) Xu, R.; Zeng, H. C. *Langmuir* **2004**, *20*, 9780.
(21) Yu, D.; Yam, V. W.-W. *J. Am. Chem. Soc.* **2004**, *126*, 13200.
(22) Li, X.; Gao, H.; Murphy, C. J.; Gou, L. *Nano Lett.* **2004**, *4*, 1903.
(23) Jin, R.; Egusa, S.; Scherer, N. F. *J. Am. Chem. Soc.* **2004**, *126*, 9900.
(24) Liu, R.; Oba, F.; Bohannan, E. W.; Ernst, F.; Switzer, J. A. *Chem. Mater.* **2003**, *15*, 4882.
(25) Urban, J. J.; Ouyang, L.; Jo, M.-H.; Wang, D. S.; Park, H. *Nano Lett.* **2004**, *4*, 1547.
(26) Spooren, J.; Rumplecker, A.; Millange, F.; Walton, R. I. *Chem. Mater.* **2003**, *15*, 1401.

(27) Agnoli, F.; Zhou, W. L.; O'Connor, C. J. *Adv. Mater.* **2001**, *13*, 1697.
(28) Tutov, A. G.; Myl'nikova, I. E.; Parfenova, N. N.; Bokov, V. A.; Kizhaev, S. A. *Sov. Phys. Solid State* **1964**, *6*, 963.
(29) Bokov, V. A.; Novikov, G. V.; Trukhtanov, V. A.; Yushchuk, S. I. *Sov. Phys. Solid State* **1970**, *11*, 2324.
(30) Shamir, N.; Gurewitz, E. *Acta Crystallogr., Sect. A* **1978**, *34*, 662.
(31) Groult, D.; Hervieu, M.; Nguyen, N.; Raveau, B. *J. Solid State Chem.* **1988**, *76*, 260.
(32) Greenwood, N. N.; Gibb, T. C., *Mössbauer Spectroscopy*; Chapman Hall: London, 1971.
(33) Wiley, J. B.; Kaner, R. B. *Science* **1992**, *255*, 1093.

Chapter V. α-Fe_2O_3 and Fe/Fe_3O_4 Nanostructures

5.1. Introduction

Monodisperse inorganic mesoscopic structures with well-defined size, shape, chemical composition, and crystallinity have attracted extensive synthetic attention because of their novel morphology-dependent properties and their relevant applications including but not limited to biosensing, catalysis, optics, and data storage.[1-8] In particular, the generation of nanostructured magnetic materials with controllable shape and size in large quantities is of significant importance due to the potential applications, ranging from ferrofluids, advanced magnetic materials, catalysts, colored pigments, high-density magnetic recording media, to use in medical diagnostic equipment.[9] Much of the existing research though has focused on the synthesis and morphological organization of phase-pure nanosized building blocks such as nanoparticles; the fabrication of nanosized composites, such as core-shell, coaxial cable, as well as one and two-dimensional structures, has not been as investigated as comprehensively.[10-17] Among magnetic materials, the Fe/Fe_3O_4 composite system has specifically attracted considerable attention due to its favorable magnetoelectric and transport (including high conductivity) properties.[18-21] Moreover, this composite has been shown to produce a novel and active heterogeneous Fenton system, important in the oxidation of organic contaminants.[22]

Most of the synthetic routes associated with composite formation follow a "bottom up" strategy, wherein growth of the resulting structure occurs through assembly of constituent molecular species. By contrast, in our approach (Figure 5.1), we were able to transform as-prepared hematite rhombohedra into nanocomposites of Fe and Fe_3O_4 by reducing hematite (α-Fe_2O_3) nanocrystals in the presence of a gaseous mixture of 5 % H_2 in N_2.[23-27] That is, our particular strategy in composite formation was to initiate in situ, localized chemical transformations of precursor particles. Practically speaking, we were able to reduce the surface of hematite rhombohedra to an iron/magnetite composite with a corresponding color change of the sample from a reddish hue of the initial precursor to the deep black of the resulting product.

We demonstrate our multi-step synthesis through the initial production of a hematite precursor, a single-crystalline rhombohedral crystal with the corundum structure, which has been previously difficult to synthesize. Hematite is thought to be catalytic in the oxidation of chlorinated pollutants in groundwater and is found in the clay fraction of tropical and sub-tropical soils, giving them their pink bright red hue. Bacteria in surface waters are known to catalyze the oxidation of magnetite (Fe_3O_4) to hematite.[28] Because of its high stability, relatively low cost, and n-type semiconducting properties with a small bandgap (2.1 eV), α-Fe_2O_3 has been associated with applications ranging from gas

sensing, catalysis, solar energy conversion, to pigmentation.[29-31] Specifically, the synthesis of rhombohedral hematite is a significant advance in nanoparticle chemistry not only because this particular morphology is a rarely observed structural motif of this material but also because this work represents the large-scale generation of a high-surface-area formulation of an industrially important material (iron oxide).

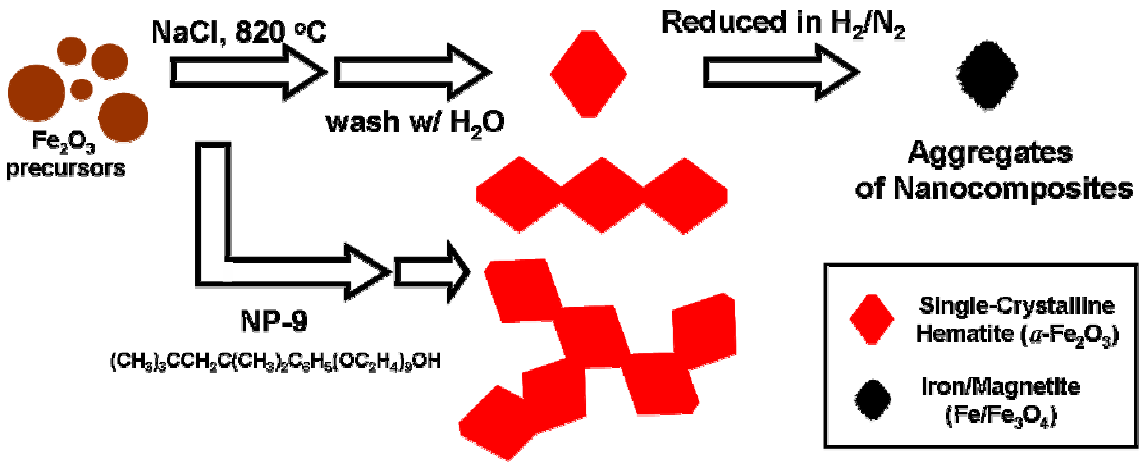

Figure 5.1. Schematic illustration of the generation of single-crystalline hematite rhombohedra (as well as other hematite structural motifs) and corresponding Fe/Fe_3O_4 nanocomposites. Reproduced from Park, T.-J. *et al*., *Chem. Mater.* **2005**, *18*, 5289.

Considerable efforts have been expended in the generation of nanoscale structures of hematite, using a variety of techniques such as chemical precipitation, sol-gel techniques, hydrothermal approaches, forced hydrolysis, and solid-state reaction, to name a representative few.[23,32-50] However, most of the aforementioned solution-phase approaches tend to involve the use of organometallic precursors, surfactants, and solvents in either potentially hazardous or rather complicated protocols. It is therefore of interest to develop an environmentally friendly and efficient methodology to synthesize iron oxides. We have been particularly interested in exploring the use of molten-salt, solid-state reactions, due to their relative environmental friendliness, simplicity, relative non-toxicity, facility of use, and versatility, as practical, generalizable, large-scale approaches to generating single-crystalline metal oxide nanomaterials.[51-55] In these reactions, since the nature of the net products strongly depends on the structural and chemical nature of the initial iron precursors, one of the main challenges of applying molten salt methods to the production of hematite has been the development of reproducible control over the size, shape, and crystallinity of the resulting structures.[56] Though this need for reliable control explains our strong motivation for generating hematite rhombohedra, there are other fundamental reasons for doing so.

It has been found that the shape of a nanoparticle, which determines the exposed crystallographic surface (and its corresponding surface energy) enclosing the particle, can have a dramatic effect on its properties. As examples, the relative intensities of X-ray diffraction peaks, the positions of bands in optical spectra, and the magnitude of sublimation energies of a wide variety of materials, including Au and Ag_2S, are intrinsically coupled with particle morphology (such as icosahedra, cubes, and tetrahedra).[57-59] With hematite in particular, changes in microhardness, electrical conductivity (*i.e.*, mobility enhancement), as well as in superparamagnetic blocking behavior are strongly associated with its physical and structural characteristics.[48,60,61] As another relevant example of the significance of shape, for magnetic nanoparticles in particular, such as the Fe/Fe_3O_4 composite synthesized herein, shape anisotropy and crystalline anisotropy are expected to have a profound influence on their intrinsic magnetic properties (such as coercivity).[9] In fact, the magnetic anisotropy (*i.e.*, higher coercivity) present in rod-shaped magnetic particles, which by contrast is not observed in symmetrically-shaped spheres or cubes, has been exploited in the use of these acicular particles in commercial magnetic recording media.

In the experiments reported herein, we were able to generate distinctive structural polymorphs of hematite iron oxide from relatively polydisperse, commercially available starting precursor materials. We were subsequently able to transform these single-crystalline α-Fe_2O_3 rhombohedral structures into their magnetic nanocrystalline composite counterparts, Fe/Fe_3O_4. These samples were characterized by a number of techniques, including scanning electron microscopy (SEM), transmission electron

microscopy (TEM), high-resolution TEM (HRTEM), energy-dispersive X-ray spectroscopy (EDS), selected area electron diffraction (SAED), X-ray diffraction (XRD), and superconducting quantum interference device (SQUID) measurements.

5.2. Experimental Section

5.2.1. Materials and Preparation

Specifically, commercial iron(III) oxide or Fe_2O_3 (Aldrich, polydisperse nanopowder), NP-9 surfactant (Aldrich, polyoxyethylene(9)nonylphenyl ether), and NaCl (Mallinckrodt, sodium chloride) were used as supplied. The choice of the surfactant was governed by its prior versatility in the preparation of elongated structures of metal oxides, its relative non-toxicity, and comparative facility of use.[52] Stoichiometric amounts of Fe_2O_3, NaCl, and NP-9 were mixed (in molar ratios of 1 : 40 : 6, 2 : 40 : 6, 3 : 40 : 6, and 6 : 40 : 6, respectively, for the generation of varying structural motifs of hematite), thoroughly ground in an agate mortar, and subsequently sonicated.

In a typical synthesis of submicron-sized, single-crystalline α-Fe_2O_3 rhombohedra, 0.5 and 20 mmol of Fe_2O_3 and NaCl, respectively, were mixed thoroughly in an agate mortar. For elongated α-Fe_2O_3 structures, 1, 1.5, and 3 mmol of Fe_2O_3 along with 20 mmol of NaCl, respectively, were meticulously mixed, after which 2 ml of NP-9 was subsequently added. The resulting mixture was ground for at least 30 min prior to sonication for an additional 5 min. Identical procedures were employed for samples containing different molar ratios of initial precursors. The resulting mixture was then placed in a ceramic crucible, inserted into a quartz tube, heated at a ramp rate of 5^{o}C per min up to an annealing temperature at 820^{o}C for 3.5 h, and cooled thereafter to room temperature. As-prepared material was subsequently washed several times with distilled water, collected by centrifugation, and dried at 120^{o}C in a drying oven.

Hematite rhombohedra were converted to their magnetic analogues, *i.e.*, composites of Fe/Fe_3O_4, through a reduction reaction in a flowing gaseous mixture. Briefly, the as-prepared hematite product was heated in a tube furnace at 360 ^{o}C for 5 h under a continuous flow of 5 % H_2 in N_2. After the gas flow was stopped, the resulting product was subsequently heated to 240 ^{o}C for 2 h, cooled to room temperature, and then collected without further treatment.

5.3. Results and Discussion

5.3.1. Iron Oxide Rhombohedra

5.3.1.1. XRD measurements: purity and crystallinity of as-prepared α-Fe_2O_3 rhombohedra

The purity and crystallinity of as-prepared hematite (α-Fe_2O_3) structures were examined using powder XRD measurements (Figure 5.2). It is evident that the observed pattern of the collected powder displayed all of the expected peaks emanating from the α-Fe_2O_3 structure with very few, if any, impurity peaks. In effect, diffraction peaks in Figure 5.2A can be indexed to the rhombohedral structure of α-Fe_2O_3 (space group: $R\bar{3}c$) with structural parameters of $a = b = 5.038$ Å, $c = 13.772$ Å, $\alpha = \beta = 90^{\circ}$, and $\gamma = 120^{\circ}$, which are in good agreement with literature results (*i.e.*, JCPDS #33-0664, Figure 5.2B).

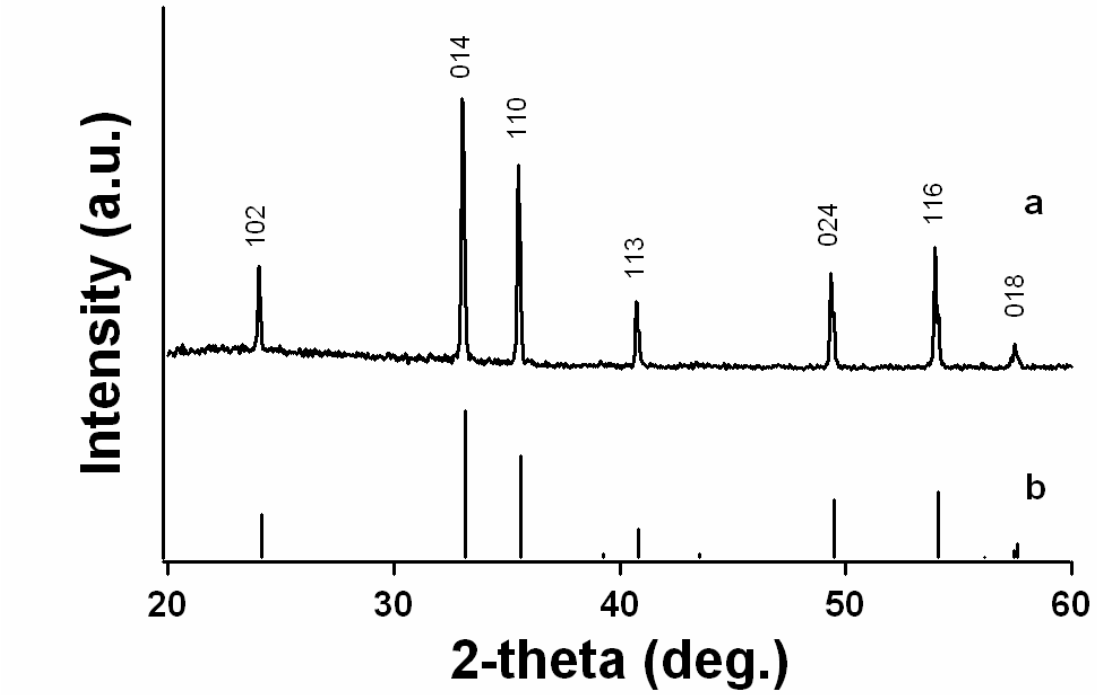

Figure 5.2. XRD patterns of as-prepared α-Fe_2O_3 rhombohedra particles (a), and of α-Fe_2O_3 from the JCPDS #33-0664 database standard (b). Reproduced from Park, T.-J. *et al*., *Chem. Mater.* **2005**, *18*, 5289.

5.3.1.2. TEM, HRTEM measurements: size, shape, chemical composition, and single-crystallinity of as-prepared α-Fe_2O_3 rhombohedra

A typical TEM image of α-Fe_2O_3 rhombohedra, generated from the current molten salt method with a 1 : 40 molar ratio of Fe_2O_3 to NaCl, is shown in Figure 5.3A. The size of the particles, which can be described in terms of the mean lengths of the shorter and longer diagonals of the rhombohedron, were measured to be 231 ± 40 and 198 ± 35 nm, respectively, with their aspect ratio calculated to be 1.2 on average. SAED data taken from an individual rhombohedral structure (Figure 5.3B) show the presence of sharp diffraction spots indicating the formation of well-developed, single-crystalline hematite particles. We note that the electron diffraction patterns obtained from different positions along the same rhombohedron as well as from different rhombohedra also show similar sharp diffraction spots. In order to confirm the chemical composition of the as-prepared structures, EDS spectra (Figure 5.3C) were taken at a number of selected positions of the sample. The elemental signatures obtained are identical within experimental accuracy, and essentially Fe and O were observed, as expected. The Cu and C signals arise from the TEM grid. In Figure 5.3D, a HRTEM image obtained from part of an individual α-Fe_2O_3 rhombohedron is displayed so as to further confirm the single-crystalline nature of our as-prepared structures. This image shows a typical crystalline domain with interplanar spacings of about 2.70 and 2.47 Å, which are comparable with the literature values of 2.700 and 2.519 Å, which correspond to the (014) and (110) planes of the hexagonal phases of the α-Fe_2O_3 rhombohedral crystal, respectively (JCPDS #33-0664).

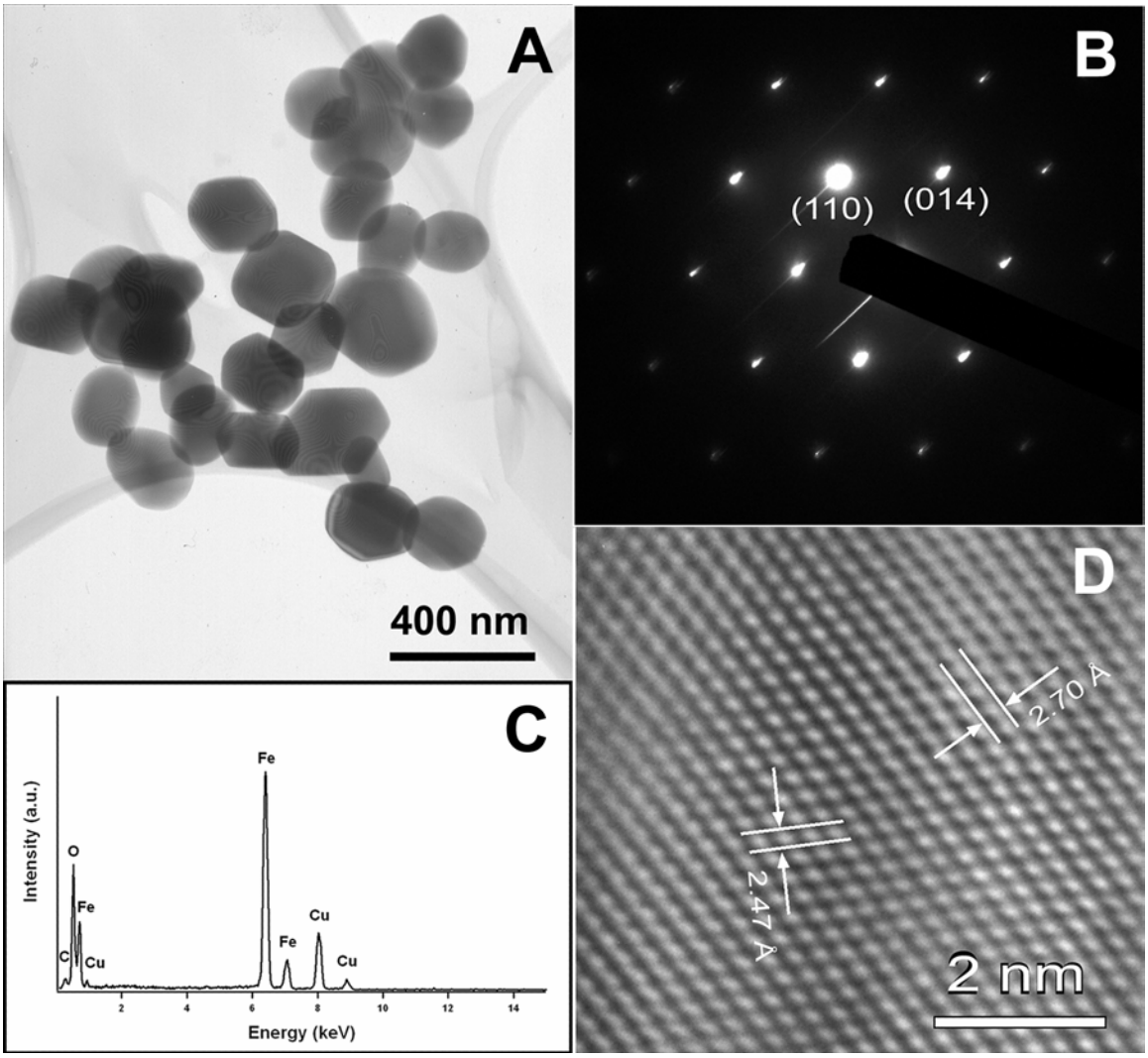

Figure 5.3. (A) TEM image of as-prepared α-Fe_2O_3 rhombohedra particles. (B) SAED pattern of an α-Fe_2O_3 rhombohedron. (C) EDS of an α-Fe_2O_3 rhombohedron. The Cu and C peaks originate from the TEM grid. (D) HRTEM image of a representative piece of an α-Fe_2O_3 rhombohedron. Reproduced from Park, T.-J. *et al*., *Chem. Mater.* **2005**, *18*, 5289.

5.3.1.3. SEM measurements: size, shape, chemical composition, and shape control of as-prepared α-Fe_2O_3 structures

Figure 5.4 shows SEM images revealing the morphologies of as-prepared α-Fe_2O_3 structures, generated from the as-described protocol. It can be observed that the α-Fe_2O_3 product, prepared using a molten salt method with a 1 : 40 molar ratio of Fe_2O_3 to NaCl, mainly consists of discrete rhombohedral structures with smooth surfaces (Figure 5.4A). The size of the particulates is consistent with that from the TEM data discussed above. It can also be observed that the faces of the α-Fe_2O_3 rhombohedra are essentially flat though some of the corners of these structures are slightly truncated.

To obtain further insight into the formation of different shapes of the α-Fe_2O_3 structures, the morphologies of α-Fe_2O_3 structures generated from the precursors, derived from 2 : 40 : 6, 3 : 40 : 6, and 6 : 40 : 6 (Fe_2O_3 : NaCl : NP-9) molar ratios, are shown in Figure 5.4B, 5.4C, and 5.4D, respectively. It can be observed that the shapes of α-Fe_2O_3 structures alter from their rhombohedral motifs into peanut-shaped structures. Moreover, the aspect ratio of these materials increases nonlinearly with higher molar ratios of Fe_2O_3 precursor to surfactant content in the system. In fact, for these molar ratios, the mean lengths of elongated α-Fe_2O_3 peanut-like structures are 1092 ± 389 (B), 1050 ± 183 (C), and 1611 ± 565 nm (D), respectively, and their mean widths (shorter side of each structure) measure 591 ± 108 (B), 329 ± 47 (C), and 476 ± 77 nm (D), respectively. Hence, their corresponding aspect ratios are 1.9, 3.3, and 3.5 for (B), (C), and (D), respectively. The aspect ratio of 3.5, observed for the product in Figure 5.4D is relatively smaller than expected. This value reflects the large degree of branching and higher overall polydispersity in the resultant iron oxide structures with increasing molar content of Fe_2O_3 and suggests the presence of numerous nucleation sites on the growing particles. Histograms of particle size (including lengths and widths) distributions for as-prepared hematite samples are shown in both Figure 5.5 and 5.6.

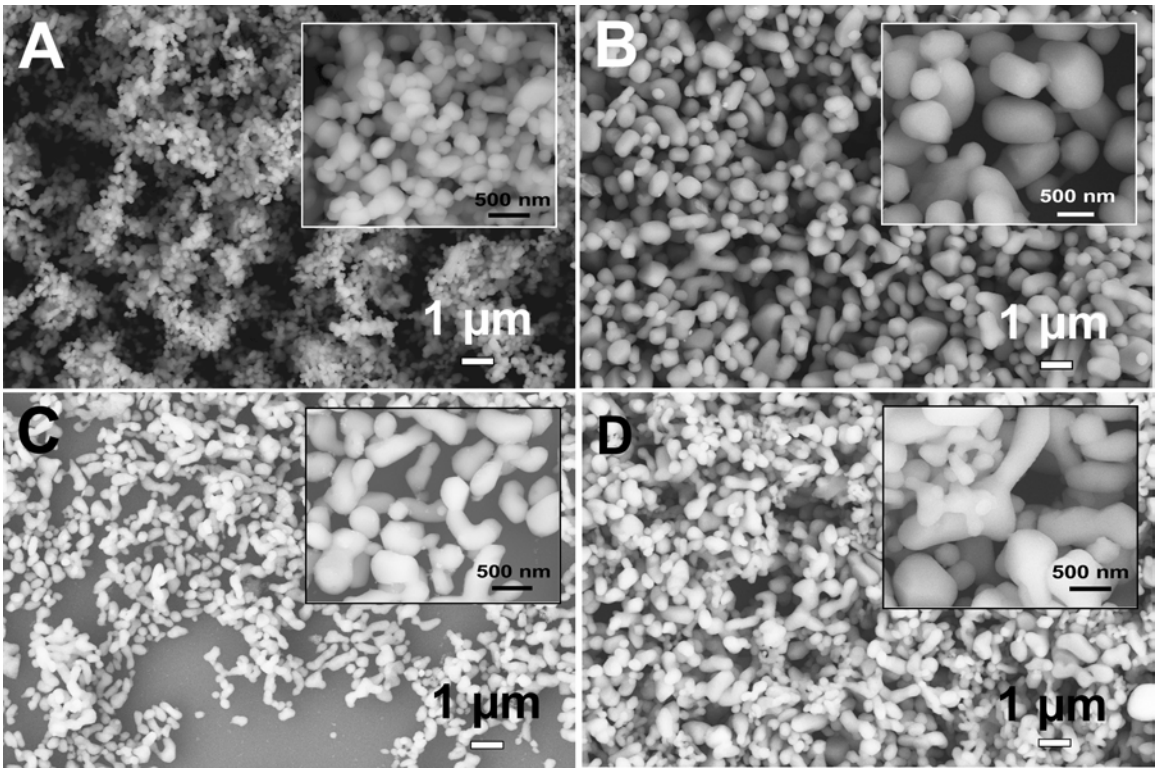

Figure 5.4. SEM images of α-Fe_2O_3 structures prepared using a molten salt method with 1 : 40 (A), 2 : 40 (B), 3 : 40 (C), and 6 : 40 (D) molar ratios of Fe_2O_3 to NaCl precursors, respectively. For the purpose of shape control, precursors in (B), (C), and (D) were added to 2 ml of NP-9, a nonionic surfactant. Insets show higher-magnification images of individual hematite particles. Reproduced from Park, T.-J. *et al*., *Chem. Mater.* **2005**, *18*, 5289.

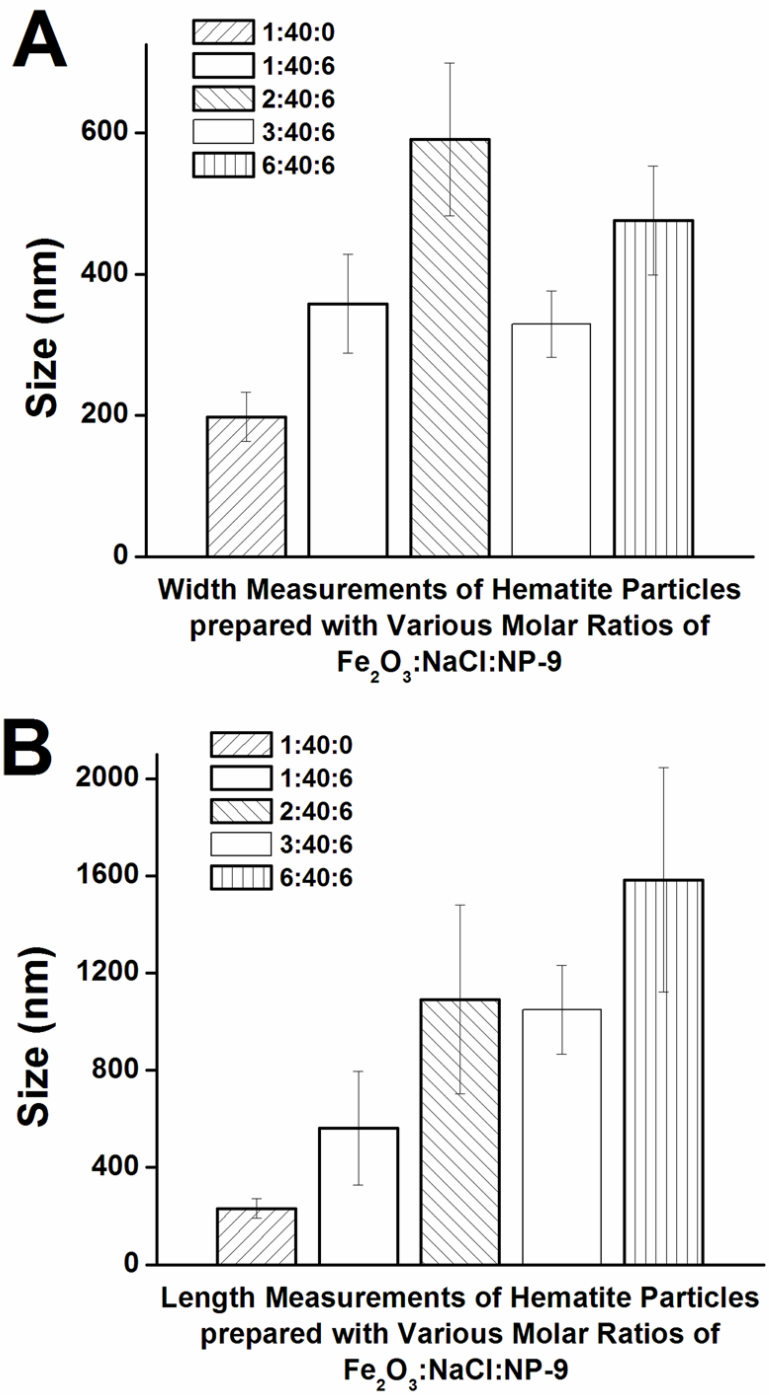

Figure 5.5. Histograms of size distributions of as-prepared hematite structures. Parameters for each structure are given in terms of width (A) and length (B). Molar ratios of reagents are given in the following order – Fe_2O_3 : NaCl : NP-9 surfactant. Reproduced from Park, T.-J. *et al*., *Chem. Mater.* **2005**, *18*, 5289.

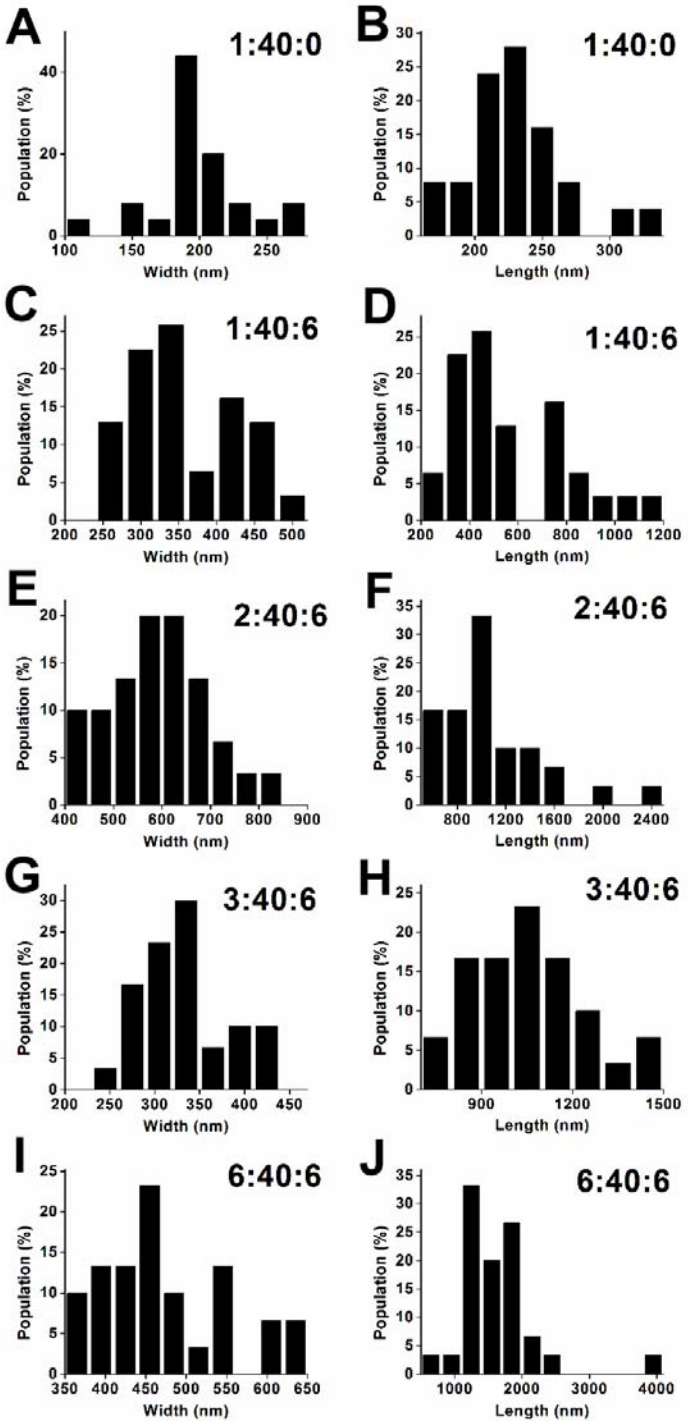

Figure 5.6. Histograms of size (widths and lengths, respectively) distributions for as-prepared hematite particles derived from commercial precursors. Molar ratios of Fe_2O_3 : NaCl : NP-9 surfactant are 1 : 40 : 0 for (A) and (B); 1 : 40 : 6 for (C) and (D); 2 : 40 : 6 for (E) and (F); 3 : 40 : 6 for (G) and (H); and 6 : 40 : 6 for (I) and (J). Reproduced from Park, T.-J. *et al*., *Chem. Mater.* **2005**, *18*, 5289.

5.3.1.4. Role of surfactant, salt, and molar ratio of precursors

To analyze the role of surfactant in this reaction, α-Fe_2O_3 products were prepared employing identical, as-reported experimental procedures in the absence of any surfactant. The morphologies of the resultant products generated from mixtures of (a) 3 : 40 and (b) 6 : 40 molar ratios of Fe_2O_3 to NaCl precursors, respectively, are shown in Figure 5.7. It is evident that all of these particles possess morphologies as well as size distributions that are consistent with the product, prepared with a molar ratio of Fe_2O_3 to NaCl precursors of 1 : 40 (Figure 5.4A and 5.5). Hence, it is apparent that the surfactant, through its dispersing ability, can play a critical role adjusting the size and shape of these binary metal oxide particles. In fact, samples prepared from identical precursor ratios with and without surfactant suggest that the presence of surfactant will cause an elongation of the resulting products and skew their size distribution, as noted in Figure 5.5. For instance, SEM images of hematite prepared from a mixture of a 1 : 40 molar ratio of Fe_2O_3 to NaCl in the presence of NP-9 are shown in Figure 5.8; they are evidently more polydisperse in terms of size and shape. In fact, SEM measurements indicate that hematite particles prepared from a molar ratio of Fe_2O_3 : NaCl : NP-9 equal to 1 : 40 : 6 possess mean widths of 358 (± 70) nm and mean lengths of 562 (± 235) nm, with a measured aspect ratio of 1.6. Nevertheless, the single-crystalline nature of all of these surfactant-treated hematite particles (Figure 5.4C and 5.4D) has been confirmed; associated TEM and SAED images are shown in Figure 5.9.

The observations described above confirm the significant role of the surfactant combined with other experimental parameters, such as the molar ratios of precursors and the addition of salt, to collectively yield single-crystalline α-Fe_2O_3 products with predictive control of size and shape. The presence of salt is expected to decrease the overall reaction temperature.[62] The liquid-like phase of the molten flux is expected to increase the mobility of its constituent components.

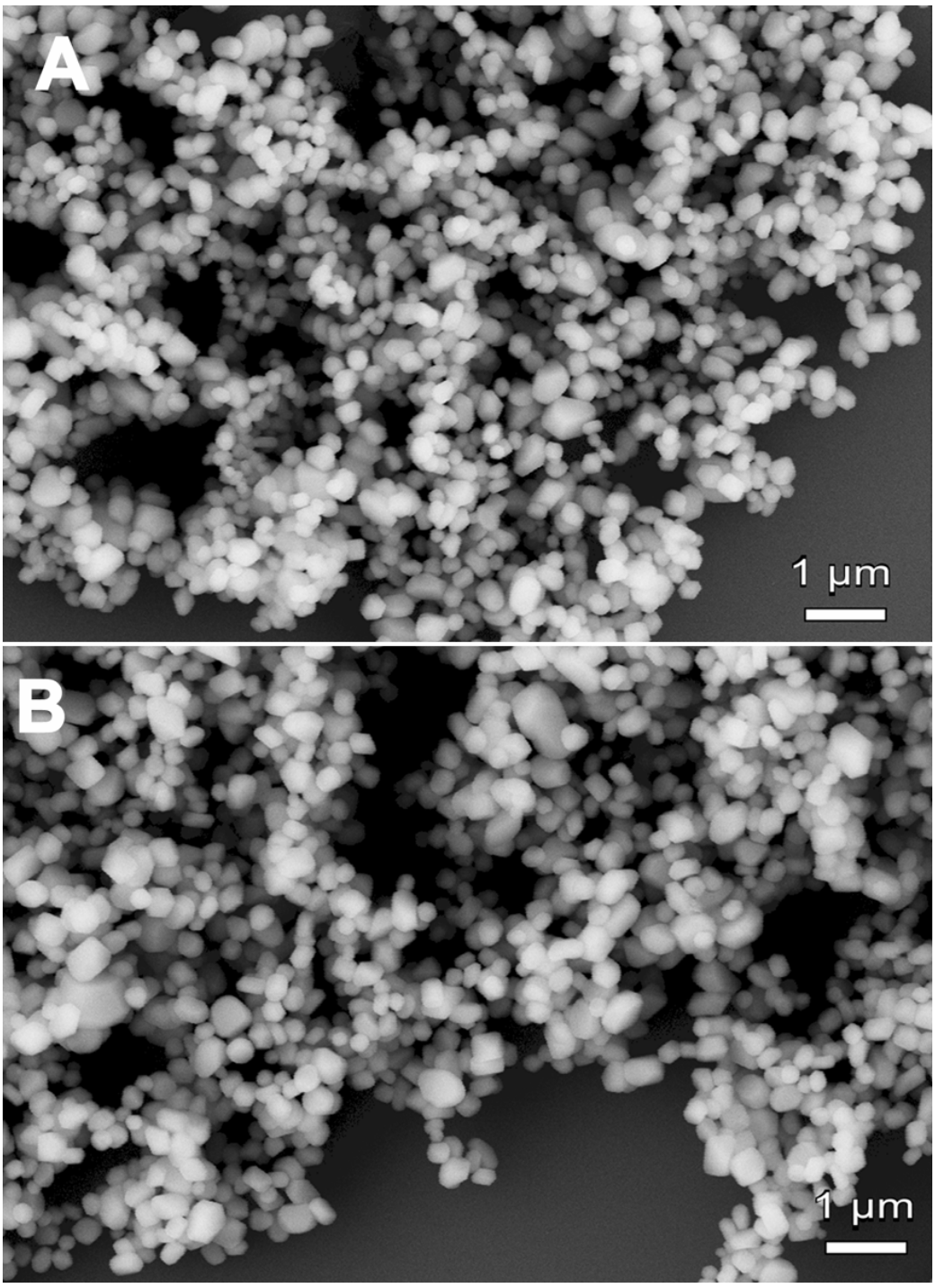

Figure 5.7. SEM images of α-Fe_2O_3 structures prepared from molar ratios of 3 : 40 (A), and 6 : 40 (B) of Fe_2O_3 : NaCl precursors, without the presence of surfactant. Reproduced from Park, T.-J. *et al*., *Chem. Mater.* **2005**, *18*, 5289.

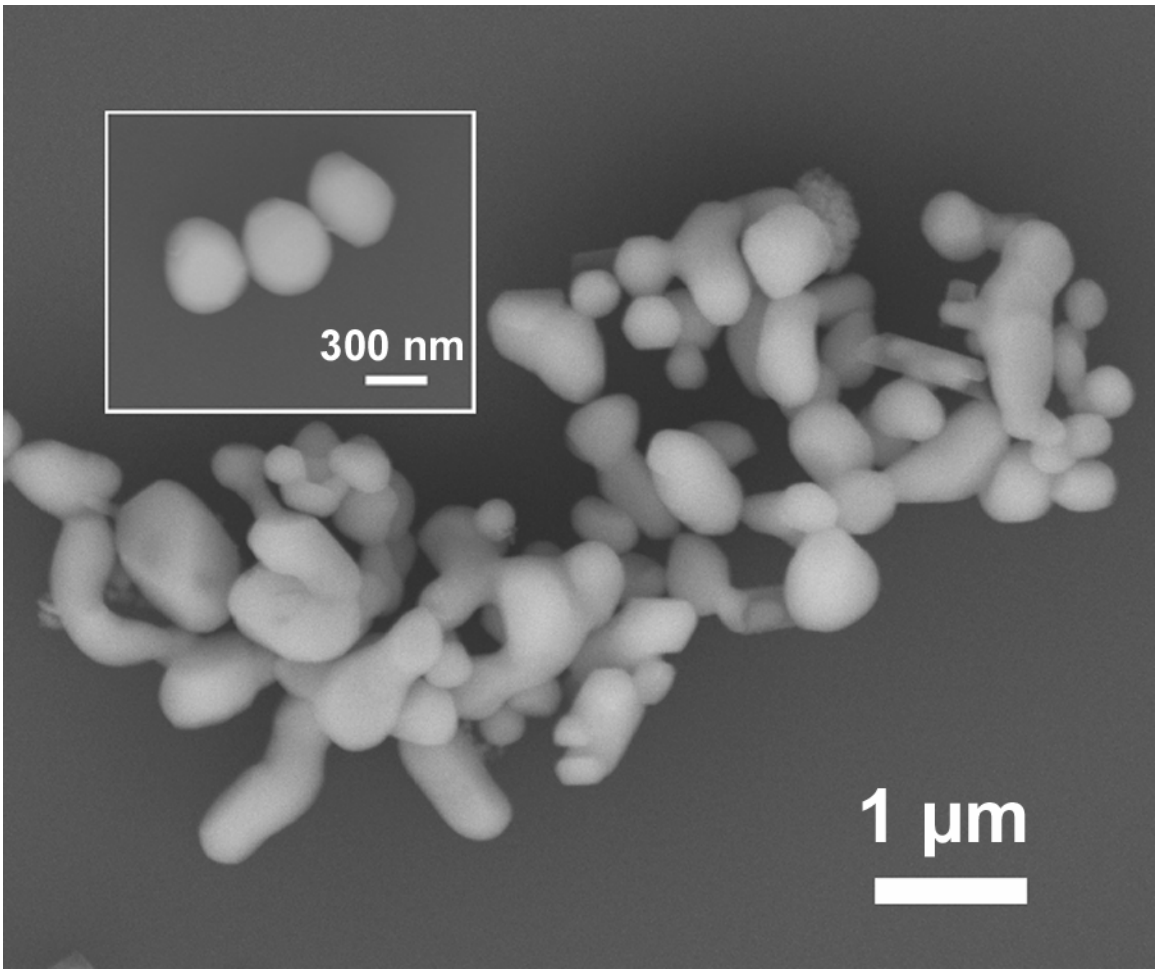

Figure 5.8. SEM image of α-Fe_2O_3 structures prepared from a molar ratio of 1 : 40 : 6 of Fe_2O_3 : NaCl : NP-9 precursors. Inset shows a higher magnification image of the product. Reproduced from Park, T.-J. *et al*., *Chem. Mater.* **2005**, *18*, 5289.

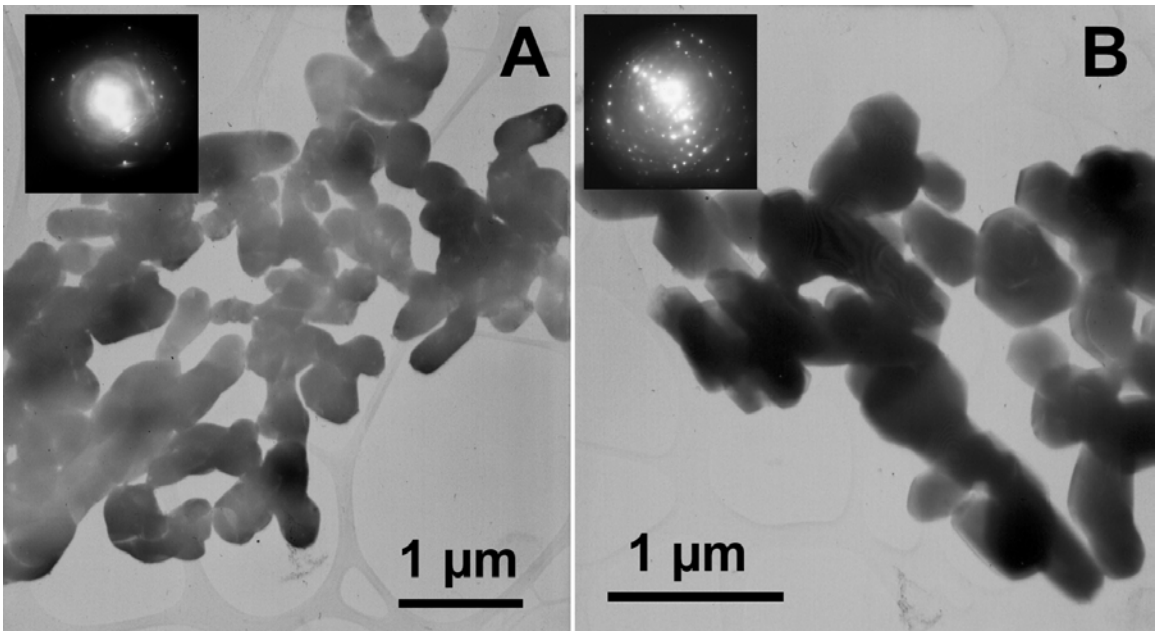

Figure 5.9. TEM images of α-Fe_2O_3 structures prepared from molar ratios of 3 : 40 (A), and 6 : 40 (B) of Fe_2O_3 : NaCl precursors, in the presence of NP-9 surfactant. Insets show representative selected area electron diffraction (SAED) images. Reproduced from Park, T.-J. *et al*., *Chem. Mater.* **2005**, *18*, 5289.

5.3.2. Fe/Fe_3O_4 nanocomposites

5.3.2.1. Size, shape, purity, and crystallinity of as-transformed Fe/Fe_3O_4 nanocomposite rhombohedra

The morphologies of the resulting Fe/Fe_3O_4 composites generated from the reduction reaction are shown in Figure 5.10A and 5.10B. It can be observed that the size distribution and shape of the resulting iron/magnetite composites are similar to those of their corresponding hematite precursors. We note that as-generated Fe/Fe_3O_4 structures possess somewhat roughened surfaces composed of multiple domains of iron and iron oxide (Figure 5.10C). We hypothesize that this morphological alteration can be attributed not only to differential rates of reduction with respect to the surface and bulk of the initial nanoparticle starting materials but also to the *in situ* formation of domains of elemental iron and magnetite. In fact, XRD data on the resulting composites of Fe and Fe_3O_4, derived from hematite precursors, in Figure 5.10D, display all of the expected peaks, in good agreement with literature results (Fe, JCPDS #06-0696; Fe_3O_4, JCPDS #19-0629), and confirm the expected chemical composition of the resulting composite Fe/Fe_3O_4 structure.

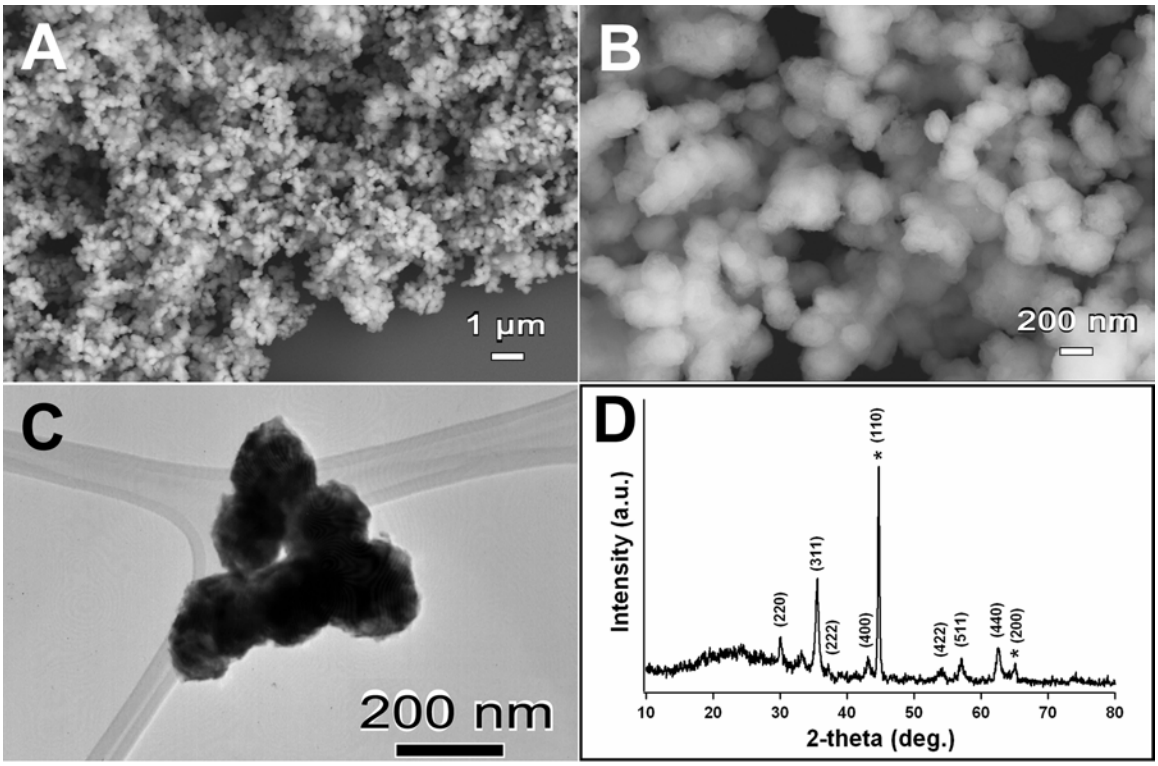

Figure 5.10. (A) A lower and (B) correspondingly higher magnification SEM image of as-transformed magnetic composites of Fe/Fe_3O_4. (C) TEM image of a cluster of individual Fe/Fe_3O_4 structures. (D) XRD pattern of as-transformed Fe/Fe_3O_4 structures. Asterisks indicate XRD peaks from Fe. Reproduced from Park, T.-J. *et al*., *Chem. Mater.* **2005**, *18*, 5289.

5.3.2.2. Chemical composition, crystallinity, and lattice spacings of as-transformed Fe/Fe_3O_4 nanocomposite rhombohedra

In order to further confirm the composition of our as-transformed magnetic materials, HRTEM has been performed on an individual Fe/Fe_3O_4 composite shown in Figure 5.11A. The SAED data taken of an individual rhombohedral structure (shown in the inset) show the presence of sharp diffraction spots and rings that could be assigned to that of Fe_3O_4. However, we note that the expected lattice spacing (2.0268 Å) of the {110} planes of Fe is very similar to the analogous lattice spacing (2.0993 Å) of the {400} planes of Fe_3O_4 and hence, these two distances are difficult to clearly differentiate between in the SAED pattern. Nevertheless, the electron diffraction patterns obtained from different areas of the composite structure also show similar results.

The higher magnification image of a typical Fe/Fe_3O_4 composite reveals that the surface of the rhombohedron is composed of multiple nanostructures with mean sizes of 11 ± 3 nm (Figure 5.11B). The nanostructures themselves are composed of multiple adjacent, discrete domain regions of Fe and Fe_3O_4 (Figure 5.11C). In Figure 5.11D, a HRTEM image obtained from a portion of an individual Fe/Fe_3O_4 composite is displayed so as to further confirm the single-crystalline nature of each individual domain of Fe and Fe_3O_4. This image shows a typical crystalline domain with an interplanar spacing of about 2.58 Å, comparable with the literature value of 2.532 Å, which corresponds to the {311} planes of the cubic phase of a Fe_3O_4 crystal (JCPDS #19-0629). In order to confirm the chemical composition of the as-prepared structures, EDS spectra (Figure 5.11E) were taken at a number of selected positions along the sample. The elemental signatures obtained are identical within experimental accuracy, and essentially only Fe and O were observed, as expected. We note that the relative intensity of oxygen for the Fe/Fe_3O_4 composite (Figure 5.11E) decreased slightly as compared with the data for the hematite precursor alone (Figure 5.11C), suggestive of a lowered oxygen density in the resulting composite structure, an observation consistent with a reduction reaction having occurred. The Cu and C signals arise from the TEM grid.

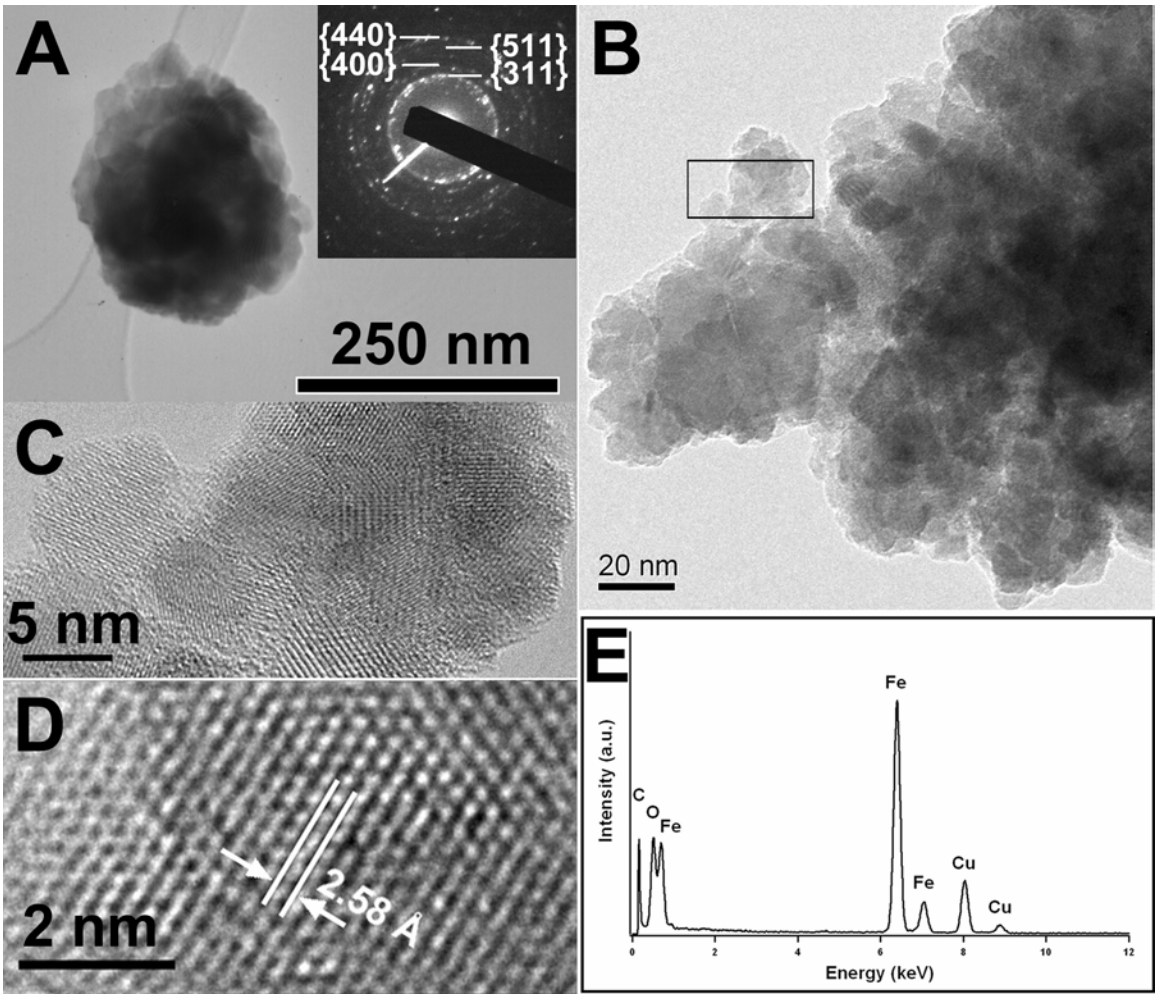

Figure 5.11. (A) TEM image of a typical individual magnetic composite of iron and magnetite. Inset shows the corresponding SAED pattern of a Fe/Fe_3O_4 rhombohedron. (B) A higher magnification image of the composite of Fe/Fe_3O_4. (C) An enlarged portion of the assembled nanostructure of Fe and Fe_3O_4, as delineated by the black square in (B). (D) A HRTEM image of a typical lattice spacing of a Fe_3O_4 structure. (E) An EDS spectrum obtained from an individual Fe/Fe_3O_4 rhombohedron. The Cu and C peaks originate from the TEM grid. Reproduced from Park, T.-J. *et al*., *Chem. Mater.* **2005**, *18*, 5289.

5.3.2.3. SQUID measurements: magnetic properties of as-transformed Fe/Fe_3O_4 nanocomposite rhombohedra

Figure 5.12A shows the presence of a hysteresis loop at room temperature of the resultant nanocrystalline Fe/Fe_3O_4 composite magnetic material, revealing strong ferromagnetic behavior. These nanocomposites consist of magnetically harder and softer phases where there is some degree of magnetic exchange coupling between the Fe and magnetite domains. The magnetization curve shows a steep increase in magnetization with increasing field. The asymmetric shape of the hysteresis loop conveys two-phase behavior, implying that the dimension of the soft phase is smaller than that of the hard phase and that, furthermore, in this nanocomposite, the hard and soft phases are not able to completely switch cooperatively. Moreover, the kink at low field is related to the magnetization reversal of the soft magnetic phase, likely magnetite in this case.[19] The saturation magnetization (M_S: ~100 emu/g) measured for the Fe/Fe_3O_4 composite is about 20 % higher than that for the magnetite phase and about 66 % higher than the value of 60.1 emu/g observed for 11.5 nm-sized magnetite nanoparticles.[21,63,64] The additional 66 % increase in M_S is consistent with and can be attributed to the presence of an extra 67 % amount of Fe (as deduced from XRD analysis) in Fe/Fe_3O_4 nanocomposites. The structural inhomogeneity of the samples has a strong influence on the M_S value measured. In addition, the relatively high coercivity observed (H_C: 250 Oe) indicates the potential applicability of these nanoscale composite magnetic structures as low-cost hard magnetic materials. Our results are also comparable with data recently reported for similar structural analogues, having important applications in biomedical fields such as biomolecular separations, targeted drug delivery, cancer diagnosis and treatment, as well as magnetic resonance imaging.[24,65]

Figure 5.12B shows the magnetic susceptibility of these nanoscale composites as a function of temperature at an applied field strength of 200 Oe, after zero field cooling (ZFC) and also, with field cooling (FC). The curves show the presence of the Verwey transition[66] at a temperature of ~135 K, which is indicative of magnetite, arising from the ordering among Fe^{3+} and Fe^{2+} ions. The relatively higher Verwey transition temperature observed relative to that of pristine magnetite (~120 K) is consistent with values recently reported for similar Fe/Fe_3O_4 composite systems,[18] and can be ascribed to the higher Fe content relative to that of Fe_3O_4. Hence, these results imply the potential usage of these materials in applications ranging from nanocomposite conductors to superconductors.[18]

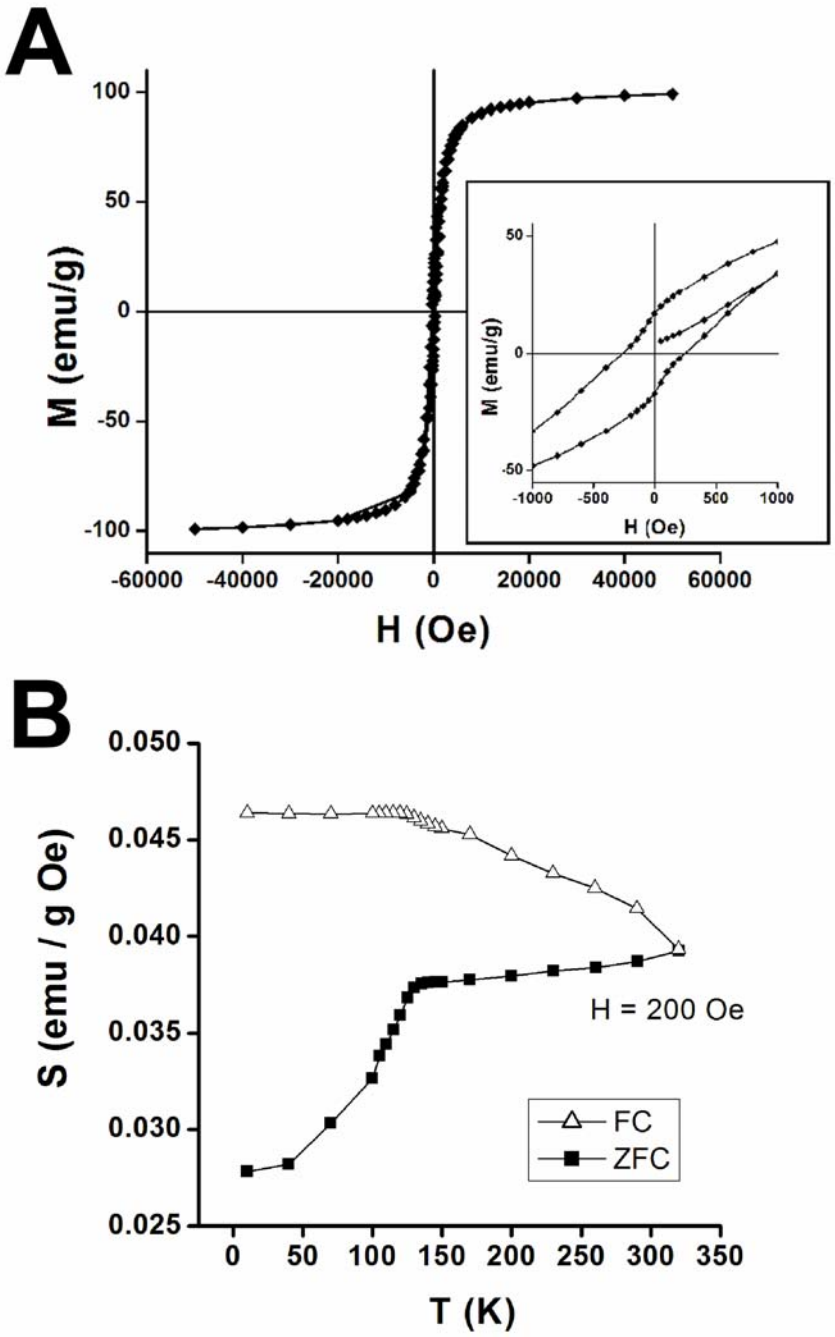

Figure 5.12. (A) Hysteresis loop at room temperature of as-transformed Fe/Fe_3O_4 composites. Inset shows the enlarged portion of the hysteresis loop revealing the coercivity of the Fe/Fe_3O_4 composite. (B) Temperature dependence of the magnetic susceptibility for Fe/Fe_3O_4 composite, showing zero field cooling (ZFC, closed circle) and field cooling (FC, closed square) curves, with an applied magnetic field set at 200 Oe. Reproduced from Park, T.-J. *et al*., *Chem. Mater.* **2005**, *18*, 5289.

For further comparison of their morphology as well as magnetic properties, SEM images and *M*/*T* curves of rhombohedra of the α-Fe_2O_3 structure and the Fe/Fe_3O_4 composite are shown, respectively, in Figure 5.13. It is clear that that the size distribution, shape, and crystallinity (see the insets) of the resulting iron/magnetite composites (B) are similar to those of their corresponding α-Fe_2O_3 rhombohedra (A) precursors. In addition, both of their intrinsic magnetic transitions, *e.g.*, the Morin transition (252 K) for α-Fe_2O_3 and the Verwey transition (135 K) for Fe/Fe_3O_4, deviate from that of bulk α-Fe_2O_3 (264 K[67,68]) and Fe_3O_4 (120 K[66]), respectively, in their *M*/*T* curves. Thus, this observation further highlights that both size as well as shape effect, at the nanoscale collectively alter the properties of our as-prepared iron oxide nanostuctures, as compared with that of the bulk.

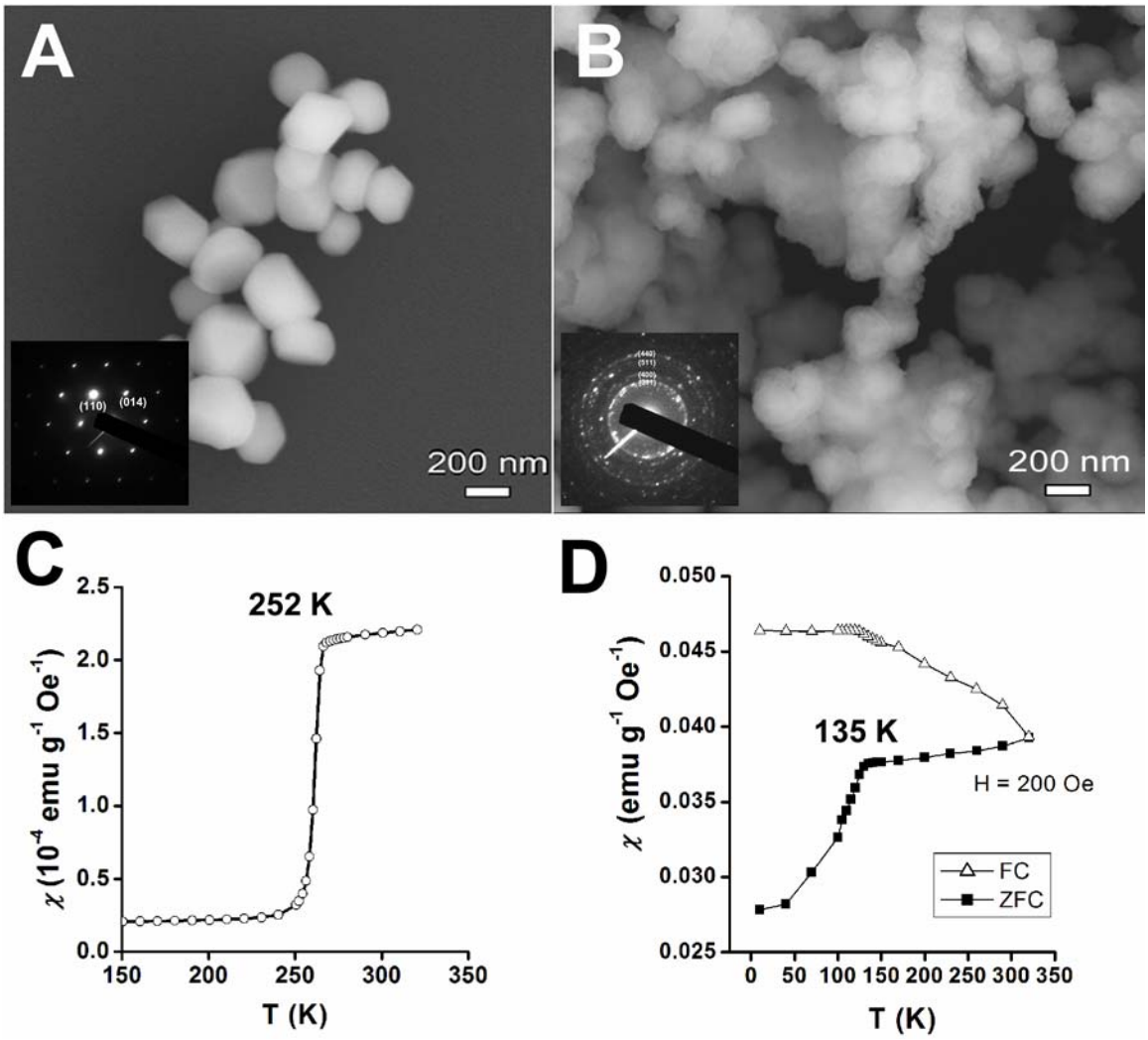

Figure 5.13. Comparative SEM images of α-Fe_2O_3 rhombohedra (A) and of the magnetic nanocomposites of Fe and Fe_3O_4 (B). In addition, comparative *M*/*T* curves of α-Fe_2O_3 rhombohedra (C) and of the magnetic nanocomposites of Fe and Fe_3O_4 (D) are shown as well. Reproduced from Park, T.-J. *et al*., *Chem. Mater.* **2005**, *18*, 5289.

5.4. Conclusions

The current work demonstrates the generation of monodisperse assemblies of rhombohedral nanocrystalline composites of Fe and Fe_3O_4 formed from a reordering of the microstructure of single-crystalline hematite rhombohedra precursors which occurred as a product of the reduction reaction in a gaseous mixture of 5 % H_2 in N_2. The main significance of the work is that we were able to create a nanocomposite with hard and soft magnetic phases juxtaposed within one discrete, anisotropic structure. Nonetheless, this work is also relevant for other important reasons.

First, we have demonstrated our ability to prepare monodisperse hematite products with controlled size, shape, and monodispersity, starting from relatively inexpensive, commercially available polydisperse, polycrystalline or amorphous precursors. Single-crystalline, monodisperse nanoscale α-Fe_2O_3 rhombohedra, as well as elongated motifs of these materials, are in fact an excellent model system to demonstrate this synthetic principle. This methodology allows for control over size, shape, and chemical composition of our as-prepared products using a simple, versatile, one-step, environmentally-friendly, and large-scale solid-state chemical reaction in the presence of NaCl and a nonionic surfactant.

Secondly, rhombohedra represent a high-surface-area, anisotropic formulation of an industrially important material (iron oxide) which is an active component of gas sensors, photocatalysts, and other types of catalytic materials. Thirdly, α-Fe_2O_3 hematite rhombohedra present themselves as a practical, low-cost chemical precursor material to the subsequent synthesis of magnetite. As previously alluded to, the development of a facile and economically viable synthetic strategy for the synthesis of hydrophilic, biocompatible magnetic particles (including magnetite) would benefit their technical use in biomedical fields, such as biomolecular separations, targeted drug delivery, tags for sensing and imaging, antitumor therapy, as well as magnetic resonance imaging.

The resulting Fe/Fe_3O_4 as well as α-Fe_2O_3 structures have been extensively characterized using a variety of microscopy, diffraction, spectroscopy, and SQUID results. As mentioned, nanostructured magnetic materials, such as the composite described herein, also have potential applications as ferrofluids, catalysts, colored pigments, and high-density magnetic recording media.[65] Hence, future research will focus on measurements (such as gas sensitivity, catalytic activity, and conductivity) of these as-generated structures to determine the net effect of shape and size on these intrinsic properties.

5.5. References

(1) Alivisatos, A. P. *Science* **1996**, *271*, 933.
(2) Ahmadi, T. S.; Wang, Z. L.; Green, T. C.; Henglein, A.; El-Sayed, M. A. *Science* **1996**, *272*, 1924.
(3) Cui, Y.; Lieber, C., M. *Science* **2001**, *291*, 851.
(4) Sun, Y.; Xia, Y. *Science* **2002**, *298*, 2176.
(5) Sun, S.; Murray, C. B.; Weller, D.; Folks, L.; Moser, A. *Science* **2000**, *287*, 1989.
(6) Bruchez, M.; Moronne, M.; Gin, P.; Weiss, S.; Alivisatos, A. P. *Science* **1998**, *281*, 2013.
(7) Wang, J.; Gudiksen, M. S.; Duan, X.; Cui, Y.; Lieber, C., M. *Science* **2001**, *293*, 1455.
(8) Xia, Y.; Yang, P.; Sun, Y.; Wu, Y.; Mayers, B.; Gates, B.; Yin, Y.; Kim, F.; Yan, H. *Adv. Mater.* **2003**, *15*, 353.
(9) Hyeon, T. *Chem. Commun.* **2003**, 927.
(10) Yang, H. G.; Zeng, H. C. *J. Am. Chem. Soc.* **2005**, *127*, 270.
(11) Park, J.; Lee, E.; Hwang, N.-M.; Kang, M.; Kim, S. C.; Hwang, Y.; Park, J.-G.; Noh, H.-J.; Kim, J.-Y.; Park, J.-H.; Hyeon, T. *Angew. Chem. Int. Ed.* **2005**, *44*, 2.
(12) Liu, Z.; Zhang, D.; Han, S.; Li, C.; Lei, B.; Lu, W.; Fang, J.; Zhou, C. *J. Am. Chem. Soc.* **2005**, *127*, 6.
(13) Kim, B.-S.; Qiu, J.-M.; Wang, J.-P.; Taton, T. A. *Nano Lett.* **2005**, *5*, 1987.
(14) Zhang, D.-F.; Sun, L.-D.; Jia, C.-J.; Yan, Z.-G.; You, L.-P.; Yan, C.-H. *J. Am. Chem. Soc.* **2005**, *127*, 13492.
(15) Tzitzios, V.; Niarchos, D.; Hadjipanayis, G.; Devlin, E.; Petridis, D. *Adv. Mater.* **2005**, *17*, 2188.
(16) Zeng, H.; Li, J.; Wang, Z. L.; Liu, J. P.; Sun, S. *Nano Lett.* **2004**, *4*, 187.
(17) Teng, X.; Yang, H. *J. Am. Chem. Soc.* **2003**, *125*, 14559.
(18) Yang, J. B.; Malik, S. K.; Zhou, X. D.; Kim, M. S.; Yelon, W. B.; James, W. J.; Anderson, H. U. *J. Phys. D: Appl. Phys.* **2005**, *38*, 1215.
(19) Zeng, H.; Li, J.; Liu, J. P.; Wang, Z. L.; Sun, S. *Nature* **2002**, *420*, 395.
(20) Bonetti, E.; Del Bianco, L.; Signoretti, S.; Tiberto, P. *J. Appl. Phys.* **2001**, *89*, 1806.
(21) Ding, J.; Miao, W. F.; Street, R.; McCormick, P. G. *Scr. Mater.* **1996**, *35*, 1307.
(22) Moura, F. C. C.; Araujo, M. H.; Costa, R. C. C.; Fabris, J. D.; Ardisson, J. D.; Macedo, W. A. A.; Lago, R. M. *Chemosphere* **2005**, *60*, 1118.
(23) Wang, H.; Zhang, X.; Liu, B.; Zhao, H.; Li, Y.; Huang, Y.; Du, Z. *Chem. Lett.* **2005**, *34*, 184.
(24) Zhao, W.; Gu, J.; Zhang, L.; Chen, H.; Shi, J. *J. Am. Chem. Soc.* **2005**, *127*, 8916.
(25) Jia, C.-J.; Sun, L.-D.; Yan, Z.-G.; You, L.-P.; Luo, F.; Han, X.-D.; Pang, Y.-C.; Zhang, Z.; Yan, C.-H. *Angew. Chem. Int. Ed.* **2005**, *44*, 4328.

(26) Ohmori, M.; Matijevic, E. *J. Colloid. Interface Sci.* **1993**, *160*, 288.
(27) Brahma, P.; Banerjee, S.; Das, D.; Mukhopadhyay, P. K.; Chatterjee, S.; Nigam, A. K.; Chakravorty, D. *J. Magn. Magn. Mater.* **2002**, *246*, 162.
(28) Brown, D. A.; Sherriff, B. L.; Sawicki, J. A. *Geochimica et Cosmochimica Acta* **1997**, *61*, 3341.
(29) Chen, J.; Xu, L.; Li, W.; Gou, X. *Adv. Mater.* **2005**, *17*, 582.
(30) Gondal, M. A.; Hameed, A.; Yamani, Z. H.; Suwaiyan, A. *Chem. Phys. Lett.* **2004**, *385*, 111.
(31) Ohmori, T.; Takahashi, H.; Mametsuka, H.; Suzuki, E. *Phys. Chem. Chem. Phys.* **2000**, *2*, 3519.
(32) Matijevic, E. *Chem. Mater.* **1993**, *5*, 412.
(33) Ocana, M.; Rodriguez-Clemente, R.; Serna, C. J. *Adv. Mater.* **1995**, *7*, 212.
(34) Wong, S. S.; Brus, L. E. *J. Phys. Chem. B* **2001**, *105*, 599.
(35) Frandsen, C.; Morup, S. *Phys. Rev. Lett.* **2005**, *94*, 027202.
(36) Jin, J.; Ohkoshi, S.-i.; Hashimoto, K. *Adv. Mater.* **2004**, *16*, 48.
(37) Woo, K.; Lee, H. J.; Ahn, J.-P.; Park, Y. S. *Adv. Mater.* **2003**, *15*, 1761.
(38) Dong, W.; Zhu, C. *J. Mater. Chem.* **2002**, *12*, 1676.
(39) Sugimoto, T.; Wang, Y.; Itoh, H.; Muramatsu, A. *Colloids Surf. A* **1998**, *134*, 265.
(40) Jing, Z.; Han, D.; Wu, S. *Mater. Lett.* **2005**, *59*, 804.
(41) Wang, X.; Chen, X.; Gao, L.; Zheng, H.; Ji, M.; Tang, C.; Shen, T.; Zhang, Z. *J. Mater. Chem.* **2004**, *14*, 905.
(42) Jones, F.; Ogden, M. I.; Oliveira, A.; Parkinson, G. M.; Richmond, W. R. *CrystEngComm* **2003**, *5*, 159.
(43) Raming, T. P.; Winnubst, A. J. A.; van Kats, C. M.; Philipse, A. P. *J. Colloid Interface Sci.* **2002**, *249*, 346.
(44) Chen, L. X.; Liu, T.; Thurnauer, M. C.; Csencsits, R.; Rajh, T. *J. Phys. Chem. B* **2002**, *106*, 8539.
(45) Hansen, M. F.; Koch, C. B.; Morup, S. *Phys. Rev. B* **2000**, *62*, 1124.
(46) Zboril, R.; Mashlan, M.; Barcova, K.; Vujtek, M. *Hyp. Interact.* **2002**, *139/140*, 597.
(47) Xu, X. N.; Wolfus, Y.; Shaulov, A.; Yeshurun, Y.; Felner, I.; Nowik, I.; Kotypin, Y.; Gedanken, A. *J. Appl. Phys.* **2002**, *91*, 4611.
(48) Zysler, R. D.; Vasquez-Mansilla, M.; Arciprete, C.; Dimitrijewits, M.; Rodriguez-Sierra, D.; Saragovi, C. *J. Magn. Magn. Mater.* **2001**, *224*, 39.
(49) Shen, X.-P.; Liu, H.-J.; Pan, L.; Chen, K.-M.; Hong, J.-M.; Xu, Z. *Chem. Lett.* **2004**, *33*, 1128.
(50) Fu, Y. Y.; Wang, R. M.; Xu, J.; Chen, J.; Yan, Y.; Narlikar, A. V.; Zhang, H. *Chem. Phys. Lett.* **2003**, *379*, 373.
(51) Park, T.-J.; Mao, Y.; Wong, S. S. *Chem. Commun.* **2004**, 2078.
(52) Park, T.-J.; Papaefthymiou, G. C.; Moodenbaugh, A. R.; Mao, Y.; Wong, S. S. *J.*

Mater. Chem. **2005**, *15*, 2099.
(53) Mao, Y.; Banerjee, S.; Wong, S. S. *J. Am. Chem. Soc.* **2003**, *125*, 15718.
(54) Mao, Y.; Wong, S. S. *J. Am. Chem. Soc.* **2004**, *126*, 15245.
(55) Mao, Y.; Park, T.-J.; Wong, S. S. *Chem. Commun.* **2005**, 5721.
(56) Zboril, R.; Mashlan, M.; Petridis, D. *Chem. Mater.* **2002**, *14*, 969.
(57) Kim, F.; Connor, S.; Song, H.; Kuykendall, T.; Yang, P. *Angew. Chem. Int. Ed.* **2004**, *43*, 3673.
(58) Lim, W. P.; Zhang, Z.; Low, H. Y.; Chin, W. S. *Angew. Chem. Int. Ed.* **2004**, *43*, 5685.
(59) Tanigaki, T.; Suzuki, H.; Kimura, Y.; Kaito, C.; Saito, Y. *Surf. Rev. Lett.* **2003**, *10*, 455.
(60) Stevenson, M. E.; Kaji, M.; Bradt, R. C. *J. Eur. Ceram. Soc.* **2002**, *22*, 1137.
(61) Miller, E. L.; Paluselli, D.; Marsen, B.; Rocheleau, R. E. *Thin Solid Films* **2004**, *466*, 307.
(62) Wiley, J. B.; Kaner, R. B. *Science* **1992**, *255*, 1093.
(63) Maruyama, T.; Shinyashiki, Y. *Thin Solid Films* **1998**, *333*, 203.
(64) Goya, G. F.; Berquó, T. S.; Fonseca, F. C.; Morales, M. P. *J. Appl. Phys.* **2003**, *94*, 3520.
(65) Deng, H.; Li, X.; Peng, Q.; Wang, X.; Chen, J.; Li, Y. *Angew. Chem. Int. Ed.* **2005**, *44*, 2782.
(66) Verwey, E. J. W. *Nature* **1939**, *144*, 327.
(67) Amin, N.; Arajs, S. *Phys. Rev. B* **1987**, *35*, 4810.
(68) Morin, F. J. *Phys. Rev.* **1950**, *78*, 819.

Chapter VI. Electronic Structure and Chemistry of FeMONS Materials

6.1. Introduction

Iron-based metal oxides, including iron oxides, iron-containing perovskite materials as well as their composite analogues, represent promising materials for the design and synthesis of technologically significant, multifunctional systems. Moreover, this class of iron-based metal oxide nanostructured (FeMONS) materials is also noteworthy for its unique and diverse characteristics, including its highly favorable optical, electronic, and magnetic properties, which are of relevance for a host of potential applications as diverse as additives, catalysts, electronic devices, magnetic recording media, information storage, spintronics, and sensors.[1-6] However, what is lacking in the field is a systematic and detailed structural characterization and correlation of the electronic structure and structural chemistry of these intriguing nanomaterials.

Hence, in this particular study, we will analyze the following materials: α-Fe_2O_3, γ-Fe_2O_3, Fe/Fe_3O_4, $BiFeO_3$, and $Bi_2Fe_4O_9$. Hematite (α-Fe_2O_3) possesses a rhombohedral symmetry (space group: $R\bar{3}c$), pertaining to the corundum structure wherein oxygen atoms are closely packed with the same density around the Fe^{3+} cations, but with a slightly different stacking, which may therefore result in slight distortions in the octahedral environment of the metal. Because of its high stability, relatively low cost, and *n*-type semiconducting properties due to its small band gap, hematite has been associated with applications ranging from gas sensing, catalysis, to solar energy conversion. Magnetite (Fe_3O_4) is a ferrite material characterized by a cubic inverse spinel structure (space group: $Fd3m$), wherein the oxygen ions form a face-centered cubic (fcc) lattice within which the Fe ions occupy tetrahedral (A) and octahedral (B) sites, with the overall formula of $Fe^{A}Fe_2^{B}O_4$. Because the ion spins of the Fe_3O_4 unit cell within the A and B sublattices couple antiferromagnetically, there is an overall magnetic moment in the structure due to the higher occupancy of B sites, and magnetite is in fact one of the most highly magnetic of the iron oxides. Furthermore, the properties of Fe_3O_4 itself can be favorably modified by the addition of Fe to generate a monodisperse composite system based on Fe and Fe_3O_4.[4] Indeed, the Fe/Fe_3O_4 composite is itself a novel and active heterogeneous Fenton catalytic system, which is important in the oxidation of organic contaminants.[7] Maghemite (γ-Fe_2O_3) maintains the same composition as hematite as well as the same physical structure as magnetite, i.e. spinel ferrites. It can be considered as a fully oxidized, Fe^{2+}-deficient magnetite possessing the formula of either $Fe_{2.67}\square_{0.33}O_4$ or $Fe(Fe_{5/3}\square_{1/3})O_4$, where $\square$ constitutes a vacancy structure.[8] Due to its spinel structure with two intersposed sublattices, maghemite is regarded as a typical representative of ferrimagnetic materials. Moreover, synthetic maghemite is often a component of

electrically conductive, magnetizable films and has been associated with potential applications in superparamagnetism.[9-11]

With the addition of bismuth, the corresponding structures are slightly more complex. For instance, $BiFeO_3$ consists of a rhombohedrally distorted simple cubic perovskite cell (space group: *R*3*c*) possessing a distorted oxygen octahedron.[12] The Fe^{3+} cation is slightly shifted away from the center of the distorted oxygen octahedron and the Bi^{3+} cation is displaced with respect to the two neighboring octahedron centers, respectively. In addition to being magnetic, $BiFeO_3$ is a member of the class of multiferroics.[13] Multiferroics are noteworthy for their unique couplings of ferroelectricity, ferromagnetism, and ferroelasticity at high temperatures.[14] Thus far, incorporation of bismuth ferrite into practical devices has been hindered by leakage problems that lead to low resistivity, presumably due to defect and non-stoichiometry related issues. Recent approaches to generating high-quality samples have focused on developing novel structural formulations, such as zero-, one-, and two-dimensional (0-D, 1-D and 2-D) nanostructures, of $BiFeO_3$ materials.[1,2,15] The structure of a related bismuth ferrite material, namely $Bi_2Fe_4O_9$, is orthorhombic (space group: *Pbam*) with two formula units per unit cell.[16] These formula units consist of evenly distributed FeO_6 octahedra and FeO_4 tetrahedra with a lower packing density than that of corresponding closed packed structures.[16] Indeed, the Bi^{3+} ions are surrounded by eight oxygens with mutually orthogonal shorter BiO_3 and longer BiO_5 units. $Bi_2Fe_4O_9$ is antiferromagnetic at room temperature; nanostructures of $Bi_2Fe_4O_9$ can be considered as novel materials for semiconductor gas sensors due to their high sensitivity and catalytic potential, and may eventually replace costly, irrecoverable platinum-, rhodium-, and palladium-based catalysts.[17] A summary of the general physical and chemical characteristics of the FeMONS materials analyzed in this study is presented in Table 6.1.

Table 6.1. General physical and chemical characteristics of Fe-based metal oxide nanostructured (FeMONS) materials in this study

FeMONS materials	Crystal system (Space group)	Fe site symmetry	Fe valence	*d* orbital occupancy	Magnetic properties at RT
α-Fe_2O_3	Rhombohedral ($R\bar{3}c$)	O_h	3+	$3d^5$ ($t_{2g}^3 e_g^2$)	Ferrimagnetic
Fe_3O_4	Cubic ($Fd3m$)	O_h (2) T_d (1)	3+ (2) 2+ (1)	$3d^5$ ($t_{2g}^3 e_g^2$) $3d^6$ ($e_g^3 t_{2g}^3$)	Ferromagnetic
γ-Fe_2O_3	Cubic or Tetragonal ($P4_132$)	O_h (2) T_d (1)	3+ (2) 2+ (1)	$3d^5$ ($t_{2g}^3 e_g^2$) $3d^6$ ($e_g^3 t_{2g}^3$)	Ferrimagnetic
$BiFeO_3$	Rhombohedral ($R3c$)	O_h	3+	$3d^5$ ($t_{2g}^3 e_g^2$)	Ferrimagnetic or antiferromagnetic
$Bi_2Fe_4O_9$	Orthorhombic ($Pbam$)	O_h (2) T_d (2)	3+	$3d^5$ ($t_{2g}^3 e_g^2$) $3d^5$ ($e_g^2 t_{2g}^3$)	Antiferromagnetic

Despite the evident importance of all of these iron-based metal oxides as functional materials, very few fundamental soft X-ray absorption spectroscopy (XAS) studies, such as near edge X-ray absorption fine structure (NEXAFS and also known as X-ray absorption near edge spectroscopy (XANES)) analyses, associated with nanoscale motifs, exist. In fact, it has been difficult to adequately correlate the structural character of these materials with their chemistry and electronic structure.

NEXAFS involves the excitation of electrons from a core level to partially filled and empty states. The decay of core hole states results in the emission of Auger electrons from valence molecular orbitals, resulting in an electron yield spectrum. Hence, the peak positions and spectral lineshape in a NEXAFS spectrum can be directly correlated with the nature of these unoccupied electronic states. The decay of core holes may also occur via the emission of fluorescent photons, which originate from the top 200 nm of the target sample as opposed to Auger electrons, which arises from the top 10 nm of the surfaces of these materials. Thus, this technique is both surface and bulk sensitive and is capable of simultaneously probing the electronic structures as well as surface imperfections and surface strain anisotropies of these small nanoparticles. Transition matrix elements and the corresponding intensities of the π^* and σ^* transitions also possess an angular dependence with respect to the plane of single-crystalline, epitaxially grown $BiFeO_3$ thin films. We have corroborated this concept with respect to the NEXAFS study of various morphological motifs (e.g. films, arrays, and powders) of carbon nanotubes.[18]

Oxygen *K*-edge as well as iron *L*-edge spectra of iron oxides have been previously reported either by electron energy loss near edge structure spectroscopy (EELS)[19-21] or by X-ray absorption near edge structure (XANES) spectroscopy.[22,23] The shape of the spectra is particularly sensitive to the nature of the 3*d* orbitals of the transition metal oxides. Correlations between the specific atomic arrangement as well as the physical and electronic structure of each iron-containing metal oxide with the corresponding position, shape, and intensity of the different characteristic features are of great interest in interpreting XAS spectra.

In the experiments reported herein, we have demonstrated our ability to employ NEXAFS spectroscopy as a particularly useful and effective technique for the systematic investigation of the electronic structure and surface properties of FeMONS materials. In particular, we have correlated the specific atomic arrangement and electronic structure within each FeMONS system with the position and intensity of different characteristic features of the relevant associated spectra.

6.2. Experimental Section

6.2.1 Materials and Preparation

The preparation methods for samples in this Chapter, for instance, *$BiFeO_3$ nanoparticles* (Chapter 2), *$BiFeO_3$ bulk* (Chapter 2), *$Bi_2Fe_4O_9$ cubes* (Chapter 4), *α-Fe_2O_3 rhombohedra* (Chapter 5), and *Fe/Fe_3O_4 nanocomposites* (Chapter 5) are described in previous Chapters.

α-Fe_2O_3 nanoparticles. Commercial amorphous iron oxide nanoscale powders (5-25 nm, Aldrich) were ground, placed in a ceramic crucible, inserted into a quartz tube, heated at a ramp rate of 5ºC per min up to an annealing temperature at 820ºC for 3.5 h, and cooled thereafter to room temperature. As-generated α-Fe_2O_3 material, which was dimensionally similar to its precursor in that it measured 5 to 25 nm, was used without additional processing treatments.

6.2.2. NEXAFS Spectroscopy

For the near-edge X-ray absorption fine structure (NEXAFS) spectroscopy study, samples were pressed onto a Cu tape and mounted onto a stainless-steel sample bar inside an ultrahigh vacuum (UHV) chamber of the U7A NIST/DOW end station at the National Synchrotron Light Source (NSLS) at Brookhaven National Laboratory. The partial electron yield (PEY) signal was collected using a channeltron electron multiplier with an adjustable entrance grid bias (EGB). A variable negative bias in the range between 20 and 200 V was applied for the current sets of data so as to prevent low-energy photoelectrons from reaching the detector. Spectra at different biases allow for surface profiling. A monochromator with a 600 line/mm grating, providing for ~0.15 eV resolution, was used for all of the NEXAFS spectra collected. In addition, the spectra were obtained at different polarization angles by rotating the sample bar with respect to the incident beam in the place of incidence. The incident beam was set at a magic angle of 54.7° relative to the sample. The magic-angle incidence removed any polarization dependence of the π– type states associated with the X-ray source.

The monochromator energy scale was calibrated using the carbon *K*-edge π* transition of graphite, located at 285.35 eV. For the oxygen *K*-edge, a photon energy calibration was performed using an oxide dip absorption feature in the I_o spectrum (from the grating) at 531.2 eV. The 531.2 eV dip had been internally calibrated to the gas-phase oxygen soft X-ray absorption. To eliminate the effect of incident beam intensity fluctuations and monochromator absorption features, the PEY signals were normalized using the incident beam intensity obtained from the photoemission yield of a clean Au grid with 90% transmittance. The edge jumps for the O *K*-edge and Fe *L*-edge are defined as intensity differences at energies before the onset of O *K*-edge and Fe *L*-edge measurements (e.g., <520 eV for O, <680 eV for Fe) and after these transitions (e.g., >575 eV for O, >740 eV for Fe), respectively. All spectra were processed through standard pre- and post-edge normalization routines. For example, the pre-edge jump was subtracted to zero, followed by post-edge jump normalization, which consisted of dividing the pre-edge jump normalized spectra by the edge jump intensity obtained far above the *K*-edge and the *L*-edge, i.e. beyond 580 eV and 760 eV, respectively. Spectra were fitted with Gaussians and an arc tangent so as to fit the resonances and the edge jump, respectively. Thus, changes in the relative spectral intensity observed essentially arise from chemical alterations in the system and are independent of total elemental content, be it Fe or O.

6.3. Results and Discussion

6.3.1. O K-edge fine structure

Analysis of the spectrum for the O *K*-edge fine structure in this study can be divided into two regions: the pre-edge and post-edge.[23] The pre-edge is defined as the low-energy region between the absorption threshold and the absorption jump, and the post-edge region extends to about 50 eV past the continuum threshold. These regions arise from transitions of electrons to bound excited electronic states and continuum states, respectively. For example, near the threshold, the oxygen 2*p* character is hybridized with the more sharply defined transition-metal 3*d* band. In the second region, the O 2*p* character is hybridized with the more weakly structured 4*sp* band. The metal 4*sp* hybridization yields a more or less constant bonding contribution beyond which the metal 3*d* hybridization accounts for specific, material-dependent effects. For example, a decrease in the intensity of the 3*d* band region relative to that of the 4*sp* band across the transition metal series was observed for late-transition-metal oxides due to a shrinking of the metal 3*d* orbitals, thereby resulting in a diminished hybridization of the metal 3*d* orbitals.[23] The spectra in this study which we can ascribe to the covalent mixing of the metal and oxygen states, through the introduction of oxygen *p* character in unoccupied states of mainly metallic character, therefore contain potentially useful structural information, concerning specific electronic and geometric structures.

6.3.1.1. Iron oxides: α-Fe_2O_3 nanoparticles, γ-Fe_2O_3 nanopowders, Fe/Fe_3O_4 nanocomposites

Figure 6.1 shows oxygen *K*-edge spectra for iron oxide samples. These spectra can be divided into two regions (e.g. the pre-edge and post-edge). However, if we consider a complete picture of the electronic structure for these iron oxide samples, the corresponding spectral signatures can be divided into and assigned to three regions consisting of four distinctive features (Figure 6.1, labeled *A*, *B*, *C*, and *D*):[21,22]

(i) transitions to unoccupied oxygen 2*p* states hybridized with metal 3*d* band, which is predominantly localized around metal-atom sites. This region contains so-called pre-edge features below 530 eV (Figure 6.1B).

(ii) oxygen 2*p* character hybridized with Fe 4*s* and 4*p* states, which originates from a scattering resonance due to multiple scattering processes of the final state photoelectron within the cage of the first oxygen shell around 540 eV (Figure 6.1C).

(iii) a diffractive region due to a backscattering process between the absorber and its nearest neighbor oxygen shell, encompassing an area from ~545 to 575 eV and consisting of two broad absorption peaks (Figure 6.1D; *C* and *D*).

The spectra display similarities in shape and position, and are in good agreement with previously reported data for the iron oxide system, with the exception of a commercial amorphous iron oxide (Fe_2O_3) precursor sample which had been used to generate α-Fe_2O_3 nanoparticles and α-Fe_2O_3 rhombohedra.

In region (i), as-expected peaks (*A*, pre-edge features) with almost identical shape, intensity and position have been observed (Figure 6.1B). For the bulk α-Fe_2O_3 single crystals, where the nearest oxygen neighbors are close-packed and surround the 3*d* iron metal atoms within an octahedral environment (O_h symmetry group), a well-resolved splitting of the feature *A* into two components with an almost identical intensity, respectively, was observed (the inset to Figure 6.1B). This splitting has been interpreted as leading to t_{2g}- and e_g- symmetry bands, separated by "ligand-field splitting" to a first approximation, which is supposed to represent a 3: 2 ratio in terms of pre-edge *A* intensity.[23]

However, to explain the observed 1 : 1 intensity for bulk α-Fe_2O_3, we need to also consider orbital hybridization effects. In theory, the e_g hybridization is twice as strong as the t_{2g} hybridization due to the fact that the metal e_g^2 orbitals in O_h symmetry are directed towards the oxygen atoms and consequently maintain a stronger overlap with the oxygen 2*p* orbitals. Moreover, there are also exchange splitting effects which possess a higher energy gap than that of the observed t_{2g}-e_g splitting for a high-spin complex. Comparison between the splitting of the feature *A* in both Fe_2O_3 (rhombohedral) and MnO (cubic) systems, both of which maintain the same d^5 configuration, provides further evidence for the importance of intrinsic symmetry considerations as primarily influencing the

observed intensities.[23]

All of these factors cannot however adequately account for our observed results with nanoscale hematite. In fact, we do not observe any splitting either for α-Fe_2O_3 nanoparticles or for α-Fe_2O_3 rhombohedral structures. Another factor governing the splitting (or lack thereof) of pre-edge peaks is associated with an induced broadening effect, arising from the multiplicity of oxygen states. These are complicating factors that are convoluted with the existence of possible impurities, nonstoichiometries, and other defects in the iron oxides studied.[20-22] As an example of the significance of these factors, wüstite FeO, for instance, possesses an electronic configuration of d^6 ($t_{2g}^4 e_g^2$) with 4 unpaired electrons. Thus, instead of a rather simple d^5 ($t_{2g}^3 e_g^2$) ionic configuration of Fe_2O_3 subject to a t_{2g}-e_g ligand-field splitting, a supplementary *d* splitting needs to be additionally considered, arising from d^6 ($t_{2g}^4 e_g^2$) electronic interactions. That is, the splittings of the *d* orbitals consist of a more complex substructure and this multiplicity explains the broad shape of the pre-edge *A* feature in FeO.[22] Moreover, it is reasonable to postulate that surface imperfections and surface strain anisotropies in our as-prepared smaller particles may induce distortion and site inequivalence in the oxygen octahedral sites surrounding the Fe ion, resulting in an additional increase in the degree of multiplicity effects. Thus, for α-Fe_2O_3 nanoparticles and α-Fe_2O_3 rhombohedral structures, the pre-edge *A* features show no explicit splitting, a fact which can be ascribed to the long-range disorder associated with size and/or surface effects as compared with that of the bulk. This observation is consistent with a previously reported result on α-Fe_2O_3 nanocrystals prepared by the sol-gel method.[24]

Qualitatively, a similar explanation can be forwarded for Fe/Fe_3O_4 nanocomposites. That is, for Fe_3O_4 itself, the overall absorption *A* feature shows one major peak with a slight shoulder instead of a well-resolved splitting.[21-23] Since there are three non-equivalent Fe sites in Fe_3O_4, namely two octahedral ones (Fe^{3+} and Fe^{2+}) and a tetrahedral one (Fe^{3+}), each of which is associated with its own unique t_{2g}-e_g (e_g-t_{2g}) ligand-field splitting, the observed *A* feature is actually a convolution of multiple components, resulting in a loss of resolution. Upon the introduction of the Fe atom, the resulting absorption peak *A* would be expected to be similar, but with the addition of a shoulder peak associated with the Fe/Fe_3O_4 nanocomposites themselves. In reality, we have observed only one absorption peak *A* without the shoulder, and the feature itself resembles that associated with hematite nanoparticles. This observation leads us to believe that the additional Fe component, with its $4s^2 3d^6$ electron configuration, interacts with the oxygen in Fe_3O_4 and thereby induces a further multiplicity in its splitting, resulting in the broadening of and a greater loss of resolution in the pre-edge *A* features associated with region (i).

In region (ii), the absorption peak *B* remains rather similar for all of the iron oxides (Figure 6.1C). It is a region where the oxygen 2*p* character is hybridized with the weakly

structured iron 4*sp* band. The extensive spread observed in region (ii) for the oxygen 2*p* character is indicative of the considerable contribution of metal 4*sp* states to the covalent nature of the iron oxides. In addition, the structure of feature *B*, including a main peak and a low-energy shoulder, is related to the O_h symmetry set up by the nearest oxygen neighbors. For example, this particular *B* structure, present in all of the iron oxides, is absent in the nonoctahedral CuO, which exhibits an obviously different structure in this region.[25] Thus, we can confirm that the O_h symmetry relationships between the oxygen and iron elements in our iron oxide nanostructures are predominantly in good agreement with that of the bulk, even though the nanostructures themselves likely possess either considerably more distortions or site inequivalencies in their octahedral environment.

In region (iii), we expect to observe two broad peaks (labeled *C* and *D*) for Fe_3O_4 and only one peak (labeled *D*) for the α-Fe_2O_3 samples (Figure 6.1D).[21] It turns out that for the nanoscale powder precursors used to generate our iron oxide nanomaterials, we note a relatively stronger peak at *C* where the intensity maximum lies at ~545 eV, an observation indicative of the presence of ferrites with an inverse spinel structure. Thus, we concluded that the nanoscale powder precursors were mainly composed of γ-Fe_2O_3, *i.e.*, the maghemite phase. This assertion could not be independently confirmed from powder X-ray diffraction patterns because of the amorphous and polycrystalline nature of the nanoscale powder precursors. Thus, this interpretation further demonstrates the significance of the use of O *K*-edge XAS as a fingerprinting technique for the determination of iron oxide phases. In fact, similar approaches have been employed to analyze the oxidation state for nanoscale iron oxide minerals through the interpretation of the fine structure in an electron energy loss spectrum (ELNES).[26]

For the Fe/Fe_3O_4 nanoscale composites, α-Fe_2O_3 nanoparticles, and α-Fe_2O_3 rhombohedra themselves, we have hardly observed *C* features, whereas the *D* features remained rather similar. Since either the *C* or *D* feature originates predominantly from single scattering events between the photoabsorber and the particular oxygen shell, this can be derived from calculations based on the one-electron, full multiple-scattering (MS) theory.[22] However, the absence of the *C* feature is related to the nature of the oxygen environment in these samples. Thus, in Fe/Fe_3O_4 nanocomposites, it can be confirmed that the Fe ($4s^2 3d^6$) component plays a crucial role in the interaction with oxygen shells so as to induce a considerable loss of single scattering events, as we have interpreted for region (i).

Additional information gained from the spectra concerns the relative peak intensity between peaks *A* and *B*, *i.e.*, I_A/I_B. For example, a decrease in the pre-peak *A* intensity relative to that of peak *B* is related to a decrease in the hole population of the 3*d* band as compared with that of the 4*sp* band. It is in effect a function of the number of unoccupied 3*d* states available for hybridization with the O 2*p* states. However, especially for d^5 and d^6 oxides, a substantial loss of intensity has been observed, which has been ascribed to

the shrinking of the 3*d* orbitals in the late transition metal oxides, resulting in a diminution of the metal 3*d* hybridization. Thus, as an example, the slightly higher values of (I_A/I_B) observed for Fe/Fe_3O_4 as compared with that of α-Fe_2O_3 samples are consistent with data reported previously.[23]

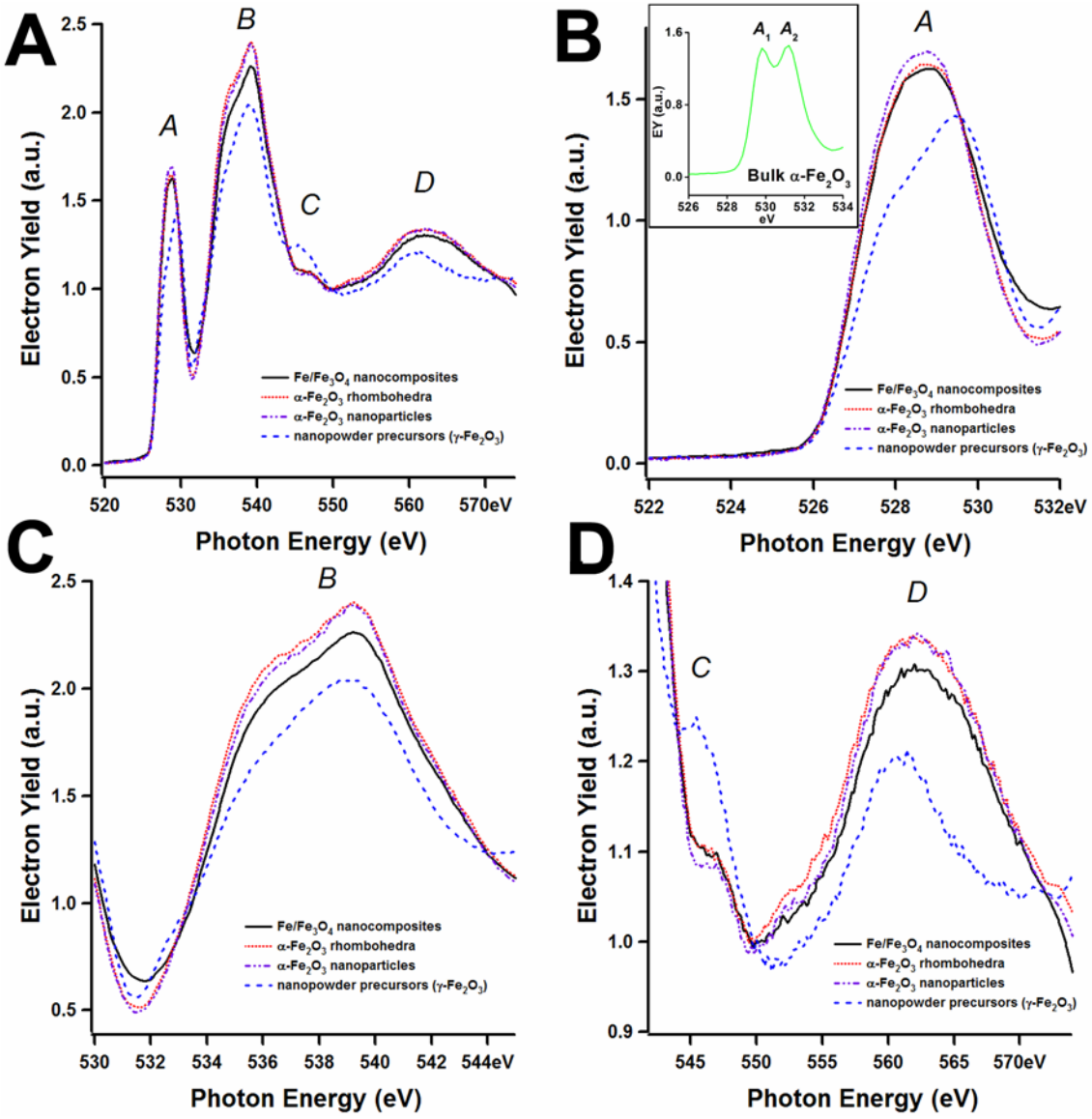

Figure 6.1. (A) Oxygen *K*-edge X-ray absorption spectra (XAS) of iron oxide nanostructures (Fe/Fe_3O_4 nanocomposites, α-Fe_2O_3 rhombohedra, α-Fe_2O_3 spherical nanoparticles, γ-Fe_2O_3 nanopowder precursors). Four distinct features are labeled as *A*, *B*, *C*, and *D*, respectively. Expanded plots of O *K*-edge XAS are shown for (B) the region (i) showing the feature *A*, (C) the region (ii) showing the feature *B*, and (D) the region (iii) showing features *C* and *D*, respectively. The inset to (B) shows an explicit splitting (A_1, A_2) in the feature *A* for bulk α-Fe_2O_3.

6.3.1.2. $BiFeO_3$ nanoparticles

Figure 6.2A shows the O *K*-edge spectra for bismuth iron oxide samples. The spectra can be qualitatively considered in the same terms as that of iron oxides: namely pre-edge and post-edge results. We do not observe a *C* feature, which is indicative of an absence of spinel ferrites, such as Fe_3O_4 or γ-Fe_2O_3, in our bismuth ferrite samples. In addition, the *D* features do not show any interpretable information, which is similar to what we observed for iron oxide nanostructures, reflecting the very weak dependence of single scattering events as a function of the size of the bismuth ferrite nanostructures.

Since $BiFeO_3$ nanoparticles (BFO NPs) maintain their rhombohedral crystallographic nature even with a decrease in their size and diameter,[2] the octahedral environment in BFO NP is more complex for the O *K*-edge spectra as compared with iron oxides alone, due to interactions involving Bi. In region (i), the *A* features for each bismuth ferrite nanoparticle show a similarity in position within experimental precision and provide for a complementary explanation as to their nearly identical crystallographic and electronic configuration. For BFO NPs, we need to consider broadening effects arising not only from their intrinsic nanoscale size but also from their inherent convoluted splitting associated with a multiplicity of oxygen states and leading a loss in spectral resolution, as we have previously observed for iron oxide nanoparticles. Indeed, we observed broader *A* features for BFO NP as compared with those for the corresponding iron oxide nanoparticles in region (i). In addition, we observed broad *A'* features (Figure 2B) at ~531.5 eV (ΔE = ~2 eV from near threshold peak values) for all of the BFO NP samples. In fact, the formation of *A'* structures is likely related to interactions between unoccupied O 2*p* and Bi 5*d* states in BFO. The position of *A'* features observed shows a shift to a lower energy region, comparable to the tendency observed upon replacement of the heavier metal atom in $La_{1-x}Sr_xFeO_3$ perovskite structures.[29]

In region (ii), the *B* feature remains rather similar for all bismuth ferrite nanoparticles. Since this is the region where the O 2*p* character combines with the Fe 4*sp* states, the relatively weaker signal intensity for bismuth ferrite nanoparticles as compared with that for iron oxide nanostructures suggests fewer contributions of the Fe 4*sp* states to the covalent nature of bismuth ferrite. Instead, the covalent nature of bismuth ferrite nanostructures can be further compensated for by contributions of Bi 5*d* orbitals hybridized with O 2*p* orbitals. We note that there might be a certain size dependence with respect to trends observed for bismuth ferrite nanostructures. However, these changes in intensity with respect to particle sizes are not obviously interpretable. It might be said though that the overall intensity ratios between bismuth ferrite nanostructures and the bulk suggests higher (I_A/I_B) values for the bulk as compared with that for nanostructures, which indicates a decrease in the hole population of the 3*d* band as compared with the 4*sp* band in the smaller bismuth ferrite nanostructures.

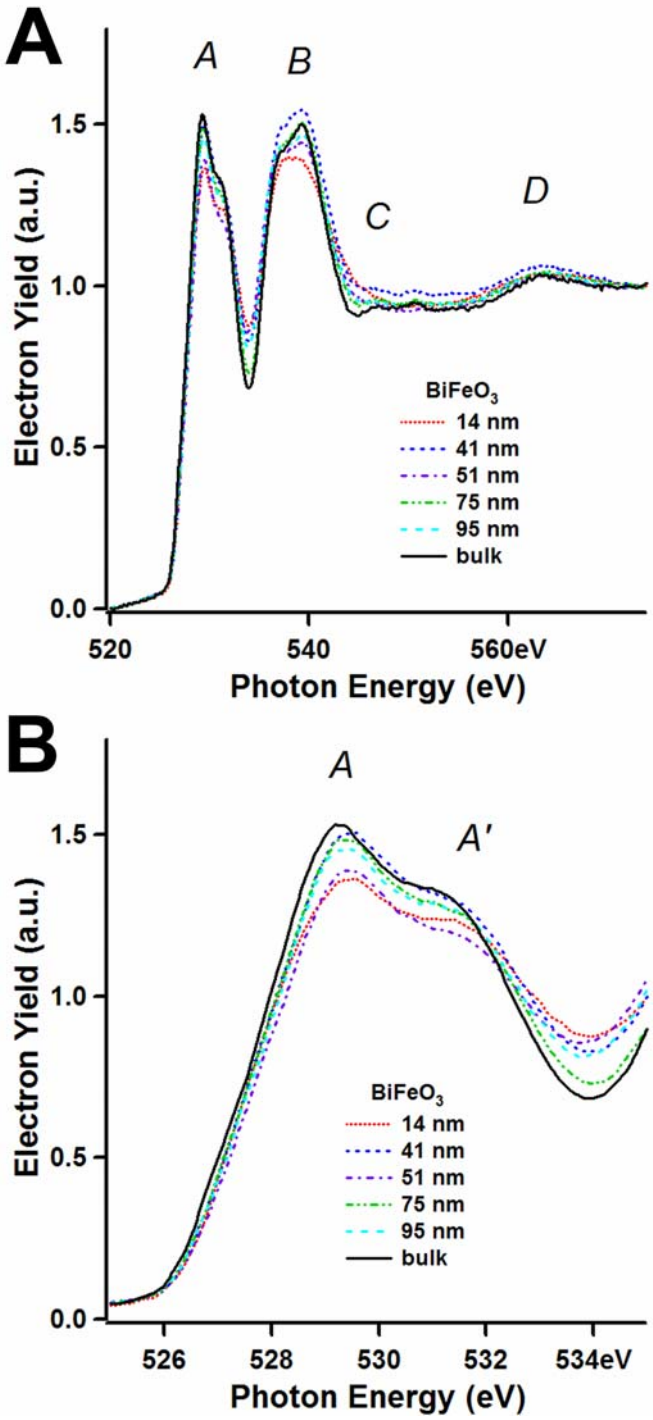

Figure 6.2. (A) Oxygen *K*-edge X-ray absorption spectra (XAS) of bismuth iron oxide ($BiFeO_3$) nanostructures as well as that of bulk. Four distinct features are labeled as *A*, *B*, *C*, and *D*, respectively. (B) Expanded plots of O *K*-edge XAS for the feature *A* which reaches to the other broad feature *A'*.

6.3.1.3. Comparisons across composition of FeMONS materials: $BiFeO_3$, $Bi_2Fe_4O_9$, α-Fe_2O_3, Fe/Fe_3O_4

In terms of a meaningful comparison across the compositions of FeMONS materials, the relevant O *K*-edge fine structures of bulk bismuth ferrite, $BiFeO_3$ nanoparticles (~95 nm), $Bi_2Fe_4O_9$ cubes, α-Fe_2O_3 rhombohedra, and Fe/Fe_3O_4 nanocomposite samples are shown in Figure 6.3. It is reasonable to postulate that the spectral similarity in shape, position, and intensity strongly depends on the composition of each FeMONS material, and such is the case for our FeMONS samples. That is, the *A* features for bismuth iron oxides lie in a slightly higher energy region as compared with that for iron oxides, reflecting the higher value of exchange splitting (Δ_{ex}) associated with the metal *d* orbital splitting in electronic configurations for bismuth iron oxides as compared with the corresponding splittings observed for iron oxides. In addition, the relatively high Δ_{ex} values, which are larger in magnitude as compared with the octahedral crystal field (10 *Dq*), are responsible for the high spin configurations observed for all of the bismuth iron oxide and iron oxide samples in this study.

We also observe that the *A'* feature is very weak, if appreciable, in the spectrum of $Bi_2Fe_4O_9$ cube samples (see Figure 6.3B). This observation can be ascribed to the absence of a considerable contribution to the energy region (i) from interactions between O 2*p* and Bi 5*d* states of $Bi_2Fe_4O_9$ cubes as compared with that of $BiFeO_3$ nanostructures. In effect, the BiO_8 structure in $Bi_2Fe_4O_9$ consists of three shorter Bi-O bonds and five longer bonds with a lower packing density. Furthermore, BiO_3 groups are isolated from the FeO_6 and FeO_4 groups in the structure. Thus, it is reasonable to ascribe this weak feature *A'* in the $Bi_2Fe_4O_9$ spectrum to the intrinsic structure of less densely packed and more highly isolated BiO groups in the $Bi_2Fe_4O_9$ system.

In region (ii), the *B* feature for iron oxide samples shows a relatively higher intensity as compared with that for bismuth iron oxide samples, which again indicates a stronger contribution from O 2*p* and Fe 4*sp* states to the covalent nature of these iron oxide samples. By comparing *B* features, for instance, the substantial partial electron yield (PEY) values of iron oxides (e.g., ~2.40 EY measured for α-Fe_2O_3 rhombohedra) exhibit higher EY than that of the corresponding bismuth iron oxides (e.g., ~1.47 EY for BFO 95 nm particles), which is indicative of more stronger covalent interaction between O 2*p* and Fe 4*sp*.

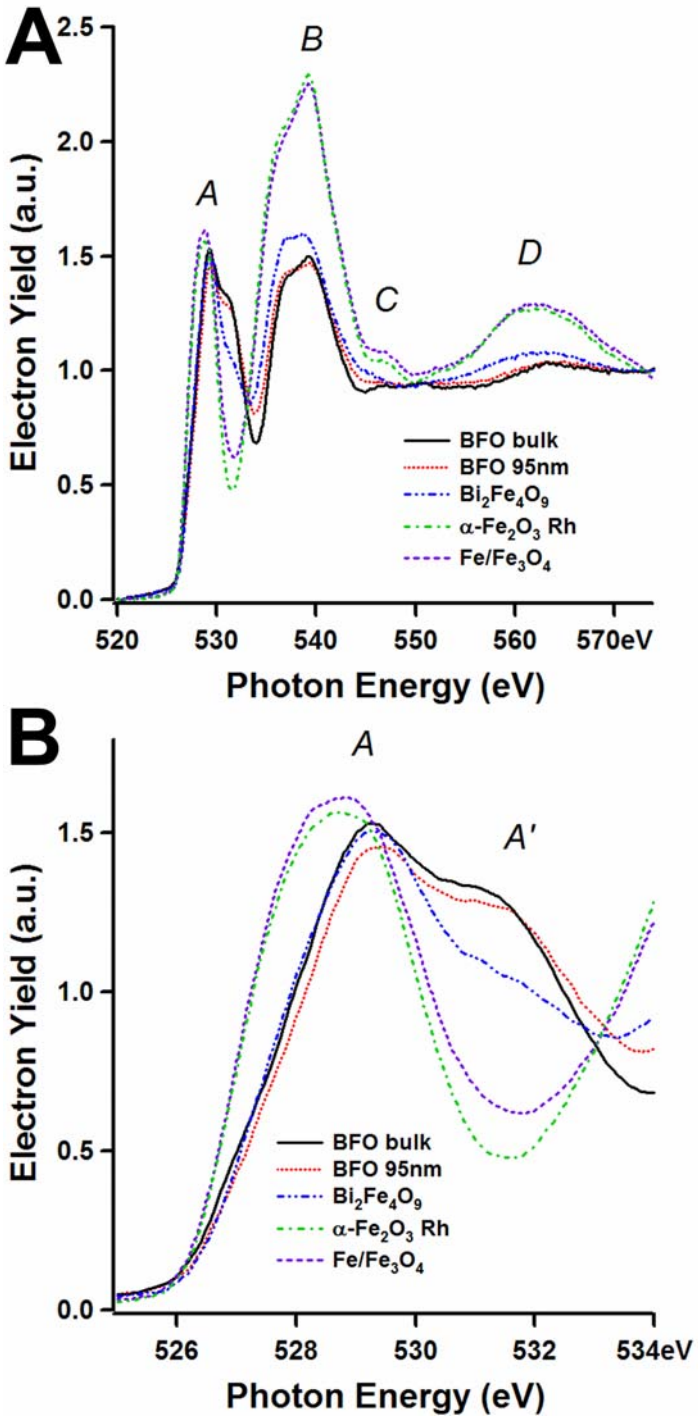

Figure 6.3. (A) Oxygen *K*-edge X-ray absorption spectra (XAS) of iron-based metal oxide nanostructured (FeMONS) materials including $BiFeO_3$, $Bi_2Fe_4O_9$, α-Fe_2O_3, and Fe/Fe_3O_4 nanostructures. O *K*-edge XAS of the bulk $BiFeO_3$ are shown for comparison as well. Four distinct features are labeled as *A*, *B*, *C*, and *D*, respectively. (B) Expanded plots of O *K*-edge XAS for the feature *A*.

6.3.2. Fe L-edge fine structure

Interpretation for the spectrum pertaining to the Fe *L*-edge fine structure in this study can be divided into two regions: the L_3- and L_2-edge. The peaks in these regions arise from transitions of electrons to bound excited electronic states and continuum states, respectively. There are two main peaks of L_3- and L_2-edges at ~ 710 eV and ~ 723 eV, which are due to electronic transitions of Fe $2p_{3/2}$ and $2p_{1/2}$ core electrons, split by the spin-orbit interaction of the Fe 2*p* core level, to an unoccupied 3*d* level highly hybridized with oxygen 2*p* orbital, respectively, as shown in Figure 6.4. Thus, Fe $L_{2,3}$-edges in this study are associated with strong excitations from the $2p^6 3d^n$ Fe ground state to corresponding $2p^5 3d^{n+1}$ states, where $n = 5$ for Fe^{3+} and $n = 6$ for Fe^{2+}, resulting from multiple effects due to strong Coulombic and exchange interactions between the 2*p* core hole and the 3*d* electrons in the final states.[21] Peak shapes and chemical shifts in the Fe *L*-edges, therefore, are sensitive to the 3*d* ground state configuration and to crystal-field interactions.

The Fe L_3- and L_2-edges, the so-called "white lines,"[28] correspond to excitations from the split spin-orbit levels $2p_{3/2}$ and $2p_{1/2}$, respectively. Ideally, the probability of transitions from $2p_{3/2}$ and $2p_{1/2}$ levels to the identical final state is governed by the degeneracy of the initial states, which is equal to 4 and 2, respectively. Thus, one can expect that the intensity ratio of L_3 with respect to L_2 (*i.e.*, I_{L3}/I_{L2}) should be 2:1. However, this theoretical calculated value deviates significantly from experimental results, *i.e.*, $I_{L3}/I_{L2} = 1 : 1$.[29] To understand this apparent discrepancy, others have analyzed the dependence of this intensity ratio on the occupation of the 3*d* states as well as on metal oxidation states[30-32] and found that this value is sensitive to differences between the iron oxidation state in the core and at the surface of the nanoparticles.[33] In addition, transitions from O 2*p* to Fe 4*s* are allowed. Hence, hybridization between O 2*p* and Fe 4*s* contributes to the background at the higher energy region. However, they are much weaker as compared with intrinsic $L_{2,3}$-edges and should not significantly influence the interpretation conveyed in this study.

6.3.2.1. Iron oxides: α-Fe_2O_3 nanoparticles, γ-Fe_2O_3 nanopowders, Fe/Fe_3O_4 nanocomposites

The Fe 2*p* XAS data of iron oxide nanostructures in this study are shown in Figure 6.4. The spectra for all of our iron oxide nanostructures exhibit rather similar features and consist of two separated white lines centered at ~710.3 and 723.3 eV, respectively, with a spin-orbit splitting of ~13 eV. Experimental parameters observed in this study show a similarity with that of typical white lines for iron oxides and their corresponding nanostructures.[21,33,34] In other words, 3*d* ground state configurations as well as the magnitude of *p*-*d* Coulomb, exchange, and crystal-field interactions remain rather similar in our iron oxide nanostructure samples. Hence, the I_{L3}/I_{L2} values observed for iron oxide nanostructures vary only slightly from 2.9 to 2.6. We note that the intensity ratios in this study were measured using a rather simple methodology which, thus, limits a quantitative comparison with the I_{L3}/I_{L2} values obtained through a curve-fitting protocol combining Hartree-Slater (HS) and either Lorentz or Gauss-type methods.[21,31]

However, qualitatively speaking, we confirmed that the I_{L3}/I_{L2} values in our iron oxide nanostructure samples increase with respect to the valence state with increasing *d* band occupancy, except for the Fe/Fe_3O_4 nanocomposites. The highest I_{L3}/I_{L2} value observed in this study, i.e., that for Fe/Fe_3O_4 (2.9), is very close to what we observe for α-Fe_2O_3 rhombohedra (2.8) and is much smaller than what one might expect. That is, the calculated I_{L3}/I_{L2} values for Fe and Fe_3O_4 are 150% higher than that for α-Fe_2O_3 alone.[21] This result suggests a considerable role for the Fe ($4s^2 3d^6$) component in the interaction with oxygen shells in Fe_3O_4, resulting in unintended contributions to the observed I_{L3}/I_{L2} values, a result that complements our O *K*-edge data.

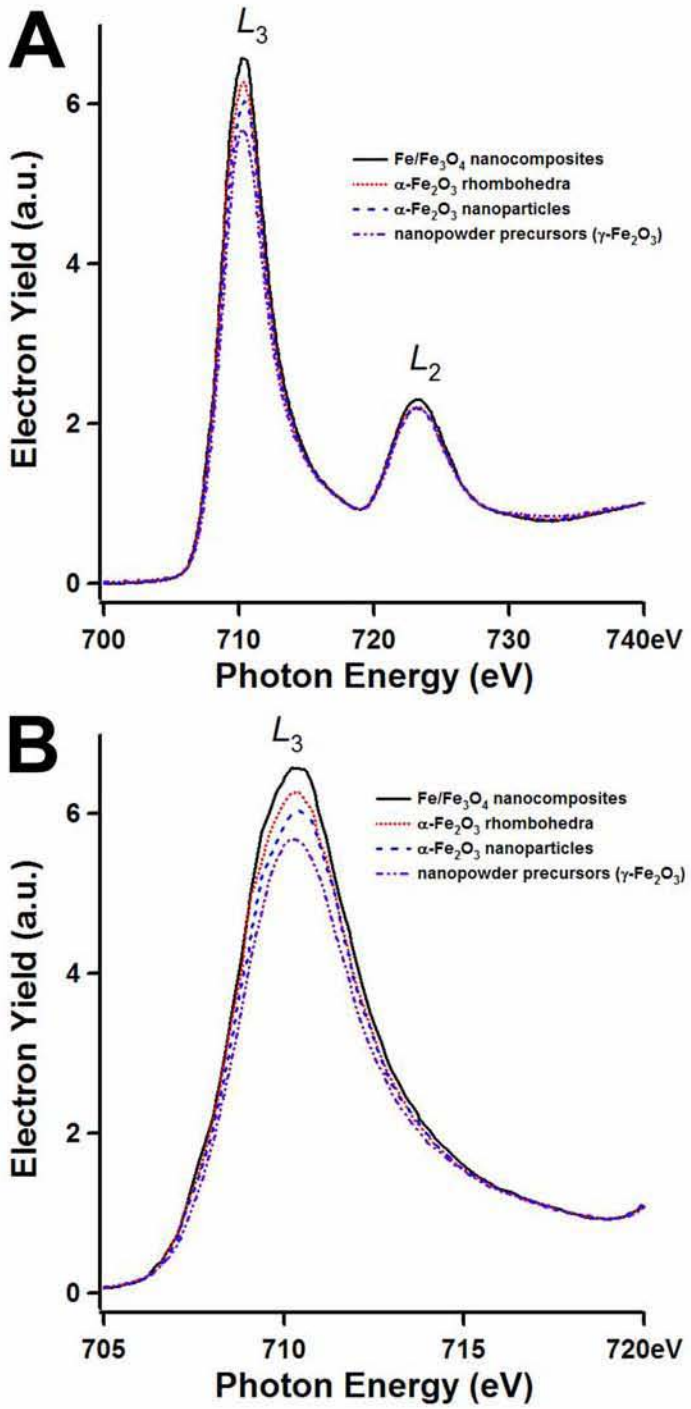

Figure 6.4. (A) Iron *L*-edge X-ray absorption spectra (XAS) of iron oxide nanostructures (Fe/Fe_3O_4 nanocomposites, α-Fe_2O_3 rhombohedra, α-Fe_2O_3 spherical nanoparticles, γ-Fe_2O_3 nanopowder precursors). (B) Expanded plots of Fe *L*-edge XAS for the L_3-edge.

6.3.2.2. $BiFeO_3$ nanoparticles

Figure 6.5A shows the Fe *L*-edge fine structures of bismuth ferrite nanoparticle samples possessing size ranges from 14 nm to 95 nm. Data for bulk bismuth ferrite are also shown for comparison. The spectra exhibit two separated white lines centered at ~710.8 and 723.9 eV, respectively, with a spin-orbit splitting of ~13.1 eV. As a qualitative comparison with that of iron oxide nanostructures, bismuth ferrite nanostructures show a very slight chemical shift toward a higher energy region for both L_3- and L_2-edges, respectively. Moreover, each white line is shifted towards a higher energy region, corresponding to an increase in sample size. For example, the difference for L_2-edges in eV between the smallest and the biggest (bulk) sample is measured to be ~0.6 eV. The detailed energy position shifts for the Fe L_2-edges are shown in Figure 6.5B.

We note that the splitting (ΔE) increases slightly with respect to an increase in the sample size as well; however, this observation lies within experimental error and may not be statistically relevant. As discussed earlier, factors including the 3*d* ground state configuration as well as *p-d* Coulomb, exchange, and crystal-field interactions of bismuth ferrite materials are responsible for the chemical shifts observed. Moreover, since bismuth ferrite nanoparticles preserve their rhombohedral crystallographic characteristics and are free from any possible substrate-induced strains which would govern the behavior of an epitaxially grown film,[2] 3*d* ground state configurations are expected to be relatively unaffected. Thus, we postulate that nanoscale size effects including surface imperfection, surface confinement effects, and surface strain anisotropies influence our observations. These imperfections within these nanoparticles may manifest themselves as coordination distortion, lattice disorder, and/or surface defects, emanating as a result of high surface-to-volume ratios.

The L_3-to-L_2 white line intensity ratios (I_{L3}/I_{L2}) observed for bismuth ferrite nanostructures are shown in Figure 6.5C. An overall decrease in I_{L3}/I_{L2} values has been observed and correlates with the size of bismuth ferrite nanoparticles, although the I_{L3}/I_{L2} value for 51 nm bismuth ferrite nanoparticles did deviate from the expected linear decrease observed. Comparisons between I_{L3}/I_{L2} values for bismuth ferrite nanoparticles and for the bulk further confirm the smaller expected I_{L3}/I_{L2} values for these smaller particles, which is also compatible with the EELS interpretation for iron oxide nanoparticles.[33] Since I_{L3}/I_{L2} are sensitive to the oxidation states of metals, a decrease in I_{L3}/I_{L2} values can potentially be ascribed to the reduction of Fe^{3+} to Fe^{2+} at the surface of bismuth ferrite nanoparticles.[33] However, a previous Mössbauer study of our samples suggests that there is no Fe^{2+} species present on any of the bismuth ferrite nanoparticles used in this study.[2] Hence, the greater degree of breakdown of *j-j* coupling due to an exchange mechanism for the ions at the surfaces of these nanoparticles might be one possible explanation for our observation.[30]

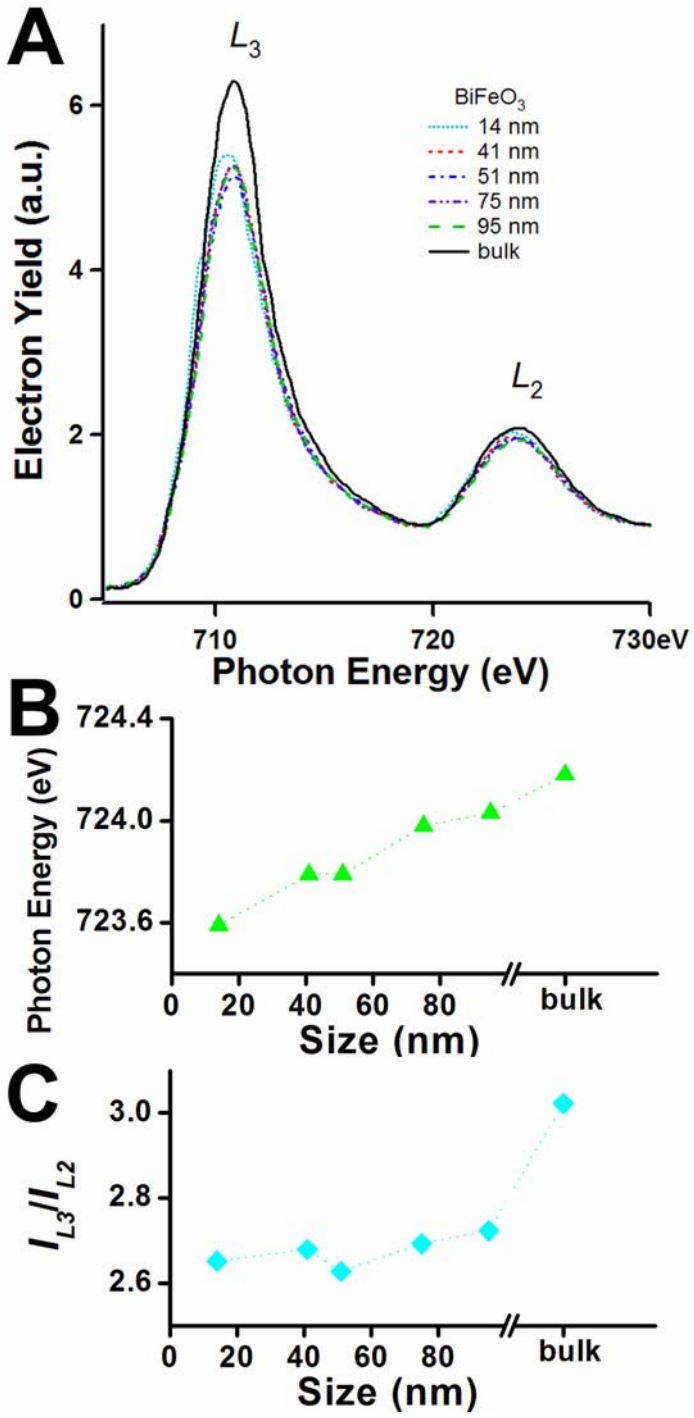

Figure 6.5. (A) Iron *L*-edge X-ray absorption spectra (XAS) of bismuth iron oxide ($BiFeO_3$) nanostructures as well as that of bulk. (B) The corresponding chemical shift in photon energy values (eV) as a function of the size (nm). (C) The corresponding intensity ratios of L_3 with respect to L_2 (I_{L3}/I_{L2}) as a function of the size (nm).

6.3.2.3. Comparisons across composition of FeMONS materials: $BiFeO_3$, $Bi_2Fe_4O_9$, α-Fe_2O_3, Fe/Fe_3O_4

Figure 6.6A shows the Fe *L*-edges for FeMONS materials, in which *L*-edge features exhibit different positions with respect to different chemical compositions. That is, both of the L_3- and L_2-edges are slightly shifted towards the higher energy regions for $BiFeO_3$ samples as compared with $Bi_2Fe_4O_9$, α-Fe_2O_3, and Fe/Fe_3O_4 samples. Within the series of bismuth ferrites, the threshold energy of $Bi_2Fe_4O_9$ cubes is positioned at a lower energy region as compared with that of $BiFeO_3$. Figure 6.6B shows the overall trend in threshold energies for Fe *L*-edges for FeMONS materials, even though we display data for the Fe L_2-edge only, for clarity. Since *L*-edge features are associated with multiple effects including electron configuration and crystal-field interactions, this observation can be explained by the presence of tetrahedral Fe sites in $Bi_2Fe_4O_9$. That is, for the FeO_4 tetrahedral sites, the iron $3d^5$ ($e_g^2 t_{2g}^3$) electronic configuration possessing a smaller e_g-t_{2g} ligand-field splitting ($\Delta_t = 4/9\Delta_o$) will participate in interactions associated with energy shifts at the Fe *L*-edges.[35,36]

This interpretation is also consistent with Fe *L*-edge observations for iron oxide samples due to the fact that Fe/Fe_3O_4 also possesses tetrahedral Fe sites. Furthermore, the Fe *L*-edges of Fe/Fe_3O_4 show slight shifts towards lower energy regions as compared with those of α-Fe_2O_3 rhombohedra. We note that since $Bi_2Fe_4O_9$ orthorhombic structures exhibit a similarity in chemical shifts comparable to structures possessing the highest symmetry, *e.g.*, cubic Fe/Fe_3O_4, the dependence of our results on crystal structure is not a significant issue. A spin-orbit splitting (ΔE) of ~13 eV was observed for our FeMONS materials, which is comparable with bulk iron metal and iron oxide compounds.[21,30] A slight increase observed with respect to the Bi-containing iron oxides ($BiFeO_3$, $Bi_2Fe_4O_9$) in the ΔE parameter (Figure 6.6C) may suggest multiple effects derived from additional contributions due to hybridization effects between Bi 5*d* and unoccupied O 2*p* states, which indirectly influences the magnitude of the spin-orbit coupling.

The L_3-to-L_2 white line intensity ratio observed is shown in Figure 6.6D. For bismuth ferrites, the (I_{L3}/I_{L2}) ratio of bulk $BiFeO_3$ is larger than that of $Bi_2Fe_4O_9$ while the corresponding I_{L3}/I_{L2} values for all of the iron oxides are comparable. The difference in the I_{L3}/I_{L2} value between $BiFeO_3$ and $Bi_2Fe_4O_9$ can be ascribed to structural considerations because $Bi_2Fe_4O_9$ has evenly distributed octahedral Fe^{3+} ions and tetrahedral Fe^{3+} ions, whereas $BiFeO_3$ maintains only octahedral Fe^{3+} ions. Thus, we can gain insight not only into the oxidation states of the metal, but also into the nature of coordination of metal oxides from these I_{L3}/I_{L2} values.

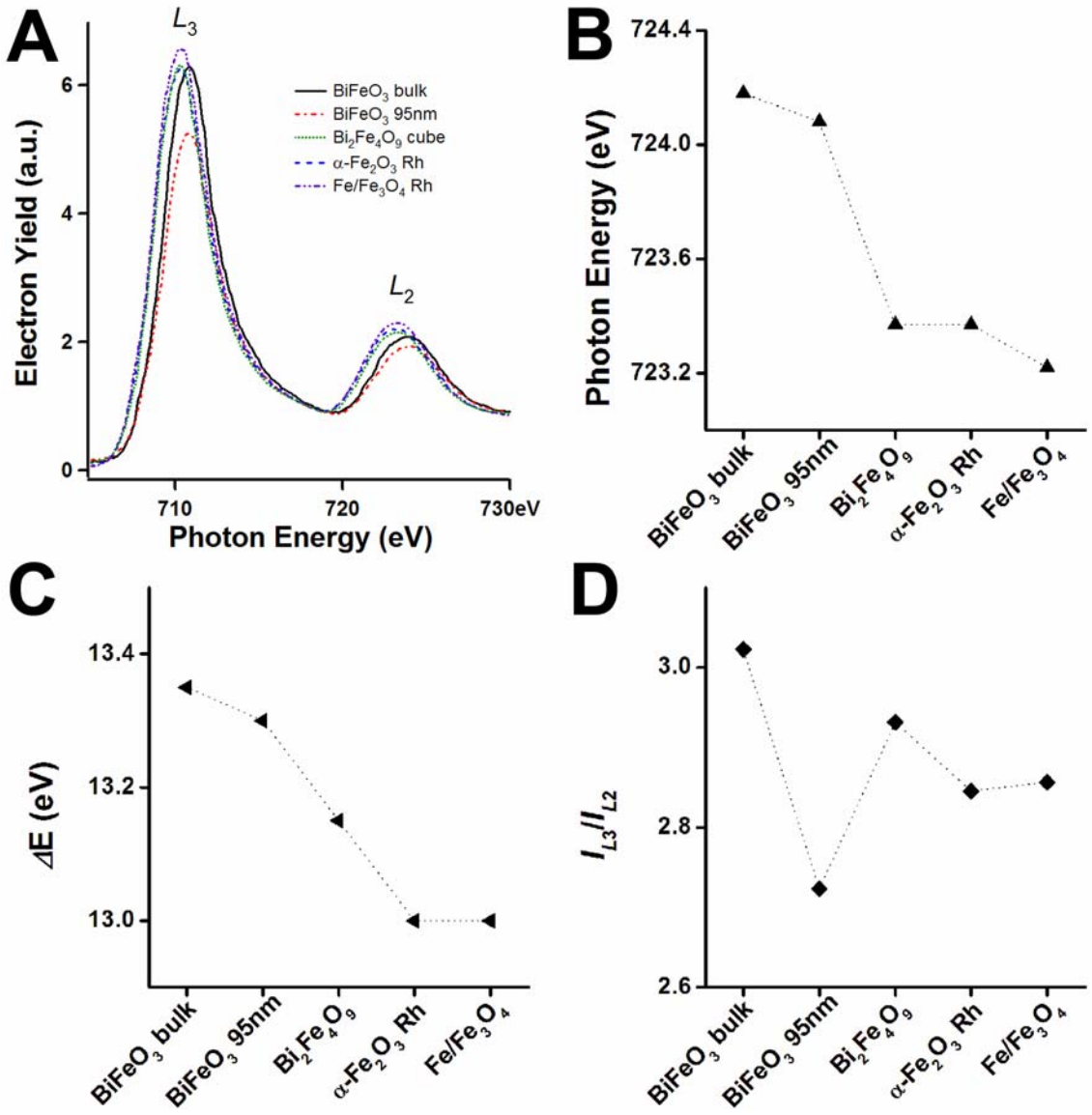

Figure 6.6. (A) Iron *L*-edge X-ray absorption spectra (XAS) of iron-based metal oxide nanostructured (FeMONS) materials including $BiFeO_3$, $Bi_2Fe_4O_9$, α-Fe_2O_3, and Fe/Fe_3O_4 nanostructures. Fe *L*-edge XAS of the bulk $BiFeO_3$ are shown for comparison as well. (B) The corresponding chemical shift in photon energy values (eV) as a function of the FeMONS composition. (C) The corresponding spin-orbit splitting (ΔE) values as a function of the FeMONS composition. (D) The corresponding intensity ratios of L_3 with respect to L_2 (I_{L3}/I_{L2}) as a function of the FeMONS materials composition.

6.4. Conclusions

The current work provides for a detailed experimental NEXAFS investigation of iron-based metal oxide nanostructured (FeMONS) materials including $BiFeO_3$, $Bi_2Fe_4O_9$, α-Fe_2O_3, γ-Fe_2O_3, and Fe/Fe_3O_4. Variations in shape, position, and intensity of the O *K*-edge and Fe *L*-edge XAS, respectively, have been analyzed in terms of electronic structure as well as the surface chemistry of nanomaterials as well as of the bulk. Surface imperfection and surface strain anisotropies in the smaller particles may induce distortion and site inequivalency of the oxygen O_h sites around the Fe ion located close to the surface, resulting in an increase in the degree of multiplicity and nonstoichiometry effects.

For example, pre-edge *A* features in the O *K*-edge for iron oxide nanoparticles show no explicit splitting as compared with that of the bulk. Lower intensity ratios (I_A/I_B) in O *K*-edge data have been observed for $BiFeO_3$ nanoparticles as compared with the bulk, indicating a decrease of hole populations in the 3*d* band as compared with the 4*sp* band in the smaller samples. Moreover, a chemical shift to the higher energy region in the Fe *L*-edge has been observed for $BiFeO_3$ nanoparticles, due to a size effect which most likely influences existing Coulomb, exchange, and crystal-field interactions.

In addition, an analysis based on an overall comparison across compositions of FeMONS materials has further revealed that soft XAS measurements may play a crucial role in determining the electronic structure and chemistry of these different materials at the nanoscale as well as the micron scale. Furthermore, it should be noted that epitaxially grown $BiFeO_3$ thin films were probed using angular dependent measurements, employing our current NEXAFS analysis (Figure 6.7). Unlike for powder samples, constituting the majority of our studies, both O *K*-edge as well as Fe *L*-edge spectra of these thin films exhibit a shift to the higher energy region for normal-theta data as compared with magic-angle and glancing-theta data. This observation further suggests the effectiveness of using NEXAFS as a probe to investigate the angular dependence of nanoscale film structures. This complementary approach in addition to calculations as well as a study of the angle/orientation dependence of aligned nanomaterials merits further attention.

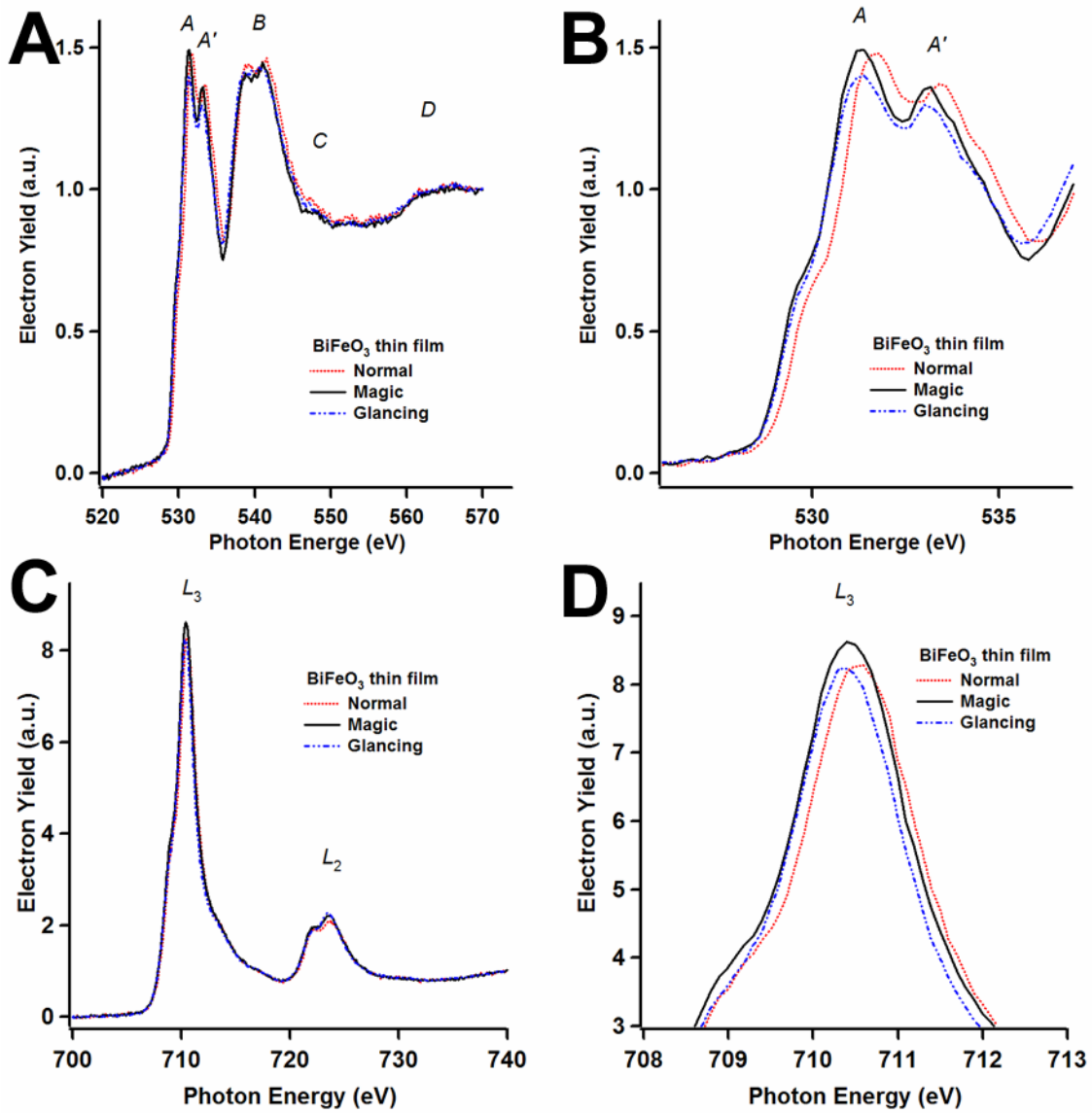

Figure 6.7. (A) Oxygen *K*-edge X-ray absorption spectra (XAS) of an epitaxially-grown $BiFeO_3$ thin film sample. Four distinctive features are labeled as *A*, *B*, *C*, and *D*, respectively. (B) Expanded plots of O *K*-edge XAS for the feature *A* which reaches to the other feature *A'*. (C) Iron *L*-edge XAS of a $BiFeO_3$ thin film sample. White lines are labeled as L_3 and L_2, respectively. (D) Expanded plots of Fe *L*-edge XAS for the L_3-edge.

6.5. References

(1) Wang, J.; Neaton, J. B.; Zheng, H.; Nagarajan, V.; Ogale, S. B.; Liu, B.; Viehland, D.; Vaithyanathan, V.; Schlom, D. G.; Waghmare, U. V.; Spaldin, N. A.; Rabe, K. M.; Wuttig, M.; Ramesh, R. *Science* **2003**, *299*, 1719.

(2) Park, T.-J.; Papaefthymiou, G. C.; Viescas, A. J.; Moodenbaugh, A. R.; Wong, S. S. *Nano Lett.* **2007**, *7*, 766.

(3) Hyeon, T. *Chem. Commun.* **2003**, 927.

(4) Zeng, H.; Li, J.; Liu, J. P.; Wang, Z. L.; Sun, S. *Nature* **2002**, *420*, 395.

(5) Chen, J.; Xu, L.; Li, W.; Gou, X. *Adv. Mater.* **2005**, *17*, 582.

(6) Han, J.-T.; Huang, Y.-H.; Wu, X.-J.; Wu, C.-L.; Wei, W.; Peng, B.; Huang, W.; Goodenough, J. B. *Adv. Mater.* **2006**, *18*, 2145.

(7) Moura, F. C. C.; Araujo, M. H.; Costa, R. C. C.; Fabris, J. D.; Ardisson, J. D.; Macedo, W. A. A.; Lago, R. M. *Chemosphere* **2005**, *60*, 1118.

(8) Schwertmann, U.; Cornell, R. M. **1991**, *Iron Oxides in the Laboratory*, VCH, Weinheim.

(9) Ziolo, R. F.; Giannelis, E. P.; Weinstein, B. A.; O'Horo, M. P.; Ganguly, B. N.; Mehrotra, V.; Russel, M. W.; Huffman, D. R. *Science* **1992**, *257*, 219.

(10) Park, J.; An, K.; Hwang, Y.; Park, J.-G.; Noh, H.-J.; Kim, J.-Y.; Park, J.-H.; Hwang, N.-M.; Hyeon, T. *Nat. Mater.* **2004**, *3*, 891.

(11) Zboril, R.; Mashlan, M.; Petridis, D. *Chem. Mater.* **2002**, *14*, 969.

(12) Kubel, F.; Schmid, H. *Acta Crystallogr. B* **1990**, *46*, 698.

(13) Schmid, H. *Ferroelectrics* **1994**, *162*, 317.

(14) Schmid, H. *Ferroelectrics* **1999**, *221*, 9.

(15) Park, T.-J.; Mao, Y.; Wong, S. S. *Chem. Commun.* **2004**, 2708.

(16) Niizeki, N.; Wachi, M. *Zeit. Kristallogra. B* **1968**, *127*, 173.

(17) Park, T.-J.; Papaefthymiou, G. C.; Moodenbaugh, A. R.; Mao, Y.; Wong, S. S. *J. Mater. Chem.* **2005**, *15*, 2099.

(18) Hemraj-Benny, T.; Banerjee, S.; Sambasivan, S.; Balasubramanian, M.; Fischer, D. A.; Eres, G.; Puretzky, A. A.; Geohegan, D. B.; Lowndes, D. H.; Han, W.; Misewich, J. A.; Wong, S. S. *Small* **2006**, *2*, 26.

(19) Grunes, L. A. *Phys. Rev. B* **1993**, *27*, 2111.

(20) Gloter, A.; Ingrin, J.; Bouchet, D.; Colliex, C. *Phys. Rev. B* **2000**, *61*, 2587.

(21) Colliex, C.; Manoubi, T.; Ortiz, C. *Phys. Rev. B* **1991**, *44*, 11402.

(22) Wu, Z. Y.; Gota, S.; Jollet, F.; Pollak, M.; Gautier-Soyer, M.; Natoli, C. R. *Phys. Rev. B* **1997**, *55*, 2570.

(23) de Groot, F. M. F.; Grioni, M.; Fuggle, J. C.; Ghijsen, J.; Sawatzky, G. A.; Petersen, H. *Phys. Rev. B* **1989**, *40*, 5715.

(24) Zhang, J.; Wu, Z. Y.; Ibrahim, K.; Abbas, M. I.; Ju, X. *Nucl. Instrum. Meth. B* **2003**,

199, 291.
(25) Grioni, M.; Czyzyk, M. T.; de Groot, F. M. F.; Fuggle, J. C.; Watts, B. E. *Phys. Rev. B* **2989**, *39*, 4886.
(26) Golla-Schindler, U.; Hinrichs, R.; Bomati-Miguel, O.; Putnis, A. *Micron* **2006**, *37*, 473.
(27) Abbate, M.; de Groot, F. M. F.; Fuggle, J. C.; Fujimori, A.; Strebel, O.; Lopez, F.; Domke, M.; Kaindl, G.; Sawatzky, G. A.; Takano, M.; Takada, Y.; Eisaki, H.; Uchida, S. *Phys. Rev. B* **1992**, *46*, 4511.
(28) Azaroff, L. V.; Pease, D. M., in *X-Ray Spectroscopy*, edited by L. V. Azaroff, McGraw-Hill, New York, 1974.
(29) Leapman, R. D.; Grunes, L. A. *Phys. Rev. Lett.* **1980**, *45*, 397.
(30) Leapman, R. D.; Grunes, L. A.; Fejes, P. L. *Phys. Rev. B* **1982**, *26*, 614.
(31) Sparrow, T. G.; Williams, B. G.; Rao, C. N. R.; Thomas, J. M. *Chem. Phys. Lett.* **1984**, *108*, 547.
(32) Paterson, J. H.; Krivanek, O. L. *Ultramicroscopy* **1990**, *32*, 319.
(33) Jasinski, J.; Pinkerton, K. E.; Kennedy, I. M.; Leppert, V. J. *Microsc. Microanal.* **2006**, *12*, 424.
(34) Waddington, W. G.; Rez, P.; Grant, I. P.; Humphreys, C. J. *Phys. Rev. B* **1986**, *34*, 1467.
(35) Byrne, E. K.; Richeson, D. S.; Theopold, K. H. *J. Chem. Soc., Chem. Commun.* **1986**, 1491.
(36) Huheey, J. E.; Keiter, E. A.; Keiter, R. L., 'Inorganic Chemistry: Principles of Structure and Reactivity', 4th Ed., HarperCollins, New York, 1993.

Chapter VII. Conclusions

Nanostructures are fundamentally different from microstructures. As a particle decreases in size to the nanoscale, a greater surface-to-volume ratio results in a significant change with respect to the properties of a particle due to predominant contributions from more active surface atoms as compared with core atoms. In conjunction with surface-area effects, confinement effects (the dominant size effect) which are caused only by their finite size, are critical. Moreover, because nanoparticles are structurally distinct, their physical properties are considered to be different from that of the corresponding bulk. Moreover, nanoparticles contain unusual forms of structural disorder (*e.g.*, bond length contraction, random disorder, and a disorder associated with atomic displacements) that can substantially modify materials' properties and thus cannot solely be considered as mainly miniaturized versions of bulk materials.

Thus, nanostructures are, in a sense, a unique state of matter – one with particular promise for new and potentially very useful products in electronics, catalysis, condensed matter physics, materials sciences, and molecular biology. The ability to synthesize, manipulate, and organize matter in a controllable manner as well as to predict and understand the properties of resulting structures are of fundamental interest, and holds forth the promise of a completely new generation of advanced materials.

In this dissertation, we have studied a class of iron-based metal oxides nanostructured (FeMONS) materials, including iron oxides, iron-containing perovskite materials as well as their composite analogues, due to their particularly intriguing physical properties such as electronic, magnetic, and elastic ones as in multifunctional systems. Moreover, with the coupling among their physical properties coexisting in the same phase, FeMONS materials can exhibit induced physical properties by an applied field of different origin. For example, ferroelectromagnets have a magnetization which can be induced by an electric field, and an electrical polarization, which can be activated by a magnetic field. This unique and strong coupling suggests the development of "smart materials" for potential applications in many areas. We have achieved the synthesis and characterization of FeMONS materials (*i.e.*, $BiFeO_3$, $BiFeO_3$–$BaTiO_3$, $Bi_2Fe_4O_9$, α-Fe_2O_3, and Fe/Fe_3O_4), investigated their magnetic properties (SQUID), and correlated their electronic structure with their structural chemistry (NEXAFS).

7.1. The size and shape as well as magnetic spin ordering of as-prepared FeMONS materials

Table 7.1 summarizes general characteristics of FeMONS materials studied in this dissertation. The size control of our nanostructures has been achieved for $BiFeO_3$ nanoparticles (NPs) in their diameters of 14, 41, 51, 75, 95, and 245 nm, for $BiFeO_3$ nanotubes (NTs) in their diameters of 160 and 270 nm, and for $Bi_2Fe_4O_9$ as well as α-Fe_2O_3 nanostructures in their elongation by varying experimental parameters specifically in molten salt methods. In this dissertation, we have also manipulated the shape of FeMONS materials including the generation of $BiFeO_3$ nanotubes, $BiFeO_3$–$BaTiO_3$ solid solution cubes, $Bi_2Fe_4O_9$ nanocubes in addition to their elongated structures, α-Fe_2O_3 rhombohedra in addition to their elongated structures, and Fe/Fe_3O_4 nanocomposite rhombohedra. Synthetic approaches employed to generate our as-prepared FeMONS materials include sol-gel methods for $BiFeO_3$ NPs, sol-gel based template synthesis for $BiFeO_3$ NTs, molten salt methods for $BiFeO_3$–$BaTiO_3$, $Bi_2Fe_4O_9$, and α-Fe_2O_3, and reduction reactions using gaseous mixtures for Fe/Fe_3O_4.

Not only as promising multiferroics, but also as general nanomaterials, the shape control of $BiFeO_3$ nanoparticles still remains a challenging issue to resolve to achieve desired practical device applications. In this dissertation, we have described the first reported studies of 0-D as well as 1-D nanostructures of $BiFeO_3$ materials. Thus far, only spherical shapes (randomly shaped structures) have been generated for 0-D nanostructures of $BiFeO_3$ materials. Cubes as well as rhombohedral nanostructures can possibly be prepared due to the intrinsic crystallographic nature of $BiFeO_3$ materials, with potential as nanoscale building blocks for promising practical applications. In addition, nanotubes as well as nanowires of $BiFeO_3$ materials have appeared as 1-D nanostructures. Moreover, nanofibers of $BiFeO_3$ materials with nanoscale diameters but with a considerably longer length (up to millimeter scale) can likely be generated by an application of electrospinning technique.

We have studied a $BiFeO_3$–$BaTiO_3$ solid solution system in Chapter III. Size and shape control at nanoscale in this area should be of great importance due to their effectiveness at resolving leakage-related issues for multiferroic $BiFeO_3$. In addition, approaches based on a nanoscience perspective (*i.e.*, generation and shape control of nanostructures) promise a fundamental model system and practical applications of solid solution systems associated with $BiFeO_3$, incorporating not only $BaTiO_3$ but also $PbTiO_3$ (or PZT) and $ReFeO_3$. Moreover, a nanoscale incorporation of $BiFeO_3$ into layered perovskites such as $SrBi_2Nb_2O_9$ and $Bi_4Ti_3O_{12}$ can attract much attention in nonvolatile random access memory (NVRAM) applications.

For $Bi_2Fe_4O_9$ nanostructures, prior to our report of submicron-sized cubes, only sheet-like nanoparticles were reported. Additional reports of nanostructures of $Bi_2Fe_4O_9$

materials include a form of nanowires. Further efforts to develop synthetic approaches to control the shapes of and to assemble the nanostructures of $Bi_2Fe_4O_9$ materials still merits attention so as to provide for potential applications in nanoscale catalysis as well as in gas sensing, in addition to their antiferromagnetic applications.

In Chapter V, we have demonstrated our ability to prepare discrete rhombohedra hematite products as well as discrete aggregates of Fe/Fe_3O_4 nanocomposites. Single-crystalline, monodisperse nanoscale α-Fe_2O_3 rhombohedra, as well as elongated motifs of these materials, are in fact an excellent model system to demonstrate the molten salt synthesis principle. Moreover, our facile transformation reaction to obtain discrete rhombohedral aggregates of nanocomposite of Fe (67%) and Fe_3O_4 (33%) can further be optimized to control the composition of Fe and Fe_3O_4 components. Thus, rhombohedral structures of Fe itself as well as Fe_3O_4 itself can also be anticipated.

Table 7.1. Summary of general characteristics of Fe-based metal oxide nanostructured (FeMONS) materials in this dissertation.

FeMONS materials	Shape	Size [a] (nm)	Synthetic approaches	Magnetic spin orderings (at RT)
$BiFeO_3$ NPs [b] (Chapter II)	Spheres	*d*, ~14 – 245	Sol-gel method	Ferrimagnetic
$BiFeO_3$ NTs [b] (Chapter II)	Tubes	*d*, ~160; *l*, ~3 μm *d*, ~270; *l*, ~50 μm; *t*, ~10	Template synthesis	Ferrimagnetic
$BiFeO_3$–$BaTiO_3$ (Chapter III)	Cubes	*d*, ~150 – 200	Molten salt method	Ferrimagnetic (or ferromagnetic)
$Bi_2Fe_4O_9$ (Chapter IV)	Cubes	*d*, ~386	Molten salt method	Antiferromagnetic
	Orthorhombics	*d*, ~662; *l*, ~1043		
	Rods	*d*, ~2 μm; *l*, ~10 μm		
α-Fe_2O_3 (Chapter V)	Rhombohedra	*d*, ~219	Molten salt method	Ferrimagnetic
	Elongated structures	*d*, ~591; *l*, ~1092 *d*, ~329; *l*, ~1050 *d*, ~476; *l*, ~1611		
Fe/Fe_3O_4 (Chapter V)	Rhombohedra	*d*, ~219 nm	Reduction reaction	Ferromagnetic

[a] Size is represented, based on the diameter (or width, *d*), length (*l*), and/or wall thickness (*t*) of nanostructures.
[b] NPs and NTs stand for nanoparticles and nanotubes, respectively.

7.2. Magnetic properties as well as electronic and structural properties of as-prepared FeMONS materials

Ferrimagnetic materials can function as ferromagnetic materials due to their spontaneous magnetization induced by an applied magnetic field. The size-dependent spontaneous magnetization observed from exploiting the sheer size effect of our as-prepared $BiFeO_3$ nanoparticles (*e.g.*, M_S at 50 kOe for 14 nm, the smallest nanoparticles for the highest magnetization: ~1.55 emu/g, 0.093 μ_B/Fe) is relatively small for general applicability as hard magnets in magnetic recording devices. Qualitatively, similar conclusions for $BiFeO_3$–$BaTiO_3$ solid solutions can be induced from the highest magnetization obtained (*e.g.*, ~1.88 emu/g at 50 kOe).

However, the outlook for specific applications such as spintronics (or spin-based electronics) and spin valves remains highly promising with $BiFeO_3$ nanostructures as well as for $BiFeO_3$–$BaTiO_3$ solid solutions, due to their high temperature multiferroic orderings when subjected to an electric as well as a magnetic field. For example, magnetic semiconductors are considered as fundamental materials for spintronics due to their multifuntionality in electric and magnetic fields. Specifically, incorporation of magnetic ions into wide band gap semiconductors such as GaN and ZnO results in potentially interesting room temperature applications, due to their high Curie temperature (T_C). Likewise, our as-prepared nanostructures of $BiFeO_3$, and of $BiFeO_3$–$BaTiO_3$ materials exhibit size-dependent spontaneous magnetization at room temperature, which is unexceptional due to the intrinsic physical properties of bulk $BiFeO_3$ at well-above room temperature (*i.e.*, T_C = ~1103 K and T_N = ~643 K). Moreover, size and shape dependent magnetic properties have been observed. The magnetic properties of as-prepared $BiFeO_3$ as well as other FeMONS materials are summarized in Table 7.2.

For the magnetic characteristics of $BiFeO_3$ nanotubes, nanotubes with a diameter of ~160 nm exhibit no coercivity indicating their superparamagnetic behavior as compared with those with a diameter of ~170 nm (*i.e.*, ~175 Oe). Both as-prepared $BiFeO_3$ nanotubes have exhibited a typical hysteretic behavior of weak ferromagnetics. The quantitative analysis of the spontaneous magnetization and magnetization measurement on the aligned $BiFeO_3$ nanotubes still remain challenging.

M/T curves for $Bi_2Fe_4O_9$ nanocubes have revealed their paramagnetic Curie temperature of -1434 K, indicative of antiferromagnetism. Moreover, their Néel temperature (~250 K) observed is slightly lowered, as compared with that of bulk (263 K). Magnetic behaviors of elongated $Bi_2Fe_4O_9$ structures are of fundamental interest, and the catalytic activity study of $Bi_2Fe_4O_9$ structures necessitate further scientific attention.

For the iron oxide nanostructures, we were able to create a nanocomposite with hard and soft magnetic phases juxtaposed within one discrete, anisotropic structure. The anisotropic structures of α-Fe_2O_3 as well as Fe/Fe_3O_4 nanostructures provide further

insights into coercivities. In their magnetic property measurements, the Fe/Fe_3O_4 nanocomposite exhibits a ~65% greater magnetization as compared with Fe_3O_4 magnetization. Furthermore, the Verwey transition temperature for our as-prepared nanocomposite increases up to ~135 K as compared with that of bulk Fe_3O_4 (~120 K). For α-Fe_2O_3 rhombohedra, the Morin transition (252 K) observed is lowered with respect to that of bulk (264 K).

The pre-edge *A* features in the O *K*-edge for our FeMONS materials provide a strong analytical tool in determining the electronic structure and chemistry of these different materials at the nanoscale as well as at the micron scale. For example, *A* features show no explicit splitting as compared with that of the bulk. Moreover, lower intensity ratios (I_A/I_B) in O *K*-edge data have been observed for $BiFeO_3$ nanoparticles as compared with that of the bulk, and a chemical shift to the higher energy region in the Fe *L*-edge has been observed for $BiFeO_3$ nanoparticles. As a complementary approach, a study of the angle/orientation dependence of aligned nanomaterials merits further attention.

Table 7.2. Summary of magnetic properties as well as electronic structure and chemistry of Fe-based metal oxide nanostructured (FeMONS) materials in this dissertation.

FeMONS materials	Magnetic properties (at RT)		Electronic structure and chemistry (Chapter VI)
	M_S at 50 kOe (emu/g)	H_C (Oe)	O *K*-edge
$BiFeO_3$ NPs [a] (≤ 100 nm) (Chapter II)	~0.36 – 1.55	~58 – 1550	Shoulder in *A* features.
$BiFeO_3$ NTs [a] (Chapter II)	N.A.[b]	0 (*d*, 160nm) ~175 (*d*, 270nm)	N.A.
$BiFeO_3$–$BaTiO_3$ (Chapter III)	~1.04 – 1.88	~660 – 3400	N.A.
Bulk $BiFeO_3$	No spontaneous magnetization observed.		Shoulder in *A* features.
$Bi_2Fe_4O_9$ cubes (Chapter IV)	T_N (~250 K) observed is lowered with respect to that of bulk (263 K). θ [d] = -1433.7 K		No shoulder in *A* features.
α-Fe_2O_3 rhombohedra (Chapter V)	The Morin transition (252 K) observed is lowered with respect to that of bulk α-Fe_2O_3 (264 K [e]).		No splitting in *A* features as compared with explicit splitting for bulk α-Fe_2O_3.
Fe/Fe_3O_4 rhombohedra (Chapter V)	M_S (emu/g)	H_C (Oe)	No splitting in *A* features.
	~100	~250	
	The Verwey transition (~135 K) observed is increased with respect to that of bulk Fe_3O_4 (~120 K).		

[a] NPs and NTs stand for nanoparticles and nanotubes, respectively.

[b] Spontaneous magnetization was observed, but quantitative magnetization measurements were not available (N.A.) due to the presence of the template in the sample.

[c] with respect to (w.r.t.)

[d] Paramagnetic Curie temperature obtained from the Curie-Weiss law, $\chi = C/(T - \theta)$.

[e] Amin, N.; Arajs, S. *Phys. Rev. B.* **1987**, *35*, 4810.

7.3. Summary and outlook

It is clear that FeMONS materials are of fundamental interest and exhibit promising chemical and physical properties that are essential for a broad range of potentially prominent technological applications. These materials provide useful building blocks for enabling the realization of a host of potentially highly complex multifunctional nanoscale device applications as diverse as additives, magnetic recording media, information storage, spintronics, and sensors. Moreover, their coupling among two or more of all of the ferroic orders coexisting in FeMONS materials suggests the development of "smart materials" for potential applications in many areas, and hence, a whole range of applications can be envisaged.

Though it is possible to produce FeMONS materials with predictable size and shape, this is not without its complications and key issues of nanostructure synthesis remain to be addressed.

1. The fabrication of crystalline nanostructures, with controllable size, shapes, and morphologies, on a large scale, using environmentally friendly protocols, represents a significant experimental challenge. In fact, reproducibly and simultaneously generating control over nanoparticle structure, surface chemistry, monodispersity, crystal structure, and assembly remains an elusive goal.
2. No clear understanding has been obtained for the nature of defects and their effects on properties in these FeMONS systems.
3. The exact growth mechanisms involved with synthetic methods used for creating FeMONS materials are often a matter of speculation. For instance, it is empirically known that factors such as temperature, ionic strength, solvent viscosity, as well as the presence or absence of organic surfactant during the experimental procedure play an important role in determining the morphology of the final products. However, the exact mechanism of how each individual variable precisely correlates with overall nanoparticle growth is rarely known. Importantly, it is experimentally non-trivial to kinetically probe the growth of these FeMONS structures.
4. Properties of nanomaterials, such as their mechanical transport, photoconductive, thermoelectric, electronic, optical, and catalytic properties, are theoretically expected to differ from those of bulk. Even though we have specifically addressed magnetic properties, little has been studied with respect to the other interesting properties of FeMONS structures due to the relative infancy of the field. Hence, it is very difficult to postulate any precise structure-property correlations at this point.
5. Potential health and environmental issues associated with these various synthetic protocols will need to be addressed in a timely fashion.

The rational design and synthesis of nanoscale materials as well as control of the formation of selected polymorphs are critical in fundamental studies, including the investigation of the shape and structural dependence of many properties, development of new pathways for materials synthesis, and the generation of new applications of nanostructured materials. FeMONS materials represent an important system for investigating low-dimensional chemistry and/or physics and are expected to provide a viable system for both interconnects and functional device elements in nanoscale electronics, magnetics, magnetoelectronics, and optoelectronics.

We believe that future work in this field will continue to focus on the development of rational nanoscale design aimed at fundamental property investigations and synthetic strategies aimed at resolving these issues with FeMONS materials, with technological advances arising from interdisciplinary contributions from teams of chemists, physicists, materials scientists, and engineers, thereby opening up new areas of nanoscience research.